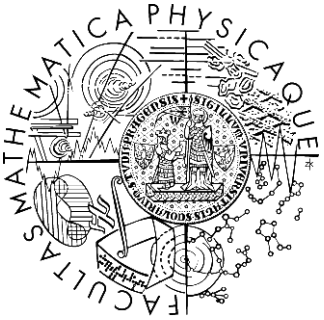

FACULTY
OF MATHEMATICS
AND PHYSICS
Charles University

DOCTORAL THESIS

Andrii Tovt

Role of surface defects in ceria-based catalysis

Department of Surface and Plasma Science

Supervisor of the doctoral thesis: doc.Mgr. Josef Mysliveček Ph.D.
Study program: Physics
Specialization: F-5 Surface and Interface Physics

Prague, 2018

I declare that I carried out this doctoral thesis independently, and only with the cited sources, literature and other professional sources.

I understand that my work relates to the rights and obligations under the Act No. 121/2000 Coll., the Copyright Act, as amended, in particular the fact that the Charles University in Prague has the right to conclude a license agreement on the use of this work as a school work pursuant to Section 60 paragraph 1 of the Copyright Act.

In…..... date.....

signature

Název: Role povrchových defektů v katalýze na oxidech ceru

Autor: Andrii Tovt

Katedra: Katedra fyziky povrchů a plazmatu

Vedoucí doktorské práce: doc. Mgr. Josef Mysliveček Ph.D., Katedra fyziky povrchů a plazmatu

Abstract: Práce se zaměřuje na analýzu základních fyzikálně-chemických vlastností modelových katalyzátorů Pt/CeO_x, atomárně dispergovaných Pt^1/CeO_x a inverzních modelových katalyzátorů $CeO_x/Cu(111)$. Byla vyvinuta metoda přípravy stabilizovaných atomově dispergovaných iontů Pt^{2+} na povrchu oxidu ceru a adsorpční místa pro ionty Pt byla studována s využitím pokročilých technik fyziky povrchů podporovaných teoretickými metodami. Byl identifikovan mechanismus stabilizace Pt^{2+} na schodech oxidu ceru a byla určena jejích kapacita pro Pt^{2+} ionty. Také byl vyvinut způsob přípravy velmi dobře uspořádaných ultratenkých vrstev oxidu ceru s různou stechiometrií a uspořádání povrchových kyslíkových vakancí a byla zkoumána interakce $CeO_x/Cu(111)$.

Klíčová slova: heterogenní katalýza, modelové systémy, katalýza jednotlivých atomů, ionty platiny, oxid ceru.

Title: Role of surface defects in ceria-based catalysis

Author: Andrii Tovt

Department: Department of Surface and Plasma Science

Supervisor of the doctoral thesis: doc. Mgr. Josef Mysliveček Ph.D., Department of Surface and Plasma Science

Abstract: This work concentrates on the analysis of fundamental physicochemical properties of $Pt\text{-}CeO_x$, single-atom Pt^1/CeO_x, and inverse $CeO_x/Cu(111)$ catalysts. Preparation method for stabilized atomically-dispersed Pt^{2+} ions on ceria was developed and adsorption sites for Pt ions were thoroughly studied using advanced surface science techniques supported by theoretical methods. The mechanism of Pt^{2+} stabilization on ceria steps was revealed and the step capacity towards Pt^{2+} ions was estimated. Also, the preparation method for well-ordered cerium oxide ultrathin films with different stoichiometry and ordering of surface oxygen vacancies was developed, and the Ceria/Cu(111) interaction was investigated.

Key words: heterogeneous catalysis, model systems, single-atom catalysis, platinum ions, cerium oxide.

Acknowledgements

I would like to thank my supervisor Josef Mysliveček for his guidance, fruitful discussions, detailed explanations and overall support during my PhD studies. Also, I'm grateful to my former supervisor Jiří Pavluch for the support and guidance during my initial steps in such complicated discipline as Surface Science. Special thanks to my colleagues Vitalii Stetsovych, Oleksandr Stetsovych, Filip Dvořák, Viktor Johánek, Iva Matolínová, Tomáš Duchoň, Daniel Mazur, and Vladimir Matolín, with whom it was always a pleasure to work.

Next, I would like to thank Anna Ostroverkh and Yevhenii Ostroverkh, who showed me moral support during my stay in Czech Republic, and Andrii Rednyk and Mykhailo Chundak who supported me during my stay in Japan. Life knowledge, obtained with the help of these people, I consider to be as valuable as the professional knowledge I received during my studies.

Last, but not least, I would like to express my special gratitude towards my parents and grandparents who stayed at my side even during the hardest times of my life abroad, and towards my younger sister who always provided a motivation to move forward.

My work was supported by Czech Science Foundation (GAČR 105-13/201462), and Grant Agency of Charles University in Prague (GAUK 105-10/259650 and GAUK 105-10/250115).

Contents

1. Introduction

1.1. Heterogeneous catalysis

Chemical industry is essential in modern world economics. It allows conversion of raw materials into various products. The development of science and technology increased the role of chemistry. The limited amount of natural resources, especially precious metals, motivates further research in the field of chemistry aiming to substitute these limited resources with more common materials.

The purpose of every chemical process is the conversion of rather cheap raw materials into more valuable products. In almost 80% of cases catalysts are used [1]. Catalyst is a material that effectively decreases the activation barrier of a chemical reaction hence causing it to run more rapidly. The three major properties of catalysts are their activity in the reaction, selectivity towards the reactants and stability at reactive conditions. Considering their physical state towards the reactants, catalysts are divided into homogeneous (those in the same physical state as the reactants) and heterogeneous (those in a different physical state compared to the reactants). We will focus our attention on heterogeneous catalysts.

In order to make the chemical reaction run smoothly one has to optimize the reacting system, process, and the catalyst. The main characteristics of a catalyst are its activity and selectivity. Technical heterogeneous catalysts, however, have to fulfill additional criteria [1]:

1. They are applied in large-scale technical reactors with reactor volumes from 1 up to several 100 m^3. This has consequences for the mass and heat transfer and the mechanical properties of the catalyst. It also requires a reasonable lifetime of the catalyst, including the rather trivial but nonetheless sometimes difficult demand to survive the chemical conditions, for example hot and strongly acidic liquid phases in the reactor.
2. The catalyst itself has to be manufactured in large scale equipment, that is, there has to be a reliable production process of solids for the catalyst, with all the challenges that are involved when it comes to the process technology of solids. The challenge is especially high when special catalysts are involved; these are only produced in small volumes and sometimes, due to long catalyst lifetime, with time elapsing between catalyst production campaigns.
3. Beyond that, however, there is also for technical catalysts the goal to improve the understanding of the elementary steps of the catalyzed reaction at the catalyst surface. In doing so, further improvements of the catalyst itself, and probably even more importantly,

the combined system of the catalyst and the catalytic process can be expected. A close co-operation between academia and industry has proven to be extremely fruitful for this task.

In order to develop more efficient catalysts, it is essential to understand the processes which occur during the chemical reaction and the contribution of a catalyst into the reaction as well as the chemical, structural and geometrical properties that determine the efficiency of a catalyst. However, under normal conditions the variety of physicochemical processes such as adsorption, desorption, diffusion, nucleation and dissociation, occurring simultaneously during the chemical reaction is large preventing examination of each of them separately [2]. In order to study each of the above-mentioned processes separately, one has to limit the influence of the other processes onto the catalytic system via setting up special conditions for preparation and measurement of this system.

1.2. Model catalysis

In order to develop catalysts with better activity, selectivity and stability, full understanding of the influence of separate parameters of a catalyst such as morphology, stoichiometry, or concentration of bulk and surface defects onto its performance in the chemical reaction is required. Simplification of the catalytic system as well as studying it under well-defined conditions allows tuning all its parameters separately resulting in better characterization of the catalyst. Model catalysts are a perspective approach and allow to achieve this [3], [4].

Model catalysts represent simplified well-ordered crystalline surfaces usually prepared and measured under well controlled conditions in ultra-high vacuum (UHV). This allows the use of various advanced surface science methods which are able to precisely measure the properties of such surfaces. However, the significant differences between the model and real catalysts represent so called “gaps” between surface science and heterogeneous catalysis: the materials gap and the pressure gap [5].

The materials gap represents the difference between the structural and compositional complexity of industrial catalysts and the well-defined surface of model catalysts of metals or oxides [6]. In order to bridge this ‘‘materials gap’’, model catalysts were developed, which allowed us to introduce certain complex features of real catalysts in a well-controlled fashion, but — at the same time — to avoid the full complexity of the real system. The development of these model systems is schematically illustrated in Figure 1.2.1 [7].

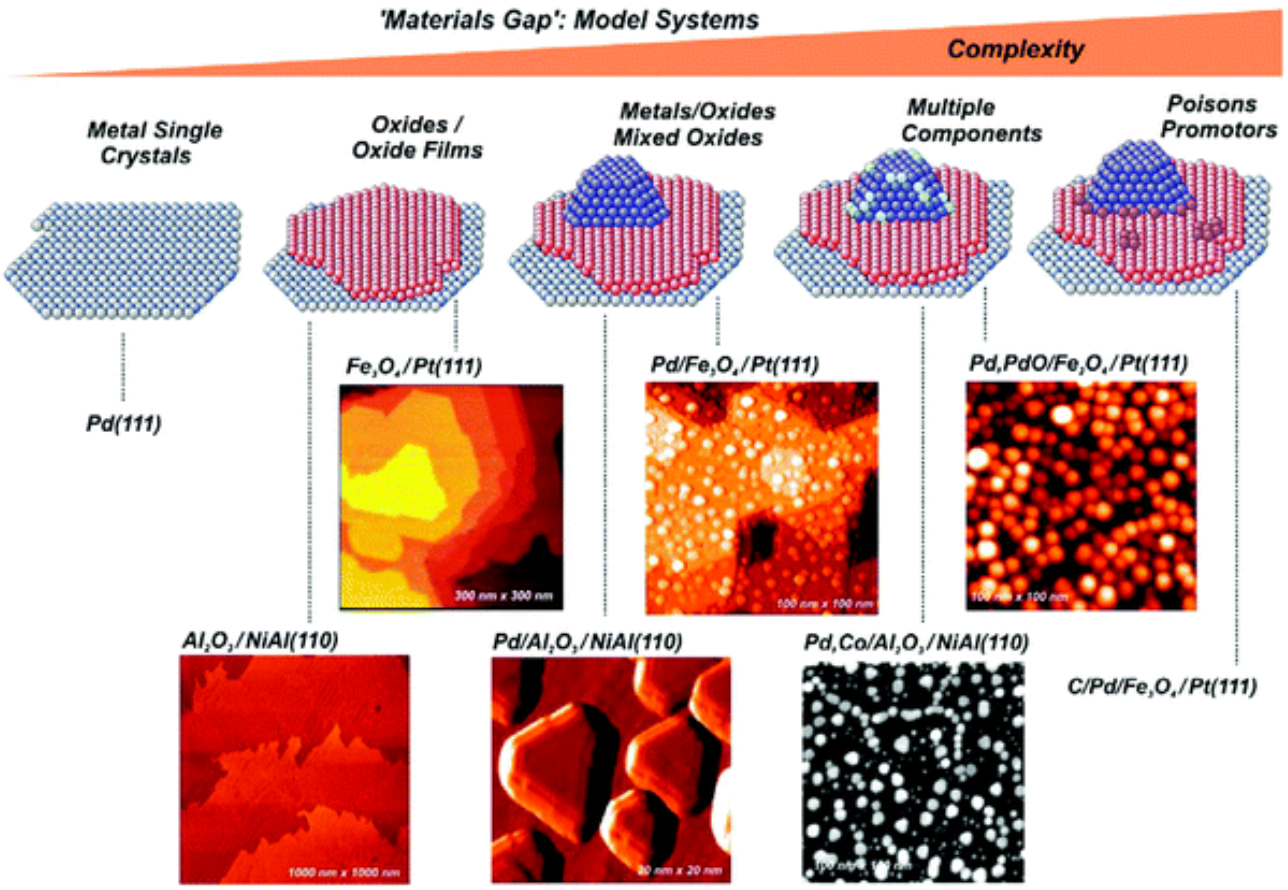

Figure 1.2.1 Development of the model systems in order to bridge the materials gap between surface science and heterogeneous catalysis, adapted from [7].

In a first step oxide nanocrystals or a well-defined epitaxial oxide film is prepared on a metal crystal surface [8], [9]. This allows detailed characterization of its physicochemical properties by a range of surface science methods such as scanning tunneling microscopy (STM) [10], [11], X-ray photoelectron spectroscopy (XPS) [12], low energy electron diffraction (LEED) and temperature programmed desorption (TPD). The charging effect of the oxide surface is diminished by using metal crystal as a substrate.

Next step involves introducing the active phase (metal nanoparticles) mainly with the help of the physical vapor deposition (PVD) [7]. The particle size can be varied by controlling the deposition parameters [13]. Further complexity of the system is achieved by additional surface modification or by introduction of additional active components, oxides or promoters.

The pressure gap is the difference in surface structure and chemistry between a catalyst under operation conditions of high temperature and pressure and under an ultrahigh vacuum (UHV) condition usual for surface science [6]. Bridging of this gap is achieved by introducing novel ambient pressure surface science methods such as high-pressure STM [14], [15], high-pressure

atomic force microscope (HP-AFM) [16], ambient pressure XPS [14], [17]; by combining the surface science methods (LEED, STM) with methods used under real conditions (infrared adsorption spectroscopy (IRAS) [18], [19], chemical reactor systems [20]–[22]), and by combining the surface science methods with theoretical calculations (Density Functional Theory, Monte-Carlo simulations) [23]–[26].

1.3 Single-atom catalysis

Metal nanoparticles on oxides possess considerable catalytic activity. These catalytic systems have enhanced active surface and lowered metal content. Recent development of these systems resulted in the development of single-atom catalysis.

In modern catalysis precious metals are used in most catalysts. Noble metals, such as Pt, Pd, Ru, Rh, and Ir represent superior heterogeneous catalysts and have been widely used in the petrochemical industry, drug production, environmental protection, and in energy conversion and storage. However, owing to the high price and low natural abundance of such noble metals, the production of these materials cannot meet the increasing demand. As an illustrative example we take a brick with the dimensions 20×10×5 cm, made of pure gold with a price of $38.1 per gram, and worth approximately $736 000. If a common brick worth 20 cents is coated with an atomically thin layer of gold, the cost of the gold layer is 1 cent and the total value is just 21 cents (Figure 1.3.1). The gold-coated brick, despite only having an extremely thin layer containing gold, is still capable of accelerating and controlling the overall chemical reaction because, essentially, only the surface atoms of the catalyst are necessary for heterogeneous catalysis. Thus, one of the strategies to cost reduction is to maximize the exposition of surface atoms of noble metals to reactants [27].

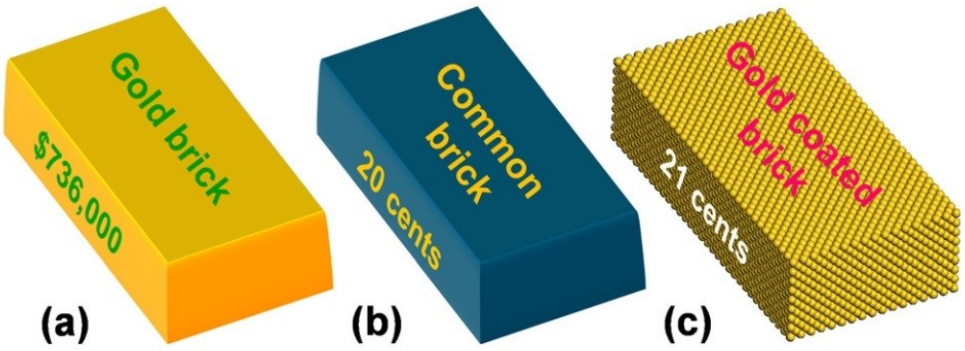

Figure 1.3.1 Prices of different bricks with a size of 20x10x5 cm; a) gold brick; b) common brick; c) common brick coated with a single atomic layer of gold atoms. Adapted from [27].

A perspective approach maximizing the efficiency of noble metals use is so called "single-atom catalysis" [28]. It is currently one of the most innovative and fastest growing research areas in the field of catalysis. Several key factors have contributed to this rapid development. Continued advancements in techniques of characterization have made feasible the experimental evidence of the presence of atomically dispersed metal species, thereby enabling an improved understanding of their structure, stability, and catalytic properties [29]. Another attractive feature is the apparent simplicity that single atoms offer with respect to the identification of the active sites of a single-atom catalyst [30].

The synthesis of single-atom catalysts and the control of the electronic properties of catalytic sites is a major challenge in heterogeneous catalysis [31]. The surface free energy of metals increases significantly with decreasing particle size, promoting aggregation of small clusters. Using an appropriate support material that strongly interacts with the metal species prevents this aggregation, creating stable, finely dispersed metal clusters with high catalytic activity [32], [33]. Model catalytic approach allows preparation of well-defined single-atom catalysts with controlled density of active sites for stabilization of metal single atoms [34]. The existing methods of preparation of single-atom catalysts include high-vacuum physical deposition techniques (e.g., a mass-selected soft-landing method and an atomic layer deposition method) and wet-chemical routes [35]–[37]. Vacuum deposition of single atoms is easier to control and can provide desirable model catalysts for fundamental studies of metal–support interactions and the particle size effect. However, it may not be possible, at least at the moment, to use this technique to produce commercial catalysts for industrial applications due to the high cost and low yield. So far, wet-chemical routes have been mainly used to synthesize single-atom catalysts because this method does not require specialized equipment and can be conveniently practiced [37].

Single-atom catalysts are efficient in various chemical reactions. Many recent works show an excellent performance of single atom catalysts in CO oxidation [38]–[57], hydrogen production [58]–[61], production of anilines [35], production of different fuels and acids (HCOOH, CH_4, CH_3OH, etc.) [62], solar cells [63], production of hyperpolarized fluids [64], hydrogenation of nitrobenzene and cyclohexanone [65]. Among the various investigated catalysts, the best performance in these reactions exhibit Au and Pt single atoms on different supports: reducible oxide thin films and clusters [66]–[69], carbon nanotubes [60], [70] and graphene [36], [59]. Platinum single-atom catalysts were estimated to have the best performance in hydrogen evolution reaction –

up to 37 times more active than the commercial samples [59]. Also, they have better activity towards the CO oxidation reaction than Ni and Ir single-atom catalysts [51], [52].

Many theoretical works explain this excellent reactivity of Pt atoms towards CO oxidation and hydrogen evolution reaction [40], [42], [43], [50], [54], [57], [59], [67]. An example of a proposed catalytic cycle of stabilization of Pt single atoms on Al_2O_3 surface is discussed in [42]. Single supported Pt atom prefers to bond to O_2 over CO. Carbon monoxide molecule, therefore, bonds to oxygenated Pt atom and forms a carbonate, which then dissociates to liberate CO_2, leaving an oxygen atom on Pt. Subsequent reaction with another CO molecule regenerates the single-atom catalyst. Supported Pt atoms are catalytically active and this catalytic activity can occur without involving the substrate [43].

Whereas the performance of Pt single atoms in chemical reactions has been broadly discussed, the stabilization mechanism of these atoms at the support is studied in few works [65], [68]. Chang et al. [68] investigated the adsorption sites of the Pt atoms on TiO_2 using aberration corrected STEM. Combining the experimental results with the systematic density functional theory calculations revealed that the most favorable Pt adsorption sites were on vacancy sites of basal oxygen atoms located in subsurface positions relative to the top surface bridging oxygen atoms. Zhang et al. [65] investigated Pt atoms on acid-modified active carbon and came to conclusion that they are stabilized by four oxygen atoms in a distorted square-planar geometry. However, the analysis of the influence of surface defects, such as steps and vacancies on the stabilization of Pt single atoms still needs clarification, the question of measuring the charge transfer between Pt single atoms or nanoparticles and an oxide support remains unanswered, and a common well-developed methodology for preparation of model Pt single-atom catalysts is still a challenge. The presented thesis is proposing the approach to solve these challenges.

1.4 Reducible metal oxides

Reducible metal oxides are among the most important and widely used substances in modern chemical industry. The main reason for this is given by their wide application in different industrial areas: heterogeneous catalysis [71], fuel and solar cells [72], [73], batteries [74], gas sensors [75] and electronic devices [76]. Reducible metal oxides show a unique property of facile absorption, storage and release of oxygen, which is essential in many catalytic reactions [77], [78]. Modifying their surface structure with metal adatoms or nanoparticles increases the number of surface active sites which improves the overall catalytic activity of the system [79].

The most investigated and used reducible oxide in modern chemistry is titanium dioxide. In addition to the above-mentioned industrial applications, it is also important in earth sciences, plays a role in the biocompatibility of bone implants, is being discussed as a gate insulator for the new generation of MOSFETS and as a spacer material in magnetic spin-valve systems, and finds applications in nanostructured form in Li-based batteries and electrochromic devices [80]. Other widely used reducible metal oxides include copper oxide [81], iron oxide [82], cobalt oxide [83], manganese oxide [84], vanadium oxide [85], praseodymium oxide [86] and cerium oxide [87].

1.5 Cerium oxide

Metallic cerium (Ce), with a $4f^2 5d^0 6s^2$ electron configuration, is highly active towards oxidizing in oxygen-rich atmosphere and forms an oxide capable of easy absorbing, storing and releasing of oxygen. This property of cerium oxide, or ceria, is being widely used in modern chemical industry [88], [89]. While storing and releasing oxygen, cerium oxide shifts between two limiting stoichiometric phases: the fully oxidized cerium dioxide (CeO_2, all cations are Ce^{4+}) and the fully reduced cerium sesquioxide (Ce_2O_3, all cations are Ce^{3+}). Bulk CeO_2 has a fluorite-like structure with face-centered cubic unit cell (lattice parameter a = 5.41134 Å) in which each cerium cation is surrounded by eight neighbor oxygen anions as shown in Figure 1.4.1 (a). The C-type structure of Ce_2O_3 [Figure 1.4.1 (b)], which is the end product of the reduction process of CeO_2, has a bixbyite structure, and can be constructed out of eight unit cells of CeO_2 with 25% oxygen vacancies ordered in a particular way [90].

CeO_2 is more stable than Ce_2O_3 which rapidly oxidizes in an oxygen-rich atmosphere. It is possible to reduce the ceria under the reducing conditions. Removing the oxygen atom stimulates the localization of two 4f electrons on two neighboring Ce^{4+} ions forming Ce^{3+} [91], [92]. Due to one excess electron, the radius of Ce^{3+} ions is bigger than of Ce^{4+}. Together with the increasing degree of reduction, the lattice parameter of cubic ceria increases. Oxygen vacancies together with other surface defects form low-coordination surface sites of a ceria surface [93], [94].

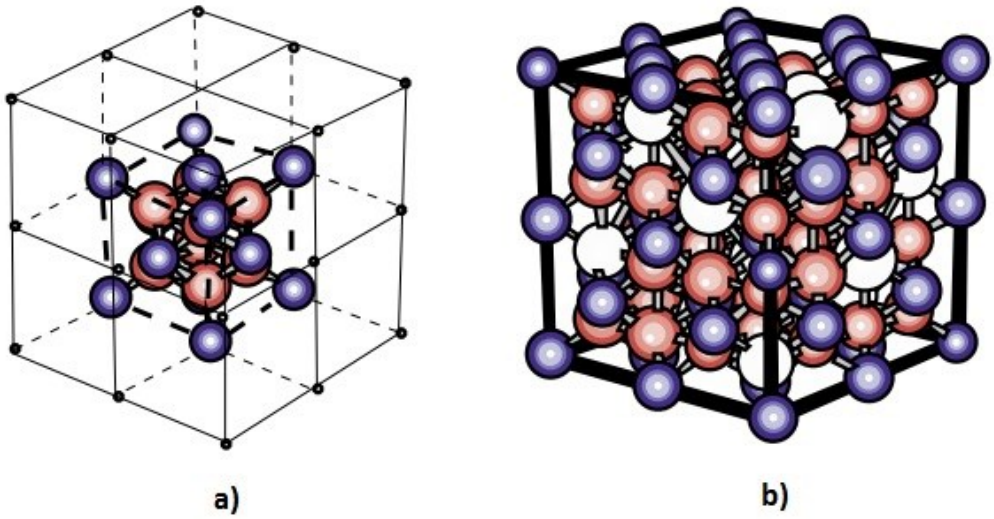

Figure 1.4.1 Bulk unit cells for CeO_2 (a) and Ce_2O_3 (C-type) (b). A cubic unit cell of C-type Ce_2O_3 can be constructed out of eight CeO_2 unit cells by increasing their volume by 3% and removing 25% of the oxygen atoms along four nonintersecting {111} diagonals. Blue, red, and white spheres indicate the cerium, oxygen atoms, and vacancies, respectively. Adapted from [90].

The preparation of thin ordered epitaxial ceria films on metal substrate has been a challenge in model catalysis. The common preparation method is the evaporation of Ce material onto the metal single crystal surface [Cu(111), Ni(111), Ru(0001)] in oxygen background atmosphere with a subsequent annealing at higher temperatures [95]–[102]. Controlling the deposition and annealing parameters provides a good control over the morphology of ceria thin films such as: the coverage of the surface, the concentration of surface adsorption sites (steps and defects) and the ordering of the film [103]. Whereas this method proves to be efficient in producing CeO_2 thin films, the question of creating well-ordered Ce_2O_3 films as well as transition CeO_x films is more challenging. The existing preparation methods are based on modifying the CeO_2 film via annealing in UHV at elevated temperatures [104], via interaction with hydrogen or methanol [105], or via the interaction with metallic ceria [106]. The first two methods lead to the formation of a reduced ceria thin film with disordered surface oxygen vacancies. The preparation method developed in our working group and based on the interaction of metallic cerium with a CeO_2 thin film allows to create reduced ceria thin films with well-ordered surface vacancies and long-range periodicity, revealed by scanning tunneling microscopy, low-energy electron diffraction, resonant photoelectron spectroscopy and X-ray photoelectron spectroscopy [107], [108]. However, the question of preparation of reduced ceria ultrathin films (2-3 monolayer thick) together with their precise characterization remains unsolved.

The presented work provides the solution to this question and gives a thorough analysis of the reduced ceria ultrathin films.

Ceria-based catalysts find their application in gas sensors [75], fuel cells [72] and three-way automotive catalysts [87], [109]–[112]. The water splitting properties of Ce_2O_3 also allow its application for hydrogen production [113], [114]. Cerium oxide has proved to be an efficient support for single-atom catalysts, its stoichiometry has a great influence on the state of the surface metal adatoms [111]. Therefore, controlling parameters of the ceria support provides the necessary control over the metal adatom state.

1.6 Experimental control of defects on CeO_x model catalysts

Every prepared model system has defects: steps, kinks, vacations, dopants, metal-oxide interface etc. The role of defects is important in catalysis. They serve as active sites in chemical reactions and they also play key role in stabilizing metal atoms in single-atom catalysts [34], [87], [91], [115], [116]. Preparing model systems with well-defined and controllable concentration of defects is an important task in model catalysis.

In our group, methods for preparation of model CeO_x thin films on Cu(111) single crystal with controllable thickness, concentration of steps and oxygen vacancies were developed [103], [106], [108]. Figure 1.6.1 shows STM and LEED images of well-ordered CeO_x films with controllable concentration of oxygen vacancies and density of steps (Figure 1.6.1). The prepared films served as a starting point in the present work and were used for reactivity measurements, stabilization of Pt atoms and development of inverse model systems with controllable stoichiometry.

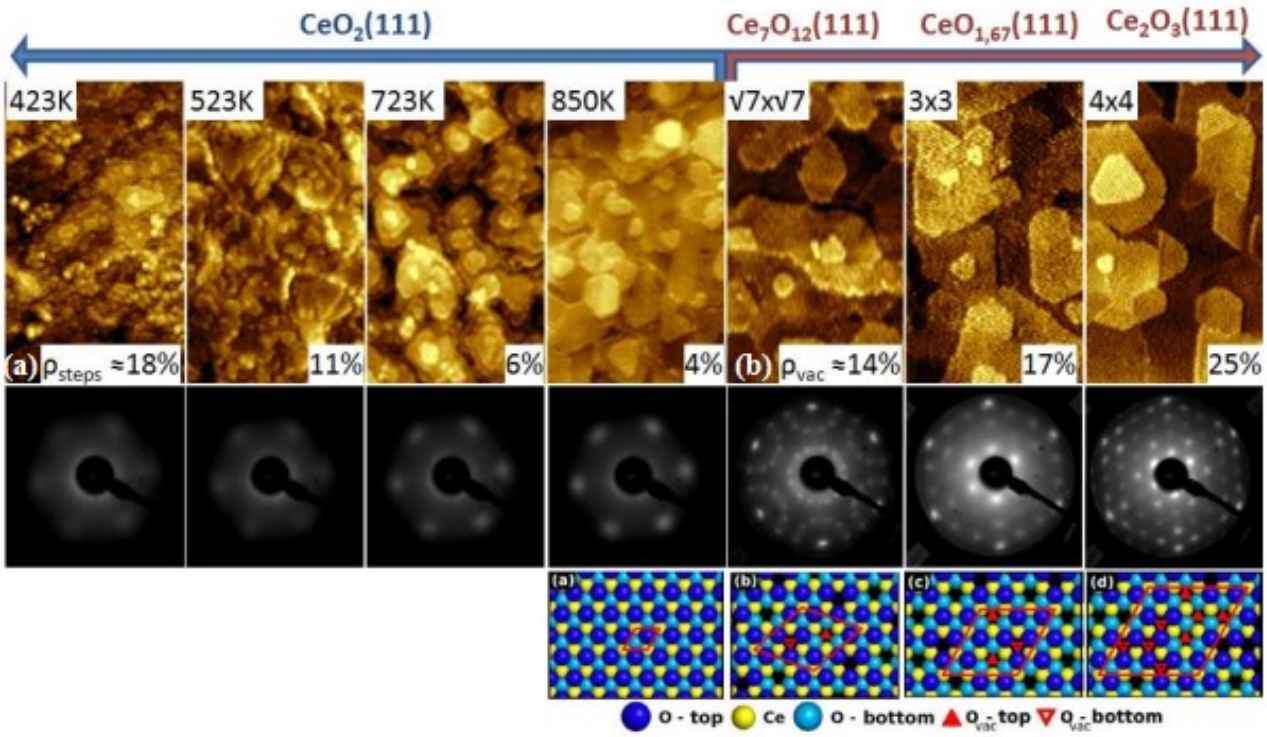

Figure 1.6.1. Overview of model ceria surfaces with adjustable step density, oxygen vacancy concentration, and oxygen vacancy ordering. In the top row, the morphology of the ceria surfaces is visible as revealed by STM (unoccupied states). Middle row shows the corresponding diffractograms obtained by LEED. Bottom row shows proposed models of the surface structure of the reduced CeO_x(111). The preparation temperature, the surface reconstructions due to ordering of surface O vacancies, and concentrations of surface oxygen vacancies (b) and surface monoatomic steps (a) are labeled in the corresponding images. Adapted from [117].

1.7 Scope of the thesis

The current work focuses on the studies of surface defects of model catalysts represented by CeO_x thin films on Cu(111), on the reaction properties of these defects, and on the role of surface defects in accommodation of the Pt deposit on CeO_x. Pt on ceria has outstanding catalytic properties, the system is thus of a great scientific interest. Presented investigations of this system led to the development of new preparation and characterization methods such as determining metal-oxide charge transfer in Pt/ceria and preparation of Pt^1/CeO_2 single-atom catalyst. It has been discovered, that ceria step edges stabilize Pt atoms in ionic Pt^{2+} state, whereas oxygen vacancies usually stabilize

it in Pt^0 or $Pt^{\delta+}$ state. The control over the surface reduction of the ceria and its surface step coverage allows to prepare Pt^1/CeO_2 single-atom catalysts with different Pt loading.

Apart from Pt stabilization properties, reactivity measurements of continuous CeO_x thin films with different stoichiometry towards H_2O dissociation were performed and the role of concentration and ordering of oxygen vacancies was estimated. Third, based on the developed preparation method of continuous CeO_x films with controllable stoichiometry, inverse model systems of ultrathin and discontinuous CeO_x films on Cu(111) with controllable stoichiometry were prepared and studied.

The presented thesis consists of five chapters. The first chapter of the thesis characterizes Pt/CeO_2 model catalysts with different Pt loading and evaluates the Pt-ceria charge transfer using SRPES and STM surface science methods. The developed charge transfer evaluation method was suggested to be applied for other model systems on ceria support. The second chapter concentrates on the preparation of Pt^1/CeO_2 model single-atom catalysts and evaluation of the influence of different surface properties of ceria on the dispersion and chemical state of Pt adatoms. Platinum single atoms were found to stabilize as Pt^{2+} ions at step edges of the fully oxidized ceria support and theoretical calculations revealed the adsorption geometry for Pt^{2+} ions. The third chapter investigates the maximum Pt load for the ceria step edges. The interplay between the surface oxygen content of ceria and Pt^{2+} concentration was estimated. The fourth chapter is dedicated to study of the H_2O adsorption onto continuous CeO_x thin films with different stoichiometry. The influence of concentration and position of surface oxygen vacancies onto the activity of the CeO_x model system towards water splitting was analyzed. Finally, the fifth chapter deals with the preparation and characterization of inverse model $CeO_x/Cu(111)$ systems with different stoichiometry. Atomically-resolved images of different surface reconstructions were obtained and the influence of metal-oxide interaction on the properties of the inverse model catalysts was examined.

2. Experimental

This chapter describes the surface science methods applied in the presented thesis. A brief introduction of the Scanning Tunneling Microscopy (STM), X-ray Photoelectron Spectroscopy (XPS), Thermodesorption Spectroscopy (TDS) and Low-Energy Electron Diffraction (LEED) is given and the relevant data processing methods is described. Special attention is given on the sample preparation procedures applied in this work.

2.1 Scanning Tunneling Microscopy

Scanning Tunneling Microscopy is a powerful tool for imaging solid surfaces down to the atomic scale invented by Binnig and Rohrer and implemented by Binnig, Rohrer, Gerber, and Weibel [118], [119]. The principle of the STM is straightforward. Figure 2.1.1 shows its essential elements. Tungsten or Pt-Ir tip is positioned upon the measuring surface using XYZ plane positioning piezoceramics. By applying a sawtooth voltage on the x piezo and a voltage ramp on the y piezo, the tip scans on the xy plane. Using the coarse positioner and the z piezo, the tip and the sample are brought to within a fraction of a nanometer within each other. The wave functions of the tip and sample overlap, enhancing the tunneling conductance. By applying the tip-sample voltage, tunneling current is generated.

The tunneling current is converted to a voltage by the current amplifier and compared with a reference value. The difference is amplified to drive the z piezo. The phase of the amplifier is selected to provide a negative feedback: if the absolute value of the tunneling current is larger than the reference value, then the voltage applied to the z piezo tends to withdraw the tip from the sample surface, and vice versa. As the tip scans over the xy plane, a two-dimensional array of equilibrium z positions, representing a contour plot of the equal tunneling-current surface, is obtained, displayed, and stored in the computer memory [120]. This scanning mode is called constant current mode. The benefit of this mode is its ability to scan uneven surfaces, but the feedback limits the scanning speed. Another scanning mode is constant height mode, where the tip is stabilized at the fixed height above the sample and the tunneling current difference is being plotted. This mode allows a very rapid scanning, but is limited to only atomically-flat surfaces. The most commonly used scanning mode is the constant current mode.

The topography of the surface is displayed on a computer screen, typically as a gray-scale image which is further stored in the memory. The gray-scale image is similar to a black-and-white television picture.

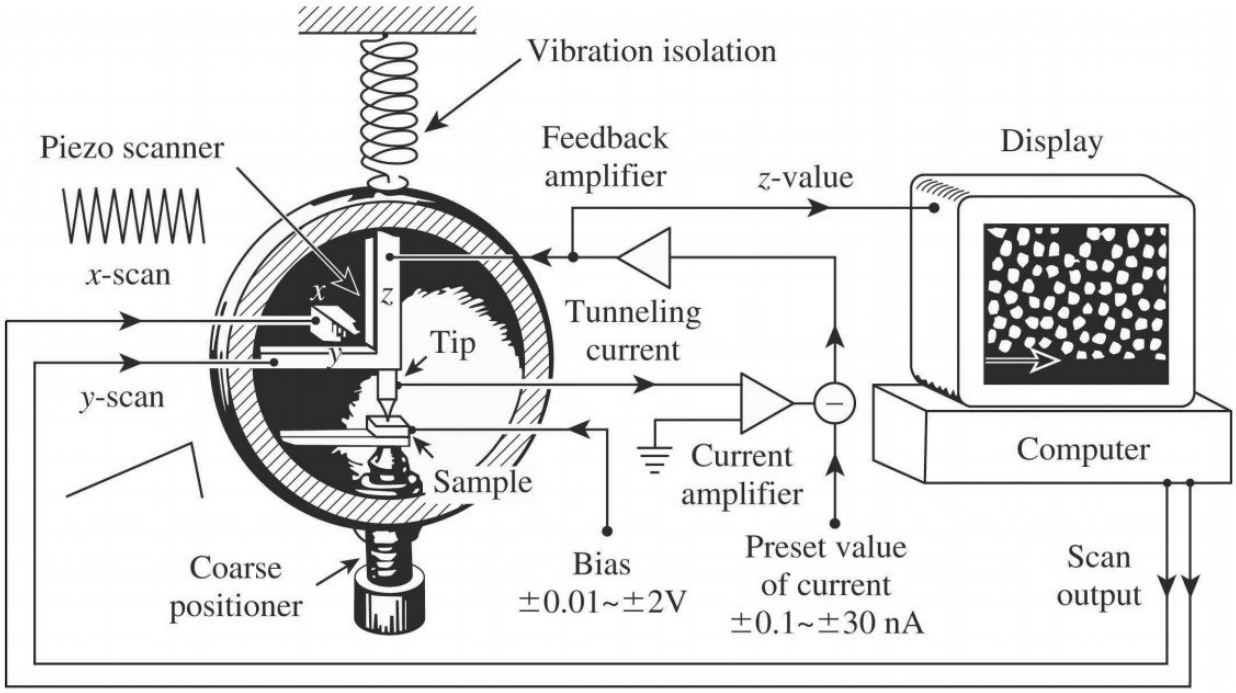

Figure 2.1.1. The scanning tunneling microscope in a nutshell. The scanning waveforms, applying on the x and y piezos, make the tip raster scan on the sample surface. A bias voltage is applied between the sample and the tip to induce a tunneling current. The z piezo is controlled by a feedback system to maintain the tunneling current constant. The voltage on the z piezo represents the local height of the topography. To ensure stable operation, vibration isolation is essential. Adapted from [120].

In order to achieve good resolution in STM several conditions have to be preserved. First, since the tip-sample distance is 1nm or less, the whole system should be isolated against the vibrations. This is achieved by making the STM unit as rigid as possible, and by reducing the influence of environmental vibration to the STM unit [120]. Second, the resolution of the microscope depends on the tip condition: cleanliness, shape and stability, therefore, different approaches were developed in order to achieve clean sharp stable tip: chemical etching, Ar sputtering, tip formation using carbon nanorods or dipole molecules, etc. Third, appropriate grounding of the electronics and the use of high-quality low-noise amplifiers are essential in order to reduce the electric noise of the system. Finally, the response of the piezo-scanner towards the voltage change is nonlinear and, therefore, appropriate time constant should be selected during scanning process in order to avoid the distortion of the image [121].

The interpretation of the STM images is not straightforward. The technique provides mapping of the electronic structure of the surface [120], modified by the electronic structure of the

tip, which not always has a direct connection with the topgraphy of the surface. The geometry and the chemical composition of the tip strongly influence the image contrast and sometimes change of the tip apex structure results in the inversion of the contrast. In order to provide satisfactory image interpretation, STM is usually coupled with other surface science methods and theoretical simulations (DFT+U, Bardeen's perturbation theory, Tersoff-Hamann approach, etc.) [122]–[124]

Despite the challenges in measurement and interpretation, STM has become a powerful surface science method and is widely used in science. It allowed to characterize and understand many surface phenomena, such as surface defects and reconstructions, adsorption sites, surface strain and surface catalytic reactions [125]–[127]. Further development of the technique allowed to obtain more information about the surface: for example, the development of Scanning Tunneling Spectroscopy provided the information of the electronic states near the Fermi level of the surface [120], modulation of the tunneling current allowed mapping of the distribution of the surface work function [128], and the development of the four-probe STM made it possible to measure surface conductivity [129]. Implementation of the ambient-pressure STM bridged the pressure gap between the model and real catalysis [127].

In this work, Scanning Tunneling Microscope surface science technique is extensively used to make quantitative characterization of the morphology of CeO_x and Pt/CeO_x systems. Analyzing the statistics of Pt clusters on ceria surface helped to reveal the optimal cluster size for maximum Pt/Ceria charge transfer value per Pt atom (Chapter 3.1). Also, statistics of Pt clusters on Pt^1/CeO_2 model system helped to disclose the existence of 90% of Pt deposit in ionic Pt^{2+} state, which was later confirmed by XPS and SRPES measurements (Chapter 3.2). STM measurements provided possibility to make quantitative evaluation of step density of CeO_2 thin films which was essential parameter in determining the step capacity towards Pt^{2+} stabilization (Chapter 3.3). Without STM measurements, the study of the influence of surface defects of ceria on stabilization of Pt ions would not be possible. In experiments concerning inverse model $CeO_x/Cu(111)$ systems, STM was used to identify morphology and ordering of the prepared films revealing (1×1), (√7×√7), (3×3) and (4×4) surface reconstructions of ceria (Chapter 3.5).

2.2 Photoelectron Spectroscopy

Many catalytic properties of the materials depend on their chemical composition. Photoelectron Spectroscopy is a non-destructive surface science technique which allows to measure electronic structure of a specimen, providing information about its chemical structure. It includes

various spectroscopy methods, depending on the energy of the used primary photons and on the implementation of the photon source: X-ray Photoelectron Spectroscopy (XPS), Ultraviolet Photoelectron Spectroscopy (UPS) and Synchrotron Radiation Photoelectron Spectroscopy (SRPES) including Resonance Photoemission Spectroscopy (RPES). In the present work XPS, SRPES and RPES measurements were broadly used in order to determine chemical composition of the prepared model systems.

X-ray Photoelectron Spectroscopy (XPS) is a is a broadly-used non-destructive, surface sensitive analytical technique. XPS provides information about the elemental composition, empirical formula of pure material, surface contamination, and chemical/electronic state of the elements [130].

The principle of XPS is based on the photoelectric effect, in which electrons (called photoelectrons) are emitted from the matter as a result of the absorption of the X-ray electromagnetic radiation. Figure 2.2.1 shows the experimental setup, the photoelectron emission process and the example of an XPS spectrum. Radiation, produced by an X-ray source (usually Al Kα or Mg Kα), is directed at the grounded sample and the emitted photoelectrons are detected by an energy analyzer. The electron excitation process can be described as a sequence of the following steps: absorption of photon by electron in the sample, excitation of the photoelectron, transport of the photoelectron through the sample to the surface and photoelectron transition to the vacuum by overcoming the surface potential barrier. The kinetic energy of the photoelectrons is detected by a hemispherical electron energy analyzer. The value of this energy equals the energy of the absorbed photon minus the binding energy of the electron in its ground state and the analyzer work function. Hence, the kinetic energy distribution provides the information about the electronic structure of the sample and is characteristic for each element. The surface sensitivity of the XPS is given by the information depth of photoelectrons associated with the inelastic mean free path of electrons (IMFP) in studied material. This parameter depends on the properties of the examined sample making precise quantitative analysis of the XPS spectra more challenging, especially for typical samples investigated in the present thesis – Pt deposit on CeOx thin films supported by Cu(111).

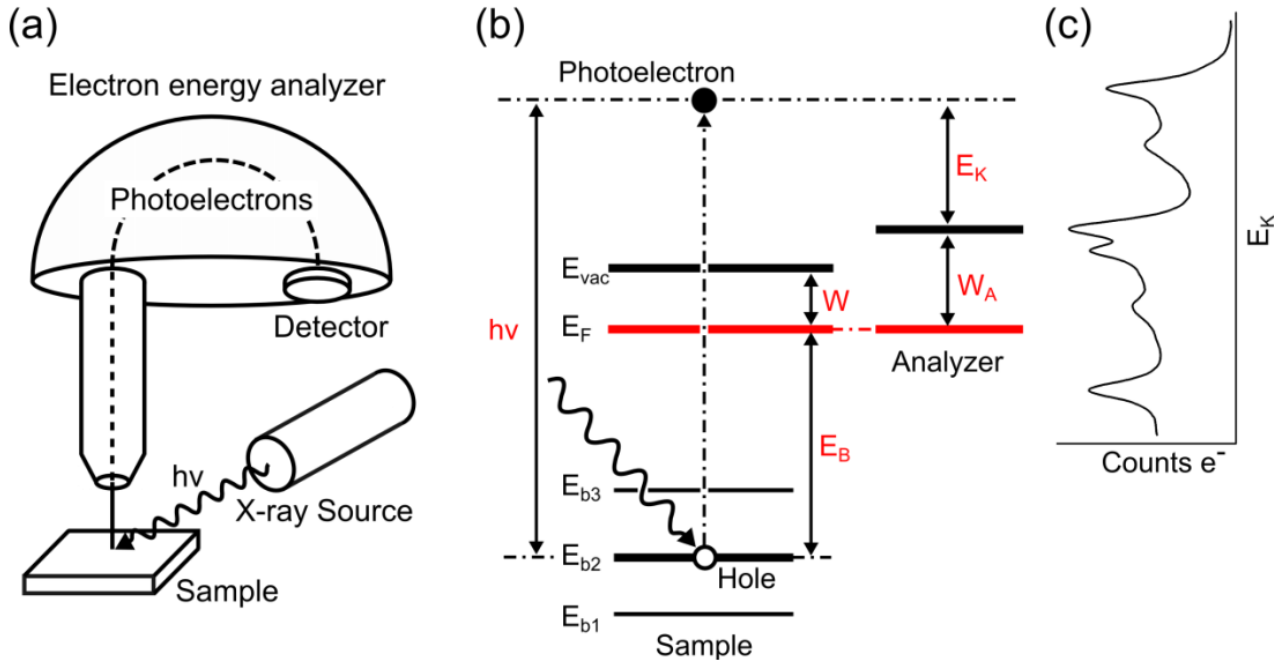

Figure 2.2.1. Schematics of XPS: (a) experimental setup; (b) the illustration of the photoelectron emission process, Eb binding energy in solids, EF fermi level, Evac vacuum level, W work function, Ek detected kinetic energy of photoelectron; (c) the illustration of XPS spectra. Adapted from [117].

In XPS with primary photon energy 1486.6 eV, IMFP for Cu 3p (binding energy [BE] = 75eV) photoelectrons travelling through CeO_2 film grown on Cu(111) crystal is 2,29 nm. Binding energy of the Pt 4f photoelectrons is 73 eV for Pt^{2+} and 71.5 eV for Pt^0. With typical CeO_x film thickness of 2.5 nm, Pt 4f spectrum contains high signal of Cu 3p doublet which overlaps with the Pt signal (Figure 2.2.2a,b). Hence, the surface sensitivity of XPS is insufficient especially for measurements of low quantities of Pt deposit. In order to achieve better surface sensitivity and exclude influence of the copper substrate, lower primary energy of photons is required. One of the ways to solve this challenge is using synchrotron radiation and the analysis method based on it: Synchrotron Radiation Photoelectron Spectroscopy (SRPES).

Synchrotron Radiation Photoelectron Spectroscopy (SRPES) is a non-destructive, surface sensitive analytical technique which allows to achieve better surface sensitivity via tuning the energy of primary photons. The assembly of SRPES is similar to XPS with only difference in the radiation source, which in case of SRPES is synchrotron radiation. The ability to select the energy of the synchrotron light provides the possibility of achieving high surface sensitivity. For example, at 180eV primary photon energy, the IMFP for Cu 3p photoelectrons is only 0.475nm which at 2.5 nm

thickness of CeO_2 film allows complete suppression of the Cu doublet from the substrate (Figure 2.2.2c).

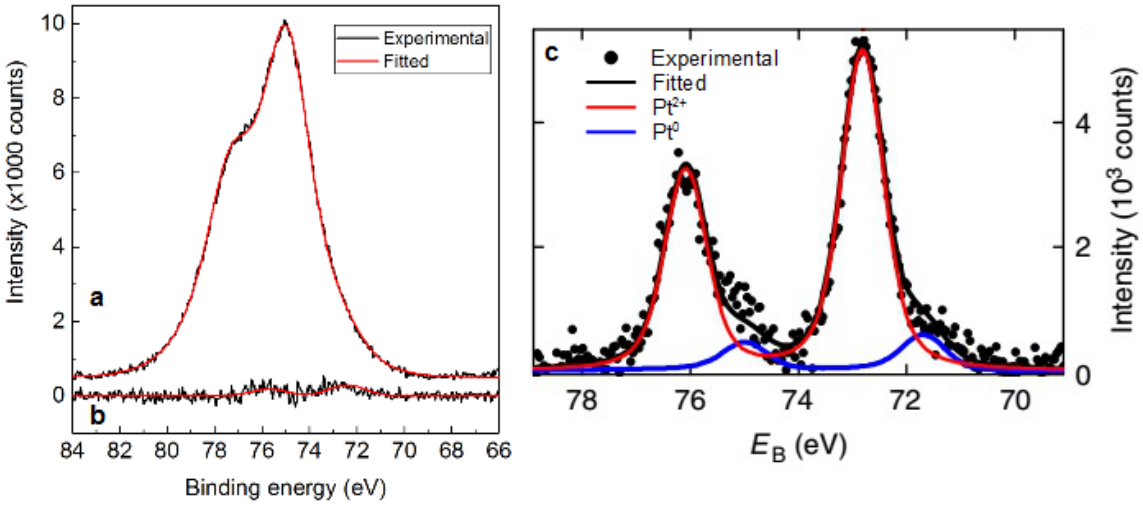

Figure 2.2.2 XPS and SRPES measurements of 0.05ML of Pt deposit on CeO_2 surface: a) XPS spectra with Cu doublet; b) same spectra with subtracted Cu doublet; c) SRPES measurements of the same film, adapted from [131].

Tuning the primary energy of the photons enables the technique of Resonant Photoemission Spectroscopy (RPES). Under certain conditions, the photon energy can be adjusted to stimulate the simultaneous emission of photoelectrons through alternative processes, e.g. the direct emission and the Auger emission. The mutual interaction of alternative emission processes gives rise to the resonant photoemission, which leads to a dramatic increase of the sensitivity of the measurements [117], [132], [133]. In cerium oxide, resonance enhancement of the Ce^{3+} and Ce^{4+} signal in the valence band allow determining the stoichiometry of the ceria samples with very high resolution and high surface sensitivity [132].

In modern science and technology, XPS is one of the most commonly used methods for chemical composition measurements. It allows characterizing different types of materials such as metals, alloys, polymers, semiconductors, geological and biological samples, and generally any samples which are compatible with high vacuum systems. Coupling the XPS with other surface science methods provides the detailed characterization of the examined surfaces. Recent development of the Ambient Pressure XPS (AP-XPS), designed for measurements at higher pressure, bridged the pressure gap to a great extent between the model and real catalysis [134].

In this work, XPS was used for quantitative characterization of the thickness and the stoichiometry of ceria thin films as well as for qualitative estimation of Pt deposit: its existence and chemical state. In order to make quantitative evaluation of the deposited low quantities of Pt and for

determining the amount of Pt^{2+} ions in the Pt deposit, SRPES measurements were performed (Chapters 3.1, 3.2). In order to estimate the stoichiometry of the reduced ceria films with high sensitivity, RPES measurements were performed (Chapters 3.1, 3.2, 3.3). XPS was also used in the measurements of reactivity of H_2O on CeO_x in order to estimate the stoichiometry of CeO_x film before and after adsorption-desorption cycles of water molecules (Chapter 3,4). In experiments concerning inverse model CeO_x/Cu(111) systems, XPS was used for evaluation of stoichiometry of ceria films (Chapter 3.5).

2.3 Low-energy Electron Diffraction

Low-energy Electron Diffraction (LEED) is a highly surface-sensitive technique used to study the crystal structure of surfaces. The schematics of the setup as well as the example of the LEED pattern are shown in Figure 2.3.1. The experimental setup consists of an electron source, a set of grids, a fluorescent screen, and a CCD camera. Electrons, emitted from the electron source, are directed at the sample. The energy of the electrons is in the range of 20-500 eV, which corresponds to their wavelengths below 0.3 nm. Since the electron wavelength is comparable with the interatomic distances in the solids, the electrons undergo diffraction. The diffracted electrons move back towards the fluorescent screen in specific directions, determined by the surface crystallography. They are energy-filtered and accelerated by a set of grids and hit the surface of the screen, causing a fluorescent glow.

LEED pattern from a well-ordered surface produces sharp diffraction spots which correspond to the image of surface lattice in reciprocal space. The distance between the LEED spots in reciprocal space is inversely proportional to the interatomic distances of the lattice in real space. Kinetic analysis of the LEED patterns provides the information about the interatomic distances, the ordering of the surface layer and surface reconstructions. Using the dynamic theory (I-V LEED), more complicated analysis of the spot intensity in relation to the electron energy can be performed and the detailed information about the lattice atomic composition can be obtained. LEED allows the determination of the lattice parameters, surface reconstructions, surface relaxations, and adsorption geometry [135].

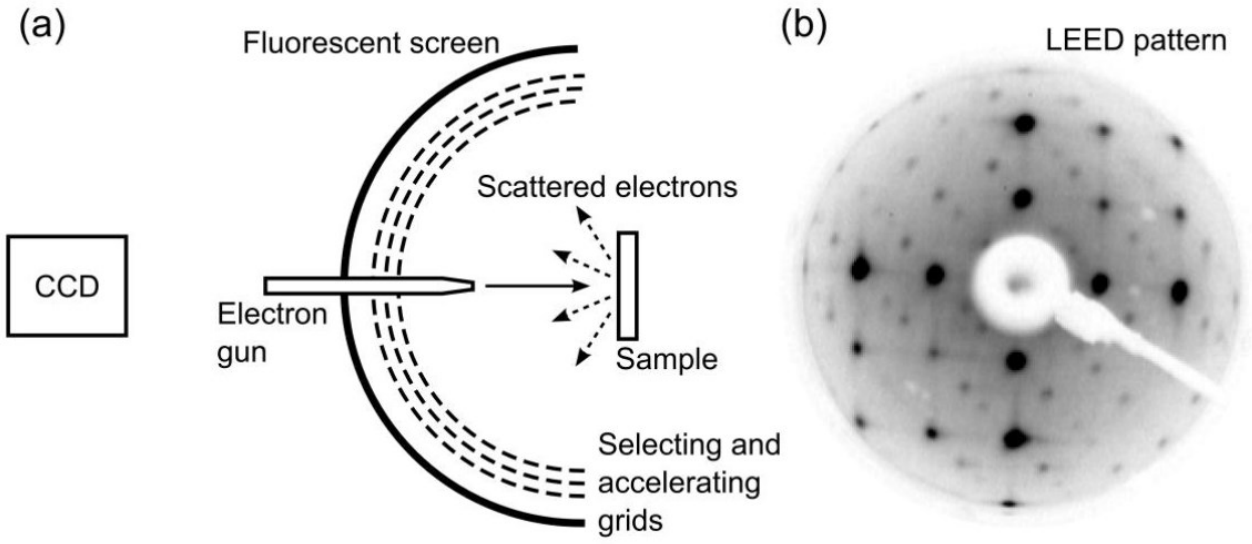

Figure 2.3.1 a) The schematics of LEED setup; b) an example of a LEED diffraction pattern. Adapted from [117].

In the presented thesis, LEED was used to control the quality of prepared ceria thin films, measure the lattice constants of ceria, and characterize the surface reconstructions determining the ordering of surface oxygen vacancies in model reduced cerium oxide films on Cu(111) substrate (Chapter 3.4, 3.5).

2.4 Temperature Programmed Desorption

Temperature Programmed Desorption (TPD, also Thermal Desorption Spectroscopy - TDS) is a technique, that provides information about chemical reactivity of studied surfaces. The schematics of the TPD setup together with an example of TPD spectrum are shown in Figure 2.4.1. During the experiment, the sample is first exposed to a specific gas, vapor or their mixture. Then, the temperature of the sample is linearly increased in time, which results in desorption of adsorbed molecules. Desorbed products are then detected by a mass spectrometer. The acquired spectrum shows the dependence of the amount of desorbed molecules on temperature. Resolution of the TPD depends on the rate of the temperature ramp: lower ramp increases the resolution of TPD but decreases the sensitivity. In the presented work, temperature ramp was selected to be 2K/s.

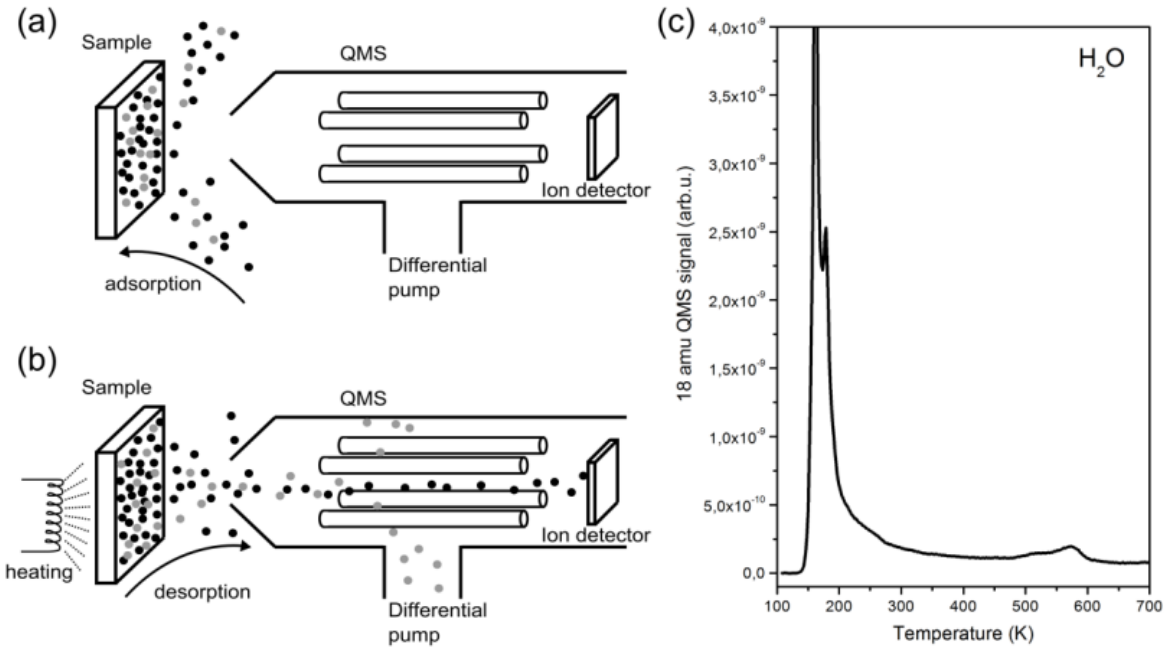

Figure 2.4.1. Schematic of TPD: a) the adsorption of gases/vapors on the surface, b) thermally stimulated desorption of adsorbates, c) an example of TPD spectra for mass 18 (H2O). Adapted from [117].

In the body of the mass spectrometer, the molecules are ionized in order to be detected. This can also cause fragmentation or multiple ionization of the molecules. Also, different molecules can have the same mass (for example, CO and NO), resulting in an overlap of their signals in TPD. All of these phenomena should be taken into account during the interpretation of the TPD spectra.

TPD is a highly surface-sensitive technique, since adsorption-desorption processes preferably occur at the surface. It provides information about the adsorption-desorption process. The desorption energies can be determined from the temperature of the maxima of the desorption peaks. The number of desorbed molecules can be obtained from the area of desorption peaks. The order of desorption is given by the shape of the desorption peaks. The kinetics of the surface reactions, the nature and the concentration of active adsorption positions on the surface, and the basic processes taking place during a surface chemical reaction can be determined by means of TPD [136], [137].

In the present work, TPD was used in reactivity measurements of reduced CeO_x thin films grown on Cu(111) single crystal towards water splitting (Chapter 3.4). H_2O molecules were adsorbed onto the film at 100K and the system was heated with a 2 K/s ramp to 700K. During the TPD cycle, the desorption of H_2, and H_2O was measured.

2.5 Experimental setup

The experiments were performed at two different laboratories located at the Department of Surface and Plasma Science of Charles University in Prague, Czech Republic, and at Material Science Beamline (MSB) at synchrotron Elettra in Trieste, Italy.

The major part of the experiments was made at Surface Science laboratory in Prague on the combined STM/XPS/LEED/TPD apparatus shown on Figure 2.4.1. The setup is operated at base pressure of the 10^{-8} Pa range and is equipped by standard tools for substrate cleaning and sample preparation: an Ar^{+} ion gun for sample cleaning, a set of e-beam evaporators for deposition of different materials, a sample holder equipped with resistive heating system and K-type chromel-alumel thermocouple, a manipulator equipped with liquid nitrogen cooling system and quartz crystal microbalance for deposition rate measurements, and a set of gas valves for adding different operating gases to the system. The system also includes several surface science methods for measuring different properties of the sample: a beetle-type STM equipped with a liquid nitrogen cooling system for low temperature measurements (95-300 K), a differentially-pumped quadrupole mass spectrometer for temperature programmed desorption (TPD) measurements, an Al K_α/Mg K_α X-ray gun with a hemispherical energy analyzer for XPS measurements, and an electron gun with rear-view LEED optics for diffraction measurements.

The whole experimental system is divided into three chambers: the load-lock, the XPS/TPD/preparation chamber and the LEED/STM chamber. In order to minimize the mechanic noise during STM measurements, the setup is equipped with the vibration insulation system. The combination of local microscopic technique with the integral techniques for the chemical and structural analysis is unique in Czech Republic and allows a complex *in-situ* study of the prepared model systems.

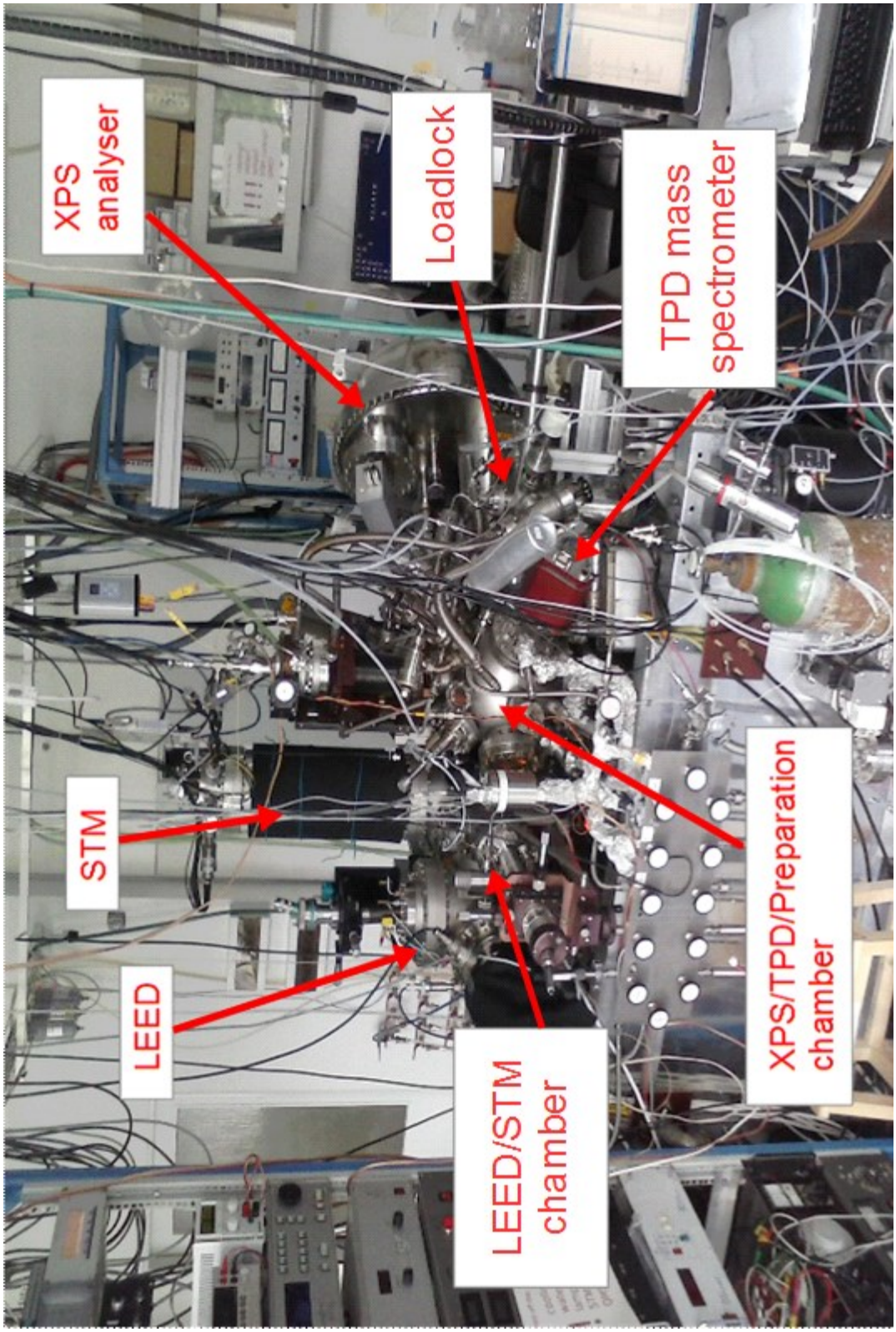

Figure 2.5.1. STM/XPS/LEED/TPD experimental setup.

A significant part of experiments was carried out at MSB at Elettra on an UHV end station with a base pressure below 5×10^{-8} Pa. The apparatus utilizes mostly linearly polarized and

monochromatic bending magnet radiation, which has a high intensity, high resolution, and tunable photon energy from 22 to 1000 eV. The surface science techniques accessible in-situ in MSB apparatus include SRPES, RPES, XPS, and LEED. The apparatus is equipped with standard tools for substrate cleaning and sample preparation, a hemispherical energy analyzer, a dual Mg K_α and Al K_α x-ray source, a QMS, an electron gun and rear view LEED optics, a gas inlet system, and a manipulator allowing cooling and heating of samples in the range of 100 – 1000 K [117]. The experiments performed at MSB represent complementary studies to the investigations accomplished in Prague and are focused on the quantitative analysis of Pt deposit on CeO_x surface grown on Cu(111) single crystal and on the high-resolution study of interaction of water with ceria films. Due to high surface sensitivity of SRPES, the detailed information is obtained on the evolution of chemical states of the near surface region of ceria and the adsorbed water during thermal treatment. RPES is utilized for high surface sensitivity and high resolution measurements of Ce^{3+} concentrations in the ceria samples.

2.5 Data processing

STM: The calibration of the STM scanner in the lateral and the vertical direction was performed based on the periodicity of Si(111) - (7 × 7) surface and the height of a monoatomic step of Cu(111), respectively. STM images were processed using Gwyddion open-source software [138]. It is a powerful tool for visualization of the microscopic data. It allows applying height and lateral profile measurements, calibration of the image and statistic measurements [138]. Applying 2-D Fast Fourier Transform (FFT) method allows detection of periodic features even in the high noise images. In this work, Gwyddion was used to calibrate and filter STM images, to extract height profiles of ceria thin films, to measure statistics of Pt clusters on ceria thin films and to examine the periodicity of atomically resolved images of inverse model CeO_x/Cu(111) system.

The evaluation of step density of ceria thin films in this work was made using more complex approach (Figure 2.5.1). First, the STM image was calibrated and filtered using Gwyddion. Second, steps were manually marked on the separate layer of the image. This layer is saved and analyzed by means of a specially developed software, where it is virtually placed upon the CeO_2(111) surface and the Ce atoms, which are crossed by the line, are counted giving the number of step edge atoms. The relation of the number of step edge Ce atoms to the overall number of surface Ce atoms yields the step density. Step density of the ceria thin films was a critical parameter in Pt^{2+}/Ceria

experiments since it determined the maximum load of the Pt^{2+} ions for a particular cerium oxide surface.

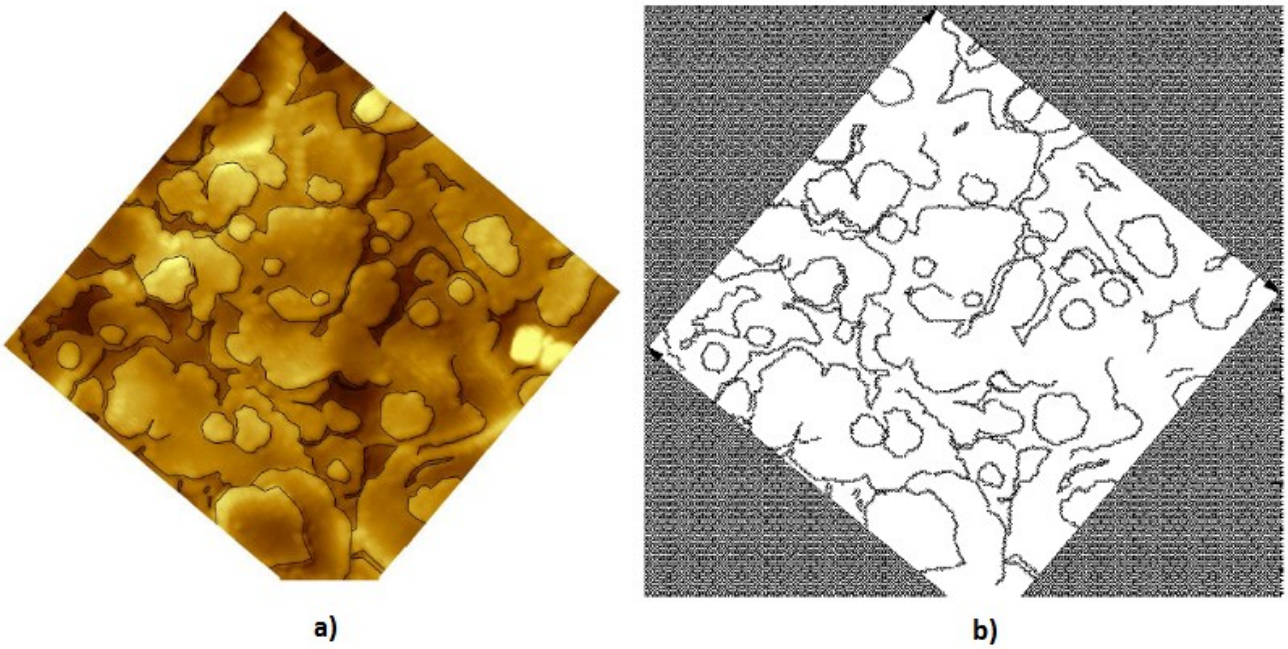

Figure 2.5.1. Evaluation of step density of ceria thin films: (a) – manual marking of the steps; (b) – counting step density using the CeO_2(111) atomic grid.

XPS/SRPES: XPS and SRPES data were fitted using the KolXPD software [139]. XPS and SRPES were used for the estimation of ceria film thickness and stoichiometry and measurements of the concentration and state of Pt adatoms. Presented core level spectra were fitted using Voigt functions (Cu $2p_{3/2}$, Ce 3d, O 1s), Gaussian and Lorentzian functions (Pt 4f) and Shirley background.

The thickness of the ceria thin films was determined from the attenuation of Cu $2p_{3/2}$ signal from Cu(111) substrate as measured by XPS. Assuming the exponential attenuation of emitted electrons in the homogeneous environment, the thickness of the ceria layer d_{CeO_2} was determined according to the relation:

$$d_{CeO_2} = \lambda_{CeO_2} \ln \frac{S_I}{S_F} \cos \theta_e$$

where the λ_{CeO_2} is IMFP in CeO_2, S_I and S_F are the areas of Cu $2p_{3/2}$ XPS spectra before and after the CeO_2 deposition, respectively, and θ_e is the emission angle of electrons (measured with respect to the surface normal). The determined thickness of the ceria thin film depends on the morphology and the coverage of the film and, therefore, is only an estimation of the real thickness of ceria. Generally, this parameter was compared with the Quartz Crystal Microbalance (QCM) measurements where a more precise estimation of the mass of ceria thin films could be made. QCM

method relies on the change of a resonance frequency of a piezocrystal while depositing different materials onto it. Knowing the parameters of the piezocrystal and the time of the deposition allows us to estimate the mass of deposited material with higher precision by using Sauerbrey equation [140].

The average stoichiometry of ceria films was evaluated through fitting of the Ce 3d spectra. The spectrum of CeO_2 consists of three u''' + v''', u'' + v'' and u + v doublets corresponding to three different final electronic states of the Ce^{4+} ions developed upon the emission of the 3d photoelectron (Figure 2.5.2). On the other hand, Ce_2O_3 spectrum consists of two u'+v' and u_0+v_0 doublets corresponding to two different final electronic states of the Ce^{3+} ions at different energies compared to the doublets of the CeO_2 spectrum. CeO_2 and Ce_2O_3 spectra were fitted according to the procedure described in [141], [142]. The stoichiometry of the CeO_{2-x} film was determined according to the relation:

$$x = 0.5 \times \frac{S_{Ce^{3+}}}{S_{Ce^{3+}} + S_{Ce^{4+}}}$$

where $S_{Ce^{3+}}$ is an overall area of Ce^{3+} doublets and $S_{Ce^{4+}}$ is an overall area of Ce^{4+} doublets in the CeO_{2-x} samples.

The concentration of Pt ions and their state was determined via fitting of Pt 4f doublets using Gaussian and Lorentzian doublets. The doublet corresponding to the Pt^0 state is at 73 eV whereas the one corresponding to the Pt^{2+} state is 1.5 eV shifted towards higher binding energies. Calculating the ratio between the area of one of these doublets to the overall area of the Pt doublets gives the information on the relative concentration of Pt^0 and Pt^{2+} ions. However, due to the low Pt content in the films, the sensitivity of the XPS was insufficient for precise estimation of the spectra, providing only general information on the state of Pt ions and their existence on the ceria surface. For quantitative measurements, SRPES experiments were performed at the synchrotron Elettra in Trieste, Italy.

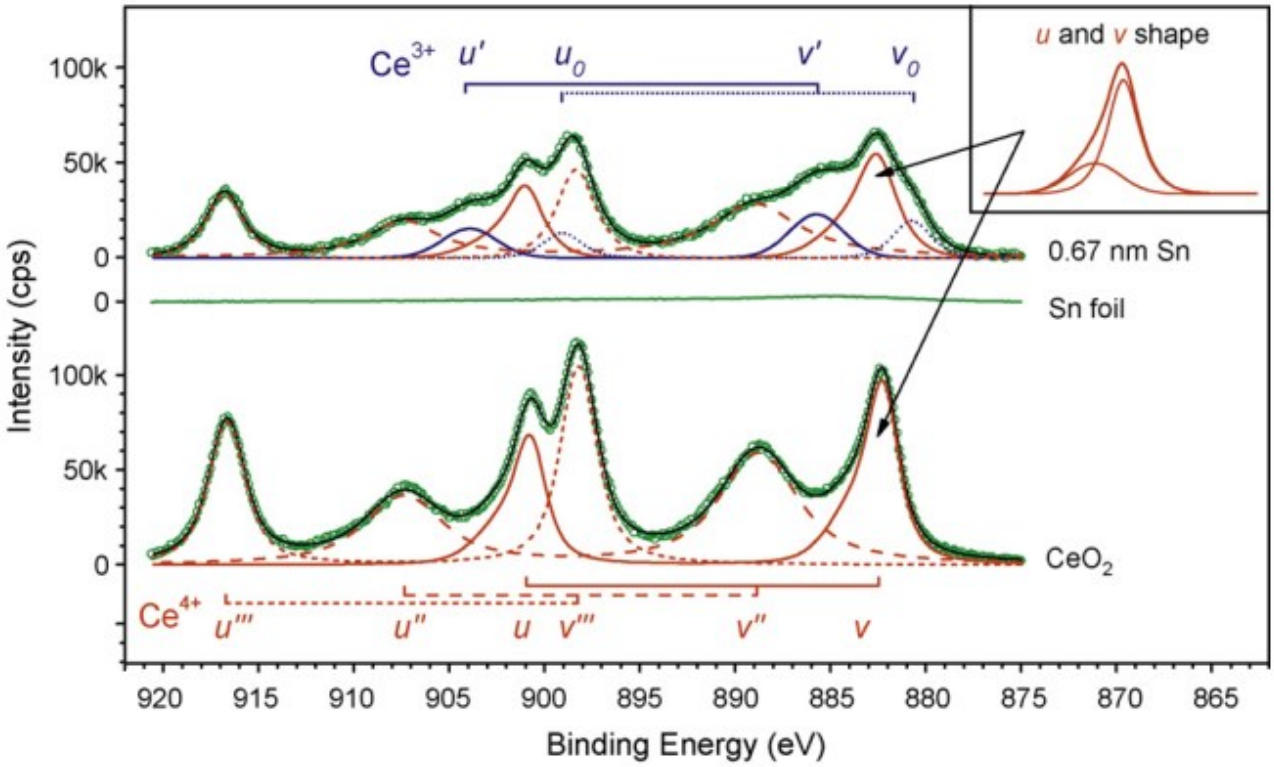

Figure 2.5.2. Fitting of the CeO_x XPS spectra which consists of three u'''+ v''', u''+ v'' and u + v doublets corresponding to Ce^{4+} and two u'+v' and u_0+v_0 doublets corresponding to Ce^{3+} states. Adapted from [141].

RPES: Resonance photoelectron spectroscopy allows us to investigate the cerium oxidation state with high sensitivity and maximal surface sensitivity. If the photon energy is tuned in the proximity of the energy, denoted RE, corresponding to the energetic difference between the empty Ce 4f and filled Ce 4d levels, photoelectrons from the Ce 4f level can be emitted by means of two mechanisms: (1) direct photoemission from the Ce 4f level, (2) photoexcitation of a 4d electron to the 4f level and subsequent decay of the intermediate state followed by transfer of energy to a 4f electron [132]. As a result, at the resonant energy hν = RE we observe a resonant enhancement of the Ce 4f photoemission relative to hν < RE and hν > RE. The enhancement of the 4f emission is so strong that even weak 4f emission such as from slightly reduced surfaces of ceria nanoparticles can be observed by the use of the resonance [132]. The resonance process of the indirect emission from $4f^1$ systems (Ce^0, Ce^{3+}) can be described by

$$4d^{10}4f^1 + h\nu \rightarrow 4d^9 4f^2 \rightarrow 4d^{10}4f^0 + e^-,$$

where hν and e^- stand for an incident photon and ejected photoelectron. The resonance process of the indirect emission from $4f^0$ systems is

$$4d^{10}4f^0 + h\nu \rightarrow 4d^9 4f^1 \rightarrow 4d^{10}4f^0 L + e^-,$$

where L denotes a hole in the valence band [132].

An example of the resonant valence band photoelectron spectra in the Ce 4d–4f photoabsorption region of a CeO_x sample is shown in Figure 2.5.3. It can be seen, that two resonances appear: one at photon energy 121.4 eV corresponding to Ce^{3+} valence state and another at 124.8 eV corresponding to CeO^{4+} state. At 115 eV there is no resonance. Resonant enhancement of the valence band emission shows a strong dependence of the valence state, which makes RPES a powerful tool for the investigation of the $Ce^{4+} \rightarrow Ce^{3+}$ transition, and which exhibits considerably higher sensitivity than XPS of the Ce 3d level. The 4f density of states can be obtained by subtracting the off-resonance spectrum from an on-resonance spectrum [132].

The resonant intensity enhancement corresponding to the on–off resonant spectra difference is designated DCe^{4+} and DCe^{3+}, respectively. The relation DCe^{3+}/DCe^{4+} provides a relative measure of concentration of Ce^{3+} ions and is called resonant enhancement ratio (RER). In this work, it is used in Chapters 3.1 - 3.3 in order to precisely determine reduction rate of the ceria thin films. In order to obtain absolute values, RER must be calibrated against XPS (Chapters 3.1, 3.3).

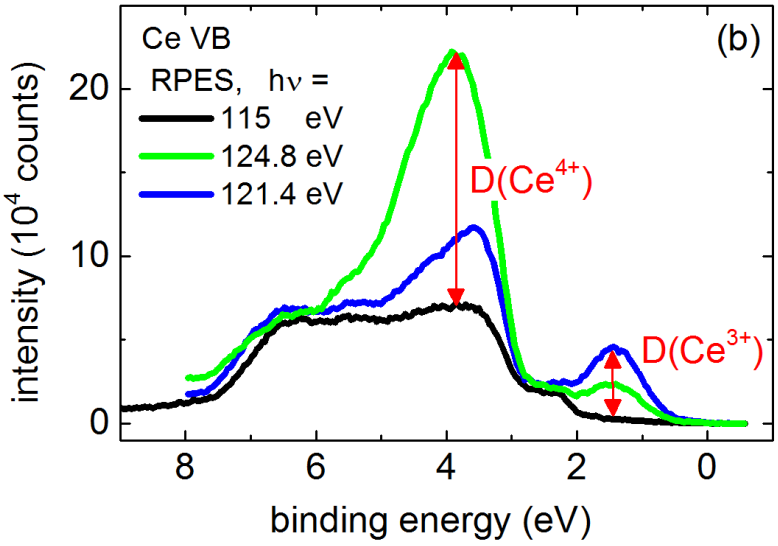

Figure 2.5.3. Resonance photoelectron spectroscopy of the cerium 4f level: Ce^{3+} and Ce^{4+} resonant features obtained for the photon energies 121.4 eV and 124.8 eV respectively.

LEED: Diffraction patterns obtained by LEED were processed by the data analysis software IGOR Pro v6.21 [143], Gwyddion [138] and Origin. The device calibration was performed by using the diffraction on Cu(111) single crystal. Sharp diffraction spots of this crystal were used as a reference for measurements of ceria lattice parameters. In order to minimize the barrel distortion of the projected LEED image, we always adjust the energy of the primary electrons so as to position

the analyzed diffraction spots of ceria and copper on the similar radius from the center of the LEED diffractogram.

2.6 Sample preparation

In the present work we developed preparation methods for cerium oxide thin films with adjustable step density and stoichiometry based on the previous works of our group [103], [108]. Copper (111) single crystal was cleaned using several cycles of Ar^+ sputtering in ultrahigh vacuum with successive annealing at 700K. Thin CeO_2 films were grown at 523K via depositing metallic Ce in oxygen background atmosphere ($p=3\text{-}5\times10^{-5}$ Pa) from Ta or Mo crucible, heated by electron bombardment. After deposition, the prepared thin films were kept at the same temperature in oxygen atmosphere for another 10 minutes. The resulting film thickness was estimated to be 2-2,5nm (Figure 2.6.1.a). This film was used as buffer layer for Pt-CeO_2 charge transfer measurements (Chapter 3.1).

Control over stoichiometry of the deposited film was achieved via its interaction with metallic cerium following an algorithm described in [106]. In order to achieve limiting Ce_2O_3 stoichiometry, metallic cerium in amount equal 1/3 of the amount used for buffer film was added at room temperature. The specimen was then annealed at 900K for 5 minutes in UHV. The resulting Ce_2O_3 film was continuous, had low step density and possessed (4×4) surface reconstruction [106], [108] (Figure 2.6.1.b). Reducing the amount of deposited metallic cerium resulted in achieving different transition stoichiometries: Ce_7O_{12} and $CeO_{1,67}$. The overall thickness of the films was 3nm. The prepared reduced ceria films were used in this work for reactivity measurements of H_2O on CeO_x (Chapter 3.4). Oxidation of the Ce_2O_3 films maintained low step density, which was used as starting point for preparation of CeO_2 films with controlled step density (Figure 2.6.1.c). Adding 0.3 ML of CeO_2 resulted in growing small 1ML high CeO_2 islands on top of the flat CeO_2 buffer layer, increasing the step density of the model system (Figure 2.6.1.d). The resulted density of step edges of the prepared film was 15% and this system was used for stabilization of Pt^{2+} ions at the surface providing sufficient morphological simplicity for STM measurements (Chapters 3.2 and 3.3).

The described reduction method for CeO_2 films was also used for preparation of inverse model CeO_x/Cu(111) systems with controlled stoichiometry. Buffer layer was prepared using oxidation of Ce deposit at room temperature. Cerium was deposited onto the Cu(111) single crystal from Ta crucible heated via electron bombardment. Cerium deposit was then exposed to 12L of O_2 at room temperature ($P=2.6\times10^{-5}$ Pa) and subsequently annealed at 700K in UHV (Figure 2.6.1.e).

Full oxidation of the film was achieved through the heating of the sample at 750K in oxygen background atmosphere ($P=2.6\times10^{-5}$ Pa) for 5 minutes. The film was then reduced via the adsorption of metallic cerium onto the surface with subsequent annealing at 900K in UHV for 5 minutes [106] (Figure 2.6.1.f). The average film thickness was determined from a quartz crystal microbalance method and was estimated to be 1-2ML (Chapter 3.5).

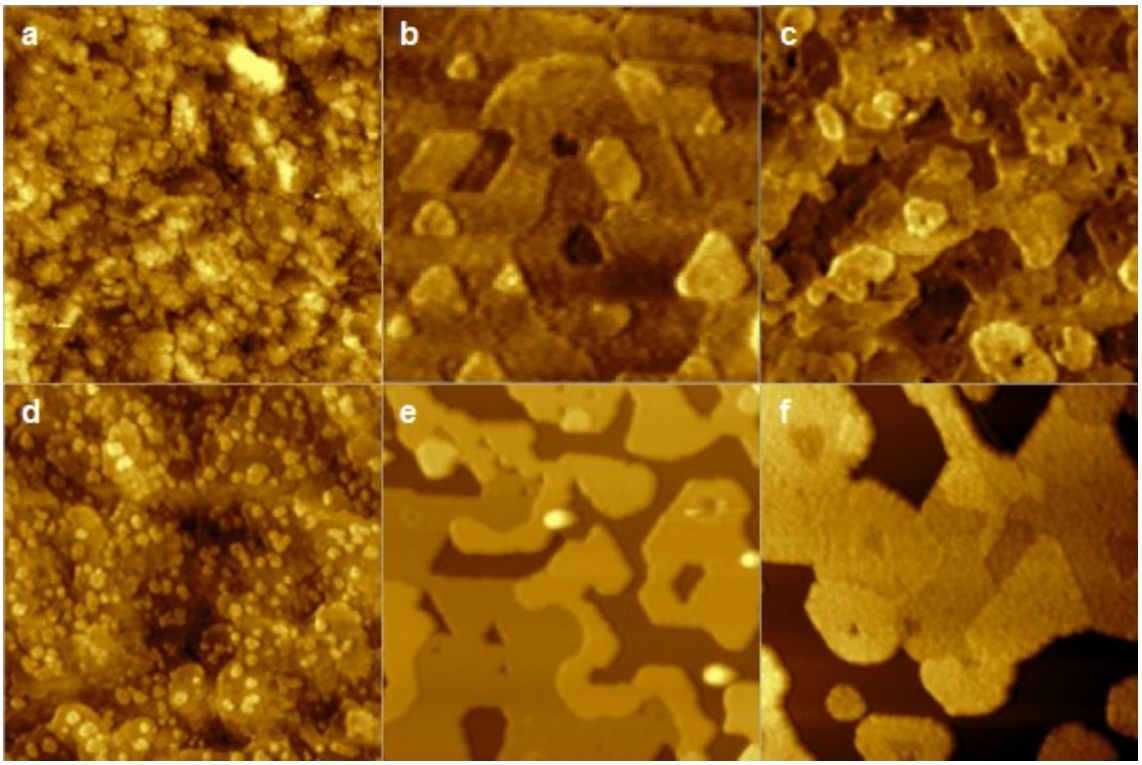

Figure 2.6.1. Morphology of the well-defined ceria thin films on Cu(111) measured with STM: a) – buffer layer of CeO_2(111) deposited and annealed at 523K; b) – reduced c-Ce_2O_3 ceria film with low step density; c) – oxidized ceria film with low step density; d) – same film with increased step density (0,15ML) due to homoepitaxy of 1 ML high CeO_2(111) islands; e) – inverse model $CeO_{1.9}$/Cu(111) system; f) – reduced inverse model CeO_x/Cu(111) system. The size of the images is 100×100nm.

Platinum was deposited onto ceria films with different stoichiometry and step density in UHV at room temperature via heating of the Pt wire with electron bombardment. Samples were subsequently heated to 700K for stabilization of Pt deposit. Adjusting the deposition time allowed control over amount of Pt at the surface. In the present work, the amount of deposited Pt was in the range of 0.03 to 3.5ML.

The deposition rate was measured using Quartz Crystal Microbalance (QCM) method and was estimated 12ML/hour for cerium and for 0.9ML/hour for Pt. Film thicknesses were determined from STM and XPS measurements and compared to the values, determined from QCM results.

3. Results and discussion

In this chapter the main results and achievements are presented in the form of three publications and two manuscripts. Each of the sections is briefly introduced. The usage of the well-defined ceria model systems for advanced studies in morphology and reactivity is presented. The first section is dedicated to the quantitative estimation of charge transfer between Pt clusters and cerium oxide surface. The second and third sections concentrate on investigation of the role of ceria step edges towards stabilization of Pt single atoms and their capacity for maximum Pt loading. The fourth section presents reactivity study of H_2O molecules on reduced ceria. Finally, the last section presents the preparation of inverse model CeO_x/Cu(111) systems with different stoichiometry and their characterization using advance surface science methods.

3.1 Counting electrons on supported nanoparticles

Noble metal nanoparticles on oxides are among the most widely-used catalytic systems in modern chemical industry. Steps towards increasing their activity and efficiency in the catalytic reactions often include optimization of the metal-oxide interactions via choosing the appropriate support materials, particle sizes, particle structures or via adding promoters [144]–[147]. Nowadays, we understand, that the catalytic activity of these systems is governed by several factors including the electronic system of the supported nanoparticles [148], their nanostructure [144], [146], their structural flexibility [149], [150], and, which is more important, their interaction with the support [147], [151]–[154].

The interaction between Pt nanoparticles and an oxide support, leading to 20-fold increase in reactivity of the system towards water-gas shift reaction, is described in literature as an electronic-metal support interaction (EMSI) and is related to the particle-support charge transfer (CT) mechanism [146], [155]. Experimental measurement of the CT has always been a challenge. In fact, it can be determined from binding energy shifts in photoelectron spectroscopy. In reality however, strong final state effects prevent reliable measurements of the small initial state effects owing to the EMSI [156]–[158]. In order to solve this question, more advanced approach has to be developed so as to estimate particle-support charge transfer value.

In this work, we study Pt nanoparticles on a well-defined cerium oxide surface. The contact between Pt and ceria results in electron transfer, reducing Ce^{4+} ions to Ce^{3+} [146], [151]. The Ce^{3+} centers can be detected with an outstanding sensitivity by resonant photoemission spectroscopy (RPES). Combining these results with structural data from STM, we are able to ‘count’ the number

of electrons transferred across the metal/oxide interface per Pt particle. Furthermore, we can provide the CT as a function of the particle size, from very small particles to large ones containing several hundreds of atoms.

The results show, that the CT value increases with the particle size reaching its maximum for particles containing from 30 to 70 Pt atoms (0.11±0.025 electrons per Pt atom). Pt nanoparticles become partially oxidized, forming $Pt^{\delta+}$ with an average charge of $\delta \sim 0.11 \pm 0.025$. For larger particles, charge transfer is suppressed. The maximum CT value per surface area amounts to 1.2×10^{18} electrons per m^2, which corresponds to approximately 17% of the surface cerium ions being reduced to Ce^{3+}. On average, one of six Ce^{4+} surface ions can be reduced to Ce^{3+} during charge transfer process. Smaller charge transfer value for smaller Pt particles can be explained through their nucleation at Ce^{3+} adsorption sites.

The experimental results were supported with the DFT calculations for Pt_8, Pt_{34} and Pt_{95} particles on $CeO_2(111)$ surface.

To this work I have contributed the key information on the statistics of the Pt cluster population as a function of increasing Pt amount on $CeO_2(111)$. Samples with different amounts of Pt deposit on $CeO_2(111)$ were prepared by evaporating Pt at room temperature and imaged with high resolution with STM (Figure 1a of the article). The obtained STM images were then analyzed and density of Pt clusters was determined. For each amount of Pt deposit several STM images from different areas of the specimen were processed. The total analyzed area of the specimen for each amount of Pt deposit remained constant. The obtained data on Pt cluster density and Pt cluster size (Figure 1b of the article) was then compared to data on charge transfer between Pt deposit and ceria substrate obtained by RPES in the collaborating laboratory; the results of this comparison is shown in Figure 2 of the article. These results were essential in evaluating the amount of transferred charge as a function of Pt cluster size, and, particularly, for determining Pt cluster sizes providing maximum charge transfer (Figure 2a of the article).

nature materials

LETTERS

PUBLISHED ONLINE: 14 DECEMBER 2015 | DOI: 10.1038/NMAT4500

Counting electrons on supported nanoparticles

Yaroslava Lykhach[1†], Sergey M. Kozlov[2†], Tomáš Skála[3], Andrii Tovt[3], Vitalii Stetsovych[3], Nataliya Tsud[3], Filip Dvořák[3], Viktor Johánek[3], Armin Neitzel[1], Josef Mysliveček[3], Stefano Fabris[4], Vladimír Matolín[3], Konstantin M. Neyman[2,5*] and Jörg Libuda[1,6*]

Electronic interactions between metal nanoparticles and oxide supports control the functionality of nanomaterials, for example, the stability, the activity and the selectivity of catalysts[1–5]. Such interactions involve electron transfer across the metal/support interface. In this work we quantify this charge transfer on a well-defined platinum/ceria catalyst at particle sizes relevant for heterogeneous catalysis. Combining synchrotron-radiation photoelectron spectroscopy, scanning tunnelling microscopy and density functional calculations we show that the charge transfer per Pt atom is largest for Pt particles of around 50 atoms. Here, approximately one electron is transferred per ten Pt atoms from the nanoparticle to the support. For larger particles, the charge transfer reaches its intrinsic limit set by the support. For smaller particles, charge transfer is partially suppressed by nucleation at defects. These mechanistic and quantitative insights into charge transfer will help to make better use of particle size effects and electronic metal–support interactions in metal/oxide nanomaterials.

Complex nanomaterials play an ever-growing role in numerous key technologies. For instance, noble metal nanoparticles on oxides are among the most common catalytic materials[6], with many applications in the chemical industry, fuel production, environmental catalysis, photocatalysis and electrocatalysis[5,7–10]. Efficient use of the precious metals in these materials is essential for cost-efficient catalytic processes. Strategies to improve the activity often rely on particle–support interactions, which are optimized by choosing specific support materials, particle sizes, particle structures, or by adding promoters[1,3–5].

For more than 30 years, particle–support interactions have been among the most intensively and most controversially discussed topics in catalysis[2,7]. Today, we understand that the catalytic activity of supported nanoparticles is governed by several interrelated physical and chemical factors, such as their electronic structure[8], their nanostructure[1,4], their structural flexibility[11,12] and, very importantly, their interaction with the support[5,9,13–15]. Understanding these phenomena is the key to tailor-made materials and has been attracting the attention of many physicists, chemists and materials engineers.

The outstanding influence of reducible supports on the activity of metal nanoparticles has been well known since the discovery of the 'strong metal–support interaction' (SMSI) by Tauster *et al.* in the late 1970s (ref. 14). Recently, Rodriguez, Illas and co-workers identified a different kind of strong metal–support interaction for a Pt/ceria catalyst, which did not lead to a decrease in activity typical for the 'classical' SMSI effect but to a 20-fold increase in the rate for the water-gas shift reaction[4]. A strong electronic interaction between Pt particles and the support is proposed to be at the origin of the effect. Campbell suggested using the term electronic metal–support interaction (EMSI) for this type of chemical enhancement[2], which also attracted a lot of attention from theory[16]. On the one hand the effect will markedly change the catalytic properties of the metal particle[1,17]. On the other hand such interactions are critical for the adhesion of particles and, therefore, for the stability of the material[18].

Depending on the magnitude of the EMSI there could be substantial charge transfer (CT) between the supported metal particle and the supporting oxide. Qualitatively, this CT has been observed by many groups (see for example refs 19,20) but, surprisingly, the amount of CT has never been quantified for supported metal particles in the catalytically relevant size range.

In fact, measuring the CT between a supported catalyst particle and the support turns out to be a serious challenge. Attempts can be traced back throughout the history of surface science and model catalysis[16,21,22]. In principle, the charge on a supported particle could be determined from binding energy shifts in photoelectron spectroscopy (PES). In practice, however, strong final state effects prevent reliable measurements of the small initial state effects owing to the EMSI (refs 23–25). Recently, Nilius *et al.* determined the charge on oxide-supported Au and Pd adatoms and clusters by scanning tunnelling microscopy (STM; refs 21,26), but this method is restricted to very small aggregates only. To the best of our knowledge, the charge on supported nanoparticles in the nanometre size regime has not been measured so far.

To address this challenge we study Pt particles supported on cerium oxide, a versatile heterogeneous catalyst with applications in hydrogen production, reforming, environmental catalysis, and electrocatalysis[10]. On contact of the Pt metal with the oxide surface, the EMSI leads to electron transfer across the metal/oxide interface[4,9]. These electrons are taken up by Ce^{4+} ions at the interface which, thereby, are reduced to Ce^{3+}. The Ce^{3+} centres can be detected with outstanding sensitivity by resonant photoemission spectroscopy (RPES; ref. 5). Note that RPES allows detection of Ce^{3+} down to surface concentration levels of 0.1% and below. Combining this information with structural data from STM, we are able to 'count' the number of electrons transferred across the metal/oxide interface per Pt particle. Specifically, we can measure the CT as

[1]Lehrstuhl für Physikalische Chemie II, Friedrich-Alexander-Universität Erlangen-Nürnberg, Egerlandstraße 3, D-91058 Erlangen, Germany. [2]Departament de Química Física and Institut de Quimica Teòrica i Computacional (IQTCUB), Universitat de Barcelona, c/ Martí i Franquès 1, 08028 Barcelona, Spain. [3]Charles University, Faculty of Mathematics and Physics, Department of Surface and Plasma Science, V Holešovičkách 2, 18000 Prague 8, Czech Republic. [4]CNR-IOM DEMOCRITOS, Istituto Officina dei Materiali, Consiglio Nazionale delle Ricerche and SISSA, Via Bonomea 265, I-34136 Trieste, Italy. [5]Institucio Catalana de Recerca i Estudis Avançats (ICREA), 08010 Barcelona, Spain. [6]Erlangen Catalysis Resource Center, Friedrich-Alexander-Universität Erlangen-Nürnberg, Egerlandstraße 3, D-91058 Erlangen, Germany. †These authors contributed equally to this work.
*e-mail: konstantin.neyman@icrea.cat; joerg.libuda@fau.de

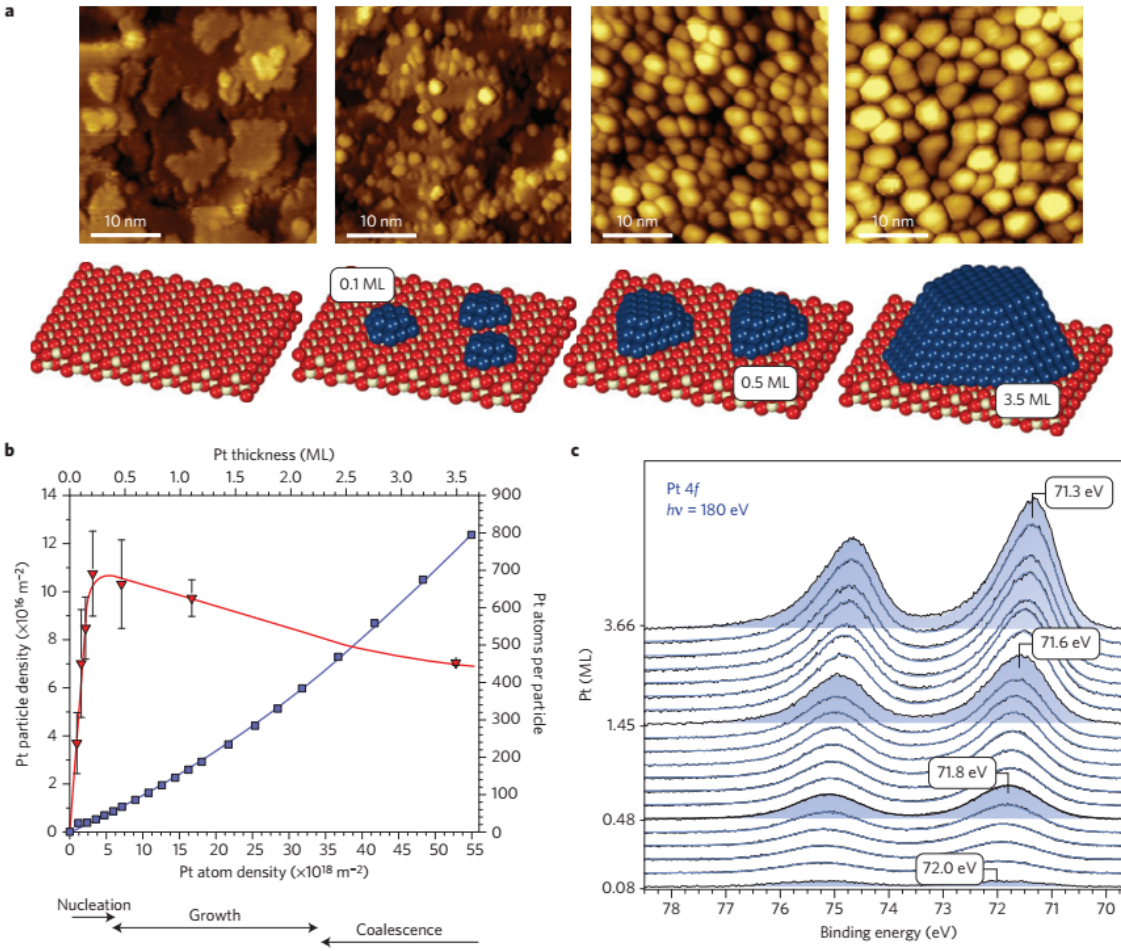

Figure 1 | Structural characterization of the Pt/CeO_2(111) model catalyst. a, Selected STM images of the surface after the deposition of different amounts of Pt. The corresponding atomic models represent typical Pt particle sizes as determined by STM and XPS (see text for details; blue, platinum; red, oxygen; ivory, cerium). **b**, Particle density (red triangles) and size (blue squares) derived from the STM and XPS data. **c**, Corresponding Pt 4*f* spectra obtained by synchrotron-radiation PES. The Pt coverage is expressed in monolayers (1 ML = 0.2266 nm). Error bars represent the total estimated error.

a function of particle size, from very small aggregates to particles containing several hundreds of atoms.

In our experiments we start from a well-ordered and well-characterized CeO_2(111) film grown on a Cu(111) single crystal under ultrahigh vacuum conditions (see Methods; ref. 27). We choose a relatively high film thickness of about 2 nm to minimize the influence of the underlying Cu substrate. Further, we used preparation conditions that yield a nearly perfectly stoichiometric oxide ($CeO_{1.998\pm0.001}$, as determined from RPES, see below). On this stoichiometric film we can also exclude the particle-induced segregation of oxygen vacancies which was discussed recently[18,28]. Onto this surface we deposited Pt by physical vapour deposition (PVD). The deposition rate was calibrated by X-ray photoelectron spectroscopy (XPS) and high-resolution Pt 4*f* spectra were recorded by means of synchrotron radiation (Fig. 1). These spectra reveal the typical shift to higher binding energy with decreasing particle size, largely dominated by the final state Coulomb charge in the photoemission process[23]. As pointed out, it is not possible to determine reliably the initial state CT from these spectra.

The particle density, size and shape were investigated by STM, which was combined *in-situ* with XPS to correlate the structural data and the Pt coverage. Whereas tip convolution effects make it difficult to extract particle sizes directly from STM, the particle density can be determined with very good precision. From the particle density and the coverage calibration from XPS (see Supplementary Information), we are able to obtain reliable information on the average number of Pt atoms per nanoparticle. Average particle sizes can then be estimated using the particle shape from STM in the limit of larger metal loading, where more reliable data can be obtained. Particle densities and sizes from this structural analysis are summarized in Fig. 1b as a function of Pt coverage. We clearly identify the regions of nucleation, particle growth and coalescence, as is typically observed for such systems. The data show that we can vary the particle size from approximately 20 to 800 Pt atoms per particle, corresponding to particle diameters between about 1 and 3.5 nm. This is a common size regime for Pt particles in heterogeneous catalysis.

Next we use this model catalyst to determine the CT between the supported particles and the oxide by RPES. Briefly, the method is based on valence band photoelectron spectroscopy at photon energies that lead to resonant enhancement of features associated either with Ce^{3+} or Ce^{4+} (refs 5,29). From these resonant enhancements

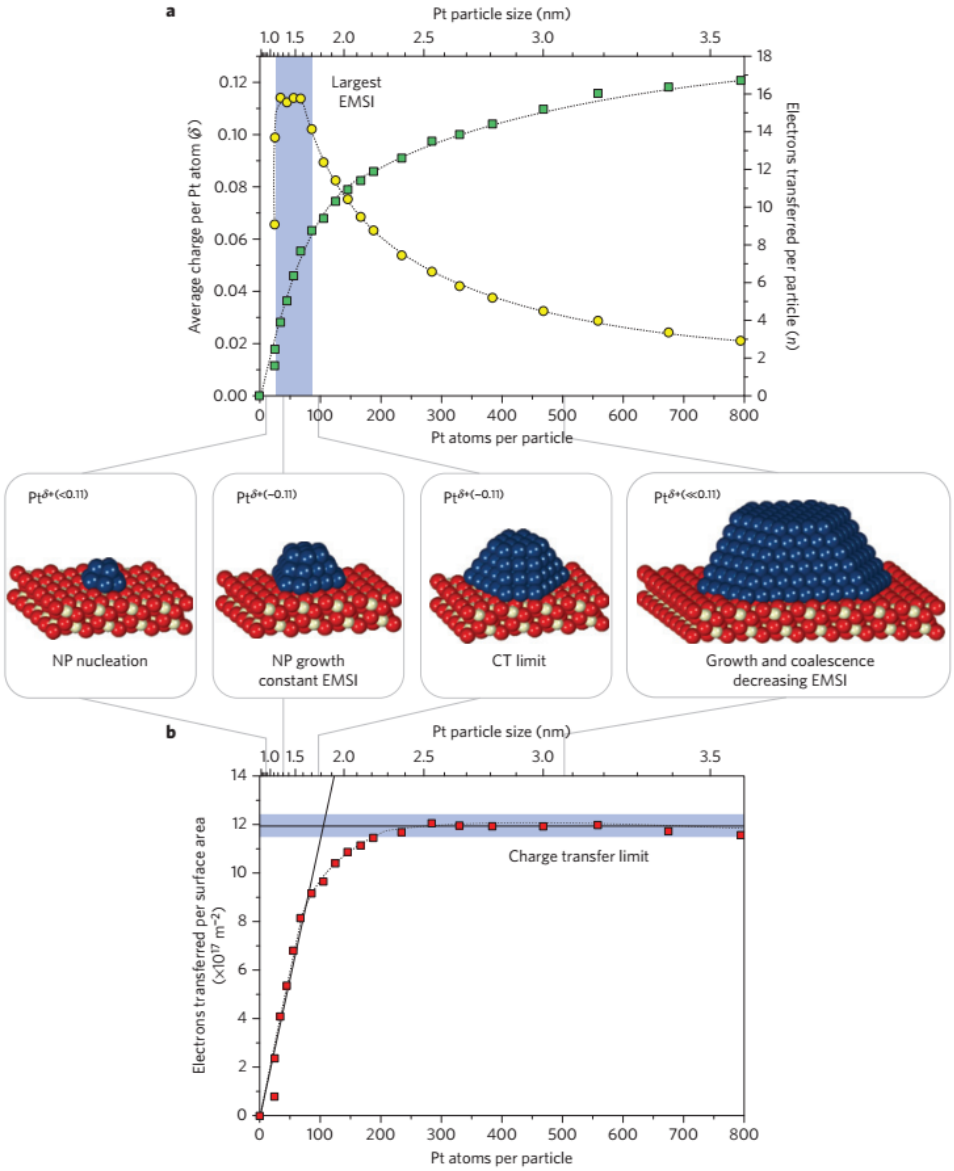

Figure 2 | 'Counting' the electrons transferred owing to the EMSI. a, The number of electrons transferred per Pt particle to the ceria support increases with increasing particle size (green squares). The partial charge per Pt atom reaches a maximum for particles with 30 to 70 atoms (yellow circles). Here, the EMSI is largest. **b**, At higher Pt coverage the total amount of transferred charge approaches a limit which we denote as the 'charge transfer limit' (red squares). The atomic models show schematically the average particle sizes in the different regions. Nanoparticle, NP.

we derive the surface concentration of Ce^{3+} by calibration with conventional XPS (see Supplementary Information for details). Using this procedure we are able to quantitatively measure the Ce^{3+} concentration and, thereby, 'count' the number of electrons that are transferred between the Pt particles and the ceria support.

The results are summarized in Fig. 2. Three important quantities are shown as a function of particle size: the number of electrons transferred per Pt particle, the number of electrons transferred per Pt atom and the number of electrons transferred per surface area. We observe that the number of electrons transferred per particle increases linearly with size for particles with up to 70 Pt atoms. For larger particles further charge transfer is suppressed. Interestingly, the charge per Pt atom shows a maximum at particle sizes between 30 and 70 Pt atoms (particle diameters between approximately 1 and 1.5 nm). Here, it reaches a peak value of about 0.11 ± 0.025 electrons per Pt atom. In other words, the Pt nanoparticles become partially oxidized, forming $Pt^{\delta+}$ with an average charge of $\delta \sim 0.11 \pm 0.025$. (The error margin mainly originates from potential shadowing effects and the calibration procedure; see Supplementary Information for details. Note that the appearance of the CT maximum does not depend on the calibration procedure.)

At higher Pt coverage the overall number of transferred electrons approaches a limit. The maximum CT per surface area amounts to 1.2×10^{18} electrons m^{-2}. This value corresponds to approximately

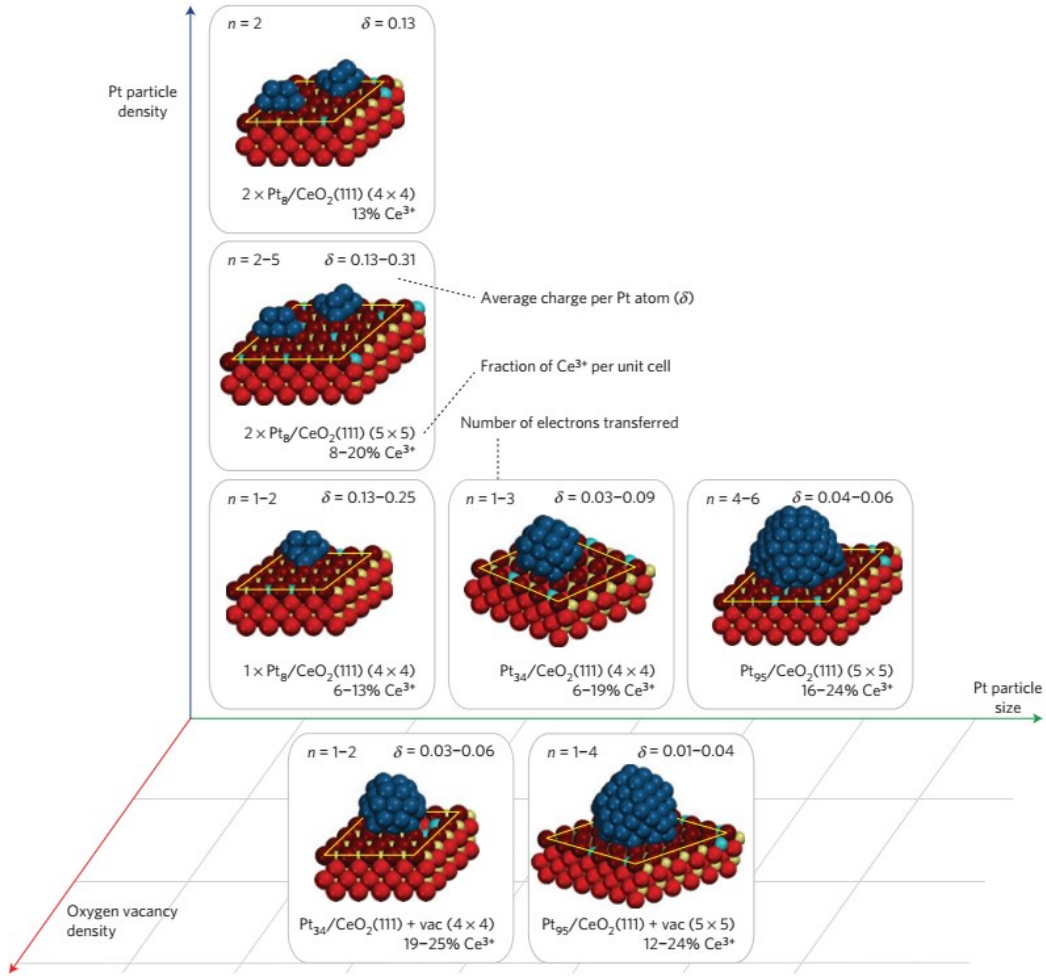

Figure 3 | Summary of density functional calculations. The particle size, the particle density, and the oxygen vacancy density on the support are important factors that control the charge transfer. A detailed description of the computational results is provided in Supplementary Table 1 (see Supplementary Information).

17% of the surface cerium ions being reduced to Ce^{3+}. We conclude that on average one out of six Ce^{4+} surface ions can be reduced to Ce^{3+}. Beyond this value no further charge transfer occurs and the average charge per Pt atom decreases if further Pt is deposited. Interestingly, the CT per Pt atom also decreases for very small aggregates. This observation is surprising, as theory predicts substantial CT even for very small aggregates[5]. Below we will show that the suppressed CT may be explained by the nucleation of Pt at Ce^{3+} defect sites. Traces of Ce^{3+} present at the pristine surface (0.5% ML) are sufficient to account for the observed effect. Previous studies have shown that these Ce^{3+} centres may serve as efficient traps for deposited metal atoms[30].

To rationalize the experimental observations we have performed systematic density functional calculations (see Methods). Using $CeO_2(111)$-supported Pt nanoparticle models we explore the influence of the particle size, of the particle density and of oxygen vacancies. Whereas many different particle sizes and structures coexist in the experiment, theoretical models are restricted to a few selected systems. Therefore, theory can only rationalize the experimental trends rather than reproduce the experimental data quantitatively.

To explore the effect of particle size, we calculate Pt_8, Pt_{34} and Pt_{95} particles on $CeO_2(111)$ (see Fig. 3 and Supplementary Information for details). For each model we were able to identify several configurations of similar energy corresponding to different numbers of electrons transferred. In practice such configurations coexist and indicate the range in which electron transfer is possible. For the Pt_8 cluster we find the transfer of 1–2 electrons from Pt_8 to $CeO_2(111)$, for Pt_{34} the transfer of 1–3 electrons is possible, and for Pt_{95} even 4–6 electrons can be transferred. This results in a partial charge $Pt^{\delta+}$ of $\delta = 0.13$–0.25 for Pt_8, of $\delta = 0.03$–0.09 for Pt_{34}, and $\delta = 0.04$–0.06 for Pt_{95}. In spite of the simplicity of the model the amount of charge transfer compares well with the experimental value of $\delta = 0.11 \pm 0.025$ for particle sizes between 30 and 70 atoms. Note that the decreasing partial charge for larger particles is also reproduced in the model.

A second observation in the experiments is that the fraction of surface Ce^{3+} centres does not exceed a value of ~17%. This number also compares well with the simulations. For the Pt_{34} cluster on a $p(4 \times 4)$ $CeO_2(111)$ supercell, we calculate a fraction of 6–19% Ce^{3+}, whereas for Pt_{95} on a $p(5 \times 5)$ $CeO_2(111)$ supercell, we obtain values of 16–24% Ce^{3+}. To explore possible limitations for CT caused by

the concentration of surface Ce^{3+} centres we varied the density of Pt_8 clusters on the surface. When two particles are placed on a $p(4 \times 4)$ supercell only two Ce^{4+} cations are reduced to Ce^{3+}, the same number as for a single particle in the same cell. If the spatial constraint is released by placing the two particles on a larger $p(5 \times 5)$ supercell the CT increases to 2–5 electrons. Hence, the electrostatic destabilization at high surface concentrations of Ce^{3+} appears to be limiting the maximum CT.

To explore the origin of the suppressed CT on very small particles, we investigated the influence of O vacancy sites. In fact, vacancies are found to reduce the net charge transfer to ceria: For example, the number of donated electrons decreases from 1–3 to 1–2 for Pt_{34} and from 4–6 to 1–4 for Pt_{95}. The reason is the lower propensity of the partially reduced ceria to accept additional electrons. Therefore, we attribute the lower CT on small clusters to nucleation at defects of the CeO_2 surface.

Finally, our calculations suggest that the CT can have a substantial influence on adsorption and, therefore, on reactivity. For instance, the CT can strengthen the adsorption of CO and H_2O by as much as 0.5 eV, whereas the effect on adsorbed oxygen is negligible (see Supplementary Information). This illustrates that the CT effect can be very important but its specific role has to be analysed individually for each reaction system.

In summary, we have quantified the CT between supported Pt nanoparticles and a well-defined ceria support that occurs as a result of the electronic metal–support interaction. We show that the CT reveals a characteristic size dependence and reaches a maximum for particles between 30 and 70 atoms, where up to 0.11 electrons are transferred per Pt atom ($Pt^{\delta+}$ with $\delta \approx 0.11$). For smaller particles, nucleation at defects hinders the CT, whereas the support limits the CT for larger particles. These results show that the CT can be tuned by adjusting the particle size, the particle structure and by the chemical properties of the support. Whereas for large particles the charge will be mainly localized at metal atoms in the vicinity of the interface, small aggregates close to the CT maximum consist of a few atomic layers only. Therefore, most of their surface atoms will carry an excess charge, a feature that may be used to modify material properties at a knowledge-driven basis.

Methods

Methods and any associated references are available in the online version of the paper.

Received 6 May 2015; accepted 3 November 2015; published online 14 December 2015

References

1. Graciani, J. *et al*. Highly active copper–ceria and copper–ceria–titania catalysts for methanol synthesis from CO_2. *Science* **345**, 546–550 (2014).
2. Campbell, C. T. Catalyst–support interactions: Electronic perturbations. *Nature Chem.* **4**, 597–598 (2012).
3. Campbell, C. T., Parker, S. C. & Starr, D. E. The effect of size-dependent nanoparticle energetics on catalyst sintering. *Science* **298**, 811–814 (2002).
4. Bruix, A. *et al*. A new type of strong metal–support interaction and the production of H_2 through the transformation of water on $Pt/CeO_2(111)$ and $Pt/CeO_x/TiO_2(110)$ catalysts. *J. Am. Chem. Soc.* **134**, 8968–8974 (2012).
5. Vayssilov, G. N. *et al*. Support nanostructure boosts oxygen transfer to catalytically active platinum nanoparticles. *Nature Mater.* **10**, 310–315 (2011).
6. Ertl, G., Knözinger, H., Schüth, F. & Weitkamp, J. *Handbook of Heterogeneous Catalysis* 2nd edn (Wiley, 2008).
7. Bell, A. T. The impact of nanoscience on heterogeneous catalysis. *Science* **299**, 1688–1691 (2003).
8. Chen, M. S. & Goodman, D. W. The structure of catalytically active gold on titania. *Science* **306**, 252–255 (2004).
9. Bruix, A. *et al*. Maximum noble metal efficiency in catalytic materials: Atomically dispersed surface platinum. *Angew. Chem. Int. Ed.* **53**, 10525–10530 (2014).
10. Trovarelli, A. & Fornasiero, P. *Catalysis by Ceria and Related Materials* (Imperial College Press, 2013).
11. Landman, U. *et al*. Factors in gold nanocatalysis: oxidation of CO in the non-scalable size regime. *Top. Catal.* **44**, 145–158 (2007).
12. Hansen, P. L. *et al*. Atom-resolved imaging of dynamic shape changes in supported copper nanocrystals. *Science* **295**, 2053–2055 (2002).
13. Fu, Q., Saltsburg, H. & Flytzani-Stephanopoulos, M. Active nonmetallic Au and Pt species on ceria-based water-gas shift catalysts. *Science* **301**, 935–938 (2003).
14. Tauster, S. J., Fung, S. C., Baker, R. T. K. & Horsley, J. A. Strong interactions in supported-metal catalysts. *Science* **211**, 1121–1125 (1981).
15. Dulub, O., Hebenstreit, W. & Diebold, U. Imaging cluster surfaces with atomic resolution: the strong metal–support interaction state of Pt supported on $TiO_2(110)$. *Phys. Rev. Lett.* **84**, 3646–3649 (2000).
16. Pacchioni, G. Electronic interactions and charge transfers of metal atoms and clusters on oxide surfaces. *Phys. Chem. Chem. Phys.* **15**, 1737–1757 (2013).
17. Sanchez, A. *et al*. When gold is not noble: nanoscale gold catalysts. *J. Phys. Chem. A* **103**, 9573–9578 (1999).
18. Campbell, C. T. & Sellers, J. R. V. Anchored metal nanoparticles: effects of support and size on their energy, sintering resistance and reactivity. *Faraday Discuss.* **162**, 9–30 (2013).
19. Luches, P. *et al*. Nature of Ag islands and nanoparticles on the $CeO_2(111)$ surface. *J. Phys. Chem. C* **116**, 1122–1132 (2011).
20. Kong, D. *et al*. Growth, structure, and stability of Ag on $CeO_2(111)$: Synchrotron radiation photoemission studies. *J. Phys. Chem. C* **115**, 6715–6725 (2011).
21. Freund, H. J., Nilius, N., Risse, T. & Schauermann, S. A fresh look at an old nano-technology: catalysis. *Phys. Chem. Chem. Phys.* **16**, 8148–8167 (2014).
22. Campbell, C. T. Ultrathin metal films and particles on oxide surfaces: structural, electronic and chemisorptive properties. *Surf. Sci. Rep.* **27**, 1–111 (1997).
23. Wertheim, G. K., DiCenzo, S. B. & Youngquist, S. E. Unit charge on supported gold clusters in photoemission final state. *Phys. Rev. Lett.* **51**, 2310–2313 (1983).
24. Kaden, W. E. *et al*. Understanding surface core-level shifts using the Auger parameter: a study of Pd atoms adsorbed on ultrathin SiO_2 films. *Phys. Rev. B* **89**, 115436 (2014).
25. Grant, A. W. & Campbell, C. T. Cesium adsorption on $TiO_2(110)$. *Phys. Rev. B* **55**, 1844–1851 (1997).
26. Nilius, N. *et al*. Electronic properties and charge state of gold monomers and chains adsorbed on alumina thin films on NiAl(110). *Phys. Rev. B* **81**, 045422 (2010).
27. Dvořák, F. *et al*. Adjusting morphology and surface reduction of $CeO_2(111)$ thin films on Cu(111). *J. Phys. Chem. C* **115**, 7496–7503 (2011).
28. Hu, S. *et al*. Ag nanoparticles on reducible $CeO_2(111)$ thin films: effect of thickness and stoichiometry of ceria. *J. Phys. Chem. C* **119**, 3579–3588 (2015).
29. Matsumoto, M. *et al*. Resonant photoemission study of CeO_2. *Phys. Rev. B* **50**, 11340–11346 (1994).
30. Pan, Y. *et al*. Titration of Ce^{3+} ions in the $CeO_2(111)$ surface by Au adatoms. *Phys. Rev. Lett.* **111**, 206101 (2013).

Acknowledgements

This work was financially supported by the European Community (FP7-NMP.2012.1.1-1 project ChipCAT, Reference No. 310191), by the 'Deutsche Forschungsgemeinschaft' (DFG) within the Excellence Cluster 'Engineering of Advanced Materials' in the framework of the Excellence Initiative, by Spanish MINECO (grant CTQ2012-34969), by the Generalitat de Catalunya (grants 2014SGR97 and XRQTC), and by the Czech Science Foundation (grant 15-06759S). The authors also acknowledge the CERIC-ERIC Consortium for access to experimental facilities and financial support and the COST Action CM1104 for additional support. Computer resources and assistance were provided by the Red Española de Supercomputación. S.M.K. is grateful to Spanish Ministerio de Educación for a pre-doctoral FPU Grant AP2009-3379. The authors thank A. Kaftan for his contribution to the numerical analysis procedure for XPS.

Author contributions

S.M.K. performed the density functional calculations. S.M.K., S.F. and K.M.N. analysed the calculated data and were involved in the preparation of the manuscript. K.M.N. supervised the theoretical work. Y.L., T.S. and N.T. performed the RPES experiments. Y.L., T.S., A.N. and J.L. were involved in the analysis of the experimental data and the preparation of the manuscript. J.L. and V.M. supervised the experimental work. A.T., V.S., F.D., V.J. and J.M. performed STM and XPS experiments.

Additional information

Supplementary information is available in the online version of the paper. Reprints and permissions information is available online at www.nature.com/reprints. Correspondence and requests for materials should be addressed to K.M.N. or J.L.

Competing financial interests

The authors declare no competing financial interests.

Methods

Spectroscopic characterization. High-resolution synchrotron-radiation photoelectron spectroscopy (SRPES) and resonant photoemission spectroscopy (RPES) studies were performed at the Materials Science Beamline (MSB), Elettra Synchrotron Light Facility in Trieste, Italy. The MSB, with a bending magnet source, provides synchrotron light in the energy range 21–1,000 eV. The ultrahigh vacuum (UHV) end-station (base pressure 1×10^{-10} mbar) was equipped with a multichannel electron energy analyser (Specs Phoibos 150), rear-view low-energy electron diffraction (LEED) optics, an argon sputter gun, and a gas inlet system. The basic set-up of the chamber includes a dual Mg/Al X-ray source. In addition, two electron-beam evaporators for Ce and Pt deposition were installed.

A single-crystal Cu(111) disc (MaTecK GmbH, 99.999%) was used as a substrate for the preparation of the CeO_2(111) films. Cu(111) was cleaned by several cycles of Ar^+ sputtering (300 K, 60 min) and annealing (723 K, 5 min) until no traces of carbon or any other contaminant were found in the photoelectron spectra. Epitaxial CeO_2(111) films were prepared by physical vapour deposition (PVD) of Ce metal (Goodfellow, 99.99%) from an electron-beam evaporator (Tectra e-flux) in an oxygen atmosphere ($p_{O_2} = 5 \times 10^{-7}$ mbar, Linde, 99.999%) at 523 K, followed by annealing of the films at 523 K in an oxygen atmosphere at the same pressure for 5 min. The preparation method[31] yielded a continuous[32], stoichiometric CeO_2(111) film with a thickness of 2.1 nm, as determined from the attenuation of the Cu $2p_{3/2}$ intensity. Low-energy electron diffraction (LEED) studies of the prepared films confirmed the epitaxial growth of CeO_2(111) with the characteristic (1.5 × 1.5) superstructure relative to the Cu(111) substrate.

Pt (Goodfellow, 99.99%) was deposited by PVD from an electron-beam evaporator (Oxford Scientific OS-Vap) onto the CeO_2(111)/Cu(111) at 300 K. To maintain a constant deposition rate of Pt, the evaporator was maintained at its working parameters with a shutter closed for 5 min before each deposition step. The nominal thickness of the deposited Pt layer was calculated from the attenuation of Cu $2p_{3/2}$ intensity under the assumption of a 3D growth model for Pt nanoparticles on CeO_2(111) (see Supplementary Information for details).

Core-level spectra of Pt 4*f*, C 1*s* and O 1*s* were acquired at 180, 410 and 650 eV, respectively. The binding energies in the spectra acquired with synchrotron radiation were calibrated with respect to the Fermi level. In addition, Al Kα radiation (1,486.6 eV) was used to measure O 1*s*, Ce 3*d* and Cu $2p_{3/2}$ core levels. All spectra were acquired at constant pass energy and at an emission angle for the photoelectrons of 20° or 0° with respect to the sample normal, respectively, when using the X-ray source or synchrotron radiation.

Valence band spectra were acquired at three different photon energies, 121.4, 124.8 and 115.0 eV, corresponding to the resonant enhancements in Ce^{3+} and Ce^{4+} ions and to off-resonance conditions, respectively. Analysis of the spectra obtained with these photon energies forms the basis of RPES. The Ce^{3+} resonance at a photon energy of 121.4 eV is caused by a super-Coster–Kronig decay involving electron emission from Ce 4*f* states located about 1.4 eV below the Fermi edge. The Ce^{4+} resonance at a photon energy of 124.8 eV involves emission of O 2*p* electrons (hybridized with Ce states) from the valence band around 4.0 eV. The valence band spectrum measured at a photon energy of 115 eV is used as a background for the calculation of the intensity difference of the features both on- and off-resonance, denoted as the resonant enhancements for Ce^{3+}, $D(Ce^{3+})$, and for Ce^{4+}, $D(Ce^{4+})$, respectively. The resonant enhancement ratio (RER), calculated as $D(Ce^{3+})/D(Ce^{4+})$, is a direct measure of the degree of reduction of cerium oxide.

The values of total spectral resolution were 1 eV (Al Kα), 200 meV ($h\nu = 115$–180 eV), 400 meV ($h\nu = 410$ eV) and 650 meV ($h\nu = 650$ eV).

During the experiment, the sample temperature was controlled by a d.c. power supply passing a current through tantalum wires holding the sample. The temperature was monitored by a K-type thermocouple attached to the back of the sample.

Scanning tunnelling microscopy and X-ray photoelectron spectroscopy. The STM/XPS experiments were performed at Charles University in Prague. The UHV set-up (base pressure of 10^{-10} mbar) was equipped with a STM system, a dual Mg/Al X-ray source, a hemispherical electron energy analyser (Specs Phoibos 150), LEED optics, and two electron-beam evaporators for depositing Ce and Pt metals. Pt was deposited on a well-ordered CeO_2(111) film grown on Cu(111) according to the procedure described for the SRPES study.

STM images were acquired with commercial Pt–Ir tips (Unisoku). The imaging of CeO_2(111) and Pt/CeO_2(111) films was performed via unoccupied states, applying a positive sample voltage with respect to the tip. We used sample voltages 2.5–3.5 V, and tunnelling currents 25–75 pA.

Density functional calculations. Periodic density functional calculations were carried out using the VASP (refs 33,34) package and employing the Perdew–Wang[35,36] (PW91) implementation of the generalized gradient approximation (GGA) for the exchange–correlation functional. An effective on-site Hubbard correction $U_{\text{eff}} = 4$ eV (refs 37) was applied to the Ce 4*f* orbitals within the GGA+U scheme (PW91+4 approximation)[38,39]. A plane-wave basis with a 415 eV cutoff for the kinetic energy and a projector-augmented wave[40] description of core–valence electron interactions were employed. Total energies were converged within 10^{-5} eV. The structures were optimized until forces on relaxed atoms became less than 0.2 eV nm^{-1}. The dimensions of the periodic p(4 × 4) and p(5 × 5) CeO_2(111) surface cells were 1.527×1.527 nm^2 and 1.909×1.909 nm^2, respectively, with 2.2 nm of vacuum separation between adjacent slabs. In the case of CeO_2(111) with O vacancies, a single vacancy was created in the surface O layer at the perimeter of the Pt/ceria interface. Owing to the size of the cells employed and the mostly ionic nature of bonds in ceria, all calculations were performed at the Γ-point in the reciprocal space.

The adhesion energies (E_{adh}) of Pt particles comprising N atoms (Pt_N) to CeO_2(111) were calculated as $E_{\text{adh}}[Pt_N] = -\{E[Pt_N] + E[CeO_2(111)] - E[Pt_N/CeO_2(111)]\}$, where $E[Pt_N]$ and $E[CeO_2(111)]$ are the total energies of an isolated Pt particle and the ceria support, respectively, and $E[Pt_N/CeO_2(111)]$ is the total energy of the supported system.

The present calculations were performed using the computational resources of CaesarAugusta (Zaragoza, Spain) and IQTCUB (Barcelona, Spain) and consumed more than 10^6 CPU hours.

References

31. Šutara, F. *et al*. Epitaxial growth of continuous CeO_2(111) ultra-thin films on Cu(111). *Thin Solid Films* **516**, 6120–6124 (2008).
32. Vari, G., Ovari, L., Kiss, J. & Konya, Z. LEIS and XPS investigation into the growth of cerium and cerium dioxide on Cu(111). *Phys. Chem. Chem. Phys.* **17**, 5124–5132 (2015).
33. Kresse, G. & Furthmüller, J. Efficient iterative schemes for *ab initio* total-energy calculations using a plane-wave basis set. *Phys. Rev. B* **54**, 11169–11186 (1996).
34. Kresse, G. & Hafner, J. *Ab initio* molecular dynamics for liquid metals. *Phys. Rev. B* **47**, 558–561 (1993).
35. Perdew, J. P. *et al*. Atoms, molecules, solids, and surfaces: applications of the generalized gradient approximation for exchange and correlation. *Phys. Rev. B* **48**, 4978 (1993); erratum **46**, 6671 (1992).
36. Perdew, J. P. & Wang, Y. Accurate and simple analytic representation of the electron-gas correlation energy. *Phys. Rev. B* **45**, 13244–13249 (1992).
37. Loschen, C., Carrasco, J., Neyman, K. M. & Illas, F. First-principles LDA+U and GGA+U study of cerium oxides: dependence on the effective U parameter. *Phys. Rev. B* **84**, 199906 (2011); erratum **75**, 035115 (2007).
38. Anisimov, V. I., Aryasetiawan, F. & Lichtenstein, A. I. First-principles calculations of the electronic structure and spectra of strongly correlated systems: The LDA+*U* method. *J. Phys. Condens. Matter* **9**, 767–808 (1997).
39. Dudarev, S. L. *et al*. Electron-energy-loss spectra and the structural stability of nickel oxide: an LSDA+U study. *Phys. Rev. B* **57**, 1505–1509 (1998).
40. Kresse, G. & Joubert, D. From ultrasoft pseudopotentials to the projector augmented-wave method. *Phys. Rev. B* **59**, 1758–1775 (1999).

3.2 Creating single-atom Pt-ceria catalysts by surface step decoration

Single-atom catalysts represent the group of supported metal catalysts with metal load dispersed as single atom [32]. This provides maximum efficiency for using metal atoms in catalytic reactions, giving an opportunity to minimize precious metal content in catalysts [151], [152]. Central challenge in the production of single-atom catalysts is understanding of specific adsorption sites on supports which provide stabilization for single metal atoms during catalytic reaction at elevated temperatures. Among the existing single-atom catalysts, highly dispersed Pt ions on ceria hold a promise for radical reduction of Pt load in critical large-scale catalytic applications — hydrogen production [152], three-way catalytic converters [159] and fuel cells [160]. Recent studies on large area ceria samples identify the necessity of nanostructuring the ceria substrates so as to obtain supported Pt^{2+} ions and propose a square-planar PtO_4 unit as a Pt^{2+}-containing surface moiety [151]. In the present study we show, that Pt^{2+} ions are stabilized at monoatomic step edges of CeO_2(111) surface. Additionally, we adjust the step density of the ceria support so as to maximize the load of Pt^{2+} ions.

In order to determine the specific adsorption sites for Pt^{2+} ions, several ceria model surfaces with different concentration of step edges and surface oxygen vacancies were prepared. Platinum particles in quantity of 0.06 ML were deposited onto these ceria surfaces and stabilized via heating at 700K. The state of Pt nanoparticles was determined from XPS and SRPES measurements. First, platinum was deposited and stabilized on flat CeO_2 surface with low density of steps and oxygen vacancies, resulting in two chemical states: metallic Pt^0 clusters and ionic Pt^{2+} atoms, as evidenced by spectroscopic measurements. Second, Pt was deposited at flat $CeO_{1.7}$ surface with increased concentration of oxygen vacancies. In this case, Pt stabilized exclusively as small Pt^0 clusters clearly seen in STM. Finally, Pt was deposited onto the oxidized CeO_2 surface with increased step density. Here, Pt preferably stabilized into Pt^{2+} state indicating the key role of step edges on the ceria surface in stabilizing monodispersed Pt^{2+} ions. Once created, Pt^{2+} ions remain stable during the repeated cycles of annealing at 700K as well as during the CO adsorption and desorption in UHV.

Platinum was also deposited onto ceria films with adjustable density of monoatomic steps. Control over density of step edges was achieved by using methods developed in our group (Figure 1.6.1). STM and SRPES measurements revealed the presence of both Pt^0 clusters and Pt^{2+} ions on stepped CeO_2 surfaces, and a direct proportionality between the observed amount of Pt^{2+} ions and the step density on the samples (Figure 2 of the publication).

High sensitivity SRPES and RPES spectroscopic measurements also revealed, that the oxidation of Pt atoms and their stabilization into Pt^{2+} ions is not accompanied by reduction of surface Ce^{4+} ions. This excludes the direct participation of ceria into the observed Pt oxidation at steps therefore indicating the involvement of other oxidizing agents in the stabilization of Pt^{2+} ions, such as excess oxygen atoms. The possible source for excess oxygen in UHV environment can be water adsorbing in sub-ML amounts from background atmosphere and undergoing dissociation on reduced ceria and Pt/ceria substrates [114], [146].

In order to support and understand the experimental observations, *ab-initio* DFT calculations were performed for adsorption sites on CeO_2(111) surfaces including oxygen vacancies, regular sites on terraces and two preferred types of steps at the CeO_2(111) surfaces. Agreement between the theory and the experiment can only be achieved when taking into account the step edges in the presence of an excess of O atoms. DFT calculations also reveal high binding energy values for Pt^{2+} ions at step edges with excess oxygen (6.6-6.7 eV).

Theoretical calculations proposed the binding mechanism for Pt ions on ceria. At step edge, Pt atom binds to four neighbor O atoms forming stable PtO_4 unit (Figure 3 of the publication). On terrace and oxygen vacancy Pt atoms are weakly bound and easy coalesce into Pt^0 clusters. At step edges, the presence of excess oxygen atoms is essential for the formation of PtO_4 moieties (Figure 4 of the publication).

The results presented in this work can be applied for the interpretation of the properties and the optimization of the Pt^{2+} load on large-area ceria supports [152], [159], [160]. In general, the step edges may represent a common type of adsorption sites providing stabilization for monodispersed metal atoms and ions in any oxide-supported single-atom catalysts [161]. Our results therefore introduce important concepts of step reactivity [162] and step engineering [163] in understanding the stability, the activity and in designing new single-atom catalysts.

My contribution to this work was preparation of ceria layers with controlled stoichiometry and density of step edges with subsequent Pt deposition and characterization of the obtained systems using STM and XPS. I have developed experimental procedures for preparing CeO_2 substrates with increased step density via homoepitaxy of CeO_2 islands on CeO_2 thin films (Figure 2.6.1 d). STM measurements revealed Pt clusters on the ceria surface. However, statistics of Pt clusters on the CeO_2 surface with high step density in comparison with QCM data indicates, that the clusters contained only 10% of the total Pt deposit. Most of the Pt deposit remained invisible in STM images. Theoretical calculations showed that Pt^{2+} species are not discernible in empty states STM imaging

because of their electronic structure. XPS and SRPES measurements showed most of the Pt to be in atomically dispersed Pt^{2+} state. In order to disclose the Pt^{2+} ions microscopically, STM imaging in empty and occupied states was performed as well as detailed STM images of the ceria islands were obtained (Figure 3.2.1a-c). STM imaging of occupied states showed better contrast of Pt_0 clusters, but Pt ions remained invisible. Hence, statistical approach based on step density evaluation and Pt^{2+} signal in SRPES together with DFT calculations was performed.

The qualitative analysis of the state of Pt deposit was made by using XPS. With XPS it was only possible to determine the existence of Pt at the ceria surface and its preferred state as metallic or ionic (Figure 2.2.2). More precise and quantitative evaluation of the Pt state was performed on a series of samples prepared under the same conditions (stoichiometry, step density, Pt amount, temperature) using SRPES at synchrotron Elettra in Trieste, Italy.

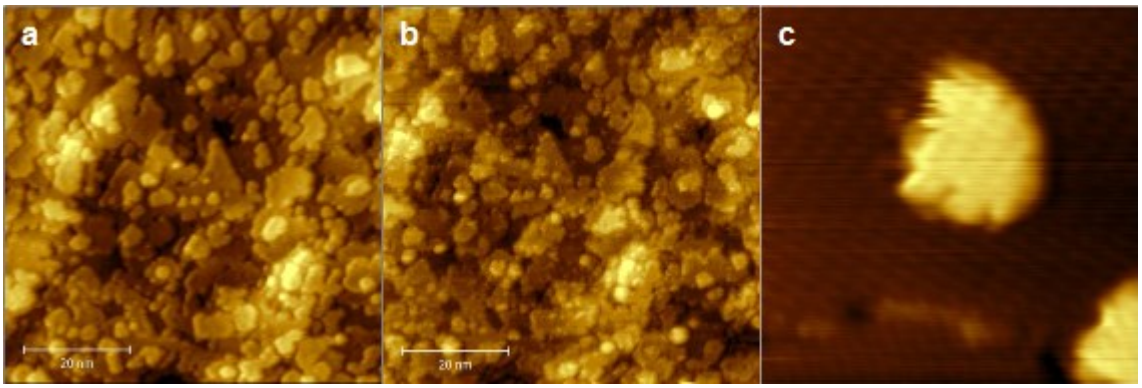

Figure 3.2.1. STM images of model Pt/CeO_2 system with 0.06ML of Pt deposit stabilized as Pt^{2+} ions: a) – imaging in empty states; b) – imaging of the same area in occupied states; c) – detailed image of a CeO_2 island in empty states (sample from Figure 1h of the publication). Even on highly resolved STM images the Pt^{2+} ions provide no specific STM contrast. The size of the a-b images is 70×70nm, c – 9.5×9.5nm.

nature COMMUNICATIONS

ARTICLE

Received 4 Sep 2015 | Accepted 20 Jan 2016 | Published 24 Feb 2016

DOI: 10.1038/ncomms10801 OPEN

Creating single-atom Pt-ceria catalysts by surface step decoration

Filip Dvořák[1,*], Matteo Farnesi Camellone[2,*], Andrii Tovt[1], Nguyen-Dung Tran[2,3], Fabio R. Negreiros[2,†], Mykhailo Vorokhta[1], Tomáš Skála[1], Iva Matolínová[1], Josef Mysliveček[1], Vladimír Matolín[1] & Stefano Fabris[2,3]

Single-atom catalysts maximize the utilization of supported precious metals by exposing every single metal atom to reactants. To avoid sintering and deactivation at realistic reaction conditions, single metal atoms are stabilized by specific adsorption sites on catalyst substrates. Here we show by combining photoelectron spectroscopy, scanning tunnelling microscopy and density functional theory calculations that Pt single atoms on ceria are stabilized by the most ubiquitous defects on solid surfaces—monoatomic step edges. Pt segregation at steps leads to stable dispersions of single Pt^{2+} ions in planar PtO_4 moieties incorporating excess O atoms and contributing to oxygen storage capacity of ceria. We experimentally control the step density on our samples, to maximize the coverage of monodispersed Pt^{2+} and demonstrate that step engineering and step decoration represent effective strategies for understanding and design of new single-atom catalysts.

[1] Charles University in Prague, Faculty of Mathematics and Physics, V Holešovičkách 2, Prague 18000, Czech Republic. [2] CNR-IOM DEMOCRITOS, Istituto Officina dei Materiali, Consiglio Nazionale delle Ricerche, Via Bonomea 265, Trieste 34136, Italy. [3] SISSA, Scuola Internazionale Superiore di Studi Avanzati, Via Bonomea 265, Trieste 34136, Italy. * These authors contributed equally to this work. † Present address: Universidade Federal do ABC. Av. dos Estados, 5001 Bairro Bangu, Santo André SP CEP 09210-580, Brasil. Correspondence and requests for materials should be addressed to J.M. (email: josef.myslivecek@mff.cuni.cz) or to S.F. (email: fabris@democritos.it).

Single-atom catalysts represent the limiting realization of supported metal catalysts with metal load ultimately dispersed as single atoms[1,2]. This maximizes the utilization of supported metals and helps development of sustainable catalytic technologies for renewable energies and environmental applications with reduced precious metal contents[3,4]. A central prerequisite for understanding and knowledge-based design of single-atom catalysts is the identification of specific adsorption sites on catalyst supports that provide the stabilization of single metal atoms under reaction conditions at elevated temperatures and pressures. For oxide supports, understanding specific adsorption sites presently concentrates on low-index oxide facets[5–9]. Single-atom catalysts are, however, nanostructured large-area materials; thus, a question arises whether single supported atoms can be stabilized at defect sites of nanostructured oxide supports.

Highly dispersed platinum (Pt) ions on ceria qualify as single-atom catalysts[2] and hold a promise of radical reduction of Pt load in critical large-scale catalytic applications—hydrogen production[3], three-way catalytic converters[10] and fuel cells[11]. Ceria surfaces provide a limited amount of low coordinated surface sites where Pt^{2+} ions can adsorb and remain stable in real applications[2,3,10,11]. Recent studies on large-area ceria samples identify the necessity of nanostructuring the ceria substrates for obtaining supported Pt^{2+} ions[2,4] and propose a square-planar PtO_4 unit as a Pt^{2+}-containing surface moiety[4]. In the present model study on the single crystalline $CeO_2(111)$ surface, we demonstrate that single-ion dispersions of Pt^{2+} are stabilized at monolayer (ML)-high ceria step edges. Pt^{2+} ions at step edges are located in PtO_4 units that can be considered the elementary building blocks of Pt^{2+}/ceria single-atom catalysts. The PtO_4 units incorporate excess O and can act as oxygen source for redox reactions. Besides clarifying the nature of Pt^{2+} stabilization on ceria, our study demonstrates the importance of step edges—the most common surface defects on oxide supports[12]—for single-atom catalyst stabilization. We experimentally adjust the step density on the ceria supports for maximizing the load of monodispersed Pt^{2+} ions. This identifies step engineering[13] and step decoration[14,15] as advanced techniques for designing new single-atom catalysts.

Results

Pt deposits on highly defined $CeO_2(111)$ surfaces. The experiments were performed on model $CeO_2(111)$ surfaces prepared as 20 to 40 Å thick ceria films on Cu(111) using procedures that allow adjusting the density of ML-high steps[16] and the density of surface oxygen vacancies on ceria surface[17]. On these highly defined surfaces, we deposit 0.06 ML of Pt, anneal at 700 K in ultra-high vacuum (UHV) and observe stabilization of Pt^{2+} species and/or nucleation of Pt clusters with scanning tunnelling microscopy (STM) and with photoelectron spectroscopy (PES). Deposition and annealing of Pt on $CeO_2(111)$ surfaces containing low concentrations of defects—ML-high steps and surface oxygen vacancies (Fig. 1a)—yield

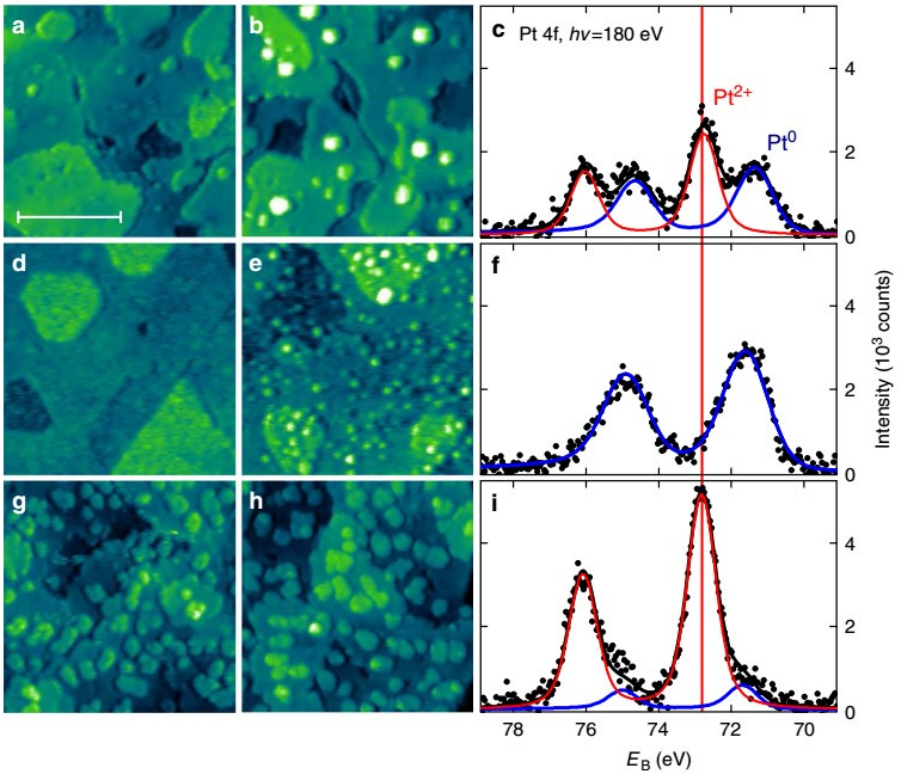

Figure 1 | Nucleation of Pt and stabilization of Pt^{2+} on ceria surfaces containing controlled amount of surface defects. (**a**–**c**) $CeO_2(111)$ surface with low density of surface oxygen vacancies and ML-high steps. (**d**–**f**) $CeO_{1.7}$ surface with increased density of surface oxygen vacancies. (**g**–**i**) $CeO_2(111)$ surface with increased density of ML-high steps. (**a**,**d**,**g**) STM images of clean surfaces before deposition of Pt. (**b**,**e**,**h**) STM images after deposition of 0.06 ML Pt and annealing at 700 K in UHV. All STM images 45 × 45 nm^2, tunnelling current 25–75 pA, sample bias voltage 2.5–3.5 V. Scale bar, 20 nm (**a**). (**c**,**f**,**i**) PES spectra of the Pt deposit after annealing. All PES spectra were acquired with photon energy $h\nu = 180$ eV (black points). Fits indicate metallic (Pt^0, blue line) and ionic (Pt^{2+}, red line) contributions to Pt 4f signal. E_B is the photoelectron binding energy.

metallic Pt^0 clusters (Fig. 1b,c) coexisting with ionic Pt^{2+} species (Fig. 1c). To determine whether the charge of the supported Pt species is selectively induced by a specific defect type, we repeat the experiment varying independently the amount of surface O vacancies—up to 0.16 ML, creating $CeO_{1.7}$ surface (Fig. 1d–f)—and the amount of ML-high steps on the $CeO_2(111)$ surface—up to 0.15 ML (Fig. 1g–i). We observe that surface oxygen vacancies do not promote the dispersion of Pt^{2+} species but lead to small metallic Pt^0 clusters (Fig. 1e,f)[18]. On the other hand, the increased step density leads to almost complete oxidation of the Pt deposit to Pt^{2+} (Fig. 1h,i) proving that step edges selectively promote the stabilization of Pt^{2+} species. Detailed STM images allow to exclude formation of three-dimensional and two-dimensional PtO_x clusters (Supplementary Fig. 1), and allow to conclude that Pt^{2+} species are incorporated in the ceria step edges. Nucleation of Pt^0 clusters and stabilization of Pt^{2+} species represent concurrent processes. Differently to Pt^0 clusters (Fig. 1b,e), Pt^{2+} species at the step edges are not discernible in empty states STM imaging (*cf.* Fig. 1g,h without and with Pt deposit) because of their electronic structure. STM imaging in occupied states on metal-supported ceria is unavailable[19].

The possibility to adjust the density of ML-high steps on the model $CeO_2(111)$ surfaces[16] allows us to obtain a quantitative correlation between the step density and the amount of Pt^{2+} species. We prepare $CeO_2(111)$ samples with step density between 0.06 and 0.20 ML[16] and deposit 0.06 or 0.18 ML Pt at 300 K. Parameters of the prepared samples are summarized in Supplementary Table 1. After annealing at 700 K the amount of Pt stabilized in the form of Pt^{2+} is determined by PES. For quantification, all relevant parameters—the density of ceria steps, deposited amount of Pt and amount of stabilized Pt^{2+}—are expressed in ML where 1 ML corresponds to the density of Ce atoms on the $CeO_2(111)$ surface, that is, $7.9 \times 10^{14}\,cm^{-2}$. The density of steps is defined as the density of Ce atoms located at the ceria step edges[20].

The amount of Pt^{2+} ions as a function of the step density is plotted in Fig. 2a. For the higher Pt coverage 0.18 ML, the analysis reveals a linear dependence between the amount of stabilized Pt^{2+} ions and the step density (Fig. 2a, blue symbols), confirming the activation of Pt oxidation to Pt^{2+} and the localization of Pt^{2+} at the surface steps. The highest step density 0.20 ML allows converting up to 80% of the Pt deposit to Pt^{2+}. The degree of oxidation of the Pt deposit increases with decreasing the amount of deposited Pt to 0.06 ML (Fig. 2a, black symbols). In this case, up to 90% of Pt converts to Pt^{2+}. The concentrations of ceria step edges and the amount of Pt^{2+} stabilized on the surface obey a classical supply-and-demand scenario characteristic for single-atom catalysts[1,4,10]: when sufficient step edges, the amount of oxidized Pt^{2+} is limited by the amount of deposited Pt. Otherwise, the amount of oxidized Pt^{2+} is limited by the step density regardless of the amount of deposited Pt. The Pt deposit exceeding the available step sites cannot be oxidized and nucleates as metallic Pt^0 clusters on the surface. Besides the high oxidative power of the step edges towards Pt, our quantitative analysis reveals also the capacity of ceria step edges to accommodate a high density of Pt^{2+} ions. Up to 0.16 ML of Pt^{2+} ions can be stabilized by the sample containing 0.18 ML of Pt deposit and 0.20 ML of steps (Fig. 2a, blue symbols). This corresponds to 80% of the step-edge sites being occupied by Pt^{2+}. In the whole range of the step densities between 0.06 and 0.20 ML, the occupation of the step-edge sites by Pt^{2+} varies between 50 and 80%.

Stability and charge state of $Pt^{2+}/CeO_2(111)$ samples. The necessity of annealing the Pt deposit on ceria in UHV at 700 K for obtaining Pt^{2+} stabilization in our experiment indicates the activated nature of Pt segregation at the ceria steps and oxidation, and implies considerable thermal stability of Pt^{2+} ions on ceria. High-temperature annealing represents a prerequisite for obtaining Pt^{2+} ions also in the experiments on large-area nanostructured ceria samples[3,4]. Once created, Pt^{2+} ions remain stable on repeated annealing at 700 K in UHV. The Pt^{2+} ions in our experiment also remain stable on adsorption and thermal desorption of CO in UHV (Supplementary Fig. 2), or on exposure to air at ambient conditions (Supplementary Fig. 3).

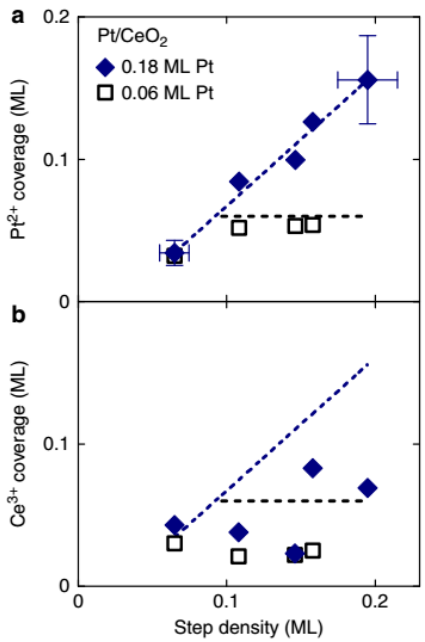

Figure 2 | Capacity of stepped $CeO_2(111)$ surface to accommodate Pt^{2+}. (**a**) Amount of Pt^{2+} stabilized on $CeO_2(111)$ substrates with different density of steps for 0.18 ML (blue symbols) and 0.06 ML (black symbols) of deposited platinum. Pt not stabilized in the form of Pt^{2+} remains metallic. Lines represent guides to the eyes. Blue line is a linear fit of 0.18 ML Pt data. Black line represents the maximum achievable amount of Pt^{2+} in the case of 100% oxidation of Pt for 0.06 ML of deposited Pt. (**b**) Reduction of the ceria surface accompanying the stabilization of Pt^{2+} ions determined by resonant PES expressed as a coverage of the surface by Ce^{3+} ions. Lines represent guides to the eyes from **a** and indicate the Pt^{2+} concentration. The Ce^{3+} concentration is lower or equal to the Pt^{2+} concentration on all samples.

Parallel to the charge state of the Pt deposit we determine the charge state of the CeO_2 support, in particular the concentration of surface Ce^{3+} ions that is indicative of reduction of the ceria surface. Contrary to the case of stabilizing Ni^{2+} ions on ceria[21], we observe that Pt oxidation during annealing is not accompanied by a corresponding reduction of $CeO_2(111)$ surface (Fig. 2b). This rules out the direct participation of ceria into the observed Pt oxidation at steps and indicates the involvement of other oxidizing agents in the Pt^{2+} stabilization, such as excess oxygen atoms. In the UHV environment of our experiments, the eligible source of excess oxygen can be water adsorbing in sub-ML amounts from background atmosphere (Supplementary Fig. 4) and undergoing dissociation on reduced ceria and Pt/ceria substrates[22,23]. In the large-area Pt^{2+}/CeO_2 catalysts displaying high concentration of Pt^{2+} ions and exceptional redox reactivity, excess O atoms may be incorporated during the synthesis that proceeds in air[3,10].

Segregation of Pt at CeO_2(111) step edges. *Ab initio* density functional theory (DFT) calculations allow to interpret the above experimental results. We calculate the segregation thermodynamics and the atomic and electronic structures of Pt atoms in representative adsorption sites on CeO_2(111) surfaces. The results for the lowest-energy configurations are summarized in Fig. 3 and Table 1. The model adsorption sites include oxygen vacancies (Fig. 3a), regular sites (Fig. 3b) and Pt clusters[24] (Fig. 3c) on the CeO_2(111) terrace, as well as two low-energy ML-high steps, which we label following ref. 25 as step I (Fig. 3d) and step II (Fig. 3e). A detailed list of the systems considered in the DFT analysis is reported in the Supplementary Note 1. The steps I and II represent the preferred types of steps at the CeO_2(111) surfaces at temperatures $<1{,}000$ K (ref. 25). On our experimental samples, the steps I and II appear in equal proportion as evidenced from the absence of triangularly shaped islands in Fig. 1a,g[25,26].

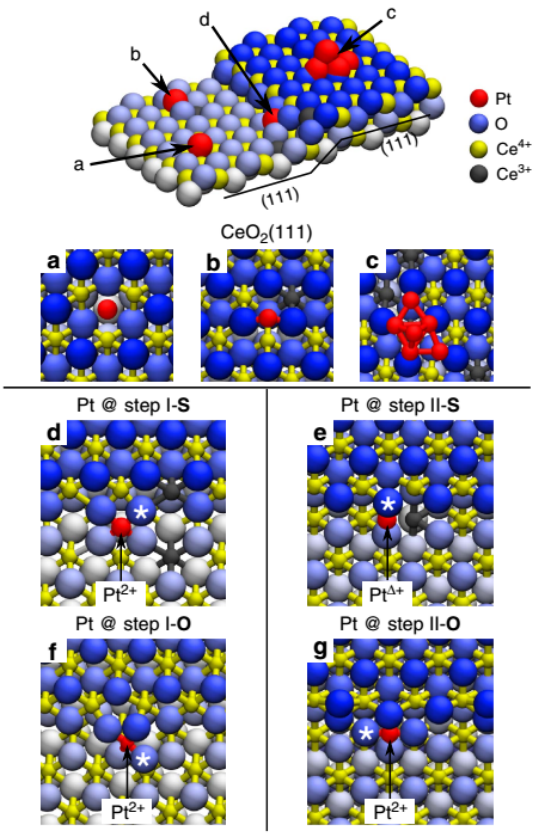

Figure 3 | Pt adsorption sites on the CeO_2(111) surface obtained from DFT calculations. (**a**) Pt adatom in a surface O vacancy, (**b**) on the stoichiometric CeO_2(111) terrace and (**c**) supported Pt_6 cluster. (**d**) Pt adatom at the stoichiometric step I (step I-S) and (**e**) at the stoichiometric step II (step II-S). (**f**) Pt adatom at the step I with excess O (step I-O) and (**g**) at the step II with excess O (step II-O). Binding energies and Bader charges are summarized in Table 1. (**d**–**g**) The * symbol denotes the O atom removed to calculate the O vacancy formation energy reported in Table 2.

In agreement with the experiment, our calculations predict the preferential segregation of Pt adatoms at the steps I and II, independently on the local step geometry and stoichiometry. The binding energies of Pt at the steps are 1.6–3.4 eV higher than at stoichiometric or defective (111) terraces (Table 1). This driving force for Pt segregation at the steps is in qualitative agreement with recent calorimetric studies of other metal clusters on CeO_2(111)[27,28], see the Supplementary Discussion. The particular binding energy and the charge state of Pt atoms at the steps depend on both the local step geometry and stoichiometry (Table 1). In the following, we show that a good agreement with all the experimental observations can only be achieved when considering segregation of Pt at steps in the presence of excess O (calculations denoted as O), while Pt segregation at stoichiometric steps (denoted S) exhibits significant discrepancies.

Pt at stoichiometric CeO_2(111) step edges. Pt segregation on step I-S yields Pt^{2+} species that are coordinated by four lattice O atoms in a characteristic PtO_4 planar unit (Fig. 3d). The PtO_4 unit is remarkably similar to that one proposed for Pt-doped ceria nanoparticles[4] and for surface reconstructions of Pd–ceria systems[29]. Instead, the different atomic structure of the step II-S edge prevents the formation of PtO_4 units, hinders the full Pt oxidation to Pt^{2+} and yields weakly oxidized $Pt^{\Delta+}$ species (Fig. 3e). Calculation results presented in Fig. 3d–g correspond to the Pt coverage at the steps 1/3 (1 Pt atom per 3 Ce step-edge atoms). For interpreting the capacity of the ceria step edges to accommodate a high density of Pt^{2+} ions, we calculate the adsorption of Pt at the ceria steps with increasing Pt coverage at the steps (Fig. 4), ranging from 1/3 to 1 (1 Pt atom per 1 Ce step-edge atom). On the step I-S, the maximum coverage of Pt^{2+} species is 2/3 (Fig. 4a). Higher Pt^{2+} coverages are unattainable and lead to nucleation of metallic Pt clusters, due to the large strain buildup resulting from long sequences of interconnected PtO_4 step units (Fig. 4b). On the step II-S, metallic Pt^0 species appear already for a coverage higher than 1/3 (Fig. 4c). Thus, on

Table 1 | Properties of Pt on CeO_2(111) obtained from DFT calculations.

Pt adsorption site	Binding energy (eV)	Formal charge	Bader charge (e)
Pt @ O vacancy	2.8	$Pt^{\Delta-}$	10.9
Pt @ CeO_2(111)	3.3	$Pt^{\Delta+}$	9.7
Pt_6 @ CeO_2(111)	4.4	Pt^0	9.9
Pt @ step I-S	5.0	Pt^{2+}	9.2
Pt @ step II-S	5.1	$Pt^{\Delta+}$	9.7
Pt @ step I-O	6.6	Pt^{2+}	8.6
Pt @ step II-O	6.7	Pt^{2+}	9.0
Pt bulk	5.5*	Pt^0	10.0

DFT, density functional theory; Pt, platinum; I-S and II-S, stoichiometric step types I and II; I-O and II-O, step types I and II with excess O atoms.
Results for the binding energies per atom, formal charges and Bader charges of Pt adatoms at the adsorption sites displayed in Fig. 3a–g. The binding energy for the Pt_6 cluster is the total binding energy divided by the number of Pt atoms. For reference, Pt bulk values are given in the last line.
*Bulk cohesive energy.

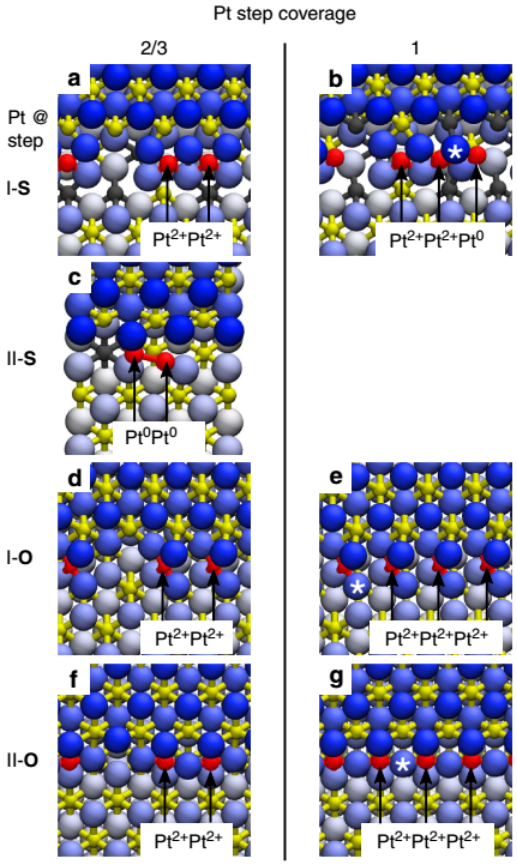

Figure 4 | Capacity of the CeO_2(111) step edges to accommodate Pt^{2+} ions obtained from DFT calculations. Calculated top views of the Pt binding to the steps I-S (**a**,**b**), step II-S (**c**), step I-O (**d**,**e**) and the step II-O (**f**,**g**) for Pt step coverage 2/3 (**a**,**c**,**d**,**f**) and 1 (**b**,**e**,**g**). At the step I-S, the limiting coverage of Pt^{2+} is 2/3 (**a**), additional Pt attaches to step edge as Pt^0 (**b**). At the step II-S, the Pt^{2+} coverage is 0. Pt atoms attach as weakly ionized $Pt^{\Delta+}$ and readily form metallic dimers (**c**) and clusters. On both steps I-O and II-O, excess oxygen can stabilize ionic Pt^{2+} at step edges as single ions appearing isolated or in groups up to 100% step coverage (**d**–**g**). The * symbol denotes the O atom removed to calculate the O vacancy formation energy reported in Table 2.

samples with equal proportion of the stoichiometric steps I and II, *ab initio* calculations predict maximum Pt^{2+} coverage at the steps ($\leq$33% of the step-edge sites) and maximum conversion of the Pt deposit to Pt^{2+} ($\leq$33% of deposited Pt) that are well below the experimental values (50–80% of step-edge sites, up to 90% of deposited Pt, *cf.* Fig. 2a).

Most importantly, the calculations on the stoichiometric steps predict that Pt segregation, oxidation and the formation of the Pt^{2+} species are always accompanied by the reduction of surface Ce atoms from Ce^{4+} to Ce^{3+} (denoted in gray in Figs 3 and 4). The resulting concentration of the Ce^{3+} ions exceeds that of the Pt^{2+} ions by a factor of 2. This is in stark contrast with the resonant PES measurements on our samples showing that the concentration of Ce^{3+} is considerably lower than the concentration of Pt^{2+} after annealing the samples (Fig. 2b). This indicates that Pt is preferentially oxidized by other mechanisms than the Pt^0/Ce^{4+} redox couple.

Table 2 | Minimum energy to remove an O atom from the CeO_2(111) surface obtained from DFT calculations.

O vacancy site	Pt step coverage	O vacancy formation energy (eV)
Pt @ step II-S	1/3	3.8
Pt @ step I-S	1/3	3.3
CeO_2(111)		2.5
step II-S	0	2.0
Pt @ step I-O	1/3	1.9
Pt @ step II-O	1/3	1.9
step I-S	0	1.8
Pt @ step I-O	1	1.8
Pt @ step II-O	1	1.7

DFT, density functional theory.
Results for steps I and II, and for Pt at steps I and II in the presence and absence of excess O. The energies for Pt @ steps were calculated by removing the O atom marked by the * symbol in Figs 3 and 4.

Pt^{2+} at CeO_2(111) step edges with excess O. Agreement between the theory and the experiment can be achieved when taking into account the step edges in the presence of an excess of O atoms. Irrespective of the local step geometry and Pt coverage at the steps, we find that excess O atoms readily bind to Pt at the ceria steps and drive a rearrangement of the step morphology forming ionized Pt^{2+} species incorporated in the planar PtO_4 moieties on both steps I and II (Fig. 3f,g). In the presence of excess of oxygen, Pt atoms bind stronger to the ceria step edges, with calculated binding energies up to 6.7 eV, which are higher than at the stoichiometric steps edges by $\sim$1.6 eV, and which are also higher than the cohesive energy of bulk metallic Pt (Table 1). This condition, which determines the stability of the Pt^{2+} species at steps with respect to metallic Pt clusters, is fulfilled only in the presence of excess oxygen at the steps. The computed electronic structure and density of states of the PtO_4 moieties at the steps I-O and II-O (Supplementary Figs 5 and 6) confirm that the $Pt^0 \rightarrow Pt^{2+}$ oxidation results from the ionic Pt–O bond in the PtO_4 planar units, and that Ce^{3+} ions do not form in agreement with the experimental evidence (Fig. 2b). The calculated maximum coverage of Pt^{2+} at the steps I-O and II-O is 100% (Fig. 4e,g and Supplementary Table 2), as interconnected assemblies of the PtO_4 units can optimally fit the periodicities of both steps I and II at calculated Pt coverages at the step edges 1/3, 2/3 and 1 (Figs 3f,g and 4d–g). The presence of excess oxygen at steps therefore explains also the maximal Pt^{2+} ionization experimentally measured on the ceria-supported catalysts.

The stabilization of excess oxygen in the PtO_4 moieties by the Pt^{2+} ions suggests an oxygen source for redox reactions and hence provides a link between the presence of highly dispersed ionic Pt species on ceria and the increased redox reactivity of Pt^{2+}/CeO_2 single-atom catalysts[3]. The oxygen buffering capacity of ceria-based catalysts is associated with easy oxygen vacancy formation. We calculate the vacancy formation energy on the clean CeO_2(111) terrace, on the stoichiometric steps and on the Pt-decorated steps (Table 2). Compared with the energy of 2.5 eV calculated on the CeO_2(111) terrace, the energies required to remove an oxygen atom bound to Pt at the stoichiometric steps are 3.3 eV (from the PtO_4 unit at the step I-S) and 3.8 eV (from the PtO_4 unit at the step II-S; see Table 2). Pt segregation at the stoichiometric step edges yields the formation of strong Pt–O bonds and therefore hinders ceria O-buffering. Much lower energies are instead needed to remove the excess O incorporated in the PtO_4 units at steps I-O and II-O, where the O vacancy formation energy can be as low as 1.7 eV, lower or comparable to the values for the stoichiometric steps without Pt (2.0–1.8 eV;

Table 2)[30]. This indicates that the dispersed Pt^{2+} ions can enhance the oxygen storage capacity of ceria-based catalysts by assisting the reversible storage of excess O atoms.

The single-ion nature of Pt^{2+} in the PtO_4 units is preserved at all coverages, even when densely packed at the ceria step edges as interconnected PtO_4 units. Indeed, the Pt charge state, its local electronic structure and the O vacancy formation energy of the densely packed PtO_4 units are comparable to that of the isolated PtO_4 units at the steps (Supplementary Fig. 7 and Table 2). The PtO_4 units exhibit a large adaptability in stabilizing at different types of surface step edges, resulting in high effectiveness and capacity of the ceria surface to accommodate the Pt^{2+} ions. Regardless of the particular organization on the surface, the PtO_4 units are also always accessible to the reactants. Thus, the square-planar PtO_4 units carrying monodispersed Pt^{2+} ions can be considered elementary building blocks of single-atom Pt-ceria catalysts.

Discussion

On large-area samples, Pt^{2+} ions on ceria show exceptional reactivity with minimum Pt load in important applications: water–gas shift reaction[3], hydrogen oxidation on the anode of proton-exchange membrane fuel cell[11] and in the three-way catalyst converter[10]. In these applications, Pt^{2+} ions on ceria exhibit long-term stability under realistic reaction conditions of elevated temperatures and ambient pressure of reactant gases[3,31,32]. Pt^{2+} in large-area samples is routinely identified with PES. Complementary measurements with extended X-ray absorption fine structure (EXAFS)[33] and high-resolution transmission electron microscopy[3,4,31,32] confirm the absence of three-dimensional Pt or PtO_x clusters and, in agreement with the advanced PES measurements[34], identify Pt^{2+} as highly dispersed surface species on ceria[32].

Our present study identifies the stabilization of monodispersed Pt^{2+} ions with one particular defect site on the ceria surface—the monoatomic step edge—and excludes the stabilization of Pt^{2+} on the oxygen vacancies. Monodispersed Pt on ceria is observed to be effective in incorporating excess oxygen even in the unfavourable conditions of UHV experiment. Excess oxygen and Pt^{2+} arrange in the square-planar PtO_4 moieties decorating different types of the surface steps at coverages up to one PtO_4 per one step-edge Ce atom. The excess oxygen can be easily detached, indicating enhancement of the redox properties of ceria loaded with the Pt^{2+} ions. Adjusting the step density and the Pt load on the model $CeO_2(111)$ surface allows maximizing the coverage of Pt^{2+}, while suppressing the nucleation of metallic Pt^0 clusters. In the present experiment, we achieve surface coverage of Pt^{2+} 0.05 ML. A further increase of the completely monodispersed ionized Pt^{2+} coverage to 0.1 ML can be expected.

Step edges on ceria have been previously identified as preferred nucleation sites for supported metal clusters[20,21,27,28,35–37]. Our present study highlights the property of the step edges on ceria to provide specific structural and electronic environments for selective formation of monodispersed, thermally and chemically stable Pt^{2+} ions. The step edges represent intrinsic defects ubiquitously present on nanostructured ceria surfaces[4,38]; our results are thus applicable for the interpretation of the properties and the optimization of the Pt^{2+} load on large-area ceria supports[3,10,11]. More generally, the step edges may represent a common type of adsorption sites providing stabilization for monodispersed metal atoms and ions in any oxide-supported single-atom catalysts[15,39]. Our results therefore introduce important concepts of step reactivity[40] and step engineering[13,14] in understanding the stability, the activity and in designing new single-atom catalysts.

Methods

Experiment. The experiments were performed on surface science apparatuses in Surface Science Laboratory in Prague (STM, laboratory X-ray PES (XPS) with $h\nu = 1{,}487$ eV (Al Kα), low-energy electron diffraction) and at the Materials Science Beamline in Trieste (PES with $h\nu = 22$–$1{,}000$ eV (synchrotron), laboratory XPS with $h\nu = 1{,}487$ eV (Al Kα) and low-energy electron diffraction).

Preparation of the ceria substrates. The ceria layers and their Pt loading were prepared using the same procedures and parameters in both laboratories, and investigated by surface science methods *in situ* without exposing to air. The procedures and parameters of all samples are summarized in Supplementary Table 1. The ceria layers were prepared by deposition of Ce metal (Ce wire 99.9%, Goodfellow Cambridge Ltd) from Ta or Mo crucible heated by electron bombardment on clean Cu(111) substrate (MaTecK GmbH) in a background pressure of 5×10^{-5} Pa of O_2 (5.0, Linde AG). The growth rate of CeO_2 was 6 ML per hour. Varying densities of 1 ML high steps on the prepared CeO_2 layers were obtained by growth of CeO_2 at constant substrate temperature 423 or 523 K (Method I in Supplementary Table 1) or linearly increasing substrate temperature from room temperature to 723 K (Method II in Supplementary Table 1)[16]. For experiments in Fig. 1, the ordered, fully oxidized layer of CeO_2 (Fig. 1a,b) and the ordered reduced layer of $CeO_{1.7}$ (Fig. 1d,e) were obtained by approach published in ref. 17 that yields the lowest step density. In this approach, first, fully reduced Ce_2O_3 layer is prepared by depositing metallic Ce on a CeO_2 layer and annealing in vacuum. Subsequently, the Ce_2O_3 layer is exposed to a controlled dose of O_2 at 5×10^{-5} Pa and annealed to obtain desired stoichiometry $CeO_{1.7}$ or CeO_2 (Method III in Supplementary Table 1). The CeO_2 surface imaged in Fig. 1g,h was obtained by depositing 0.3 ML CeO_2 on the $CeO_2(111)$ substrate as in Fig. 1a, forming small ML-high islands. This homoepitaxy of CeO_2 on CeO_2 yields clearly arranged samples with high step density (Method IV in Supplementary Table 1).

Characterization of the ceria substrates. The thickness of the ceria layers was determined from the attenuation of the substrate Cu $2p_{3/2}$ XPS signal measured at $h\nu = 1{,}487$ eV. For calculations, we used inelastic mean free path of electrons in CeO_2 11.2 Å. The thickness of the ceria layers was set between 20 and 40 Å or 7 and 12 ML with 1 ML corresponding to 3.1 Å, the distance between Ce(111) atomic planes of CeO_2. In this range of thickness, the coverage of the Cu substrate by ceria ranges between 97 and 100 % (ref. 17). For determining the density of 1 ML high steps, we use a semi-automated procedure when the first step outlines are marked in STM images manually. Step outlines are then mapped onto a properly scaled and rotated hexagonal mesh of surface Ce atoms. The atoms that are closest to the outlines are automatically identified as step-edge atoms and their density evaluated in ML. The error in determining the density of 1 ML high steps is estimated to be ± 10 % and is marked in Fig. 2a.

Preparation of the Pt deposit. Pt was deposited on the ceria layers from a Pt wire (99.99%, MaTecK GmbH) heated by electron bombardment. Pt was deposited on the sample surface at 300 K and subsequently stabilized by increasing the sample temperature to 700 K at the rate $2\,K\,s^{-1}$. Both Pt deposition and annealing proceeded in the UHV background pressure 5×10^{-8} Pa or below. The thermal treatment supports the ionization of Pt to Pt^{2+}.

Characterization of the Pt deposit. The amount of Pt was calculated from the deposition time after calibrating the constant evaporation rate of the Pt evaporator. The evaporation rate was determined by a Quartz Crystal Microbalance and/or in a dedicated experiment from the thickness of 4-ML-thick Pt layers on $CeO_2(111)$/Cu(111) determined by attenuation of the substrate Cu $2p_{3/2}$ XPS signal measured at $h\nu = 1{,}487$ eV. This dedicated experiment was used to correlate Pt evaporation rates between the two experimental apparatuses. For calculations, we used inelastic mean free path of electrons in Pt 8 Å. The fraction of Pt^{2+} after thermal treatment was determined by fitting the ionic Pt^{2+} and neutral Pt^0 component in the PES Pt 4*f* spectrum measured at $h\nu = 180$ eV (*cf.* Fig. 1c,f,i). The error in determining the Pt and Pt^{2+} amounts on the studied samples is ± 20 % and is marked in Fig. 2a. This error represents the calibration error of the Pt evaporation rate.

Resonant PES. Reduction of the ceria surface after deposition of Pt and thermal treatment was determined with resonant PES of Ce 4*f* state. We determine the so-called resonant enhancement ratio (RER) as defined in refs 41,42 from measurements of intensities of Ce^{3+} and Ce^{4+} components of valence-band resonant PES Ce 4*f* spectra of CeO_2 measured off-resonance ($h\nu = 115$ eV) and on-resonance ($h\nu = 121.4$ eV for the Ce^{3+} component and $h\nu = 124.8$ eV for the Ce^{4+} component). The value of resonant enhancement ratio represents an upper estimate of the concentration of Ce^{3+} ions on the ceria surface and is plotted in Fig. 2b[17,42].

STM imaging. STM measurements were performed with commercial Pt–Ir tips (Unisoku). STM imaging of $CeO_2(111)$ and $Pt/CeO_2(111)$ films was available only

via unoccupied states. We used sample voltages 2.5–3.5 V and tunnelling currents 25–75 pA.

Theory. All calculations were based on the DFT and were performed using the spin-polarized GGA + U approach[43], employing the Perdew–Burke–Ernzerhof exchange-correlation functional[44] and ultrasoft pseudopotentials[45]. The spin-polarized Kohn–Sham equations were solved with a plane-wave basis set and the Fourier representation of the charge density was limited by kinetic cutoffs of 40 and 320 Ry, respectively. The Quantum-ESPRESSO computer package was used in all the calculations[46]. In the Hubbard U term, the occupations of the f-orbitals were defined in terms of atomic wave function projectors and the value of the parameter U was set to 4.5 eV, following our previous studies[47,48].

Slab models. The ceria (111) surfaces were modelled with periodic (3 × 3) slabs being three CeO_2 ML thick and separated by more than 10 Å of vacuum in the direction perpendicular to the surface. The Brillouin zone was sampled at Gamma point. In the present work, we considered two low-energy ML-high steps that we label following ref. 25 as step I and step II. The edge of both step I and step II steps are oriented along the $[1\bar{1}0]$ direction. These surface steps were modelled with vicinal surfaces described with monoclinic periodic slabs separated by > 10 Å of vacuum in the direction perpendicular to the (111) terrace. The dimensions of the cells were 17.97×11.67 Å^2 along the $[1\bar{1}2]$ and $[1\bar{1}0]$ directions (step I) and 15.72×11.67 Å^2 along the $[1\bar{1}2]$ and $[1\bar{1}0]$ (step II). All the vicinal surfaces slabs included three CeO_2 ML. This thickness was shown to be sufficient to calculate the structural and thermodynamic properties of these steps[25]. The complete set of surface structures and systems considered in this work is listed in the Supplementary Note 1. All these systems were structurally optimized according to the Hellmann–Feynman forces. During the geometry optimization, the atomic positions of the lowermost CeO_2 ML were constrained, as well as those of the Ce atoms in the central ML, except for the Ce atoms below the step edge.

Energetics. Binding energies were computed as $1/N_{Pt}$ ($E_{slab} + N_{Pt}\ E_{Pt} - E_{slab/Pt}$), where $E_{slab/Pt}$ is the total energy of the ceria slab containing N_{Pt} atoms of Pt, E_{slab} is the total energy of the corresponding relevant (stoichiometric, reduced or oxidized) Pt-free ceria slab and E_{Pt} is the total energy of a Pt atom in vacuum. The energies required to form an oxygen vacancy Ov were calculated as ($E_{slab/Ov} + ½\ E_{O2} - E_{slab}$), where $E_{slab/Ov}$ and E_{slab} are the total energies of the ceria supercell with and without the O vacancy, respectively, whereas E_{O2} is the total energy of a gas-phase O_2 molecule compensated for the known overbinding predicted by (semi)local functionals for O_2.

References

1. Yang, X. *et al.* Single-atom catalysts: a new frontier in heterogeneous catalysis. *Acc. Chem. Res.* **46,** 1740–1748 (2013).
2. Flytzani-Stephanopoulos, M. & Gates, B. C. Atomically dispersed supported metal catalysts. *Annu. Rev. Chem. Biomol. Eng.* **3,** 545–574 (2012).
3. Fu, Q., Saltsburg, H. & Flytzani-Stephanopoulos, M. Active nonmetallic Au and Pt species on ceria-based water-gas shift catalysts. *Science* **301,** 935–938 (2003).
4. Bruix, A. *et al.* Maximum noble-metal efficiency in catalytic materials: atomically dispersed surface platinum. *Angew. Chem. Int. Ed.* **53,** 10525–10530 (2014).
5. Qiao, B. *et al.* Single-atom catalysis of CO oxidation using Pt_1/FeO_x. *Nat. Chem.* **3,** 634–641 (2011).
6. Novotný, Z. *et al.* Ordered array of single adatoms with remarkable thermal stability: $Au/Fe_3O_4(001)$. *Phys. Rev. Lett.* **108,** 216103 (2012).
7. Parkinson, G. S. *et al.* Carbon monoxide-induced adatom sintering in a $Pd\text{-}Fe_3O_4$ model catalyst. *Nat. Mater.* **12,** 724–728 (2013).
8. Bliem, R. *et al.* Subsurface cation vacancy stabilization of the magnetite (001) surface. *Science* **346,** 1215–1218 (2014).
9. Li, F., Li, Y., Zeng, X. C. & Chen, Z. Exploration of high-performance single-atom catalysts on support M_1/FeO_x for CO oxidation via computational study. *ACS Catal.* **5,** 544–552 (2015).
10. Hatanaka, M. *et al.* Ideal Pt loading for a Pt/CeO_2-based catalyst stabilized by a Pt–O–Ce bond. *Appl. Catal. B Environ.* **99,** 336–342 (2010).
11. Fiala, R. *et al.* Proton exchange membrane fuel cell made of magnetron sputtered Pt–CeO_x and Pt–Co thin film catalysts. *J. Power Sources* **273,** 105–109 (2015).
12. Gong, X.-Q., Selloni, A., Batzill, M. & Diebold, U. Steps on anatase $TiO_2(101)$. *Nat. Mater.* **5,** 665–670 (2006).
13. Barth, J. V, Costantini, G. & Kern, K. Engineering atomic and molecular nanostructures at surfaces. *Nature* **437,** 671–679 (2005).
14. Vang, R. T. *et al.* Controlling the catalytic bond-breaking selectivity of Ni surfaces by step blocking. *Nat. Mater.* **4,** 160–162 (2005).
15. Gong, X., Selloni, A., Dulub, O., Jacobson, P. & Diebold, U. Small Au and Pt clusters at the anatase $TiO_2(101)$ surface: behavior at terraces, steps, and surface oxygen vacancies. *J. Am. Chem. Soc.* **130,** 370–381 (2008).
16. Dvořák, F. *et al.* Adjusting morphology and surface reduction of $CeO_2(111)$ thin films on Cu(111). *J. Phys. Chem. C* **115,** 7496–7503 (2011).
17. Duchoň, T. *et al.* Ordered phases of reduced ceria as epitaxial films on Cu(111). *J. Phys. Chem. C* **118,** 357–365 (2014).
18. Zhou, Y., Perket, J. M. & Zhou, J. Growth of Pt nanoparticles on reducible CeO_2 (111) thin films: effect of nanostructures and redox properties of ceria. *J. Phys. Chem. C* **114,** 11853–11860 (2010).
19. Shao, X., Jerratsch, J.-F., Nilius, N. & Freund, H.-J. Probing the 4f states of ceria by tunneling spectroscopy. *Phys. Chem. Chem. Phys.* **13,** 12646–12651 (2011).
20. Lu, J.-L., Gao, H.-J., Shaikhutdinov, S. & Freund, H.-J. Morphology and defect structure of the $CeO_2(111)$ films grown on Ru(0001) as studied by scanning tunneling microscopy. *Surf. Sci.* **600,** 5004–5010 (2006).
21. Zhou, Y. & Zhou, J. Interactions of Ni nanoparticles with reducible $CeO_2(111)$ thin films. *J. Phys. Chem. C* **116,** 9544–9549 (2012).
22. Mullins, D. R. *et al.* Water dissociation on $CeO_2(100)$ and $CeO_2(111)$ thin films. *J. Phys. Chem. C* **116,** 19419–19428 (2012).
23. Bruix, A. *et al.* A new type of strong metal-support interaction and the production of H_2 through the transformation of water on $Pt/CeO_2(111)$ and $Pt/CeO_x/TiO_2(110)$ catalysts. *J. Am. Chem. Soc.* **134,** 8968–8974 (2012).
24. Negreiros, F. R. & Fabris, S. Role of cluster morphology in the dynamics and reactivity of subnanometer Pt clusters supported on ceria surfaces. *J. Phys. Chem. C* **118,** 21014–21020 (2014).
25. Kozlov, S. M., Viñes, F., Nilius, N., Shaikhutdinov, S. & Neyman, K. M. Absolute surface step energies: accurate theoretical methods applied to ceria nanoislands. *J. Phys. Chem. Lett.* **3,** 1956–1961 (2012).
26. Torbrügge, S., Cranney, M. & Reichling, M. Morphology of step structures on $CeO_2(111)$. *Appl. Phys. Lett.* **93,** 073112 (2008).
27. James, T. E., Hemmingson, S. L. & Campbell, C. T. Energy of supported metal catalysts: from single atoms to large metal nanoparticles. *ACS Catal.* **5,** 5673–5678 (2015).
28. James, T. E., Hemmingson, S. L., Ito, T. & Campbell, C. T. Energetics of Cu adsorption and adhesion onto reduced $CeO_2(111)$ surfaces by calorimetry. *J. Phys. Chem. C* **119,** 17209–17217 (2015).
29. Colussi, S. *et al.* Nanofaceted Pd-O sites in Pd-Ce surface superstructures: Enhanced activity in catalytic combustion of methane. *Angew. Chem. Int. Ed.* **48,** 8481–8484 (2009).
30. Kozlov, S. M. & Neyman, K. M. O vacancies on steps on the $CeO_2(111)$ surface. *Phys. Chem. Chem. Phys.* **16,** 7823–7829 (2014).
31. Fiala, R. *et al.* Pt–CeO_x thin film catalysts for PEMFC. *Catal. Today* **240,** 236–241 (2015).
32. Hatanaka, M. *et al.* Reversible changes in the Pt oxidation state and nanostructure on a ceria-based supported Pt. *J. Catal.* **266,** 182–190 (2009).
33. Nagai, Y. *et al.* Sintering inhibition mechanism of platinum supported on ceria-based oxide and Pt-oxide-support interaction. *J. Catal.* **242,** 103–109 (2006).
34. Matolín, V. *et al.* Platinum-doped CeO_2 thin film catalysts prepared by magnetron sputtering. *Langmuir* **26,** 12824–12831 (2010).
35. Zhou, J., Baddorf, A. P., Mullins, D. R. & Overbury, S. H. Growth and characterization of Rh and Pd nanoparticles on oxidized and reduced $CeO_x(111)$ thin films by scanning tunneling microscopy. *J. Phys. Chem. C* **112,** 9336–9345 (2008).
36. Zhou, Y., Perket, J. M. & Zhou, J. Growth of Pt nanoparticles on reducible $CeO_2(111)$ thin films: effect of nanostructures and redox properties of ceria. *J. Phys. Chem. C* **114,** 11853–11860 (2010).
37. Zhou, Y. & Zhou, J. Growth and sintering of Au – Pt nanoparticles on oxidized and reduced $CeO_x(111)$ thin films by scanning tunneling microscopy. *J. Phys. Chem. Lett.* **1,** 609–615 (2010).
38. Sayle, T. X. T., Parker, S. C. & Sayle, D. C. Oxidising CO to CO_2 using ceria nanoparticles. *Phys. Chem. Chem. Phys.* **7,** 2936–2941 (2005).
39. Castellani, N. J., Branda, M. M., Neyman, K. M. & Illas, F. Density functional theory study of the adsorption of Au atom on cerium oxide: effect of low-coordinated surface sites. *J. Phys. Chem. C* **113,** 4948–4954 (2009).
40. Zambelli, T., Wintterlin, J., Trost, J. & Ertl, G. Identification of the 'active sites' of a surface-catalyzed reaction. *Science* **273,** 1688–1690 (1996).
41. Matolín, V. *et al.* Water interaction with $CeO_2(111)/Cu(111)$ model catalyst surface. *Catal. Today* **181,** 124–132 (2012).
42. Mullins, D. R. The surface chemistry of cerium oxide. *Surf. Sci. Rep.* **70,** 42–85 (2015).
43. Cococcioni, M. & de Gironcoli, S. Linear response approach to the calculation of the effective interaction parameters in the LDA + U method. *Phys. Rev. B* **71,** 035105 (2005).
44. Perdew, J. P. J., Burke, K. & Ernzerhof, M. Generalized gradient approximation made simple. *Phys. Rev. Lett.* **77,** 3865–3868 (1996).
45. Vanderbilt, D. Soft self-consistent pseudopotentials in a generalized eigenvalue formalism. *Phys. Rev. B* **41,** 7892–7895 (1990).
46. Giannozzi, P. *et al.* QUANTUM ESPRESSO: a modular and open-source software project for quantum simulations of materials. *J. Phys. Condens. Matter* **21,** 395502 (2009).

47. Fabris, S., de Gironcoli, S., Baroni, S., Vicario, G. & Balducci, G. Taming multiple valency with density functionals: a case study of defective ceria. *Phys. Rev. B* **71,** 041102 (2005).
48. Fabris, S., Vicario, G., Balducci, G., De Gironcoli, S. & Baroni, S. Electronic and atomistic structures of clean and reduced ceria surfaces. *J. Phys. Chem. B* **109,** 22860–22867 (2005).

Acknowledgements

This work was supported by Czech Science Foundation (contract numbers 15-06759S and 13-10396S), and by the European Union via the FP7-NMP-2012 project chipCAT under contract number 310191 and the EU FP7 COST action CM1104. A.T. acknowledges the support of the Grant Agency of the Charles University, contract number 2048514. S.F. acknowledges the support provided by the Humboldt Foundation through a Friedrich Wilhelm Bessel Research Award. The high-performance computing resources were gratefully provided by ISCRA initiative of CINECA. CERIC-ERIC consortium is acknowledged for financial support.

Author contributions

F.D., A.T., M.V., T.S., I.M., J.M. and V.M. designed and performed the experiments. M.F.C., N.-D.T., F.R.N. and S.F. performed the DFT calculations. All authors interpreted the experimental and computational results. J.M., S.F., T.S., I.M. and V.M. wrote the manuscript. F.D., A.T., J.M., I.M., V.M. and S.F. provided funding.

Additional information

Supplementary Information accompanies this paper at http://www.nature.com/naturecommunications

Competing financial interests: The authors declare no competing financial interests.

Reprints and permission information is available online at http://npg.nature.com/reprintsandpermissions/

How to cite this article: Dvořák, F. *et al.* Creating single-atom Pt-ceria catalysts by surface step decoration. *Nat. Commun.* 7:10801 doi: 10.1038/ncomms10801 (2016).

3.3 Controlling Pt dispersion on ceria by surface oxygen content

In previous chapter, the conditions for stabilization of Pt^{2+} ions were analyzed. It was shown, that Pt stabilizes in Pt^{2+} state at step edges of stoichiometric CeO_2, and in the excess oxygen at step edges. In this chapter, detailed analysis of the influence of the surface oxygen content of ceria film on the stabilization of Pt^{2+} ions is presented.

Thin films of ceria were prepared on Cu(111) single crystal using the procedure described in [103], [131]. The resulting step density of the films was estimated to be 15%. Films were prepared stoichiometric CeO_2 and slightly reduced CeO_x. Control over stoichiometry of the ceria film was achieved via heating the sample in methanol background atmosphere at 650K and, depending on the annealing time, different degrees of reduction of the film were obtained. Different quantities of Pt were added onto the surface and the whole system was heated at 700K for the stabilization of Pt deposit. Morphology of the film was measured using STM and stoichiometry of the film as well as quantitative analysis of Pt deposit was estimated using SRPES and RPES. The obtained experimental results were compared with the DFT calculations.

The results indicated that in oxygen rich conditions the concentration of Pt^{2+} ions increases with the increasing Pt load of the film. The appearance of three-dimensional metallic Pt clusters is observed on the STM for Pt amounts of 10-15% ML. Further increasing of the Pt deposit resulted in increasing both Pt^0 and Pt^{2+} signals in SRPES. Pt^{2+} signal reached a saturation of approximately 20% ML at 50% ML Pt deposition. Without exposing the system to oxygen, the appearance of Pt^0 clusters in the course of Pt exposition resulted in partial reduction of CeO_2 surface and destabilization of Pt^{2+} ions. The present experiments, mainly the observation of saturation coverage of 20% ML Pt^{2+} on a substrate with 15%ML monoatomic steps, and the stability of the Pt^{2+} deposit, show that the capacity of step edges to accommodate Pt^{2+} is maximized in oxygen rich conditions and a minimum of 1 Pt^{2+} ion is stabilized per 1 step edge adsorption position.

Initial reduction of the ceria surface rapidly decreased the concentration of Pt^{2+} species leading to their disappearance at a particular critical degree of reduction of the CeO_x surface. According to previous observations, monoatomic step edges of ceria play a key role in stabilizing Pt^{2+} ions [131]. At the same time, they also represent sites, where lattice oxygen is most weakly bound [99], [164]. Considering the preferential O removal at the step edges, and the step edge concentration of 15% on our samples, the critical degree of reduction may correspond to the removal of lattice O atoms at step edges. Without lattice O, the step edges lose the ability to stabilize

Pt^{2+}. Hence, we suppose that the critical reduction degree for ceria surface preventing Pt^{2+} stabilization may correspond to the complete reduction of step edges.

Experimental measurements of fully oxidized Pt-Ceria systems in oxygen rich conditions revealed enhanced content of Pt^{2+} species. At initial step coverage of 15% ML concentration of Pt^{2+} ions reached 20%. Theoretical modeling provided possible explanation of such phenomenon which is based on the influence of excess oxygen atoms on the formation of PtO_4 moieties at ceria step edges.

Theoretical calculations supported the phenomena observed in the experiment. Assuming the presence of excess oxygen at step edges during Pt^{2+} stabilization, the capacity of a step was estimated to be up to 5 Pt^{2+} ions per 3 step edge adsorption positions.

The prepared Pt/ceria system is highly promising for experiments concerning redispersion of Pt species, i.e. decomposition of metallic Pt clusters in favor of monodispersed Pt^{2+} ions. In the changing conditions of the surface chemical reactions, our results indicate that the Pt/ceria catalyst can react very flexibly making available a rich variety of configurations that provide the stabilization of monodispersed Pt^{2+}. Analyses of the binding energy of Pt^{2+} in the PtO_4 moieties indicate important consequences for exploiting and engineering the dispersion of Pt in Pt/ceria catalysts: on reduced and stoichiometric ceria, monodispersed Pt^{2+} ions and Pt adatoms at step edges can coexist with the metallic Pt clusters. In the presence of excess oxygen, binding energy of Pt^{2+} at ceria step edges exceeds the cohesive energy of Pt bulk triggering the technologically important process of redispersion.

My contribution to this work was preparation and measurement of the Pt-ceria model systems using STM and XPS. I have developed one-step experimental procedures for preparing CeO_2 samples with step density 15% allowing faster and better defined experiments (Figure 3.3.1). The emergence of Pt^0 clusters was detected in STM using measuring modes in occupied and empty states. Qualitative analysis of the Pt deposit was made using XPS, where the existence of Pt deposit at the surface and its preferential state could be deduced. In parallel, more precise quantitative SRPES measurements were performed at synchrotron Elettra in Trieste, Italy.

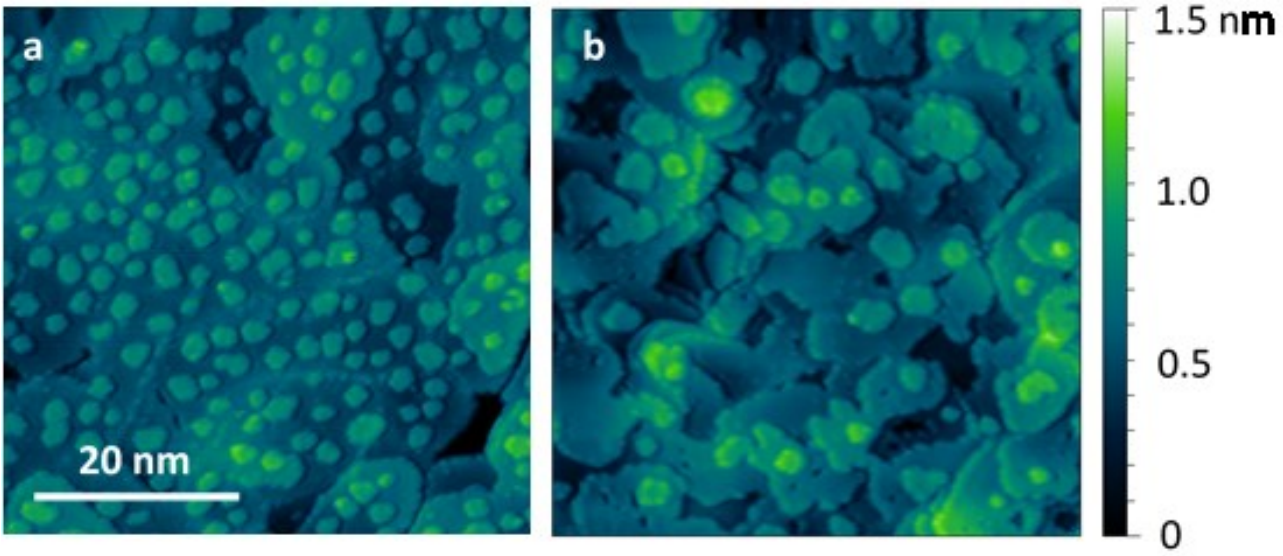

Figure 3.3.1: CeO_2(111) substrates with 15 % of monoatomic steps used in the present study. (a) Multi-step procedure described in Section 2.6, Figure 2.6.1 d. Substrate is obtained by deposition of 0.3 ML CeO_2 at RT on a Cu(111) supported CeO_2(111) thin film with the lowest achievable density of substrate steps (approx. 4%), followed by annealing to 800 K. CeO_2(111) thin film with the lowest step density is obtained by oxidation of a 20 Angstrom Ce_2O_3 thin film prepared according to Refs. [106], [108]. (b) One-step procedure. Substrate is obtained by deposition of 20 Angstrom of CeO_2(111) on Cu(111) at 250^{o}C and subsequent annealing to 800 K. Substrates from (a), (b) are eventually reduced by repeated annealing in vacuum to 700 K and/or by adsorption of methanol and desorption at 700 K, both approaches conserving the density of surface monoatomic steps 15%.

Controlling Pt dispersion on ceria by surface oxygen content

Andrii Tovt[1], Luigi Bagolini[2], Filip Dvořák[2,a], Nguyen-Dung Tran[2,3], Mykhailo Vorokhta[1], Klára Ševčíková[1], Viktor Johánek[1], Matteo Farnesi Camellone[2], Tomáš Skála[1], Iva Matolínová[1], Josef Mysliveček[1,*], Stefano Fabris[2,*], Vladimír Matolín[1]

[1] Charles University, Faculty of Mathematics and Physics, V Holešovičkách 2, 180 00 Praha 8, Czech Republic

[2] CNR-IOM DEMOCRITOS, Istituto Officina dei Materiali, Consiglio Nazionale delle Ricerche, Via Bonomea 265, Trieste 34136, Italy.

[3] SISSA, Scuola Internazionale Superiore di Studi Avanzati, Via Bonomea 265, Trieste 34136, Italy

[a] Present Address: University of Pardubice, Faculty of Chemical Technology, Nám. Čs. Legií 565, 53002 Pardubice, Czech Republic

* josef.myslivecek@mff.cuni.cz, fabris@iom.cnr.it

Abstract:

Experimental strategies for obtaining the highest dispersions of oxide supported metals, including single-atom dispersion, allow development of advanced, resource- and cost-effective catalysts. We investigate the role of oxygen atoms on the $CeO_2(111)$ surface in the stabilization of Pt as monodispersed Pt^{2+} ions or, concurrently, as metallic Pt clusters. We demonstrate that the necessary condition for the formation of Pt^{2+} ions is the availability of lattice O or excess O atoms at surface step edges. Although Pt^{2+} ions can exist on partially reduced surfaces, excess O atoms are required to maximize the capacity of the surface to accommodate Pt^{2+} and for triggering the redispersion of Pt clusters. Over a wide range of O concentrations, Pt^{2+} ions are located at ceria step edges as various configurations of fourfold oxygen-coordinated PtO_4 units. Our study provides the rationale for the oxidation and reduction strategies for controlling and optimizing the dispersion of Pt in ceria-based catalysts.

Introduction:

Oxide supported metal catalysts belong to the most widely used heterogeneous catalysts. Increasing the metal dispersion in the oxide supported metal catalysts has proven to positively influence the activity [1] and the stability of the metal load [2] as well as the selectivity of the catalyzed reactions [3] giving rise to the concept of catalysis by single supported atoms (single-atom catalysis) [4–6]. In single-atom catalysts, minimal amounts of atomically dispersed precious metals are expected to yield an ultimate effectiveness and selectivity in many relevant chemical reactions [7]. In parallel to the identification and characterization of new oxide supported single-atom catalysts [8–11] model single atom catalysts are being investigated where single metal atoms and ions are supported on single crystalline oxide surfaces [12–14]. Highly defined morphology and the broad spectrum of applicable analytical methods on model catalysts effectively contribute to elucidating the stability [15], the reaction mechanisms [16], and the nature of the active sites [13] in single-atom catalysts.

The nature of the active sites in single-atom catalysis is often concealed by their highly dynamic character [17,18], and for many relevant catalysts arguments are found both for the activity of single supported atoms and ions [9,19–22] and for small metallic clusters [23–26]. A close relationship between the single-atom dispersion and the activity of small metallic clusters is being utilized in advanced procedures for precise control of the dispersion of metal load in heterogeneous catalysts, especially Pt. Single-atom dispersion of Pt, usually obtained by annealing of the catalysts in oxygen-rich atmospheres [27,28], represents a technological step for obtaining smallest metallic Pt clusters upon subsequent controlled reduction, and becomes an indispensable ingredient in the recipes for preparing highly active [29] and highly stable catalysts [30] by means of Pt redispersion [31–33].

Using a model single-atom catalyst $Pt/CeO_2(111)$ we demonstrate that it is the surface oxygen content of the catalyst support determining whether the Pt deposit be stabilized as monodispersed Pt^{2+} ions or as metallic Pt clusters. Pt/ceria catalysts represent an important class of single-atom catalysts [11] exhibit high

effectiveness of Pt usage in industrially relevant applications [34–36], and provide efficient redispersion of Pt load [27,29,30,37]. On model $CeO_2(111)$ surfaces, atomically dispersed Pt^{2+} ions reside in stable adsorption positions at monoatomic step edges [14]. The stability of the atomically dispersed Pt^{2+} state has been demonstrated to depend sensitively on the oxidation state of the ceria support [38,39]. In the present experimental and ab-initio study on stoichiometric and reduced $CeO_2(111)$ surfaces we demonstrate that Pt^{2+} formation becomes inhibited when the ceria step edges lose the lattice oxygen atoms [40]. The oxygen atmosphere over $CeO_2(111)$ surfaces, on the other hand, allows bonding of excess oxygen at the step edges and formation of dense arrangements of PtO_4 moieties maximizing the capacity of the surface to accommodate single Pt^{2+} ions. The excess oxygen on the $CeO_2(111)$ surfaces is triggering the redispersion of Pt by energetically favoring the binding of Pt in the PtO_4 moieties over incorporation of Pt in metallic Pt clusters.

Experimental Results:

Model single-atom Pt/ceria catalysts are prepared by deposition of Pt on a stepped oxidized $CeO_2(111)$ surface followed by annealing in vacuum at 700 K for activating the conversion of deposited metallic Pt to monodispersed Pt^{2+} ions [14]. The present experiments are performed on $CeO_2(111)$ surfaces with density of monoatomic steps 0.15 ML (Figure S1; ML represents a monolayer, 1 ML = 7.9×10^{14} cm^{-2} and corresponds to density of Ce atoms on the $CeO_2(111)$ surface). To determine the influence of surface oxygen content on the stabilization of Pt^{2+} ions we observe the evolution of the Pt deposit on the samples during repeated evaporation and annealing of Pt under oxidizing or reducing conditions. As a primary indicator of the single-atom dispersion of Pt deposited on ceria we consider the presence of Pt^{2+} signal in the Pt 4f synchrotron radiation photoelectron spectra (SRPES) of the samples (Figure S2a) [14,21,31]. Determined are also the complementary Pt^0 signal in the Pt4f SRPES (Figure S2a) and the highly surface sensitive resonant enhancement ratio (RER) from resonant photoelectron spectroscopy (RPES) of the CeO_x valence band (VB) as a measure of surface concentration of Ce^{3+} ions (Figure S2b).

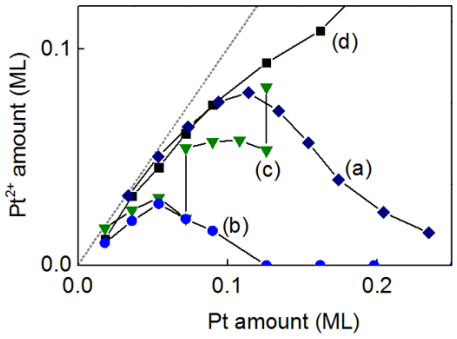

Figure 1: Evolution of Pt^{2+} SRPES signal on ceria samples upon stepwise deposition of Pt and annealing at 700 K after each deposition. (a) stoichiometric CeO_2 sample, Pt deposition and annealing in vacuum (b) reduced CeO_x sample, Pt deposition and annealing in vacuum (c) reduced CeO_x sample, Pt deposition and annealing in vacuum, two intermittent oxidations in O_2 (d) stoichiometric CeO_2 sample, deposition of Pt in vacuum, annealing in 5×10^{-5} Pa O_2. Lines represent guides to the eyes. Dotted line indicates the expected Pt^{2+} signal for complete conversion of Pt deposit to Pt^{2+}.

Characteristic scenarios of the evolution of the Pt^{2+} concentration in the Pt deposit are displayed in Figure 1, the complementary Pt^0 and RER signals are in Figure S3. For stoichiometric $CeO_2(111)$ sample (Figure 1a, Figure S3d), Pt^{2+} amount – monodispersed ions – is equal to the deposited Pt amount up to 0.05 ML (Figure 1), followed, upon further deposition of Pt, by an increase of the concurrent Pt^0 signal – metallic Pt clusters (Figure S3d). The appearance of Pt clusters is followed with a reduction of the CeO_2 substrate (increase in RER, Figure S3d) and, within next few Pt depositions, Pt^{2+} concentration drops indicating depletion of the population of monodispersed Pt^{2+} ions. The observed scenario corresponds well with recent experimental observations of destabilization of Pt^{2+} population on ceria in reducing environments of H_2 [38] and CH_3OH [39], and the catalytic action of metallic Pt clusters on the destabilization [38,39]. In the present

experiment, the reduction of the samples occurs during annealing to 700 K via clean-off of ceria surface from residual carbon (Figure S4). The residual carbon is deposited on the sample e.g. during Pt deposition.

In Figures 1b and S3b we demonstrate that Pt^{2+} can exist on a slightly reduced $CeO_x(111)$ surface. Prior to Pt deposition, RER of the sample was 0.28. Upon initial Pt deposition, Pt^{2+} signal as well as Pt^0 signal is observed indicating the coexistence of monodispersed Pt^{2+} ions and Pt clusters. The maximum of Pt^{2+} concentration is reached for Pt amount 0.05 ML. For higher Pt amounts, stabilization of Pt in the form of Pt^0 clusters is dominating and reduction of the substrate together with the destabilization of the Pt^{2+} population is observed in qualitative agreement with the stoichiometric $CeO_2(111)$ sample in Figure 1a and S3d. We can determine the critical stoichiometry of the $CeO_x(111)$ surface that does not allow any Pt^{2+} stabilization. We prepare a series of $CeO_x(111)$ surfaces with RER between 0.36 (Figure S3a) and 0.02 (Figure S3d) and perform Pt deposition and stabilization on these surfaces. We may conclude that for RER >= 0.3 no Pt^{2+} stabilization is observed and the Pt deposit nucleates as Pt^0 clusters. RER of the as prepared $CeO_x(111)$ samples can be used for quantitative considerations because prior to Pt deposition Ce^{3+} concentration on the $CeO_x(111)$ surface is determined solely by the amount of O vacancies [41]. Upon Pt deposition, Ce^{3+} concentration is additionally influenced by charge transfer between Pt^{2+} ions or Pt^0 clusters and the ceria substrate [14,42].

The destabilized population of Pt^{2+} on the slightly reduced $CeO_x(111)$ surface can be recovered upon annealing the sample at 700 K in oxygen. This is shown in Figure 1c and S3e. Intermittent annealing at 700 K in 5×10^{-5} Pa O_2 after reaching Pt coverages of 0.07 ML and 0.12 ML has recovered the Pt^{2+} concentration to the level comparable with Pt^{2+} concentration on the stoichiometric $CeO_2(111)$ sample (Figure 1a). This process was accompanied by a corresponding decrease of the Pt^0 SRPES signal indicating the redispersion of the Pt^0 clusters, i.e. decomposition of metallic Pt clusters in favor of monodispersed Pt^{2+} ions.

Pt^{2+} concentration and stability on the $CeO_2(111)$ surface can be maximized by depositing Pt on the stoichiometric $CeO_2(111)$ in vacuum and performing the Pt^{2+} stabilization via annealing at 700 K in 5×10^{-5} Pa O_2. Results of this experiment are presented in Figures 1d and S3f, and, for the extended range of the Pt coverages up to 0.7 ML, in Figure 2. Under oxygen rich conditions, initially, all deposited Pt is stabilized as Pt^{2+} ions. From about 0.05 ML Pt deposition above, the signal of metallic Pt^0 is detected and it is increasing during further Pt deposition. Pt^{2+} signal, on the other hand, is reaching a saturation of approximately 0.2 ML at 0.5 ML Pt deposition. The appearance of the Pt^0 signal is related to the nucleation of metallic Pt clusters [14,38,39] that are evidenced on the STM images in Figure 2 for Pt coverage of 0.1-0.15 ML and higher. Pt^{2+} species, on the other hand, were not associated with any observable STM features (Figure S5, [14]). The evolution of Pt^{2+} and Pt^0 signals in oxygen rich conditions clearly illustrates the competition between the trapping of Pt as Pt^{2+} atoms in energetically preferred, but limited in quantity, stable adsorption positions, and the nucleation of Pt clusters [43,44]. The preferential adsorption positions have been identified previously as monoatomic step edges providing binding sites for Pt^{2+} ions in square-planar PtO_4 moieties [14].

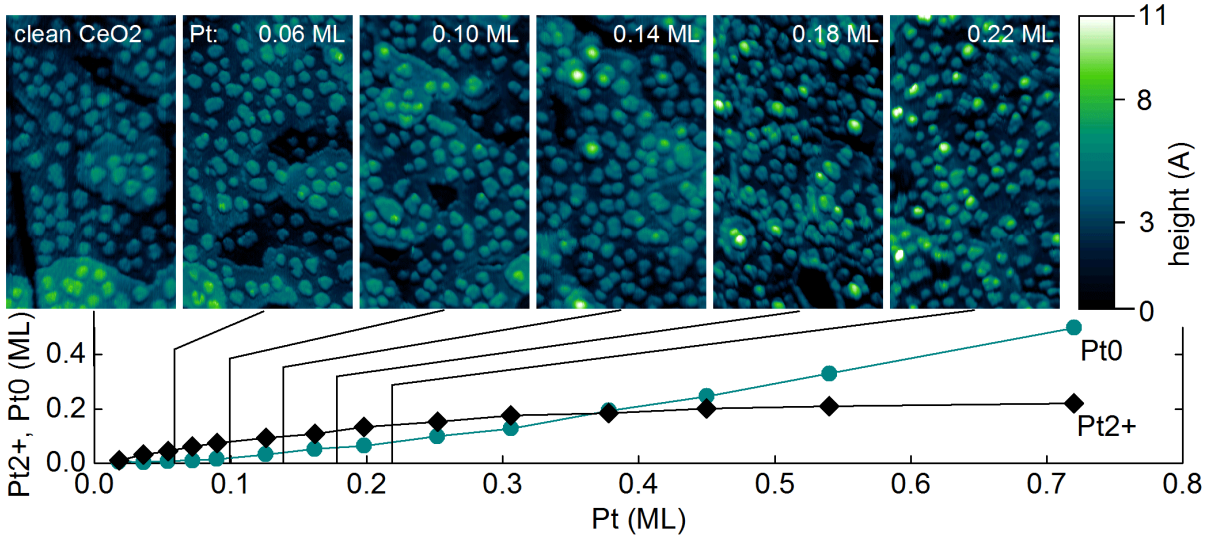

Figure 2: Evolution of Pt^{2+} and Pt^{0} XPS signals during deposition of Pt on CeO_2(111) and annealing of Pt in O_2. In the presence of oxygen, the capacity of CeO_2(111) to accommodate Pt^{2+} is maximized and Pt^{2+} population saturates at a concentration approximately 0.2 ML. Pt not stabilized in the form of Pt^{2+} ions nucleates as metallic Pt clusters that are distinguished on the STM images at Pt coverage of 0.1-0.15 ML and higher. Width of the STM images is 40 nm.

Calculations:

Ab-initio DFT simulations aim at validating the role of oxygen content on the CeO_2(111) and CeO_{2-x}(111) surfaces on the stabilization of monodispersed Pt^{2+} species. The model systems employed in the present theoretical analysis are vicinal surface slabs exposing (111) terraces and two different monoatomic step geometries, which we label as Step I and Step II following Refs. [14,40,45]. In both cases, the lateral size of the periodic supercell is 3 lattice units along the step edge. We introduce Pt atoms, excess O atoms, and O vacancies at step edges and investigate the charge state of Pt and Ce atoms. The amounts of Pt, O, Pt^{2+}, Pt^{0}, and Ce^{3+} are expressed as step coverages σ_Y where Y is one of the Pt, O, Pt^{2+}, Pt^{0}, and Ce^{3+} species, and σ_Y is the concentration of this species relative to step edge Ce atoms.

To study the effects of oxygen content, we consider stoichiometric step edges (denoted S), over-stoichimetric edges containing excess O atoms with σ_O=1/3-6/3 (denoted as $O_{+1/3}$-$O_{+6/3}$), and sub-stoichiometric edges obtained by removing a lattice oxygen atom from the step edge (denoted as $O_{-1/3}$, Supplementary Figures S6, S7). In the over-stoichiometric steps, the excess O adatoms bind preferentially to the step edges forming peroxide groups (supplementary Information and Figure S6, S7), similarly to the adsorption on flat ceria terraces [46,47]. In the sub-stoichiometric steps, step edges are the preferential sites to form O vacancies [40]. N Pt atoms (N=1-6, σ_{Pt}=1/3-6/3) were introduced at the step edges as isolated species, linear chains, and clusters, considering several morphologies and distributions of reduced Ce^{3+} ions (Supplementary Discussion, Tables S1-S8). Given the large number of calculations required to create a complete set of results covering all the cases reported above, we perform a full analysis for Step I and validate the findings on Step II only for a selected subset of cases.

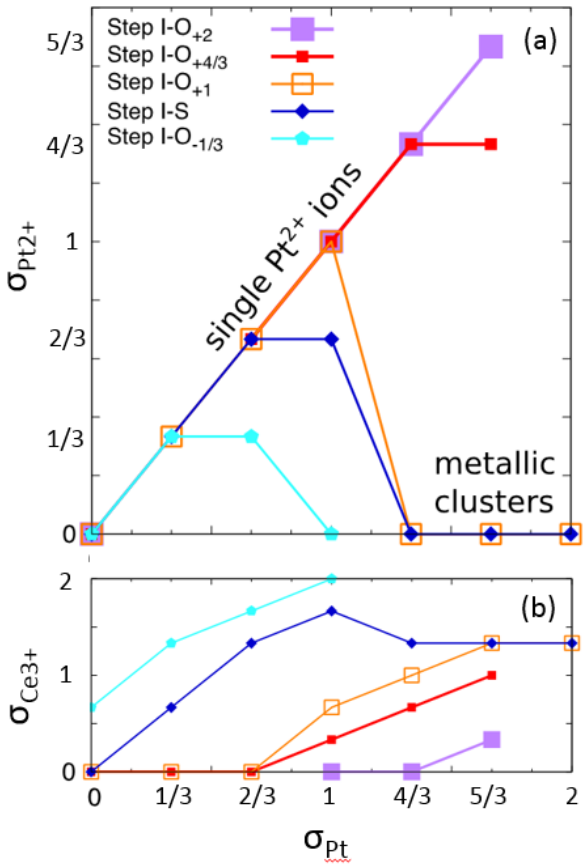

Figure 3: Number of Pt^{2+} (a) and of Ce^{3+} ions (b) that form on the step edge from the adsorption of neutral Pt atoms. The numbers of deposited Pt, and of resulting Pt2+ and Ce3+ ions are expressed in step coverages σ_{Pt}, σ_{Pt2+}, and σ_{Ce3+}, respectively. Step coverage 1 is defined as 1 species per step Ce atom. The results refer to the model Step I and different symbols/colors refer to the surface oxygen content of the step.

The results displayed in Figure 3 demonstrate the role of step-edge oxygen content for the stabilization of Pt^{2+} species on $CeO_2(111)$ and $CeO_{2-x}(111)$ surface steps. Following the layout of the experimental data presented in Figures 1 and S3, Figure 3a reports the number of Pt^{2+} species resulting from depositing a particular amount of Pt atoms on a step edge with a specific oxygen content. The numbers of metallic and ionic Pt atoms in the supercell are reported in terms of the step coverages σ_{Pt} and σ_{Pt2+}, respectively. The ionic or metallic state of the Pt atoms were determined on the basis of the Bader charge analysis as described in the Supplementary Information and reported in Tables S1-S9. Figure 3b reports the number of Ce^{3+} ions resulting from depositing a given amount of Pt atoms on the step edge. The Ce^{3+} ionic state of the Ce ions was obtained from the projection coefficients of the charge density on the atomic-like Ce 4f wavefunctions and the number of Ce^{3+} ions for each supercell is reported in Tables S1-S8. Calculated Pt binding energies (BE) of the Pt atoms, ions, and clusters for the considered step edges and Pt amounts are displayed in Figure 4 together with the adsorption geometries, which are also reported in the Supplementary Tables S1-S9. Color coding in Figure 4 is the same as in the Figure 3.

For σ_{Pt}<=2/3, every Pt atom deposited on the stoichiometric Step I (Step I-S, blue symbols) is converted to a Pt^{2+} species by transferring 2 electrons to the ceria surface and reducing 2 Ce^{4+} ions to Ce^{3+} (Figure 3a). This is evident in the linear increase of the number of Ce^{3+} ions up to σ_{Pt} =2/3 (Figure 3b, blue symbols). Additional Pt atoms deposited on the Step I-S are not completely oxidized to Pt^{2+}. This is demonstrated by the change of slope of the σ_{Ce3+} curve for σ_{Pt} between 2/3 and 1, leading to 3 Pt atoms in the supercell accompanied with only 5 reduced Ce^{3+} ions instead of 6. σ_{Pt} > 1 yield the nucleation of metallic Pt clusters (Table S1) and the decay of the σ_{Pt2+}. This transition from dispersed single-ions to metallic clusters

becomes also apparent in the thermodynamics (Figure 4, blue lines), which shows the preferential aggregation of the dispersed Pt^{2+} species into metallic clusters for $\sigma_{Pt}>1$.

The transition from dispersed single-ions to metallic clusters involves charge redistribution and charge transfer between the ceria substrate and Pt deposit that however does not affect substantially the degree of surface reduction: For $\sigma_{Pt} = 1$, σ_{Ce3+} reaches a maximum at 5/3 and remains constant at 4/3 also after nucleation of Pt clusters. This is in agreement with previous works demonstrating that ceria-supported Pt clusters and nanoparticles yield partial reduction of the substrate due to charge transfer [42,48]. We note that a residual number of Pt ionic species persists on the surface also after nucleation of the metallic clusters (Table S1). The computed charges of these ionic species in the cluster, ~9.3 e, are larger (i.e. less ionic) than those of the monodispersed Pt^{2+} species, ~8.3-8.5 e, but smaller than the metallic species, ~10 e; Pt species in the clusters can thus be designated as partially charged, $Pt^{\delta+}$, with partial charge of a particular atom depending on its position within the cluster. $Pt^{\delta+}$ species are not identified in the experiment (Figure S2a), their presence is only influencing the shift of the experimentally determined Pt^0 peak in SRPES. Our calculations show that in all cases presented in this work the Pt^{2+} species with Bader charge ~8.3-8.5 e are always incorporated in the characteristic PtO_4 moiety described previously [14] confirming that the intensity of the Pt^{2+} signal in SRPES is the correct measure of the density of monodispersed Pt^{2+} ions.

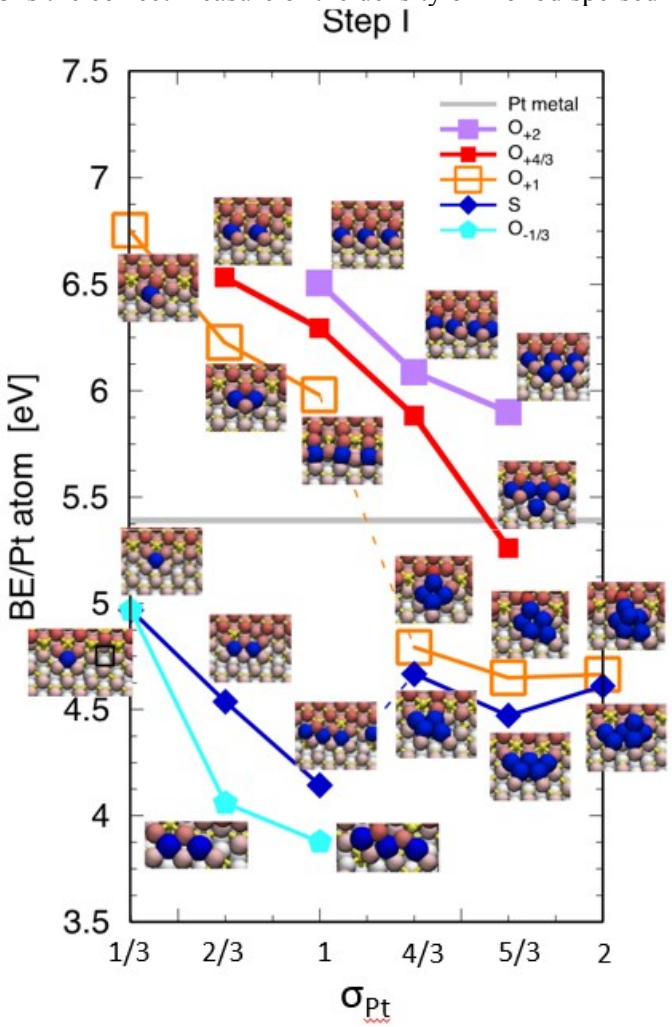

Figure 4: Average binding energy (BE/Pt atom) of the structures resulting from depositing Pt atoms with step coverage σ_{Pt} on the model ceria Step I. The gray horizontal line indicates the calculated cohesive energy of metallic Pt. The insets show the atomistic structure of the corresponding Pt adsorbates. O atoms are represented with different shades of red, while blue and yellow are used for the Pt and Ce atoms.

We show here that step edges accommodating excess O atoms allow to increase the maximum conversion of the deposited Pt to ionic Pt^{2+} species. For step edges having a full coverage of excess O atoms (Step I-O_{+1}, orange symbols in Figure 3a), the metallic-to-ionic conversion is linear up to $\sigma_{Pt} = 1$, thus larger than for the stoichiometric Step I-S. Metallic species appear only for $\sigma_{Pt} > 1$. The analysis of the ceria degree of reduction, Figure 3b, points to a different mechanism of Pt^{2+} formation that is active in the presence of excess O. Differently from the stoichiometric steps, here the Pt deposit is oxidized by the excess O atoms and not by the lattice Ce atoms. As a result, the conversion to Pt^{2+} for $\sigma_{Pt} <= 1$ does not involve ceria reduction and therefore $\sigma_{Ce3+} = 0$ (Figure 3b, orange symbols). At $\sigma_{Pt} = 1$ full reduction of the excess O atoms is achieved; for higher x(Pt) the nucleation of metallic clusters does not lead to further ceria reduction, similarly to the stoichiometric step edge, reaching the same σ_{Ce3+} saturation limit as with Step I-S. Note that also in this case, the calculations predict the persistence of partially charged $Pt^{\delta+}$ species at high Pt coverage (Supplementary Tables S2).

Larger amounts of excess O atoms at the steps further increase the fraction of deposited Pt that is fully oxidized to Pt^{2+}. For Step I-$O_{+4/3}$ and I-O_{+2}, complete metallic-to-ionic conversion is predicted up to $\sigma_{Pt} = 4/3$ and 5/3, respectively (Figure 3, red and purple symbols). The high Pt^{2+} step density that can be achieved in these Step I-$O_{+4/3}$ and -O_{+2} model systems result from the Pt incorporation in PtO_4 units forming single and double rows along the step edge (insets in Figure 4 corresponding to the purple symbols and Tables S3-S4).

The presence of O vacancies at ceria step edges, on the other hand, hinders the Pt conversion to Pt^{2+}. but does not completely suppress the formation of Pt^{2+} species. We report in Figure 3a the results obtained for the reduced Step I-$O_{-1/3}$ (cyan symbols) obtained by removing one of the three step-edge O atoms in the supercell. Calculations on this model step evidence that the Pt^{2+} stabilization process by the step edges is a highly local property, which is not affected by the step structure neighboring the PtO_4 moiety. Pt atoms that bind to the step edge one lattice site away from the vacancy, i.e. to stoichiometric-like regions of the step edge, are shown to be converted to Pt^{2+} ions following the same mechanisms reported for Step I-S. The calculated Pt binding energies (BE) to this stoichiometric-like region of the reduced Step I-$O_{-1/3}$ is equal to the one calculated for the stoichiometric step Step I-S (Figure 4, Table S8). Obviously, the maximum Pt^{2+} concentration that can be achieved on the reduced Step I-$O_{-1/3}$ is smaller than on the stoichiometric Step I-S. This is because, on reduced step edges, the fraction of stoichiometric-like step sites available for Pt binding and conversion to Pt_{2+} is less than 100% due to the presence of the O vacancies.

The results calculated for Step II (Supplementary Figure S8 and Table S5-S9) support the main conclusion reported above for Step I, i.e. that step edges with excess O atoms favor the Pt conversion and dispersion as ionic Pt^{2+} species. With stoichiometric Step II-S, its different geometry compared to the stoichiometric Step I-S prevents the stabilization of Pt^{2+} species. Pt atoms at Step II-S stabilize as monodospersed partially charged $Pt^{\delta+}$ species. Monodispersed Pt^{2+} ions on Step II can be formed in the presence of excess O species at the step edge. Indeed, 100% of the Pt atoms deposited on Step II-O_{+1} is converted to Pt^{2+} (Figure S8a) for $\sigma_{Pt} <= 1$. Compared to Step I-O_{+1}, for $\sigma_{Pt} > 1$ the geometry of Step II-O_{+1} allows stabilization of second row of monodispersed Pt which is now partially charged $Pt^{\delta+}$. With step II-O_{+1} we have also investigated the situation when the system is forced to nucleation of clusters. It turns out that the decoration of step edges with PtO4 rows containing Pt2+ is, for the same σ_{Pt}, energetically more favorable than Pt aggregation in metallic clusters (Table S6). Monodispersed $Pt^{\delta+}$ ions on Step II can be stabilized in the vicinity of O vacancy at the step edge, see Table S8. Calculations on Steps II with different amounts of surface oxygen suggest that the Pt^{2+} stabilization effect of surface step edges is a general property that is not dependent on the geometry of the specific step model used in the simulations.

Our calculations provide an important information on the effects of oxygen content of the CeO_2(111) and CeO_{2-x}(111) surfaces and steps on the adsorption energetics of Pt^{2+} and Pt^0 species. We report in Figures 4 and S8 the average binding energy (BE/Pt atom) of the deposited Pt atoms on the ceria Step I and Step II systems described above. The calculated binding energies are compared to the cohesive energy of metallic Pt bulk (gray horizontal line). For stoichiometric Step I-S and II-S (blue symbols) all the calculated BEs are lower than the cohesive energy of metallic Pt. According to our BE calculations, at stoichiometric ceria steps, Pt single ions/atoms and Pt_N clusters (N=3-6) are less stable than large metallic supported Pt particles. The role of excess surface oxygen in stabilizing single Pt^{2+} ion dispersions is demonstrated by the larger BEs calculated for the over-stoichiometric systems (orange, red, and purple symbols). The set of calculations for Step-I clearly shows the continuous shift of the BE to larger values with increasing content of excess O from

Step I-O_{+1} to Step I-O_{+2}. The physical origin of this shift is the larger amount of O atoms available at the oxidized step edges that allow to accommodate multiple rows of PtO_4 units. As anticipated above, O vacancies on the ceria step edges do not affect Pt^{2+} formation and its adsorption energetics on the stoichiometric regions of the partially-reduced steps.

Discussion:

The calculated results on the evolution of the Pt^{2+} population on ceria substrates with increasing Pt coverage are in qualitative agreement with the experiment. In particular, for a wide range of the oxygen content on the samples, from O-defective to samples with excess O, a maximum in the evolution of Pt^{2+} is observed with increasing Pt coverage, shifting to higher values of Pt^{2+} with increasing O content on the surface. In the calculations, the existence of this maximum is an intrinsic property of the Pt-ceria system to accommodate Pt^{2+} ions as PtO_4 moieties at step edges, and the related charge transfer of electrons from Pt atoms to ceria substrate, and is not primarily accompanied with creating O vacancies on the surface. In the experiments, nucleation of Pt clusters makes reduction of the samples by reducing agents more efficient, and the destabilization of Pt^{2+} population proceeds further via losses of surface O, complicating the quantitative interpretation of the experimental results.

The PtO_4 moiety at the step edge containing an isolated Pt^{2+} ion represents a universal motif arranging itself in many point, linear, and bilinear patterns on Steps I and II for all considered O contents of the ceria surface. Monoatomic steps at the $CeO_2(111)$ surface expose the lattice oxygen atoms arranged in the preferred square-planar geometry for PtO_4 stabilization, and, in addition, allow the excess O atoms to combine with lattice O atoms in the square-planar geometry and stabilize PtO_4, too.

For reduced $CeO_x(111)$ surfaces, the calculations suggest that on the reduced step edge two neighboring lattice O atoms are sufficient to stabilize an isolated PtO_4 moiety (Figure 4, Step I-S, $\sigma_{Pt} = 1/3$). In the experiment, we may determine the minimal oxygen content in the surface necessary for the stabilization of Pt^{2+} ions from the critical RER of 0.3 when no Pt^{2+} stabilization is observed on samples with RER >= 0.3 (Figures S3a – S3d). RER, as a qualitative indicator of CeO_x reduction, can be calibrated against the quantitative measure of Ce^{3+} concentration obtained from XPS of Ce3d (Figure S2c, Supplementary discussion). Considering the information depth of the SRPES and XPS measurements, and the exclusive localization of Ce^{3+} ions at the surface of the used experimental samples ([49], see also calculated geometries in Figure S6) we obtain the concentration of surface Ce^{3+} ions $p_{surf} = 0.9 \times$ RER (Supplementary discussion). The critical RER of 0.3 thus corresponds to surface Ce^{3+} concentration of approximately 0.3 ML.

On reduced $CeO_x(111)$ surfaces with monoatomic steps, O vacancies are preferentially localized at the step edges with 1 step edge O vacancy inducing localization of 2 Ce^{3+} ions in the vicinity of the step edge [40]. For the surfaces with step density of 0.15 ML used in our experiment, Ce^{3+} concentration of 0.3 ML is expected for the situation when all step edge O atoms are removed. The disappearance of Pt^{2+} stabilization in the experiment can thus be related to complete reduction of surface step edges. Apparently, PtO_4 moieties and Pt_{2+} ions in the experiment are able to nucleate as isolated and independent entities provided that lattice O at step edges is locally available.

On the samples with excess oxygen, on the other hand, increasing amount of the excess O atoms at the step edge allows nucleating of increasingly dense arrangements of PtO_4 moieties forming linear or bilinear structures of PtO_4 moieties at the step edges (Figure 4). Eventually, the concentration of stabilized Pt^{2+} may exceed the density of ceria step edges. This is observed in the experiments when the capacity of the surface to accommodate Pt^{2+} is maximized by sample treatment in O_2 atmosphere. Indeed, Pt^{2+} concentrations of up to 0.2 ML are obtained on the samples containing 0.15 ML steps (Figure 2). Besides the favorable square-planar geometry excess O atoms are adopting at ceria step edges, excess O atoms are also accommodating the charge released during the stabilization of the Pt^{2+} ions in PtO_4 moieties, and increase the capacity of the system to accommodate Pt^{2+} ions that is delimited by the capacity of the system to accommodate, at the step edges, the Ce^{3+} ions with increased ionic radii compared to Ce4+ ions.

Excess O atoms preventing the charge transfer between the Pt^{2+} ions and the substrate improve considerably the stability of the Pt^{2+} ions. Indeed in our calculations, only the Pt^{2+} configurations containing excess O atoms provide stronger stabilization to the Pt^{2+} ions compared to the cohesion of bulk Pt (Figure 4). This is an important consequence for the redispersion of Pt when Pt clusters dissolve at the expense of the growing Pt^{2+} population as observed in our experiments with intermittent oxidation of Pt deposit on

$CeO_2(111)$ (cf. Figure 1c, S3e). Based on the calculated energetics we can conclude that the excess O represents a necessary prerequisite for the experimental realization of the redispersion of Pt on ceria substrates.

On stoichiometric and reduced $CeO_2(111)$ substrates, Pt^{2+} stabilization in PtO_4 moieties is provided only at Step I, and the binding energy of Pt_{2+} is smaller than the cohesion of bulk Pt. However, considering the calculated non-monotonous evolution of the Pt binding energy for increasing σ_{Pt} (blue curves in Figures 4 and S7) we may expect the coexistence of the monodispersed Pt^{2+} species and metallic Pt clusters on the ceria substrates. In addition, Steps Type II can provide support for the monodispersed, partially charged $Pt^{\delta+}$ atoms. This is an important consequence for considering the catalysis over stoichiometric and reduced Pt/ceria. Under mild reducing conditions, Pt population on ceria can be bimodal containing both small metallic Pt clusters and monodispersed Pt^{2+} and $Pt^{\delta+}$ species.

Conclusions:

We have performed experiments and calculations studying behavior of Pt deposit on stoichiometric and reduced $CeO_2(111)$ substrates over a wide range of Pt and surface O concentrations. The experiments and simulations illustrate the extreme driving force for the Pt deposit on $CeO_2(111)$ to create isolated Pt^{2+} ions in PtO_4 configurations. On the reduced substrates, the Pt^{2+} is stabilized as soon as there appear any O atoms at the steps, lattice or excess. In the oxidizing atmospheres, excess O is incorporated at step edges creating new and more dense PtO_4 moieties, these incurring modifications of the oxygen storage capacity of the system. In the varying conditions of the surface chemical reactions, our results indicate that the Pt/ceria catalyst can react very flexibly making available a rich variety of configurations that provide the stabilization of monodispersed Pt^{2+} ions. Analyses of the binding energy of Pt^{2+} in the PtO_4 moieties indicate important consequences for exploiting and engineering the dispersion of Pt in Pt/ceria catalysts: on reduced and stoichiometric ceria, monodispersed Pt^{2+} ions and $Pt^{\delta+}$ adatoms at step edges can coexist with the metallic Pt^0 clusters. In the presence of excess oxygen, binding energy of Pt^{2+} at ceria step edges exceeds the cohesive energy of Pt bulk triggering the technologically important process of Pt redispersion.

Acknowledgments:

This work was supported by the Czech Science Foundation, Project 15-06759S and 13-10396S, by the Ministry of Education of the Czech Republic, Project LM 2015057, by the European Union via the FP7-NMP-2012 project chipCAT under contract number 310191, and the EU FP7 COST action CM1104. The authors acknowledge the CERIC−ERIC Consortium for access to experimental facilities and financial support.

Experimental details:

The experiments were performed at the Materials Science Beamline at Synchrotron Elettra, Italy, and in the Surface Physics Laboratory in Prague. We have performed stepwise deposition of small amounts of Pt on model stoichiometric $CeO_2(111)$ and slightly reduced $CeO_x(111)$ surfaces containing a well-defined amount of monolayer-high steps [14]. Stepped surfaces of $CeO_2(111)$ provide a suitable model for real ceria catalysts [27,50], and allow drawing quantitative conclusions on the character of the Pt deposit [14,42].

$CeO_2(111)$ was prepared as a 20-30 Angstrom thick film on Cu(111) single crystalline substrate by two alternative methods [14,51] both yielding approximately 0.15 ML step sites on the $CeO_2(111)$ surface. STM images of the clean stepped $CeO_2(111)$ surfaces and the details of the preparation methods are displayed in Figure S1. $CeO_x(111)$ surfaces were obtained by repeated annealing of $CeO_2(111)$ surfaces in vacuum and/or by adsorption and thermal desorption of methanol, both approaches conserving the step density on the samples. $CeO_2(111)$ and $CeO_x(111)$ surfaces were exposed with Pt atoms evaporated from e-beam heated Pt wire in small amounts of the order 0.02 ML. The amount of Pt was determined by deposition time after calibrating Pt evaporation rate by a combination of quartz crystal microbalance measurements and XPS intensities of Pt 4f and (attenuation of) substrate Cu $2p_{3/2}$ peaks [14]. After each Pt deposition the samples were flash heated at 700 K in vacuum or in O_2 atmosphere to promote the thermally activated stabilization of Pt^{2+} ions [11,14].

In between the Pt deposition steps, the charge state of the Pt deposit was determined from Pt4f synchrotron radiation PES spectrum [11,14] (SRPES) measured at normal emission using photon energy hv = 180 eV (Figure S2a). The charge state of the ceria support was determined by combination of the information

from XPS of Ce3d measured 20° off normal by Al Kα (Figure S2c) and the information from resonant PES (RPES) measurement of CeO_x valence band (VB) at normal emission (Figure S2b). XPS of Ce3d has been fitted for Ce^{3+} and Ce^{4+} contributions following the approach by Skála et al. [52]. In RPES measurements, ceria reduction has been expressed as so called resonance enhancement ratio (RER) [53,54] determined from resonance enhancements of Ce 4f states of Ce^{3+} and Ce^{4+} ions in VB photoelectron spectra taken at 115 eV, 121.4 eV, and 124.8 eV - photon energies off resonance, on Ce^{3+} resonance, and on Ce^{4+} resonance.

Concentration of Ce^{3+} ions on the reduced ceria samples can be sensitively detected using RER. For quantification of Ce^{3+} concentration, the RER signal is calibrated against XPS signal [42] under an assumption that the concentration of Ce^{3+} ions is homogeneous over the information depth of RPES and XPS, i.e. 3-6 ML. For our experimental setup, this calibration is plotted in Figure S9 and yields bulk Ce^{3+} concentration $P_{bulk} = 0.2 \times RER$ in agreement with Ref. [42], see Supplementary Discussion. Generally, however, Ce^{3+} ions tend to accumulate in the near surface region of $CeO_x(111)$ samples [55]. For the smallest reductions, all Ce^{3+} ions are expected to localize in the surface monolayer (1st ML) of $CeO_x(111)$ samples [49]. We may thus impose another limiting assumption that all Ce^{3+} ions in the investigated samples are localized within the 1st ML. This yields the calibration of surface Ce^{3+} concentration $P_{surf} = 0.9 \times RER$, see Supplementary Discussion.

Computational details:

All the calculations were based on the density functional theory employing the Perdew, Burke and Ernzerhof (PBE) generalised gradient-corrected approximation [56] for the exchange and correlation functional. The spin polarized Kohn-Sham equations were solved in the plane-wave and (ultrasoft) pseudo potential framework applying periodic boundary conditions as implemented in the Quantum ESPRESSO package [57]. The plane-wave basis sets used to describe the electronic wavefunction and density were 40 and 320 Ry, respectively.

The ceria-based materials were simulated with the PBE+U approach in the implementation of Cococcioni and de Gironcoli [58], which includes an additional Hubbard-U term to the Kohn-Sham functional that disfavors fractional occupancies of the Ce 4f states. The value of the parameter U was set to 4.5 eV.

The adsorption of Pt atoms and clusters with ceria step edges was modelled with periodic supercells describing vicinal surfaces. To verify that the main conclusions of the calculations do not depend on the specific details of the step edge geometry we selected two of the lowest-energy model steps proposed in Ref. [40]. Following this work, we label our two model step surfaces as Type I and Type II. In both models, the step edge exposes 3 independent O atoms, separates two (111) terraces and is oriented along the [110] direction. The lateral dimensions of the monoclinic supercells were (17.97, 11.67) Å and (15.72, 11.67) Å for Step-Type I and II, respectively, along the [112] and [110] directions correspondingly. The supercell slabs comprised nine atomic layers and their surfaces were separated by more than 11 Å of vacuum in the direction perpendicular to the (111) terrace. All the atomistic structures were relaxed according to the calculated Hellman- Feynman forces until the maximum force was less than 0.02 eV/Å. During the structural relaxation, the lowest three atomic layers were constrained to their bulk equilibrium coordinates, as well as the Ce atoms in the central O-Ce-O trilayers far from the step edge. Integrals in the Brillouin zone were calculated at the gamma point. Computational details are reported in the Supplementary Information.

References:

[1] Q. Fu, H. Saltsburg, M. Flytzani-Stephanopoulos, Active Nonmetallic Au and Pt Species on Ceria-Based Water-Gas Shift Catalysts, Science (80-.). 301 (2003) 935–938. doi:10.1126/science.1085721.

[2] M. Hatanaka, N. Takahashi, T. Tanabe, Y. Nagai, K. Dohmae, Y. Aoki, et al., Ideal Pt loading for a Pt/CeO2-based catalyst stabilized by a Pt–O–Ce bond, Appl. Catal. B Environ. 99 (2010) 336–342. doi:10.1016/j.apcatb.2010.07.003.

[3] H. Wei, X. Liu, A. Wang, L. Zhang, B. Qiao, X. Yang, et al., FeOx-supported platinum single-atom and pseudo-single-atom catalysts for chemoselective hydrogenation of functionalized nitroarenes, Nat. Commun. 5 (2014) 5634. doi:10.1038/ncomms6634.

[4] M. Flytzani-Stephanopoulos, B.C. Gates, Atomically Dispersed Supported Metal Catalysts, Annu. Rev. Chem. Biomol. Eng. 3 (2012) 545–574. doi:10.1146/annurev-chembioeng-062011-080939.

[5] X. Yang, A. Wang, B. Qiao, J. Li, J. Liu, T. Zhang, Single-Atom Catalysts: A New Frontier in Heterogeneous Catalysis, Acc. Chem. Res. 46 (2013) 1740–1748. doi:10.1021/ar300361m.

[6] J. Liu, Catalysis by Supported Single Metal Atoms, ACS Catal. 7 (2017) 34–59. doi:10.1021/acscatal.6b01534.

[7] J.M. Thomas, Catalysis: Tens of thousands of atoms replaced by one, Nature. 525 (2015) 325–326. doi:10.1038/525325a.

[8] B. Qiao, A. Wang, X. Yang, L.F. Allard, Z. Jiang, Y. Cui, et al., Single-atom catalysis of CO oxidation using Pt1/FeOx., Nat. Chem. 3 (2011) 634–41. doi:10.1038/nchem.1095.

[9] J. Lin, A. Wang, B. Qiao, X. Liu, X. Yang, X. Wang, et al., Remarkable performance of Ir1/FeO(x) single-atom catalyst in water gas shift reaction., J. Am. Chem. Soc. 135 (2013) 15314–7. doi:10.1021/ja408574m.

[10] M. Flytzani-Stephanopoulos, Gold atoms stabilized on various supports catalyze the water-gas shift reaction., Acc. Chem. Res. 47 (2014) 783–92. doi:10.1021/ar4001845.

[11] A. Bruix, Y. Lykhach, I. Matolínová, A. Neitzel, T. Skála, N. Tsud, et al., Maximum Noble-Metal Efficiency in Catalytic Materials: Atomically Dispersed Surface Platinum, Angew. Chemie Int. Ed. 53 (2014) 10525–10530. doi:10.1002/anie.201402342.

[12] Z. Novotný, G. Argentero, Z. Wang, M. Schmid, U. Diebold, G.S. Parkinson, Ordered Array of Single Adatoms with Remarkable Thermal Stability: Au/Fe_{3}O_{4}(001), Phys. Rev. Lett. 108 (2012) 216103. doi:10.1103/PhysRevLett.108.216103.

[13] X. Zhou, W. Yang, Q. Chen, Z. Geng, X. Shao, J. Li, et al., Stable Pt Single Atoms and Nanoclusters on Ultrathin CuO Film and Their Performances in CO Oxidation, J. Phys. Chem. C. 120 (2016) 1709–1715. doi:10.1021/acs.jpcc.5b11362.

[14] F. Dvořák, M. Farnesi Camellone, A. Tovt, N. Tran, F.R. Negreiros, M. Vorokhta, et al., Creating single-atom Pt-ceria catalysts by surface step decoration, Nat. Commun. 7 (2016) 10801. doi:10.1038/ncomms10801.

[15] G.S. Parkinson, Z. Novotny, G. Argentero, M. Schmid, J. Pavelec, R. Kosak, et al., Carbon monoxide-induced adatom sintering in a Pd-Fe3O4 model catalyst., Nat. Mater. 12 (2013) 724–8. doi:10.1038/nmat3667.

[16] R. Bliem, J. van der Hoeven, A. Zavodny, O. Gamba, J. Pavelec, P.E. de Jongh, et al., An Atomic-Scale View of CO and H2 Oxidation on a Pt/Fe 3O4 Model Catalyst, Angew. Chemie Int. Ed. 54 (2015) 13999–14002. doi:10.1002/anie.201507368.

[17] Y.-G. Wang, D. Mei, V.-A. Glezakou, J. Li, R. Rousseau, Dynamic formation of single-atom catalytic active sites on ceria-supported gold nanoparticles, Nat. Commun. 6 (2015) 6511. doi:10.1038/ncomms7511.

[18] Y.-G. Wang, D.C. Cantu, M.-S. Lee, J. Li, V.-A. Glezakou, R. Rousseau, CO Oxidation on Au/TiO 2 : Condition-Dependent Active Sites and Mechanistic Pathways, J. Am. Chem. Soc. 138 (2016) 10467–10476. doi:10.1021/jacs.6b04187.

[19] M. Moses-DeBusk, M. Yoon, L.F. Allard, D.R. Mullins, Z. Wu, X. Yang, et al., CO oxidation on supported single Pt atoms: experimental and ab initio density functional studies of CO interaction with Pt atom on θ-Al2O3(010) surface., J. Am. Chem. Soc. 135 (2013) 12634–45. doi:10.1021/ja401847c.

[20] G. Vilé, D. Albani, M. Nachtegaal, Z. Chen, D. Dontsova, M. Antonietti, et al., A Stable Single-Site Palladium Catalyst for Hydrogenations, Angew. Chemie Int. Ed. 54 (2015) 11265–11269. doi:10.1002/anie.201505073.

[21] L. Nie, D. Mei, H. Xiong, B. Peng, Z. Ren, X.I.P. Hernandez, et al., Activation of surface lattice oxygen in single-atom Pt/CeO 2 for low-temperature CO oxidation, Science (80-.). 358 (2017) 1419–1423. doi:10.1126/science.aao2109.

[22] C. Wang, X.-K. Gu, H. Yan, Y. Lin, J. Li, D. Liu, et al., Water-Mediated Mars–Van Krevelen Mechanism for CO Oxidation on Ceria-Supported Single-Atom Pt 1 Catalyst, ACS Catal. 7 (2017) 887–891. doi:10.1021/acscatal.6b02685.

[23] K. Ding, A. Gulec, A.M. Johnson, N.M. Schweitzer, G.D. Stucky, L.D. Marks, et al., Identification of active sites in CO oxidation and water-gas shift over supported Pt catalysts, Science (80-.). 350 (2015) 189–192. doi:10.1126/science.aab3501.

[24] M.D. Rossell, F.J. Caparrós, I. Angurell, G. Muller, J. Llorca, M. Seco, et al., Magnetite-supported palladium single-atoms do not catalyse the hydrogenation of alkenes but small clusters do, Catal. Sci. Technol. 6 (2016) 4081–4085. doi:10.1039/C6CY00596A.

[25] Y. Lykhach, A. Bruix, S. Fabris, V. Potin, I. Matolínová, V. Matolín, et al., Oxide-based nanomaterials for fuel cell catalysis: the interplay between supported single Pt atoms and particles, Catal. Sci. Technol. 7 (2017) 4315–4345. doi:10.1039/C7CY00710H.

[26] Y. Chen, J. Lin, L. Li, B. Qiao, J. Liu, Y. Su, et al., Identifying Size Effects of Pt as Single Atoms and Nanoparticles Supported on FeO x for the Water-Gas Shift Reaction, ACS Catal. 8 (2018) 859–868. doi:10.1021/acscatal.7b02751.

[27] J. Jones, H. Xiong, A.T. DeLaRiva, E.J. Peterson, H. Pham, S.R. Chala, et al., Thermally stable single-atom platinum-on-ceria catalysts via atom trapping, Science. 353 (2016) 150–154. doi:10.1126/science.aaf8800.

[28] M. Moliner, J.E. Gabay, C.E. Kliewer, R.T. Carr, J. Guzman, G.L. Casty, et al., Reversible Transformation of Pt Nanoparticles into Single Atoms inside High-Silica Chabazite Zeolite, J. Am. Chem. Soc. 138 (2016) 15743–15750. doi:10.1021/jacs.6b10169.

[29] A.M. Gänzler, M. Casapu, P. Vernoux, S. Loridant, F.J. Cadete Santos Aires, T. Epicier, et al., Tuning the Structure of Platinum Particles on Ceria In Situ for Enhancing the Catalytic Performance of Exhaust Gas Catalysts, Angew. Chemie Int. Ed. 56 (2017) 13078–13082. doi:10.1002/anie.201707842.

[30] Y. Nagai, K. Dohmae, Y. Ikeda, N. Takagi, T. Tanabe, N. Hara, et al., In Situ Redispersion of Platinum Autoexhaust Catalysts: An On-Line Approach to Increasing Catalyst Lifetimes?, Angew. Chemie Int. Ed. 47 (2008) 9303–9306. doi:10.1002/anie.200803126.

[31] M. Hatanaka, N. Takahashi, N. Takahashi, T. Tanabe, Y. Nagai, A. Suda, et al., Reversible changes in the Pt oxidation state and nanostructure on a ceria-based supported Pt, J. Catal. 266 (2009) 182–190.

doi:10.1016/j.jcat.2009.06.005.

[32] K. Morgan, A. Goguet, C. Hardacre, Metal Redispersion Strategies for Recycling of Supported Metal Catalysts: A Perspective, ACS Catal. 5 (2015) 3430–3445. doi:10.1021/acscatal.5b00535.

[33] E.D. Goodman, J.A. Schwalbe, M. Cargnello, Mechanistic Understanding and the Rational Design of Sinter-Resistant Heterogeneous Catalysts, ACS Catal. 7 (2017) 7156–7173. doi:10.1021/acscatal.7b01975.

[34] H. Shinjoh, M. Hatanaka, Y. Nagai, T. Tanabe, N. Takahashi, T. Yoshida, et al., Suppression of Noble Metal Sintering Based on the Support Anchoring Effect and its Application in Automotive Three-Way Catalysis, Top. Catal. 52 (2009) 1967–1971. doi:10.1007/s11244-009-9371-5.

[35] R. Fiala, M. Vaclavu, A. Rednyk, I. Khalakhan, M. Vorokhta, J. Lavkova, et al., Pt–CeOx thin film catalysts for PEMFC, Catal. Today. 240 (2015) 236–241. doi:10.1016/j.cattod.2014.03.069.

[36] R. Fiala, A. Figueroba, A. Bruix, M. Vaclavu, A. Rednyk, I. Khalakhan, et al., High efficiency of Pt2+- CeO2 novel thin film catalyst as anode for proton exchange membrane fuel cells, Appl. Catal. B Environ. 197 (2016) 262–270. doi:10.1016/j.apcatb.2016.02.036.

[37] T. Wu, X. Pan, Y. Zhang, Z. Miao, B. Zhang, J. Li, et al., Investigation of the Redispersion of Pt Nanoparticles on Polyhedral Ceria Nanoparticles, J. Phys. Chem. Lett. 5 (2014) 2479–2483. doi:10.1021/jz500839u.

[38] Y. Lykhach, A. Figueroba, M.F. Camellone, A. Neitzel, T. Skála, F.R. Negreiros, et al., Reactivity of atomically dispersed Pt2+ species towards H2 : model Pt–CeO 2 fuel cell catalyst, Phys. Chem. Chem. Phys. 18 (2016) 7672–7679. doi:10.1039/C6CP00627B.

[39] A. Neitzel, V. Johánek, Y. Lykhach, T. Skála, N. Tsud, M. Vorokhta, et al., Reduction of Pt2+ species in model Pt–CeO2 fuel cell catalysts upon reaction with methanol, Appl. Surf. Sci. 387 (2016) 674–681. doi:10.1016/j.apsusc.2016.06.156.

[40] S.M. Kozlov, K.M. Neyman, O vacancies on steps on the CeO2(111) surface, Phys. Chem. Chem. Phys. 16 (2014) 7823. doi:10.1039/c4cp00136b.

[41] N. Skorodumova, S. Simak, B. Lundqvist, I. Abrikosov, B. Johansson, Quantum Origin of the Oxygen Storage Capability of Ceria, Phys. Rev. Lett. 89 (2002) 166601. doi:10.1103/PhysRevLett.89.166601.

[42] Y. Lykhach, S.M. Kozlov, T. Skála, A. Tovt, V. Stetsovych, N. Tsud, et al., Counting electrons on supported nanoparticles, Nat. Mater. 15 (2016) 284–288. doi:10.1038/nmat4500.

[43] J. Kwak, J. Hu, D. Mei, C. Yi, D. Kim, Coordinatively unsaturated Al3+ centers as binding sites for active catalyst phases of platinum on γ-Al2O3, Science (80-.). 5208 (2009) 1670–1673. http://www.sciencemag.org/content/325/5948/1670.short (accessed November 4, 2014).

[44] R. Bliem, R. Kosak, L. Perneczky, Z. Novotny, O. Gamba, D. Fobes, et al., Cluster nucleation and growth from a highly supersaturated adatom phase: silver on magnetite., ACS Nano. 8 (2014) 7531–7. doi:10.1021/nn502895s.

[45] S.M. Kozlov, F. Viñes, N. Nilius, S. Shaikhutdinov, K.M. Neyman, Absolute Surface Step Energies: Accurate Theoretical Methods Applied to Ceria Nanoislands, J. Phys. Chem. Lett. 3 (2012) 1956–1961. doi:10.1021/jz3006942.

[46] M. Huang, S. Fabris, Role of surface peroxo and superoxo species in the low-temperature oxygen buffering of ceria: Density functional theory calculations, Phys. Rev. B. 75 (2007) 081404. doi:10.1103/PhysRevB.75.081404.

[47] Y. Zhao, B. Teng, X. Wen, Y. Zhao, Q. Chen, L. Zhao, et al., Superoxide and Peroxide Species on CeO 2 (111), and Their Oxidation Roles, J. Phys. Chem. C. 116 (2012) 15986–15991.

doi:10.1021/jp3016326.

[48] F.R. Negreiros, S. Fabris, Role of Cluster Morphology in the Dynamics and Reactivity of Subnanometer Pt Clusters Supported on Ceria Surfaces, J. Phys. Chem. C. 118 (2014) 21014–21020. doi:10.1021/jp506404z.

[49] G.E. Murgida, M.V. Ganduglia-Pirovano, Evidence for subsurface ordering of oxygen vacancies on the reduced CeO2(111) surface using density-functional and statistical calculations, Phys. Rev. Lett. 110 (2013) 1–5. doi:10.1103/PhysRevLett.110.246101.

[50] P. Furler, J. Scheffe, M. Gorbar, L. Moes, U. Vogt, A. Steinfeld, Solar Thermochemical CO 2 Splitting Utilizing a Reticulated Porous Ceria Redox System, Energy & Fuels. 26 (2012) 7051–7059. doi:10.1021/ef3013757.

[51] F. Dvořák, O. Stetsovych, M. Steger, E. Cherradi, I. Matolínová, N. Tsud, et al., Adjusting Morphology and Surface Reduction of CeO2(111) Thin Films on Cu(111), J. Phys. Chem. C. 115 (2011) 7496–7503. doi:10.1021/jp1121646.

[52] T. Skála, F. Šutara, K.C. Prince, V. Matolín, Cerium oxide stoichiometry alteration via Sn deposition: Influence of temperature, J. Electron Spectros. Relat. Phenomena. 169 (2009) 20–25. doi:10.1016/j.elspec.2008.10.003.

[53] V. Matolín, I. Matolínová, F. Dvořák, V. Johánek, J. Mysliveček, K.C. Prince, et al., Water interaction with CeO2(111)/Cu(111) model catalyst surface, Catal. Today. 181 (2012) 124–132. doi:10.1016/j.cattod.2011.05.032.

[54] D.R. Mullins, The surface chemistry of cerium oxide, Surf. Sci. Rep. 70 (2015) 42–85. doi:10.1016/j.surfrep.2014.12.001.

[55] T. Duchoň, F. Dvořák, M. Aulická, V. Stetsovych, M. Vorokhta, D. Mazur, et al., Ordered Phases of Reduced Ceria As Epitaxial Films on Cu(111), J. Phys. Chem. C. 118 (2014) 357–365. doi:10.1021/jp409220p.

[56] J.P.J. Perdew, K. Burke, M. Ernzerhof, Generalized Gradient Approximation Made Simple., Phys. Rev. Lett. 77 (1996) 3865–3868. doi:10.1103/PhysRevLett.77.3865.

[57] P. Giannozzi, S. Baroni, N. Bonini, M. Calandra, R. Car, C. Cavazzoni, et al., QUANTUM ESPRESSO: a modular and open-source software project for quantum simulations of materials, J. Phys. Condens. Matter. 21 (2009) 395502. doi:10.1088/0953-8984/21/39/395502.

[58] M. Cococcioni, S. de Gironcoli, Linear response approach to the calculation of the effective interaction parameters in the LDA + U method, Phys. Rev. B. 71 (2005) 035105. doi:10.1103/PhysRevB.71.035105.

[59] V. Stetsovych, F. Pagliuca, F. Dvořák, T. Duchoň, M. Vorokhta, M. Aulická, et al., Epitaxial Cubic Ce2O3 Films via Ce–CeO2 Interfacial Reaction, J. Phys. Chem. Lett. 4 (2013) 866–871. doi:10.1021/jz400187j.

[60] S. Tanuma, C.J. Powell, D.R. Penn, Calculations of electron inelastic mean free paths (IMFPS). IV. Evaluation of calculated IMFPs and of the predictive IMFP formula TPP-2 for electron energies between 50 and 2000 eV, Surf. Interface Anal. 20 (1993) 77–89. doi:10.1002/sia.740200112.

SUPPORTING INFORMATION

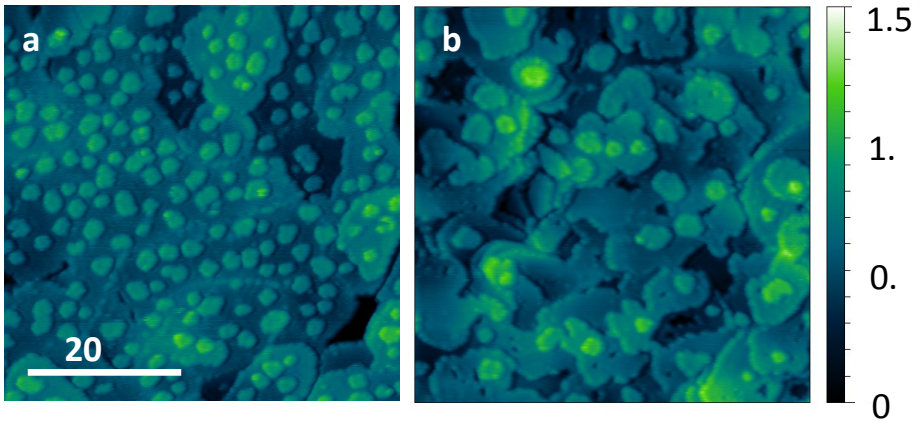

Figure S1: CeO_2(111) substrates with 0.15 ML of monoatomic steps used in the present study. (a) Substrate obtained by deposition of 0.3 ML CeO_2 at RT on a Cu(111) supported CeO_2(111) thin film with the lowest achievable density of substrate steps (approx 0.04 ML), followed by annealing to 800 K. CeO_2(111) thin film with the lowest step density is obtained by oxidation of a 20 Å thick Ce_2O_3 film prepared according to Refs. [55,59]. (b) Substrate obtained by deposition of 20 Å of CeO_2(111) on Cu(111) at 520 K and subsequent annealing to 800 K. Substrates from (a), (b) are eventually reduced by repeated annealing in vacuum to 700 K and/or by adsorption of methanol and desorption at 700 K, both approaches conserving the density of surface monoatomic steps 0.15 ML.

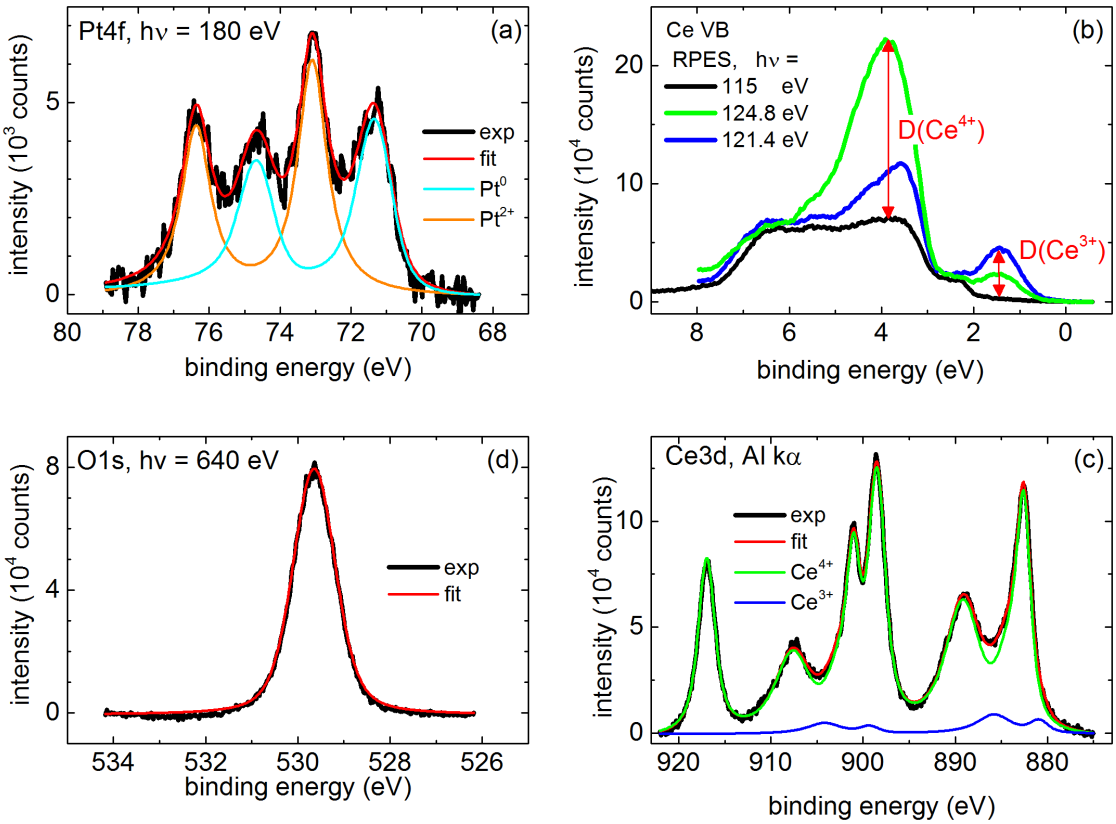

Figure S2: Examples of the experimental data and the fitting procedures to obtain quantitative information. The displayed data correspond to the sample in the Figure S3c, Pt amount 0.09 ML.

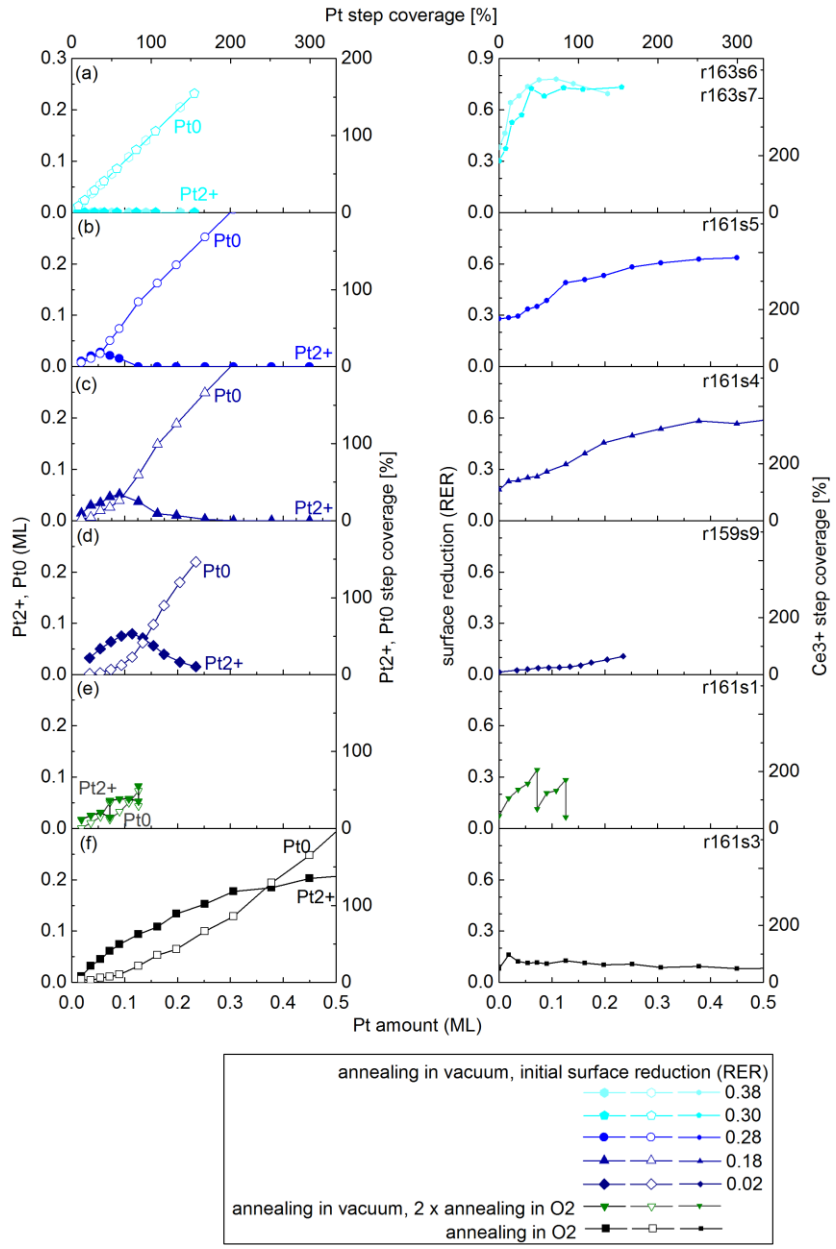

Figure S3: Concentration of Pt^{2+} ions and metallic Pt^0 atoms, and RER during Pt deposition and annealing on CeO_2 and CeO_x(111) samples as described in Figure 1 (S3b, S3d-f) and other CeO_x samples (S3a, S3c). Initial surface reduction (RER of the CeO_x samples before deposition of Pt) determines whether Pt^{2+} ions will be formed. RER >= 0.3 (S3a) inhibits Pt^{2+} formation. With RER < 0.3 Pt^{2+} ions are forming at the beginning of the Pt deposition (S3b-S3d). Intermittent annealing in O^2 can recover the Pt^{2+} population (S3e) via redispersion of Pt^0 clusters. Pt^{2+} population is maximized by deposition and annealing of Pt in 5 × 10^{-5} Pa O_2 (S3f).

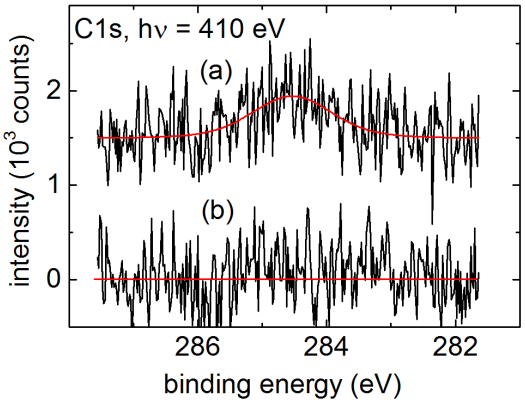

Figure S4: (a) carbon deposited on the sample during evaporation of Pt at room temperature. (b) clean-off of carbon upon annealing of the Pt deposit at 700 K in vacuum. The amount of the deposited C varies slightly between different samples. It is small (<= 1000 counts after every Pt deposition) for the sample in Figures 1a and S3d, medium (<= 2000 counts after every Pt deposition) for the samples in Figures 1b and S3b, 1d and S3f, S3a, S3c, and increased (<= 3000 counts after every Pt deposition) for the sample in Figure 1c and S3e. The displayed data correspond to the sample in the Figure S3c, Pt amount 0.09 ML.

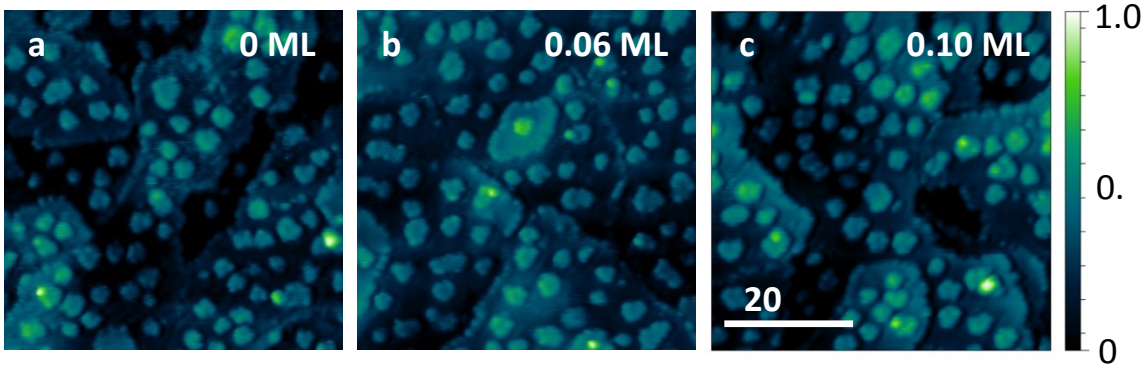

Figure S5: High resolution STM images of CeO_2(111) samples during initial stages of deposition of Pt and Pt annealing in O_2 atmosphere. The morphology of clean and Pt covered samples is qualitatively the same. At Pt coverage between 0.1 and 0.15 ML, metallic Pt clusters are being identified, compare Figure 2.

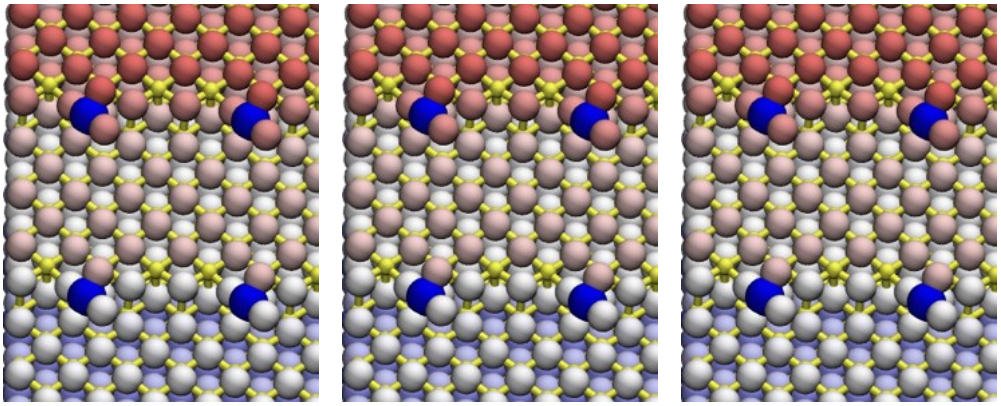

*Figure S6: Computational supercells used to simulate the Step I-$O_{-1/3}$ (a), Step I-S (b), Step I-O_{+1} (c). A square mark the position of the O vacancy, while the * symbol mark the excess O atoms forming peroxide groups at the step edge. O atoms are represented with different shades of red, while blue and yellow are used for the Pt and Ce atoms.*

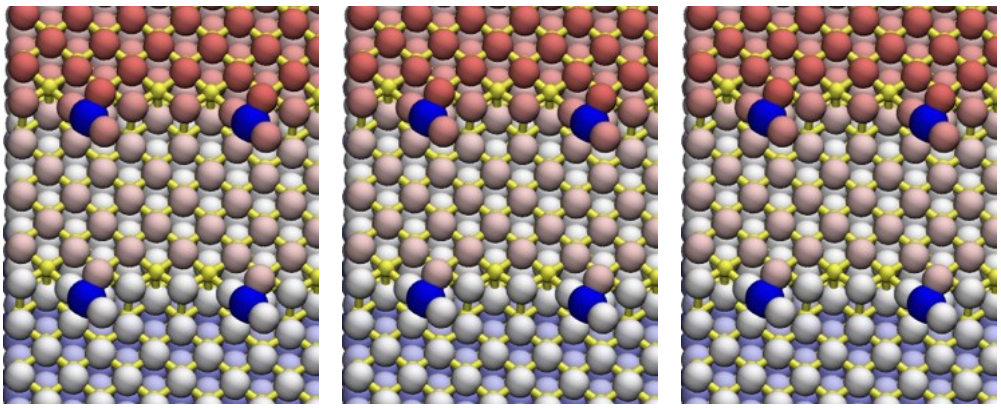

Figure S7: Computational supercells used to simulate the Step II-$O_{-1/3}$ (a), Step II-S (b), Step II-O_{+1} (c).

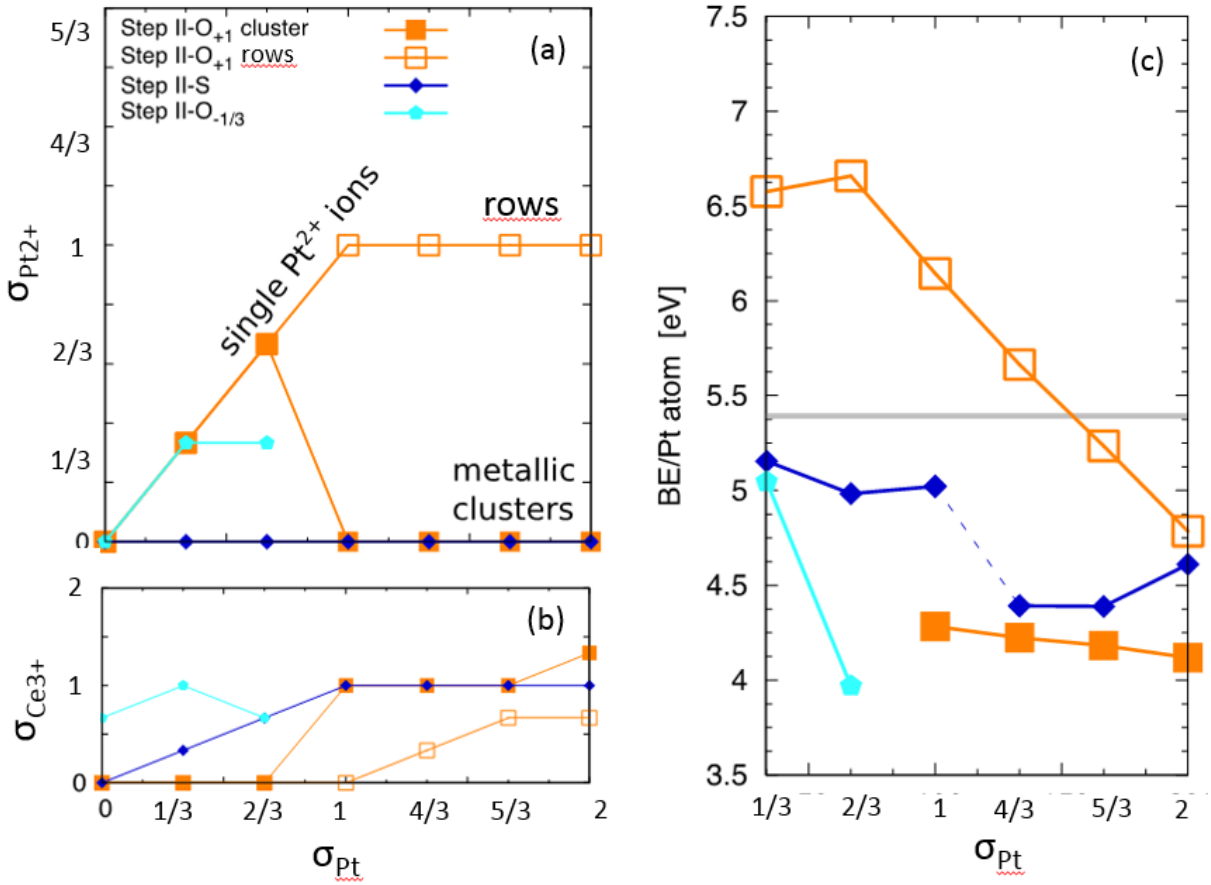

Figure S8: Number of Pt^{2+} (a) and of Ce^{3+} ions (b) that form on the Step II upon the adsorption of Pt. (c) Average binding energy (BE/Pt atom) of the structures resulting from depositing Pt atoms with step coverage σ_{Pt} on Step II. The gray horizontal line indicates the calculated cohesive energy of metallic Pt. Definitions and color codes as in Figure 3.

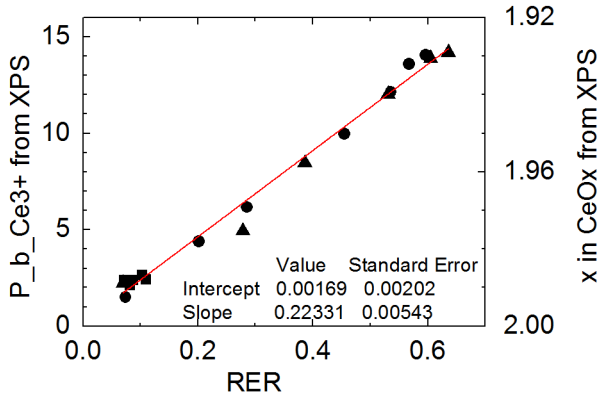

Figure S9: Experimental dependence between the bulk concentration of Ce^{3+} in the ceria samples determined by XPS of Ce3d , and the RER calculated from RPES of Ce4f.

Supplementary Discussion: *Determining the surface Ce^{3+} concentration from RPES and XPS measurements*

In the present work, surface Ce^{3+} concentration is determined based on highly sensitive resonant enhancement ratio (RER), a value straightforwardly determined from resonant photoemission measurements of Ce4f VB state [53,54]. Calibration of the RER for Ce^{3+} concentration is performed comparing the measured values of RER for a range of clean and Pt exposed CeO_x(111) samples with Ce^{3+} concentrations determined from XPS of Ce3d [42]. XPS of Ce3d represents a less sensitive measure of Ce^{3+} concentration than RER, and requires a complex analysis [52] yielding, however, a quantitative information.

An implicit assumption in analyzing XPS of Ce3d for Ce^{3+} concentration is that the Ce^{3+} concentration be constant over the information depth of XPS [42]. In such case, peak areas of Ce^{3+} and Ce^{4+} in XPS of Ce3d (A_{Ce3+}, A_{Ce4+}) are considered proportional to concentrations of Ce^{3+} and Ce^{4+} in the sample, and the relative bulk concentration of Ce3+, P_{bulk}, is obtained as

$$P_{bulk} = A_{Ce3+} / (A_{Ce3+} + A_{Ce4+}). \quad (1)$$

For the experimental setup used in the present work, P_{bulk} obtained from XPS is plotted against the corresponding RER determined from SRPES in Figure S8. This calibration allows us to determine P_{bulk} in the present experiments based on the values of RER as

$$P_{bulk} = 0.2 \times RER, \quad (2)$$

in good agreement with the calibration of Ref. [42].

The linearity of the dependence in Figure S8, and its intercept at (0,0) indicate that in the observed range of RER values, both RER and XPS of Ce3d are well-defined measures of Ce^{3+} concentration. The information depth of XPS of Ce3d and RER is related to the mean free path of the corresponding photoelectrons which evaluates according to TPP2M formula [60] as λ_{XPS}=10.9 Å (585 eV photoelectrons escaping from CeO_2 20° off normal) and λ_{RER}=4.9 Å (120 eV photoelectrons escaping from CeO_2 along normal). Defining the information depth ι as the depth from which 90% of the XPS or SRPES signal is coming we obtain $\iota_{XPS}=2.3 \times \lambda_{XPS}$=25 Å, and $\iota_{RER}=2.3 \times \lambda_{RER}$=11 Å; for CeO_x(111) the values of ι are in the range of 3-7 ML thickness (1 ML is 3.12 Å thick).

Previous experiments and theoretical considerations [49,55] confirm that Ce^{3+} ions in reduced samples tend to accumulate near the surface, and, for the lowest reduction, all Ce^{3+} ions are expected to reside in the topmost monolayer of the sample [49]. In such case, the above calibration of bulk Ce^{3+} concentration would be underestimating the actual surface concentration of Ce^{3+}. We may analyze the experimental XPS and SRPES data under the assumption of exclusive localization of Ce^{3+} in the topmost monolayer and obtain the corresponding surface Ce^{3+} concentration P_{surf}. This assumption is expected to hold for P_{surf} up to 0. 25 ML [49].

For the evaluation we consider the quantitative XPS data and sum the expected XPS signals J from the topmost and the lower lying monolayers of the sample. Thus,

$J_{Ce3+} = P_{surf} \times W,$
(3)

where W is the instrumentation constant, and

$$J_{Ce4+} = W - J_{Ce3+} + \sum_{n=1}^{\infty}(W \exp(-nd/\lambda_{XPS})). \quad (4)$$

Evaluating now, formally,

$$J_{Ce3+} / (J_{Ce3+} + J_{Ce4+}) = P_{surf}\,(1 - \exp(-d/\lambda_{XPS})) \quad (5)$$

we obtain

$$P_{surf} = Q\, J_{Ce3+} / (J_{Ce3+} + J_{Ce4+}), \quad (6)$$

$$\text{where } Q = 1/ (1 - \exp(-d/\lambda_{XPS})). \quad (7)$$

Comparing now the expected XPS signals J_{Ce3+}, J_{Ce4+} to the areas of experimental XPS peaks A_{Ce3+}, A_{Ce4+} appearing in the calibration of P_{bulk} from the XPS (1) we obtain for the surface Ce_{3+} concentration

$$P_{surf} = Q\, P_{bulk}, \quad (8)$$

under the assumption that all Ce^{3+} atoms reside in the topmost monolayer of the sample.

The extent of the correction Q depends on the mean free path of the photoelectrons; for XPS of Ce3d yielding the quantitative information in our experiments Q = 4.0. Combining (2) and (8) we obtain the surface Ce^{3+} concentration determined form the values of RER in our experimental setup

$$P_{surf} = 0.9 * RER. \quad (9)$$

Supplementary Discussion: *Computational charge analysis and binding energies.*

The Bader charge analysis was used to determine the charge state of the supported Pt ions. The results are reported in the Tables below. It is well known that charge population analysis do not provide an absolute measure of the oxidation state of a given element. To define the charge state of Pt, we employ here a definition that is similar to the experimental approach, i.e. we focus on the electrons transferred to the Ce atoms of the substrate. According to this approach, if the adsorption of one Pt atom leads to the presence of 2 Ce^{3+} ions, we define it as Pt^{2+}. On the basis of the calculated Bader charges, we can set a cutoff value of 9.0 e. Pt atoms with Bader charge < 9.0 e are defined as Pt2+. Bader charges between 9 and 9.4 e can be associated to partially oxidized atoms $Pt^{\delta+}$. Bader charges > 9.5 e are considered metallic species Pt^0.

For the supported Pt clusters, we started from the Pt_6 cluster whose supported geometry was fully optimized with a basin-hopping global minimization algorithm [48]. Smaller clusters were obtained by removing one Pt atom a time from this Pt_6 cluster, relaxing the atomic coordinates, and, for each Pt_n case, selecting the lowest energy configuration for further analysis. A full global minimization was not performed again.

The average binding energies (BE) of the systems involving Pt_n atoms on the ceria substrate were computed using the usual formula: $BE = - 1/ n [E(Pt_n\text{-surf}) - (E(Pt_n) + E(surf)]$. $E(Pt_n\text{-surf})$, $E(Pt_n)$ and E(surf) are the total energies of the combined Pt-ceria system, and of the isolated Pt_n atoms/cluster and surface, respectively.

Supplementary tables containing all configurations considered in present study. For each configuration the geometry of the platinum bonding environment is shown in the configuration column. Binding energies, number of reduced cerium atoms and Bader charges are shown.

Step1 S	Configuration	Binding Energy (eV)	#Ce3+	Pt Bader Charge
1/3	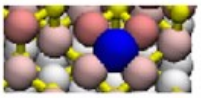	-4.9677	2	8.62
2/3	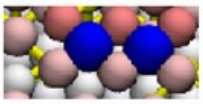	-4.5366	4	8.66 8.62
3/3	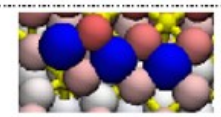	-4.1434	5	8.57 8.63 9.46
4/3	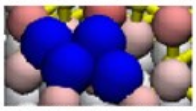	-4.9677	4	9.29 9.64 9.15 9.56
5/3		-4.4719	4	9.32 9.71 9.32 9.60 9.37
6/3	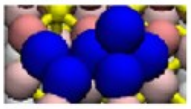	-4.6108	4	9.35 9.57 9.32 9.69 9.17 10.13

Table S1. Step I-S. For each value of Pt step coverage σ_{Pt} we report the relaxed geometry, average BE per Pt atom, number of reduced cerium atoms and Bader charges.

Step1 O_{+1}	Configuration	Binding Energy (eV)	#Ce3+	Pt Bader Charge
1/3	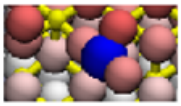	-6.7529	0	8.11
2/3	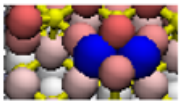	-6.2265	0	8.55 8.55
3/3	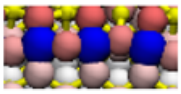	-5.9811	2	8.35 8.35 8.37
4/3	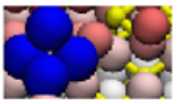	-4.7927	3	9.22 9.40 9.58 9.15
5/3	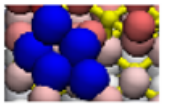	-4.6497	3	9.27 9.37 9.61 9.50 9.58
6/3	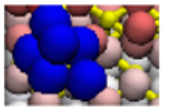	-4.6654	4	9.26 9.37 9.59 9.47 9.56 10.02

Table S2. Step I-O_{+1}. For each value of Pt step coverage σ_{Pt} we report the relaxed geometry, average BE per Pt atom, number of reduced cerium atoms and Bader charges.

Step1 $O_{+4/3}$	Configuration	Binding Energy (eV)	#Ce3+	Pt Bader Charge
2/3	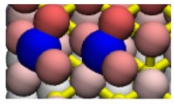	-6.5309	0	8.09 8.12
3/3	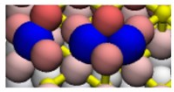	-6.2929	1	8.42 8.18 8.43
4/3	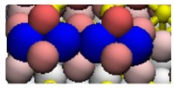	-5.8827	2	7.17 7.21 8.50 8.53
5/3	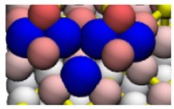	-5.2606	3	7.21 7.20 8.50 8.55 9.14

Table S3. Step I-$O_{+4/3}$. For each value of Pt step coverage σ_{Pt} we report the relaxed geometry, average BE per Pt atom, number of reduced cerium atoms and Bader charges.

.

Step1 O_{+2}	Configuration	Binding Energy (eV)	#Ce3+	Pt Bader Charge
3/3	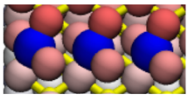	-6.5054	0	8.09 8.08 8.07
4/3	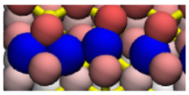	-6.0877	0	8.51 8.36 8.15 8.45
5/3	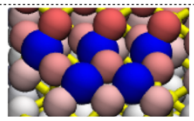	-5.8995	1	8.33 8.31 8.28 8.56 8.51

Table S4. Step I-O_{+2}. For each value of Pt step coverage σ_{Pt} we report the relaxed geometry, average BE per Pt atom, number of reduced cerium atoms and Bader charges.

Step2 Stoichiometric	Configuration	Binding Energy (eV)	#Ce3+	Pt Bader Charge
1/3	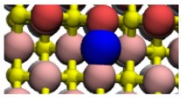	-5.1549	1	9.27
2/3	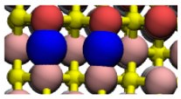	-4.9838	2	9.29 9.34
3/3	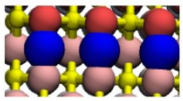	-5.0223	3	9.32 9.43 9.34
4/3	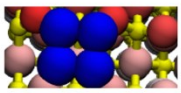	-4.3915	3	9.64 9.63 9.54 9.49
5/3	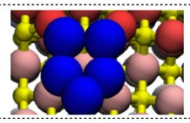	-4.3888	3	9.66 9.6 9.67 9.53 9.55
6/3	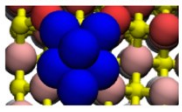	-4.6110	3	9.65 9.65 9.60 9.56 9.55 10.00

Table S5. Step II-S. For each value of Pt step coverage σ_{Pt} we report the relaxed geometry, average BE per Pt atom, number of reduced cerium atoms and Bader charges.

Step2 O_{+1}	Configuration	Binding Energy (eV)	#Ce3+	Pt Bader Charge
1/3	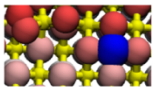	-6.5755	0	8.33
2/3	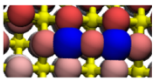	-6.6577	0	8.27 8.26
3/3	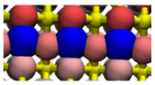	-6.1447	0	8.46 8.45 8.46
4/3	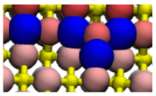	-5.6636	1	8.48 8.48 8.56 9.25
5/3	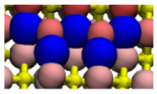	-5.2350	2	8.60 8.46 8.48 9.25 9.24
6/3	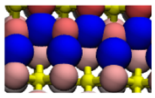	-4.7845	2	8.51 8.50 8.51 9.28 9.36 9.33

Table S6. Step II-O_{+1} ridge. For each value of Pt step coverage σ_{Pt} we report the relaxed geometry, average BE per Pt atom, number of reduced cerium atoms and Bader charges.

Step2 Clusters O_{+1}	Configuration	Binding Energy (eV)	#Ce3+	Pt Bader Charge
3/3	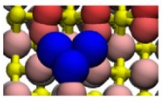	-4.2832	3	9.61 9.29 9.20
4/3	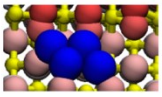	-4.2238	3	9.70 9.65 9.31
5/3	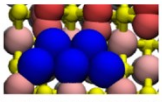	-4.1815	3	9.69 9.71 9.64 9.28 9.36
6/3	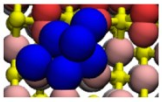	-4.1188	4	9.44 9.58 9.56 9.58 9.50 10.00

Table S7. Step I-O_{+1} clusters. For each value of Pt step coverage σ_{Pt} we report the relaxed geometry, average BE per Pt atom, number of reduced cerium atoms and Bader charges.

$O_{-1/3}$	Configuration	Binding Energy (eV)	#Ce3+	Pt Bader Charge
Step I 1/3	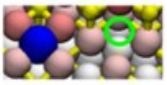	-4.9677	4	8.60
Step I 2/3	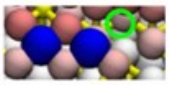	-4.0599	5	8.62 9.15
Step I 3/3	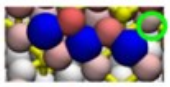	-3.8761	6	8.54 9.31 9.48
Step II 1/3	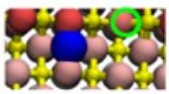	-5.1892	4	9.20

Table S8. Step I-$O_{-1/3}$ and Step II- $O_{-1/3}$. For each value of Pt step coverage σ_{Pt} we report the relaxed geometry, average BE per Pt atom, number of reduced cerium atoms and Bader charges. The position of the vacancy is marked with a square.

3.4 Bulk Hydroxylation and Effective Water Splitting by Highly Reduced Cerium Oxide: The Role of O Vacancy Coordination

In almost every catalytic reaction ceria-based catalysts are operated in water-rich environment. The interaction of water with reduced CeO_x relevant for reaction conditions in classical [165], [166] and emerging catalytic applications[167]–[169], as well as for hydrogen production via thermochemical cycling of ceria [170]–[172] is of special interest. Recent TPD studies showed that the possibility of splitting H_2O molecules on CeO_x that leads to molecular H_2 and lattice O atoms increases with increasing concentration of O vacancies on the CeO_x surface. Present work analyses the interaction of H_2O molecules with ceria films with different degree of reduction. The role of concentration of oxygen vacancies as well as their ordering onto water splitting was analyzed.

Thin CeO_2 films were grown on Cu(111) substrate via deposition of cerium in oxygen background atmosphere ($P=5\times10^{-5}$ Pa) with subsequent annealing at 523K. Afterwards, films were reduced using an approach described in [106], [108]. The resulting stoichiometry of the film was Ce_2O_3. Ceria films with intermediate stoichiometries (Ce_7O_{12} and $CeO_{1.67}$) were also prepared and the reactivity of all prepared samples towards H_2O was studied. The prepared reduced ceria films were cooled down to 100K and water molecules were adsorbed. The films were then linearly heated to 700K (2K/s) and temperature-programmed desorption (TPD) products corresponding to H_2 and H_2O were detected by a mass spectrometer. Films were analyzed by XPS and LEED after each TPD cycle. In order to achieve better surface sensitivity, the same experiments were performed at the synchrotron Elettra in Trieste, Italy and the films were characterized by using SRPES and LEED after each TPD cycle.

Analysis of XPS and TPD spectra showed high production of H_2 for cubic c-Ce_2O_3 films, and their simultaneous oxidation. After 10 TPD cycles, the stoichiometry of the films stabilized at Ce_7O_{12} value, further oxidation of the films in the conditions of TPD in UHV was slow. Preforming higher expositions of water (100L) did not change the stoichiometry of the films.

In order to explain the reactivity of the Ce_2O_3 film, experimental results were compared with DFT calculations. After analyzing of the obtained data, we related the reactivity of c-Ce_2O_3 and its water incorporation capacity to the intrinsic presence of next nearest neighbor (NNN) O vacancies and to their cooperative effect to stabilize 3-fold coordinated bulk OH species originating from the dissociation of H_2O. The discovered relation showed the dependence of the reactivity of the ceria films towards water splitting not only on the number of oxygen vacancies, but also on their positions

in the film and discovered a bulk channel for the oxidation of ceria by water. Our work suggests that controlling the concentration and the coordination of oxygen vacancies in ceria is a valuable design principle that can foster the functionality of ceria-based heterogeneous catalysts, and that can be related to the more general concept of strain engineering of oxide catalytic materials [173].

My contribution to this work was preparation of the ceria films with different concentration and coordination of the oxygen vacancies (Figure 1.6.1 b) and performing the TPD experiments. In order to enhance the reactivity of the ceria films towards water splitting, the prepared model system was eventually modified by adding Pt deposit onto CeO_x surface. The resulting system showed a property of oxidizing completely even during TPD cycles in UHV indicating a catalytic effect of Pt clusters on the oxidation of ceria by making this system attractive for further reactivity studies.

ACS Catalysis

Research Article

Cite This: ACS Catal. 2018, 8, 4354−4363

pubs.acs.org/acscatalysis

Bulk Hydroxylation and Effective Water Splitting by Highly Reduced Cerium Oxide: The Role of O Vacancy Coordination

Filip Dvořák,[†,⊥] Lucie Szabová,[‡] Viktor Johánek,[†] Matteo Farnesi Camellone,[§] Vitalii Stetsovych,[†,∥] Mykhailo Vorokhta,[†] Andrii Tovt,[†] Tomáš Skála,[†] Iva Matolínová,[†] Yoshitaka Tateyama,[‡] Josef Mysliveček,[*,†] Stefano Fabris,[*,§] and Vladimír Matolín[†]

[†]Charles University, Faculty of Mathematics and Physics, V Holešovičkách 2, 18000 Prague 8, Czech Republic

[‡]Center for Green Research on Energy and Environmental Materials (GREEN), National Institute for Materials Science (NIMS), 1-1 Namiki, Tsukuba, Ibaraki 305-0044, Japan

[§]CNR-IOM DEMOCRITOS, Istituto Officina dei Materiali, Consiglio Nazionale delle Ricerche, Via Bonomea 265, 34136 Trieste, Italy

Supporting Information

ABSTRACT: Reactions of reduced cerium oxide CeO_x with water are fundamental processes omnipresent in ceria-based catalysis. Using thin epitaxial films of ordered CeO_x, we investigate the influence of oxygen vacancy concentration and coordination on the oxidation of CeO_x by water. Upon changing the CeO_x stoichiometry from CeO_2 to Ce_2O_3, we observe a transition from a slow surface reaction to a productive H_2-evolving CeO_x oxidation with reaction yields exceeding the surface capacity and indicating the participation of bulk OH species. Both the experiments and the ab initio calculations associate the effective oxidation of highly reduced CeO_x by water to the next-nearest-neighbor oxygen vacancies present in the bixbyite c-Ce_2O_3 phase. Next-nearest-neighbor oxygen vacancies allow for the effective incorporation of water in the bulk via formation of OH^- groups. Our study illustrates that the coordination of oxygen vacancies in CeO_x represents an important parameter to be considered in understanding and improving the reactivity of ceria-based catalysts.

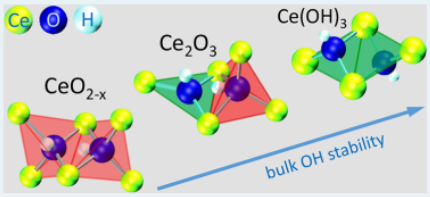

KEYWORDS: *hydrogen production, model catalyst, point defect, strain, Ce_7O_{12}, Ce_3O_5, Ce_2O_3*

INTRODUCTION

In virtually every catalytic application, ceria-based catalysts are operated in water-rich environment. Of special interest is the interaction of water with reduced CeO_x relevant for reaction conditions in classical[1,2] and emerging catalytic applications,[3−5] as well as for hydrogen production via thermochemical cycling of ceria.[6−8] Thermogravimetry experiments reveal that, ultimately, reduced CeO_x becomes fully oxidized by water releasing H_2 as a product of water splitting. The process is kinetically limited by the rate of the related surface reactions.[9] The effectiveness of oxidation of CeO_x by water has been studied by temperature-programmed desorption (TPD) in model catalytic studies.[10−13] These works suggest that the possibility of splitting H_2O molecules on CeO_x that leads to molecular H_2 and lattice O atoms increases with increasing concentration of O vacancies on the CeO_x surface. The small yields of this irreversible adsorption of H_2O are explained by static density functional theory (DFT) calculations that predict a high barrier to form molecular H_2 adsorbate from surface OH groups on stoichiometric $CeO_2(111)$ and reduced $CeO_x(111)$ surfaces,[14] as well as by ab initio molecular dynamics simulations of the water/ceria interface.[15]

Compared to broadly studied surface chemical reactions on ceria[16,17] interactions of reactants with ceria bulk constituted, until recently, a hypothetical option. In the case of interactions of H_2 or H_2O molecules with CeO_x samples, hydrogen-sensitive experimental techniques are starting to provide evidence of subsurface and bulk hydride (CeH) and hydroxyl (OH) species in CeO_x.[18−20] Here, we identify a *bulk reaction channel* for the oxidation of CeO_x by water. We investigate, by means of surface science experiments and ab initio calculations, the interaction of H_2O with thin films of CeO_x with well-defined morphology, stoichiometry, and crystallography. We observe an exceptional H_2 yield upon interaction of H_2O with bixbyite Ce_2O_3, beyond the capacity of surface reaction. Ab initio calculations reveal a key intermediate of this chemical reaction: bulk-stabilized OH groups resulting from H_2O dissociation. The stabilization effect is traced back to the geometry of OH incorporation in the next-nearest neighbor (NNN) oxygen vacancies present in the bixbyite Ce_2O_3.

The role played by the spatial coordination of the oxygen vacancies toward the stabilization of OH in bulk ceria is further stressed by model calculations predicting a substantial stabilization of OH on pairs of NNN vacancies present in

Received: December 21, 2017
Revised: March 30, 2018

DOI: 10.1021/acscatal.7b04409
ACS Catal. 2018, 8, 4354−4363

less-reduced CeO_x phases. This indicates the possibility of activation of the bulk reaction channel in real micro- and nano-structured ceria-based catalysts, since a local increase of O vacancy concentration is being documented in near-surface regions,[21] strained regions,[22] or in the vicinity of dislocations.[23] The bulk reactivity of CeO_x represents a new *ansatz* in understanding and improving the effectiveness of ceria-based catalysis and energy conversion.

RESULTS AND DISCUSSION

Surface Science Experiments. Samples of bulk-reduced CeO_x are prepared by exposing epitaxial $CeO_2(111)$ thin films on a Cu(111) substrate with metallic Ce as described previously.[22,24] This procedure yields thin films that can be considered as terminations of ordered crystallographic phases of bulk ι-Ce_7O_{12}, and bixbyite c-Ce_2O_3,[25,26] and of an ordered phase of intermediate stoichiometry, $CeO_{1.67}$.[22,24,27] Schematic view of the film surfaces and of the $CeO_2(111)$ reference are displayed in Figure 1, complete characteristics of the samples

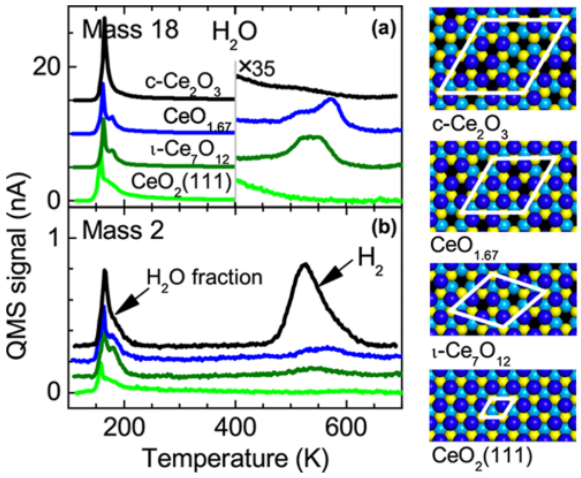

Figure 1. Results of TPD of H_2O on ordered thin films of c-Ce_2O_3, $CeO_{1.67}$, ι-Ce_7O_{12}, and a reference $CeO_2(111)$: (a) mass 18 amu and (b) mass 2 amu. H_2O exposure 2.5 L @ 100 K. Right – a schematic top view of these thin films. Black are the oxygen vacancies, and white outlines represent the surface unit cells.

are listed in Table S1. This set of samples with graded O vacancy concentration and distinctly changing O vacancy coordination allows, in principle, investigating coordination chemistry of O vacancies in ceria.[28]

We perform temperature-programmed desorption (TPD) of H_2O with a starting exposure of 2.5 L H_2O at 100 K sample temperature. The results for mass 18 amu (key fragment ion of H_2O) are shown in Figure 1a and for mass 2 amu (key fragment ion of H_2) in Figure 1b. For the $CeO_2(111)$ surface, the desorption of multilayer and monolayer molecular water is observed at approximately 150 and 170 K, similarly to previous studies.[10,12] The TPD spectra for the ι-Ce_7O_{12} and $CeO_{1.67}$ samples display additional peaks between 500 and 600 K that correspond to the recombination of dissociated water molecules (Figure 1a), and to the recombination of surface hydroxyl groups producing H_2 (Figure 1b).[10−12] Finally, the TPD spectrum for the c-Ce_2O_3 sample shows no peak corresponding to the desorption of monolayer molecular water (approximately at 170 K in all other samples, see Figure 1a), while it is dominated by an intense desorption peak at approximately 500 K corresponding to the desorption of recombined H_2 molecules (Figure 1b). The latter peak indicates a very effective oxidation of c-Ce_2O_3 by water.

In all cases, the reaction of CeO_x samples with water is causing oxidation of the samples. Repeating the TPD of H_2O on the samples from Figure 1 thus generates samples with structure changing from c-Ce_2O_3 to $CeO_{1.67}$ and ι-Ce_7O_{12} and allows investigating the reaction of H_2O with samples of an intermediate structure and stoichiometry. H_2 and H_2O yields from repeated TPD measurements including the yields from TPD in Figure 1 are presented in Figures 2a,b. The accompanying evolution of the CeO_x sample stoichiometry (index x) as obtained from X-ray photoelectron spectroscopy (XPS) of Ce 3d[29] is presented in Figure 2c. The sample with the initial structure and stoichiometry of c-Ce_2O_3 displays effective oxidation and a considerable H_2 production during the first 4 cycles of H_2O adsorption and TPD. After the fourth H_2O adsorption and TPD cycle, the oxidation of the sample slows down to minute changes of the CeO_x stoichiometry of about Δx = 0.005 per each TPD cycle. This slow-down of the reaction yield occurs when the sample stoichiometry approaches the stoichiometry of the $CeO_{1.67}$ sample.

The oxidation of the c-Ce_2O_3 sample involves the nucleation and growth of the $CeO_{1.67}$ surface phase at the expense of the c-Ce_2O_3 phase, without participation of other surface phases. The coexistence of the c-Ce_2O_3 and $CeO_{1.67}$ surface phases is observed by STM on partly oxidized c-Ce_2O_3 samples (Figure S1). It is also confirmed by the electron diffraction (LEED) reported in Figure 2e. The LEED patterns obtained during repeated H_2O adsorption/TPD experiments on the c-Ce_2O_3 sample (Figure 2e, ①–③) show the gradual conversion of the c-Ce_2O_3 (4 × 4 LEED pattern) into the $CeO_{1.67}$ phase (3 × 3 LEED pattern).[22,30] The effective oxidation and the considerable H_2 production upon interaction of CeO_x with water observed during repeated TPD on the c-Ce_2O_3 sample can thus be attributed solely to the c-Ce_2O_3 phase, while the $CeO_{1.67}$ and ι-Ce_7O_{12} phases (Figure 2e, ④, ⑤) exhibit slow oxidation kinetics.

The oxidation of CeO_x by water has been traditionally interpreted as a surface chemical reaction in which the surface OH groups recombine to form H_2 molecules and lattice O species.[10,12,14] However, the high hydrogen yields measured upon interaction of c-Ce_2O_3 with H_2O indicate that H atoms can be accumulated as bulk species in c-Ce_2O_3 during water exposure and can be subsequently released at higher temperatures. Indeed, H_2 yield as high as 8×10^{14} cm^{-2} is observed (Figure 2a, first TPD) corresponding to oxidation of 5–6 monolayers of c-Ce_2O_3 to $CeO_{1.67}$ in one TPD cycle. A monolayer (ML) represents a stack of O, Ce and O layers as in $CeO_2(111)$. In terms of O vacancy concentration the transition from c-Ce_2O_3 to $CeO_{1.67}$ represents a change from 4×10^{14} cm^{-2} to 2.6×10^{14} cm^{-2} O vacancies in 1 ML. O vacancy concentration is calculated relative to O concentration in 1 ML of CeO_2.

Interestingly, H_2 yield upon repeated H_2O adsorption/TPD cycles from c-Ce_2O_3 seems to be independent of the amount of OH on the sample surface. The amount of surface OH has been measured by highly surface-sensitive synchrotron radiation photoelectron spectroscopy (SRPES) at $h\nu$ = 640 eV. The area of the OH peak in SRPES O 1s spectrum measured at 300 K during different H_2O adsorption–

DOI: 10.1021/acscatal.7b04409
ACS Catal. 2018, 8, 4354–4363

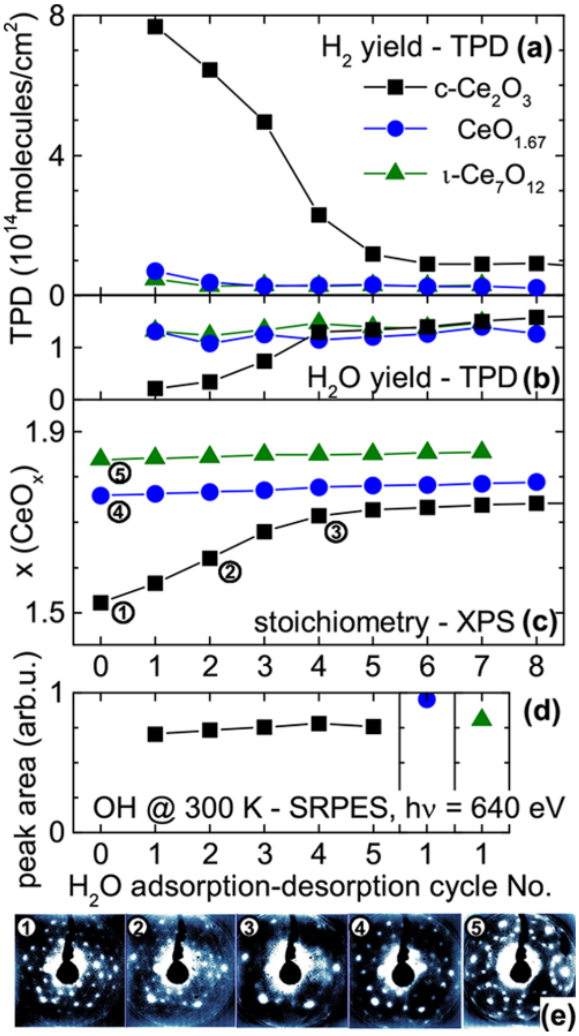

Figure 2. Repeated H_2O adsorption/TPD cycles on the samples from Figure 1. Cycle 0, before TPD; cycle 1, data from Figure 1, H_2O exposure 2.5 L @ 100 K; cycle >1, subsequent cycles, H_2O exposure 5 L @ 100 K. (a) H_2 recombination yield. (b) H_2O recombination yield. (c) Stoichiometry of the samples (index x in CeO_x) averaged over XPS information depth. (d) Area of the OH peak in O 1s SRPES spectrum of water-exposed samples measured @ 300 K. (e) LEED pattern of the samples at characteristic stages of the experiment measured at 64 eV; cf. panel (c). ① 4 × 4, ②, ③ transition from 4 × 4 to 3 × 3, ④ 3 × 3, ⑤ $\sqrt{7} \times \sqrt{7}$. Lines in panels a–d represent guides to the eyes.

desorption cycles is plotted in Figure 2d. This SRPES OH signal is almost constant for samples that differ in H_2 yield by as much as 1 order of magnitude (cf. c-Ce_2O_3 and ι-Ce_7O_{12} samples upon first TPD). This observation indicates that, prior to desorption, OH groups on highly reduced samples must be partly incorporated in the bulk where their SRPES signal is attenuated (see Appendix 1 in the Supporting Information).

Ab Initio Calculations. We perform periodic DFT calculations aiming at identifying the origin of the high H_2 yield observed for the oxidation of the c-Ce_2O_3 phase by water. Since, apparently, the kinetics of the H_2 evolution is sufficiently fast to perform TPD experiments, we focus on explaining the thermodynamic origin of the observed phenomena. To support the hypothesis that water can be accumulated in the bulk of c-Ce_2O_3 and to understand the influence of these bulk OH species on the H_2 desorption measured in the TPD experiments, we calculate the reaction free energy for two relevant reactions: (A) water incorporation into the bulk of different CeO_x systems during water exposure and (B) hydrogen desorption during the TPD experiments. To this end, we perform two sets of calculations addressing the corresponding reactions:

$$Ce_mO_n(s) + H_2O(g) \rightarrow Ce_mO_{n-1}(OH)_2(s) \quad (1A)$$

$$Ce_mO_{n-1}(OH)_2(s) \rightarrow Ce_mO_{n+1}(s) + H_2(g) \quad (1B)$$

We investigate the CeO_x systems ($x = n/m$) displayed in Figure 3 and differing in the number and arrangement of O vacancies (O_v), with $1.5 \leq x \leq 2$. The systems in Figures 3a–3c, $CeO_{1.968}$, $CeO_{1.75}$, and c-Ce_2O_3, exhibit ordered and isotropic arrangement of O vacancies with vacancy–vacancy distances of 11.1, 5.7, and 4.1 Å, respectively. The O vacancies in the fully reduced c-Ce_2O_3 phase represent the highest density arrangement of O vacancies in cerium oxides, a three-dimensional network of next nearest-neighboring (NNN) O vacancies (with respect to the O sublattice). The systems in Figures 3e–3g, $CeO_{1.937}$, $CeO_{1.75}$(NNN), and Ce_3O_5 exhibit different arrangements of NNN O vacancy pairs. $CeO_{1.937}$ represents an isolated pair of NNN O vacancies (Figure 3e). $CeO_{1.75}$(NNN) represents one-dimensional rows of NNN O vacancies along the ⟨110⟩ directions (Figure 3f). Ce_3O_5 represents two-dimensional hexagonal arrangement of NNN O vacancies (Figure 3g). All the considered CeO_x systems have been described in previous theoretical studies.[26,27] In addition, a reference calculation has been performed on a cerium hydroxide system, $Ce(OH)_3$ (Figure 3d). The equilibrated lattice parameters for the considered super cells as well as the relative distances between the O vacancies and the Ce^{3+} ions are reported in the Table S2.

In the reactions 1A and 1B, $Ce_mO_{n-1}(OH)_2$ and Ce_mO_{n+1} denote the systems resulting from incorporating one water molecule in the CeO_x bulk supercells and from the subsequent desorption of one hydrogen molecule, respectively. The ab initio thermodynamics approach[31] is used to calculate the reaction Gibbs free energies

$$\Delta G_A(T, p_{H_2O}) = E[Ce_mO_{n-1}(OH)_2] - E[Ce_mO_n] - \mu_{H_2O}(T, p_{H_2O}) \quad (2A)$$

$$\Delta G_B(T, p_{H_2}) = E[Ce_mO_{n+1}] - E[Ce_mO_{n-1}(OH)_2] + \mu_{H_2}(T, p_{H_2}) \quad (2B)$$

on the basis of the total energy E of the different systems calculated at $T = 0$ K and of the chemical potentials μ of the gas-phase molecular species involved in the reactions. The latter terms include the zero point energy (calculated) and entropic contributions (taken from experimental data in thermodynamic tables).[32] Following previous works,[33] the entropic contributions to the free energy differences from the solid systems are neglected.

The CeO_x systems considered in the calculations for the water incorporation reaction are reported in Table 1, where we describe the stoichiometry and the actual numbers of atoms present in the supercells modeling the initial and final states of the reactions. For all the reduced CeO_x systems investigated in this work, the incorporation of a water molecule at a bulk O

DOI: 10.1021/acscatal.7b04409
ACS Catal. 2018, 8, 4354–4363

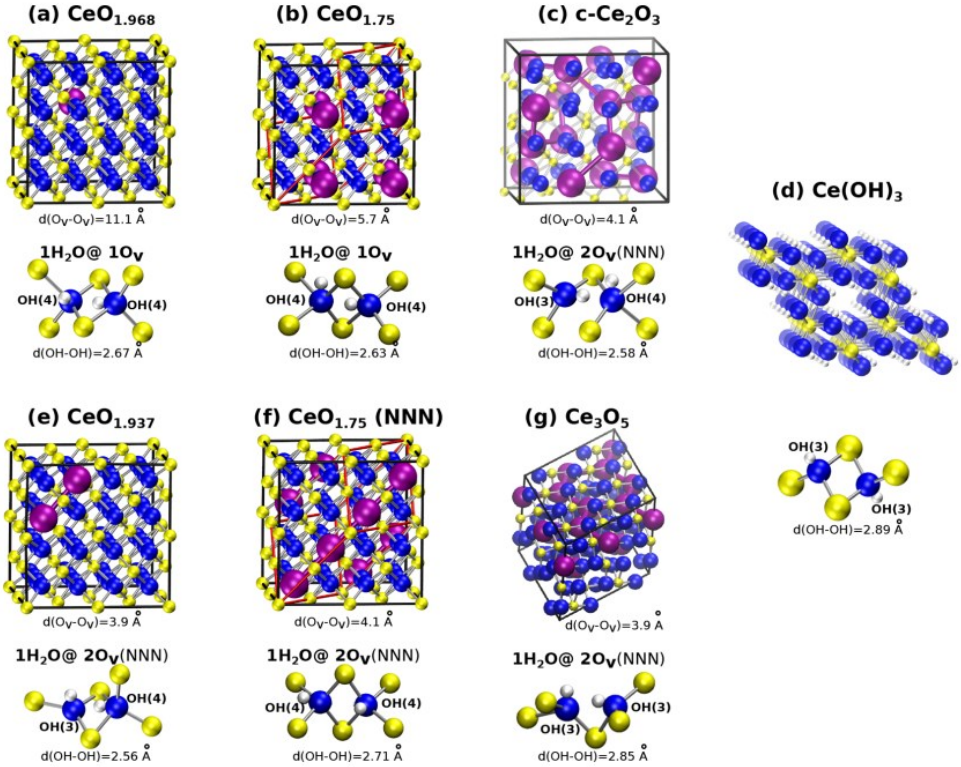

Figure 3. Supercells used in the DFT calculations to model (a−c and e−g) CeO_x systems differing in the density and arrangement of O vacancies, and (d) cerium hydroxide. O vacancies (O_v) are displayed as purple spheres. Yellow and blue spheres represent Ce and O atoms, respectively. $d(O_v\text{-}O_v)$ denotes the minimum distance between vacancies. Below each supercell we report the crystal environment around the OH groups resulting from including one water molecule in the supercell. OH(4) and OH(3) denote the 4-fold and 3-fold coordination of the OH groups with respect to the neighboring Ce ions.

Table 1. Parameters of the Supercells Used to Model Water Incorporation into Bulk CeO_x Systems and Corresponding Reaction Energy per Water Molecule Calculated on the Basis of the Total Energies at T = 0 K[a]

	$d(O_v-O_v)$ [Å]	initial	final	d(OH−OH) [Å]	ΔG_A [eV/H_2O] T = 0, P = 0 [eV]
$CeO_{1.968}$	11.06	$Ce_{32}O_{63}$	$Ce_{32}O_{62}$ $(OH)_2$	2.67	0.14
$CeO_{1.75}$	5.75	Ce_8O_{14}	Ce_8O_{13} $(OH)_2$	2.63	0.12
c-Ce_2O_3	4.14	$Ce_{32}O_{48}$	$Ce_{32}O_{47}$ $(OH)_2$	2.58	−0.31
c-Ce_2O_3	4.14	$Ce_{32}O_{48}$	32 $Ce(OH)_3$	2.89	−1.23
$CeO_{1.937}$	3.93	$Ce_{32}O_{62}$	$Ce_{32}O_{61}$ $(OH)_2$	2.56	−0.22
$CeO_{1.75}$(NNN)	4.06	Ce_8O_{14}	Ce_8O_{13} $(OH)_2$	2.71	0.23
Ce_3O_5	3.90	$Ce_{36}O_{60}$	$Ce_{36}O_{59}(OH)_2$	2.85	−1.15

[a]"Initial" and "final" indicate the composition of the periodic supercells used to model the reactant and products, respectively.

vacancy yields its spontaneous dissociation and two bulk OH^- groups, one of them filling the existing O vacancy, the other resulting from proton binding to an O atom neighboring to the O vacancy. Similarly to the case of water dissociation at a surface O vacancy[34−36] the process does not modify the number of reduced Ce^{3+} ions in CeO_x. We have also considered the possible formation of H^- species at O vacancies but these turned out not to be relevant for the water dissociation and accumulation in reduced bulk ceria. This issue will be discussed later in the context of ceria hydrogenation. We note that, while in reduced ceria the charge-compensating Ce^{3+} ions tend to occupy NNN sites with respect to O vacancy, we find that in the presence of bulk OH^- groups the Ce^{3+} ions prefer to occupy NN sites with respect to the OH^- group (see Table S2).

Water Splitting. The reaction free energy ΔG_A for the water incorporation reaction calculated at T = 0 K (reaction 1A) are reported in Table 1, while we plot in Figure 4 the T dependence of ΔG_A calculated at the experimental conditions of water adsorption (T = 100 K and $P_{H_2O} = 3 \times 10^{-6}$ Pa). These DFT simulations show that the reaction ΔG_A for the bixbyite c-Ce_2O_3 phase is slightly negative and always lower than the ΔG_A for the partially reduced $CeO_{1.968}$ and $CeO_{1.75}$ systems. For the fully reduced c-Ce_2O_3 bulk phase, the calculations predict that water incorporation is thermodynamically feasible for T < 120 K (see red line in Figure 4), while it is endothermic for the partially reduced $CeO_{1.968}$ and $CeO_{1.75}$ systems at all temperatures (black and gray lines). Temperature favors water in the

DOI: 10.1021/acscatal.7b04409
ACS Catal. 2018, 8, 4354−4363

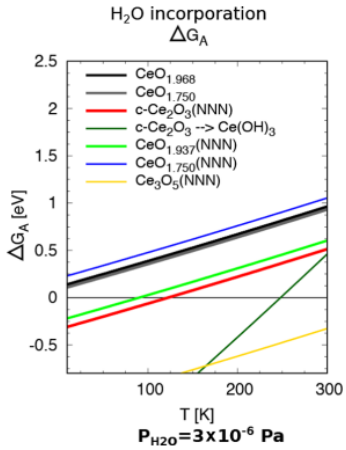

Figure 4. Calculated Gibbs free energy (ΔG_A) for water incorporation in a set of CeO_x bulk systems. The data are plotted for the partial pressure of H_2O measured during water exposure (p_{H_2O} = 3 × 10^{-6} Pa). Negative values of ΔG_A indicate favorable water incorporation in the bulk.

gas phase because of the large entropic contribution of the gas entering in the calculated thermodynamics of the reaction 2A.

Role of Coordination of O Vacancies. The simulations allow for identifying a structural explanation for the distinct properties of the c-Ce_2O_3 phase toward water bulk incorporation and dissociation, which we propose being controlled by the coordination and relative distance between O vacancies. In the considered partially reduced $CeO_{1.968}$, and $CeO_{1.75}$ systems, the shortest distance between O vacancies involves at least the fourth shell of neighboring O atoms in the O sublattice, that is, 11.1 and 5.75 Å, respectively (see Figures 3a, b). Instead, in the c-Ce_2O_3 phase, the O vacancies are next nearest neighbors (NNN) in the O sublattice, and they form a network with $d(O_v–O_v)$ = 4.1 Å (purple spheres in Figure 3c).

The dissociation of a water molecule at an isolated O vacancy or at a pair of NNN O vacancies turns out to be very different, both from the structural and thermodynamic points of view. The 2 OH^- groups resulting from water dissociation at an isolated O vacancy in $CeO_{1.968}$ are embedded in the pristine cubic fluorite structure of CeO_2 and therefore are both 4-fold coordinated by Ce ions (Figure 3a). The same is true for the more reduced $CeO_{1.75}$ system. As a result, when the O vacancies are well separated, $d(O_v–O_v)$ > 5 Å, the free energy for water dissociation is weakly dependent on the density of O_v and H_2O: $CeO_{1.968}$ and $CeO_{1.75}$ yield the same reaction free energies (ΔG_A within 0.04 eV, Table 1 and Figures 3a, b) despite differing by a factor of 2.3 in the density of O vacancies and of the incorporated OH species.

Instead, when a water molecule dissociates in the c-Ce_2O_3 phase, the network of NNN O vacancies allows for the 2 OH^- groups to depart from the 4-fold coordinated sites and to reach a more stable configuration in which one hydroxyl group is 3-fold and the other is 4-fold coordinated, respectively (Figure 3c). This is in perfect agreement with the general property of OH groups to be 3-fold coordinated in many metal hydroxides, for example, $Ni(OH)_2$, $Fe(OH)_2$, $Mn(OH)_2$, $Ga(OH)_3$, $Gd(OH)_3$. Indeed, the highest ΔG_A is achieved by forming bulk cerium hydroxide $Ce(OH)_3$ (dark green line in Figure 4), in which all the OH groups are 3-fold coordinated (Figure 3d). The network of NNN O vacancies of the c-Ce_2O_3 phase thus facilitates the formation of the preferred 3-fold coordination of the OH^- groups.

We have verified this hypothesis by studying water dissociation in structures including pairs of NNN O vacancies in the cubic lattice of CeO_2. Structures including NNN O vacancy pairs (or VV2 vacancies, in the notation of ref 26) often represent the lowest energy configurations expected in bulk-reduced CeO_x.[26] To this end we considered the $CeO_{1.937}$ (isolated pair of NNN O_v, Figure 3e), $CeO_{1.750}$(NNN) (rows of NNN O_v, Figure 3f), and Ce_3O_5 (hexagonal 2D arrangement of NNN O_v, Figure 3g). In these configurations the distance between the O vacancies are 3.9–4.1 Å, correspondingly, thus very similar to the $O_v–O_v$ distance in the c-Ce_2O_3 phase, 4.1 Å (Figure 3c). In the $CeO_{1.937}$ and Ce_3O_5 systems, the more open bulk structure due to the NNN O vacancy pairs allows one (in $CeO_{1.937}$) or two (in Ce_3O_5) of the OH groups displacing from a 4-fold to a 3-fold coordination (Figures 3e and 3g). Correspondingly, the calculated ΔG_A for these configurations (green and yellow lines in Figure 4, see also Table 1) is negative and exothermic as the ΔG_A for the c-Ce_2O_3 phase. On the other hand, the small supercell used to model water incorporation in the $CeO_{1.75}$(NNN) system leads to a high density of OH groups ordered along the <110> directions that prevents the structural relaxation of the OH groups described above. As a result, all OH groups remain 4-fold coordinated (Figure 3f) and, in agreement with our hypothesis, the water incorporation reaction is endothermic (blue line in Figure 4).

On the basis of the thermodynamics and structural analysis presented above, we therefore conclude that the bixbyite c-Ce_2O_3 phase is capable to accumulate water in its bulk at temperatures and pressures compatible with the present experimental settings. Water incorporation is mediated by the ability of the OH^- groups resulting from the accommodation of a H_2O molecule in a pair of NNN O vacancies to structurally relax and adopt the favorable 3-fold coordination with respect to the neighboring Ce atoms. Our results are general for c-Ce_2O_3 and reduced CeO_x phases, therefore, pointing to the important role of O vacancy coordination in the chemical reactivity of cerium oxides.[37] Especially, different structures of NNN O vacancy pairs, including the isolated NNN O vacancy pair, can provide the accommodation for the H_2O molecule (Figures 3e and 3g). The spatial constraints observed in calculations on certain arrangements of NNN O vacancy pairs (Figure 3f) may be alleviated in the extended CeO_x samples.

Experimental evidence for the activity of NNN O vacancy pairs in the oxidation of less reduced CeO_x phases by water is beyond the scope of the present TPD study. NNN O vacancy pairs are expected in the experimental thin film $CeO_{1.67}$ samples with O vacancy structure proposed in ref 27 (different from that used in the calculations of Ce_3O_5 in Figure 3g, cf. Figure 1, Table S1). The experimentally measured H_2 yield from TPD of water on the $CeO_{1.67}$ samples of 1 × 10^{14} cm^{-2} (at maximum) (Figure 2a) may be partly due to the accommodation of water in the NNN vacancy pairs predicted on the surface of this sample at a density 9 × 10^{13} cm^{-2} (Figure 1).[27] However, the TPD experiments do not allow to discriminate the H_2 yield of the reaction channel via NNN O vacancy pairs from the H_2 yield of the plain surface reaction. Indeed, H_2 yield observed on the $CeO_{1.67}$ samples is comparable to the H_2 yield observed on the Ce_7O_{12} samples that contain no NNN O vacancy pairs (Figure 1).

DOI: 10.1021/acscatal.7b04409
ACS Catal. 2018, 8, 4354–4363

Hydrogen Desorption. We now focus on the reaction 1B. The reaction thermodynamics for H_2 desorption from hydroxylated CeO_x bulk systems calculated at $T = 0$ is reported in Table 2, while we plot in Figure 5 the T dependency of ΔG_B

Table 2. Energy for H_2 Desorption (eV/H_2 Molecule) from the Bulk CeO_x Systems Calculated on the Basis of the Total Energies at $T = 0$ K[a]

	initial	final	ΔG_B $T = 0$, $P = 0$ [eV]
$CeO_{1.968} + H_2O$	$Ce_{32}O_{62}(OH)_2$	$Ce_{32}O_{64}$	−0.20
$CeO_{1.75} + H_2O$	$Ce_8O_{13}(OH)_2$	Ce_8O_{15}	−0.73
$c\text{-}Ce_2O_3 + H_2O$	$Ce_{32}O_{47}(OH)_2$	$Ce_{32}O_{49}$	1.43
$CeO_{1.937} + H_2O$	$Ce_{32}O_{61}(OH)_2$	$Ce_{32}O_{63}$	0.10
$CeO_{1.75}$(NNN) + H_2O	$Ce_8O_{13}(OH)_2$	Ce_8O_{15}	−0.69
$Ce_3O_5 + H_2O$	$Ce_{36}O_{59}(OH)_2$	$Ce_{36}O_{61}$	0.18

[a]"Initial" and "final" indicate the composition of the periodic supercells used to model the reactant and products, respectively.

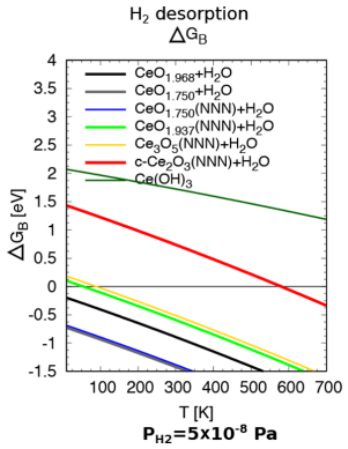

Figure 5. Calculated Gibbs free energy ΔG_B for H_2 desorption from bulk H species in CeO_x systems. The data are plotted for the partial pressure of H_2 measured during the TPD experiments ($p_{H_2} = 5 \times 10^{-8}$ Pa). Negative values of ΔG_B indicate preferential desorption of molecular H_2 in the gas phase from bulk H species.

calculated at the measured pressure during the TPD experiments (5×10^{-8} Pa H_2O, 5×10^{-8} Pa H_2). The singular properties of the $c\text{-}Ce_2O_3$ phase stand out also in this case. OH^- groups in the samples having both OH groups 4-fold coordinated [$CeO_{1.968}$, $CeO_{1.75}$, and $CeO_{1.75}$(NNN)] are thermodynamically unstable not only with respect to molecular water, as shown above, but also with respect to molecular H_2. The calculated $\Delta G_B < 0$ for $CeO_{1.75}$, $CeO_{1.968}$, and $CeO_{1.75}$(NNN) indicate preferential formation of H_2 rather than bulk OH^- groups. The stability of bulk OH^- groups in these phases is therefore ruled out. Instead, in the bulk of $c\text{-}Ce_2O_3$, OH groups are predicted to be stable with respect to H_2 for a wide T range, up to ~570 K ($\Delta G_B > 0$). This is in good agreement with the experimental TPD data that identify a desorption peak of H_2 at T ~ 520 K from the $c\text{-}Ce_2O_3$ sample (Figure 1b). Our calculations explain why this strong desorption peak is measured only on samples containing the $c\text{-}Ce_2O_3$ phase and unveil its atomistic origin. It results from dissociated water forming OH groups incorporated in the bulk of $c\text{-}Ce_2O_3$ during exposure at 100 K ($\Delta G_A < 0$, Figure 5). These bulk hydroxyls are stabilized by the favored 3-fold OH^- coordination allowed by the network of NNN O vacancies of the $c\text{-}Ce_2O_3$ phase. The calculated thermodynamics for H_2 desorption from the $Ce_3O_5 + H_2O$ and $CeO_{1.937} + H_2O$ systems, which, similarly to the $c\text{-}Ce_2O_3$ phase, show 3-fold coordinated OH^- groups (Figures 3e and 3g), confirm this hypothesis (yellow and light green lines in Figure 5), although ΔG_B turns negative at lower temperatures than for the $c\text{-}Ce_2O_3$ phase.

According to the calculations, H_2 desorption from the bulk OH^- groups in $c\text{-}Ce_2O_3$ leads to $c\text{-}Ce_2O_3$ oxidation via partial filling of its O vacancies. We relate the reactivity of $c\text{-}Ce_2O_3$ and its water incorporation capacity to the intrinsic presence of NNN O vacancies and to their cooperative effect to stabilize 3-fold coordinated bulk OH species. Since the number of O_v decreases upon formation of bulk OH^- groups from water, the partial oxidation resulting from H_2 desorption should therefore decrease the water-incorporation capacity during repeated cycles of H_2O-adsorption/H_2-desorption. This is indeed compatible with the measured data during repeated TPD experiments (see Figure 2). We remark that both the bulk OH^- accumulation and the high yield of H_2 production require sufficient hydroxyl bulk diffusion. Due to the supercell sizes, we could not address this kinetic issue. However, the experimental data suggest that bulk diffusion of OH is active in our thin-film $c\text{-}Ce_2O_3$ samples at low T and that it is not limiting the observed reactions 1A and 1B.

Hydroxylation versus Hydrogenation of the CeO_x Bulk. We point out an important difference in the reaction products resulting from water or hydrogen dissociation (i.e., hydrogenation) in the $c\text{-}Ce_2O_3$ phase that are schematically displayed in Figure 6. As reported above, water dissociation leads to bulk hydroxylation (Figure 6a) and to bulk incorporation of H in the form of OH^- species. According to this mechanism, partial oxidation of $c\text{-}Ce_2O_3$ is predicted only after H_2 desorption from the OH^- groups (Figure 6a, reaction 1B), in agreement with the XPS measured parallel to the TPD experiment (Figure S2). For the case of $c\text{-}Ce_2O_3$ hydrogenation, our DFT calculations predict that the lowest-energy product involves the incorporation of H at bulk O_v sites in the form of H^- species, together with OH^- species (Figure 6b). This H^-/OH^- pair results from the heterolytic H_2 dissociation that is typically observed upon H_2 accommodation on irreducible oxides.[28,36] The originating H^-/OH^- pair does not modify the degree of reduction of Ce_2O_3.

On the contrary, the homolytic H_2 dissociation that forms two OH^- species (Figure 6c) is leading to a configuration that is 0.73 eV higher in energy. Although these OH^- species are the same as the products of water splitting, the OH^- pair resulting from the homolytic H_2 dissociation generates an excess of 2 electrons that cannot be properly accommodated by the fully reduced Ce^{3+} sublattice, breaking the electron counting rules in cerium oxides[28,36] and increasing the energy of this product. We therefore predict that bulk $c\text{-}Ce_2O_3$ hydrogenation would entail heterolytic H_2 dissociation and H^- species, at variance of oxidized and partially reduced CeO_x ceria surfaces, where the homolytic H_2 dissociation is known to be preferred.[38−41] We also note that reversing the reaction 1B is not equivalent to the hydrogenation of $c\text{-}Ce_2O_3$ but to hydrogenation of partially oxidized Ce_2O_3.

Finally, the water and hydrogen dissociations in bulk $c\text{-}Ce_2O_3$ are different also from the thermodynamic point of view: the

DOI: 10.1021/acscatal.7b04409
ACS Catal. 2018, 8, 4354−4363

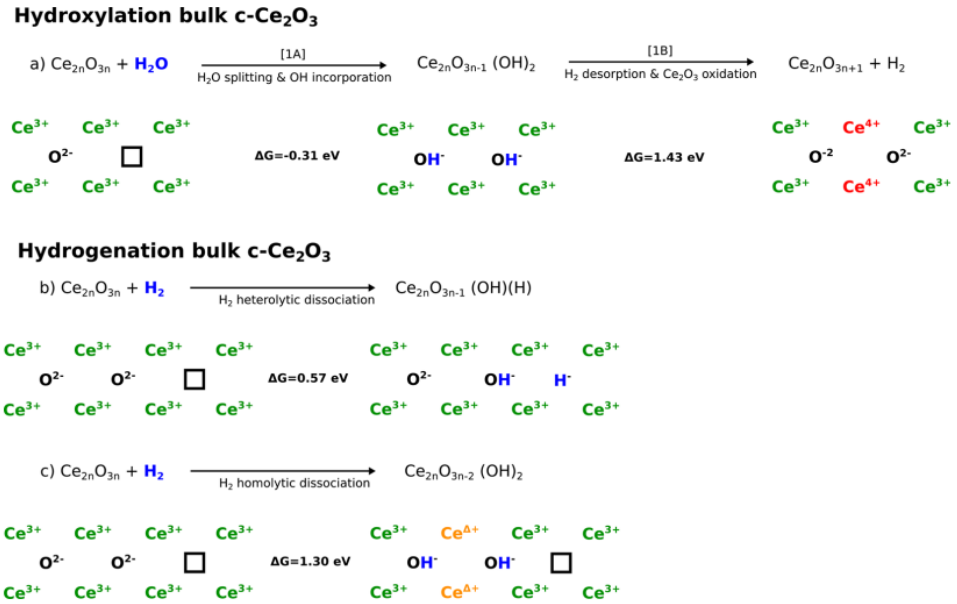

Figure 6. Hydroxylation (a) vs hydrogenation (b, c) of bulk c-Ce_2O_3. Reaction free energy for the homolytic (b) and heterolytic (c) dissociation mechanisms calculated for T = 0 K. □ denotes an oxygen vacancy.

overall calculated free energy for water dissociation is slightly negative while for hydrogenation it is positive already at T = 0 K (Figure 6b). Finite temperature will therefore make it even more endothermic because of the high entropic contribution of the H_2 reactant in the gas phase. It is however possible that the stability of H^- species at O vacancies is increased in partially reduced CeO_x, since these species are compatible with the hydride detected by neutron spectroscopy in CeO_x,[19] and with bulk H species detected on CeO_x with nuclear reaction analysis.[20]

Having identified the origins of the c-Ce_2O_3 capacity to accumulate bulk OH groups at the experimental conditions, we can use the ab initio thermodynamic approach to extrapolate the results at normal conditions of T and the partial pressures of H_2O and H_2. We plot in Figure S3 the dependency of the critical temperature T^* on the partial pressure of molecular water (Figure S3a) and hydrogen (Figure S3b). We define T^* as the temperature at which the reaction free energy turns from exothermic ($T < T^*$) to endothermic ($T > T^*$). This analysis shows that the bulk hydroxylation and effective water splitting of highly reduced CeO_x, as measured at UHV conditions, should be active at atmospheric pressure conditions, too (thin vertical black line). The effect of higher pressure is to increase the stability of the bulk OH species, which can be accumulated in the presence of water up to 200−300 K at $p = 10^5$ Pa. Moreover, atmospheric pressure would increase the onset for H_2 desorption from these bulk species to above 900 K.

CONCLUSIONS

In the present work, we have identified a bulk reaction channel for oxidation of CeO_x by water. This reaction channel is activated during the interaction of H_2O with the bixbyite c-Ce_2O_3 phase. We have proven that the stabilization of the key intermediate of this reaction, the OH^- in the bulk of c-Ce_2O_3 is mediated by a particular spatial coordination of O vacancies: a network of next-nearest-neighbor O vacancies in bixbyite c-Ce_2O_3, and, more generally, by pairs of NNN O vacancies in less-reduced CeO_x phases.

Our experiments and calculations clarify key aspects of the reaction pathways and reaction intermediates in the early experiments on H_2 generation by thermochemical cycling of CeO_x between Ce_2O_3 and CeO_2.[6] In the present thermochemical and catalytic applications the CeO_x stoichiometry is usually far from Ce_2O_3.[1−7] Still, the NNN oxygen vacancy pairs mediating the productive CeO_x oxidation by water may appear and contribute to the reactivity of real micro- and nanostructured ceria-based catalysts. Because of the general correspondence between the vacancy formation energy and strain in ceria,[23] the accumulation of O vacancies and creation of active NNN vacancy pairs may be expected via introduction of dislocations, lattice distortions, heterointerfaces, and grain boundaries or cracks in the ceria samples.[23,42−44] Our work suggests that controlling the concentration and the coordination of oxygen vacancies in ceria is a valuable design principle that can foster the functionality of ceria-based heterogeneous catalysts, and that can be related to the more general concept of strain engineering of oxide catalytic materials.[45]

METHODS

Surface Science Experiments. Experiments have been performed in the Surface Physics Laboratory (SPL) in Prague, Czech Republic, on an experimental system combining scanning tunneling microscopy (STM), laboratory X-ray photoelectron spectroscopy (XPS), low-energy electron diffraction (LEED), and temperature-programmed desorption (TPD) techniques in situ with sample preparation and cleaning. In parallel, experiments were performed at the Materials Science Beamline (MSB) at Synchrotron Elettra in Trieste, Italy where synchrotron radiation-excited photoelectron spectroscopy (SRPES) at $h\nu$ = 21−1000 eV is available together with laboratory XPS, LEED, and sample preparation and cleaning.

DOI: 10.1021/acscatal.7b04409
ACS Catal. 2018, 8, 4354−4363

Thin films of ordered CeO_x were prepared by the same experimental procedures in both facilities yielding the same sample characteristics as to the surface crystallographic structure (LEED), thickness and average sample stoichiometry (XPS, $h\nu$ = 1486.6 eV) and the effectiveness of sample oxidation by water (evolution of XPS upon repeated TPD of H_2O, Figure 2c). The sample preparation has been described in detail in refs 22 and 24. First, a continuous epitaxial thin film of CeO_2(111) is deposited on a clean Cu(111) substrate via thermal evaporation of Ce metal in O_2 background atmosphere. Substrate temperature is 523 K, O_2 pressure 5×10^{-5} Pa, growth rate 5 ML CeO_2(111) per hour. After deposition, the thin film is annealed in the same O_2 background at 800 K for 10 min. The epitaxial thin film of CeO_2(111) is further reduced by deposition of metallic Ce in ultra−high vacuum (UHV) at 300 K and subsequent annealing in UHV to 900 K. This yields thin films of CeO_x with distinct crystallographic structures due to the ordering of oxygen vacancies O_v (Figure 1). Care has been taken that samples of the ordered CeO_x exhibit single-phase LEED pattern indicating a homogeneous structure of the samples. In the case of superposition of two phases observed in LEED, the sample was further reduced by Ce and/or oxidized in a background atmosphere of 5×10^{-5} Pa O_2 to obtain a single-phase LEED.[22,24]

In the SPL laboratory, TPD experiments were performed, and the sample crystallographic structure (LEED) and stoichiometry (XPS of Ce 3d) were investigated prior to and after the TPD cycles. SPL results are presented in Figures 1, 2a−c, S1, S2a, and S4a-c. In the MSB laboratory, the samples were exposed by water at low temperature and then annealed to increasingly higher temperatures alternated with characterization of the surface crystallographic structure (LEED), sample chemical state (SRPES of O 1s, hν = 640 eV), and sample stoichiometry (XPS of Ce 3d, $h\nu$ = 1486.6 eV). MSB results are presented in Figures 2d and e, S2b, and S4d. Methods of acquisition and quantification of the relevant experimental data are detailed in Figure S4.

Ab Initio Calculations. The periodic spin-polarized DFT calculations have been performed using the PBE functional[46] and Vanderbilt's ultrasoft pseudopotetials,[47] as implemented in the plane-wave Quantum espresso code.[48] The basis set cutoffs for the representation of the electron wave function and density were 40 and 320 Ry, respectively. Integrals in the Brillouin zone were calculated on regular grids of $4 \times 4 \times 4$ k-points for the $CeO_{1.968}$, Ce_3O_5, and c-Ce_2O_3 phases, and of $6 \times 6 \times 6$ k-points for the $CeO_{1.75}$ and $CeO_{1.75}$(NNN) phases. A Hubbard U term[49] acting on the Ce-4f orbitals was added to the PBE energy functional in all calculations. In line with our previous works,[40,50−52] the value of U equal to 4.5 eV was used. The pure and defective CeO_x systems with x ranging between 1.5 and 1.968 were modeled with the periodic supercells displayed in the Figure 3. These were simple cubic for the bulk $CeO_{1.968}$ (95 atoms), $CeO_{1.937}$ (94 atoms), fcc cubic for the $CeO_{1.75}$ (22 atoms) system, and hexagonal for the Ce_3O_5 (96 atoms) and $Ce(OH)_3$ (14 atoms). In all cases, the calculations were performed at the equilibrium lattice parameters of the corresponding systems, which are reported in the Table S2. The relative arrangement of O_v and Ce^{3+} ions in each supercell used in the calculations is reported in Table S2 as well as the energy difference between the lowest-energy configuration of O_v and Ce^{3+} ions (compare refs 26 and 53−56) and other metastable ones. The free energies of the reactions have been calculated with the ab initio thermodynamics approach.[31]

■ ASSOCIATED CONTENT

Supporting Information

The Supporting Information is available free of charge on the ACS Publications website at DOI: 10.1021/acscatal.7b04409.

Parameters of the samples, STM image of the coexistence of the c-Ce_2O_3 and $CeO_{1.67}$ phases, equilibrium lattice parameter and relative distance between Ce^{3+} ions and O vacancies or OH groups, TPD of H_2O from c-Ce_2O_3, evolution of the stoichiometry of the Ce_2O_3 sample, dependency of T^* on the partial pressure of H_2O and H_2 for the water dissociation and H_2 evolution reactions, examples of experimental data and evaluation of experimental values, and attenuation of bulk OH signal in SRPES. (PDF)

■ AUTHOR INFORMATION

Corresponding Authors

*E-mail: josef.myslivecek@mff.cuni.cz.
*E-mail: fabris@iom.cnr.it.

ORCID

Lucie Szabová: 0000-0003-1901-1490
Yoshitaka Tateyama: 0000-0002-5532-6134
Josef Mysliveček: 0000-0003-2305-2711
Stefano Fabris: 0000-0003-2562-8788

Present Addresses

[⊥]University of Pardubice, Faculty of Chemical Technology, Nám. Čs. Legií 565, 53002 Pardubice, Czech Republic.
[∥]Institute of Physics, Academy of Sciences of the Czech Republic, Na Slovance 2, 18221 Prague 8, Czech Republic.

Notes

The authors declare no competing financial interest.

■ ACKNOWLEDGMENTS

We would like to thank Dimitri Balakin for the assistance with preparing the experimental samples. This work was supported by the Czech Science Foundation, Project 15-06759S and 13-10396S, by the Ministry of Education of the Czech Republic, Project LM 2015057, by the European Union via the FP7-NMP-2012 project chipCAT under contract number 310191, and the EU FP7 COST action CM1104. The authors acknowledge the CERIC−ERIC Consortium for access to experimental facilities and financial support. S.F. acknowledges the support provided by the Humboldt Foundation through a Friedrich Wilhelm Bessel Research Award. L.S. and Y.T. thank the support by MEXT KAKENHI Grant Number JP15H05701. This research used computational resources of NIMS and the HPCI systems through the HPCI System Research Projects (Project IDs: hp170174, hp170169).

■ REFERENCES

(1) Twigg, M. V. Progress and Future Challenges in Controlling Automotive Exhaust Gas Emissions. *Appl. Catal., B* **2007**, *70*, 2−15.
(2) Boaro, M.; de Leitenburg, C.; Dolcetti, G.; Trovarelli, A. The Dynamics of Oxygen Storage in Ceria−Zirconia Model Catalysts Measured by CO Oxidation under Stationary and Cycling Feedstream Compositions. *J. Catal.* **2000**, *193*, 338−347.
(3) Hornés, A.; Hungría, A. B.; Bera, P.; Cámara, A. L.; Fernández-García, M.; Martínez-Arias, A.; Barrio, L.; Estrella, M.; Zhou, G.; Fonseca, J. J.; Hanson, J. C.; Rodriguez, J. A. Inverse CeO_2/CuO Catalyst As an Alternative to Classical Direct Configurations for Preferential Oxidation of CO in Hydrogen-Rich Stream. *J. Am. Chem. Soc.* **2010**, *132*, 34−35.

DOI: 10.1021/acscatal.7b04409
ACS Catal. 2018, 8, 4354−4363

(4) Zhou, G.; Barrio, L.; Agnoli, S.; Senanayake, S. D.; Evans, J.; Kubacka, A.; Estrella, M.; Hanson, J. C.; Martínez-Arias, A.; Fernández-García, M.; Rodriguez, J. A. High Activity of $Ce_{1-x}Ni_xO_{2-y}$ for H(2) Production through Ethanol Steam Reforming: Tuning Catalytic Performance through Metal-Oxide Interactions. *Angew. Chem., Int. Ed.* **2010**, *49*, 9680−9684.
(5) Kubacka, A.; Si, R.; Michorczyk, P.; Martínez-Arias, A.; Xu, W.; Hanson, J. C.; Rodriguez, J. A.; Fernández-García, M. Tungsten as an Interface Agent Leading to Highly Active and Stable Copper−ceria Water Gas Shift Catalyst. *Appl. Catal., B* **2013**, *132*−*133*, 423−432.
(6) Abanades, S.; Flamant, G. Thermochemical Hydrogen Production from a Two-Step Solar-Driven Water-Splitting Cycle Based on Cerium Oxides. *Sol. Energy* **2006**, *80*, 1611−1623.
(7) Chueh, W. C.; Falter, C.; Abbott, M.; Scipio, D.; Furler, P.; Haile, S. M.; Steinfeld, A. High-Flux Solar-Driven Thermochemical Dissociation of CO_2 and H_2O Using Nonstoichiometric Ceria. *Science* **2010**, *330*, 1797−1801.
(8) Thomas, J. M. Heterogeneous Catalysis and the Challenges of Powering the Planet, Securing Chemicals for Civilised Life, and Clean Efficient Utilization of Renewable Feedstocks. *ChemSusChem* **2014**, *7*, 1801−1832.
(9) Chueh, W. C.; Haile, S. M. A Thermochemical Study of Ceria: Exploiting an Old Material for New Modes of Energy Conversion and CO_2 Mitigation. *Philos. Trans. R. Soc., A* **2010**, *368*, 3269−3294.
(10) Kundakovic, L.; Mullins, D.; Overbury, S. Adsorption and Reaction of H_2O and CO on Oxidized and Reduced Rh/CeO_x(111) Surfaces. *Surf. Sci.* **2000**, *457*, 51−62.
(11) Chen, B.; Ma, Y.; Ding, L.; Xu, L.; Wu, Z.; Yuan, Q.; Huang, W. Reactivity of Hydroxyls and Water on a CeO_2(111) Thin Film Surface: The Role of Oxygen Vacancy. *J. Phys. Chem. C* **2013**, *117*, 5800−5810.
(12) Mullins, D. R.; Albrecht, P. M.; Chen, T.-L.; Calaza, F. C.; Biegalski, M. D.; Christen, H. M.; Overbury, S. H. Water Dissociation on CeO_2(100) and CeO_2(111) Thin Films. *J. Phys. Chem. C* **2012**, *116*, 19419−19428.
(13) Gao, Y.; Li, R.; Chen, S.; Luo, L.; Cao, T.; Huang, W. Morphology-Dependent Interplay of Reduction Behaviors, Oxygen Vacancies and Hydroxyl Reactivity of CeO_2 Nanocrystals. *Phys. Chem. Chem. Phys.* **2015**, *17*, 31862−31871.
(14) Hansen, H. A.; Wolverton, C. Kinetics and Thermodynamics of H_2O Dissociation on Reduced CeO_2(111). *J. Phys. Chem. C* **2014**, *118*, 27402−27414.
(15) Farnesi Camellone, M.; Negreiros Ribeiro, F.; Szabová, L.; Tateyama, Y.; Fabris, S. Catalytic Proton Dynamics at the Water/Solid Interface of Ceria-Supported Pt Clusters. *J. Am. Chem. Soc.* **2016**, *138*, 11560−11567.
(16) Mullins, D. R. The Surface Chemistry of Cerium Oxide. *Surf. Sci. Rep.* **2015**, *70*, 42−85.
(17) Montini, T.; Melchionna, M.; Monai, M.; Fornasiero, P. Fundamentals and Catalytic Applications of CeO_2-Based Materials. *Chem. Rev.* **2016**, *116*, 5987−6041.
(18) Gill, L.; Beste, A.; Chen, B.; Li, M.; Mann, A. K. P.; Overbury, S. H.; Hagaman, E. W. Fast MAS 1 H NMR Study of Water Adsorption and Dissociation on the (100) Surface of Ceria Nanocubes: A Fully Hydroxylated, Hydrophobic Ceria Surface. *J. Phys. Chem. C* **2017**, *121*, 7450−7465.
(19) Wu, Z.; Cheng, Y.; Tao, F.; Daemen, L.; Foo, G. S.; Nguyen, L.; Zhang, X.; Beste, A.; Ramirez-Cuesta, A. J. Direct Neutron Spectroscopy Observation of Cerium Hydride Species on a Cerium Oxide Catalyst. *J. Am. Chem. Soc.* **2017**, *139*, 9721−9727.
(20) Werner, K.; Weng, X.; Calaza, F.; Sterrer, M.; Kropp, T.; Paier, J.; Sauer, J.; Wilde, M.; Fukutani, K.; Shaikhutdinov, S.; Freund, H.-J. Toward an Understanding of Selective Alkyne Hydrogenation on Ceria: On the Impact of O Vacancies on H_2 Interaction with CeO_2(111). *J. Am. Chem. Soc.* **2017**, *139*, 17608−17616.
(21) Chueh, W. C.; McDaniel, A. H.; Grass, M. E.; Hao, Y.; Jabeen, N.; Liu, Z.; Haile, S. M.; McCarty, K. F.; Bluhm, H.; El Gabaly, F. Highly Enhanced Concentration and Stability of Reactive Ce^{3+} on Doped CeO_2 Surface Revealed in Operando. *Chem. Mater.* **2012**, *24*, 1876−1882.
(22) Duchoň, T.; Dvořák, F.; Aulická, M.; Stetsovych, V.; Vorokhta, M.; Mazur, D.; Veltruská, K.; Skála, T.; Mysliveček, J.; Matolínová, I.; Matolín, V. Ordered Phases of Reduced Ceria As Epitaxial Films on Cu(111). *J. Phys. Chem. C* **2014**, *118*, 357−365.
(23) Sun, L.; Marrocchelli, D.; Yildiz, B. Edge Dislocation Slows down Oxide Ion Diffusion in Doped CeO_2 by Segregation of Charged Defects. *Nat. Commun.* **2015**, *6*, 6294.
(24) Stetsovych, V.; Pagliuca, F.; Dvořák, F.; Duchoň, T.; Vorokhta, M.; Aulická, M.; Lachnitt, J.; Schernich, S.; Matolínová, I.; Veltruská, K.; Skála, T.; Mazur, D.; Mysliveček, J.; Libuda, J.; Matolín, V. Epitaxial Cubic Ce_2O_3 Films via Ce−CeO_2 Interfacial Reaction. *J. Phys. Chem. Lett.* **2013**, *4*, 866−871.
(25) Kümmerle, E. A.; Heger, G. The Structures of C−$Ce_2O_{3+\delta}$, Ce_7O_{12}, and $Ce_{11}O_{20}$. *J. Solid State Chem.* **1999**, *147*, 485−500.
(26) Murgida, G. E.; Ferrari, V.; Ganduglia-Pirovano, M. V.; Llois, A. M. Ordering of Oxygen Vacancies and Excess Charge Localization in Bulk Ceria: A DFT+U Study. *Phys. Rev. B* **2014**, *90*, 115120.
(27) Olbrich, R.; Murgida, G. E.; Ferrari, V.; Barth, C.; Llois, A. M.; Reichling, M.; Ganduglia-Pirovano, M. V. Surface Stabilizes Ceria in Unexpected Stoichiometry. *J. Phys. Chem. C* **2017**, *121*, 6844−6851.
(28) Barteau, M. A. Organic Reactions at Well-Defined Oxide Surfaces. *Chem. Rev.* **1996**, *96*, 1413−1430.
(29) Skála, T.; Šutara, F.; Prince, K. C.; Matolín, V. Cerium Oxide Stoichiometry Alteration via Sn Deposition: Influence of Temperature. *J. Electron Spectrosc. Relat. Phenom.* **2009**, *169*, 20−25.
(30) Höcker, J.; Menteş, T. O.; Sala, A.; Locatelli, A.; Schmidt, T.; Falta, J.; Senanayake, S. D.; Flege, J. I. Unraveling the Dynamic Nanoscale Reducibility (Ce^{4+} → Ce^{3+}) of CeO_x-Ru in Hydrogen Activation. *Adv. Mater. Interfaces* **2015**, *2*, 1500314.
(31) Reuter, K.; Scheffler, M. Composition, Structure, and Stability of RuO_2(110) as a Function of Oxygen Pressure. *Phys. Rev. B: Condens. Matter Mater. Phys.* **2001**, *65*, 35406.
(32) Stull, D. R.; Prophet, H. *JANAF Thermochemical Tables*, 2nd ed.; U.S. National Bureau of Standards: Washington, DC, 1971.
(33) Reuter, K.; Scheffler, M. Composition and Structure of the RuO_2(110) Surface in an O_2 and CO Environment: Implications for the Catalytic Formation of CO_2. *Phys. Rev. B* **2003**, *68*, 45407.
(34) Fernández-Torre, D.; Kośmider, K.; Carrasco, J.; Ganduglia-Pirovano, M. V.; Pérez, R. Insight into the Adsorption of Water on the Clean CeO_2 (111) Surface with van Der Waals and Hybrid Density Functionals. *J. Phys. Chem. C* **2012**, *116*, 13584−13593.
(35) Szabová, L.; Tateyama, Y.; Matolín, V.; Fabris, S. Water Adsorption and Dissociation at Metal-Supported Ceria Thin Films: Thickness and Interface-Proximity Effects Studied with DFT+U Calculations. *J. Phys. Chem. C* **2015**, *119* (5), 2537−2544.
(36) Calatayud, M.; Markovits, A.; Menetrey, M.; Mguig, B.; Minot, C. Adsorption on Perfect and Reduced Surfaces of Metal Oxides. *Catal. Today* **2003**, *85*, 125−143.
(37) Esch, F.; Fabris, S.; Zhou, L.; Montini, T.; Africh, C.; Fornasiero, P.; Comelli, G.; Rosei, R. Electron Localization Determines Defect Formation on Ceria Substrates. *Science* **2005**, *309*, 752−755.
(38) Carrasco, J.; Vilé, G.; Fernández-Torre, D.; Pérez, R.; Pérez-Ramírez, J.; Ganduglia-Pirovano, M. V. Molecular-Level Understanding of CeO_2 as a Catalyst for Partial Alkyne Hydrogenation. *J. Phys. Chem. C* **2014**, *118*, 5352−5360.
(39) García-Melchor, M.; López, N. Homolytic Products from Heterolytic Paths in H_2 Dissociation on Metal Oxides: The Example of CeO_2. *J. Phys. Chem. C* **2014**, *118*, 10921−10926.
(40) Negreiros, F. R.; Camellone, M. F.; Fabris, S. Effects of Thermal Fluctuations on the Hydroxylation and Reduction of Ceria Surfaces by Molecular H_2. *J. Phys. Chem. C* **2015**, *119*, 21567−21573.
(41) Fernández-Torre, D.; Carrasco, J.; Ganduglia-Pirovano, M. V.; Pérez, R. Hydrogen Activation, Diffusion, and Clustering on CeO_2(111): A DFT+U Study. *J. Chem. Phys.* **2014**, *141*, 014703.
(42) Ackermann, S.; Sauvin, L.; Castiglioni, R.; Rupp, J. L. M.; Scheffe, J. R.; Steinfeld, A. Kinetics of CO_2 Reduction over Nonstoichiometric Ceria. *J. Phys. Chem. C* **2015**, *119*, 16452−16461.
(43) Scheffe, J.; Jacot, R.; Patzke, G.; Steinfeld, A. Synthesis, Characterization and Thermochemical Redox Performance of Hf, Zr

and Sc Doped Ceria for Splitting CO_2. *J. Phys. Chem. C* **2013**, *117*, 24104−24114.
(44) Szabová, L.; Stetsovych, O.; Dvořák, F.; Farnesi Camellone, M.; Fabris, S.; Mysliveček, J.; Matolín, V. Distinct Physicochemical Properties of the First Ceria Monolayer on Cu(111). *J. Phys. Chem. C* **2012**, *116*, 6677−6684.
(45) Yildiz, B. "Stretching" the Energy Landscape of oxides—Effects on Electrocatalysis and Diffusion. *MRS Bull.* **2014**, *39*, 147−156.
(46) Perdew, J. P. J.; Burke, K.; Ernzerhof, M. Generalized Gradient Approximation Made Simple. *Phys. Rev. Lett.* **1996**, *77*, 3865−3868.
(47) Vanderbilt, D. Soft Self-Consistent Pseudopotentials in a Generalized Eigenvalue Formalism. *Phys. Rev. B* **1990**, *41*, 7892−7895.
(48) Giannozzi, P.; Baroni, S.; Bonini, N.; Calandra, M.; Car, R.; Cavazzoni, C.; Ceresoli, D.; Chiarotti, G. L.; Cococcioni, M.; Dabo, I.; Dal Corso, A.; de Gironcoli, S.; Fabris, S.; Fratesi, G.; Gebauer, R.; Gerstmann, U.; Gougoussis, C.; Kokalj, A.; Lazzeri, M.; Martin-Samos, L.; Marzari, N.; Mauri, F.; Mazzarello, R.; Paolini, S.; Pasquarello, A.; Paulatto, L.; Sbraccia, C.; Scandolo, S.; Sclauzero, G.; Seitsonen, A. P.; Smogunov, A.; Umari, P.; Wentzcovitch, R. M. QUANTUM ESPRESSO: A Modular and Open-Source Software Project for Quantum Simulations of Materials. *J. Phys.: Condens. Matter* **2009**, *21*, 395502.
(49) Cococcioni, M.; de Gironcoli, S. Linear Response Approach to the Calculation of the Effective Interaction Parameters in the LDA + U Method. *Phys. Rev. B* **2005**, *71*, 35105.
(50) Fabris, S.; Vicario, G.; Balducci, G.; De Gironcoli, S.; Baroni, S. Electronic and Atomistic Structures of Clean and Reduced Ceria Surfaces. *J. Phys. Chem. B* **2005**, *109*, 22860−22867.
(51) Ghosh, P.; Farnesi Camellone, M.; Fabris, S. Fluxionality of Au Clusters at Ceria Surfaces during CO Oxidation: Relationships among Reactivity, Size, Cohesion, and Surface Defects from DFT Simulations. *J. Phys. Chem. Lett.* **2013**, *4*, 2256−2263.
(52) Dvořák, F.; Farnesi Camellone, M.; Tovt, A.; Tran, N.; Negreiros, F. R.; Vorokhta, M.; Skála, T.; Matolínová, I.; Mysliveček, J.; Matolín, V.; Fabris, S. Creating Single-Atom Pt-Ceria Catalysts by Surface Step Decoration. *Nat. Commun.* **2016**, *7*, 10801.
(53) Wang, B.; Xi, X.; Cormack, A. N. Chemical Strain and Point Defect Configurations in Reduced Ceria. *Chem. Mater.* **2014**, *26*, 3687−3692.
(54) Han, X.; Amrane, N.; Zhang, Z.; Benkraouda, M. Oxygen Vacancy Ordering and Electron Localization in CeO_2: Hybrid Functional Study. *J. Phys. Chem. C* **2016**, *120*, 13325−13331.
(55) Ganduglia-Pirovano, M. V.; Murgida, G. E.; Ferrari, V.; Llois, A. M. Comment on "Oxygen Vacancy Ordering and Electron Localization in CeO_2: Hybrid Functional Study". *J. Phys. Chem. C* **2017**, *121*, 21080−21083.
(56) Han, X.; Amrane, N.; Zhang, Z.; Benkraouda, M. Reply to "Comment on 'Oxygen Vacancy Ordering and Electron Localization in CeO_2: Hybrid Functional Study'". *J. Phys. Chem. C* **2017**, *121*, 21084−21086.

DOI: 10.1021/acscatal.7b04409
ACS Catal. 2018, 8, 4354−4363

3.5 Ordered phases of reduced ceria as inverse model catalysts

Considering the results obtained for continuous ceria films prepared by using methods of precise control over ceria morphology and stoichiometry developed in our group, these methods were applied for inverse model CeO_x/Cu(111) systems. While under "normal" model catalysts we understand metal particles on oxide surfaces, inverse model catalysts represent oxide particles grown on metal surfaces.

Inverse model catalysts have attracted much attention during the last decade due to their increased number of active sites at the oxide-metal interface [174]–[177]. At decreased thicknesses of an oxide film, the influence of the substrate becomes crucial leading to the emergence of new phenomena which change structural, electronic and chemical properties of the oxide film [176], [178]. Analysis of such influence is, therefore, important for the developing of catalysts with controllable morphology, stoichiometry and concentration of surface defects. The study of the interaction between cerium oxide layer and metal support led to the development of catalysts with enhanced activity towards water-gas shift reaction [175], [179].

For the presented preparation of inverse model catalysts, ultrathin ceria films (1-2ML) were grown on Cu(111) substrate via deposition of metallic cerium in UHV and its subsequent oxidation in oxygen background atmosphere at room temperature. STM, XPS and LEED measurements revealed the resulting film to be discontinuous, well ordered and partially reduced (estimated stoichiometry was $CeO_{1.85}$). Further oxidation of the film at room temperature maintained its stoichiometry at $CeO_{1.85}$ to $CeO_{1.9}$. Stoichiometric CeO_2 film was obtained only via oxidation at high temperature (700K) which resulted, parallel to oxidation of $CeO_{1.85}$ to CeO_2, also in oxidation of the copper substrate. These experiments reveal the existence of an activation barrier for oxidation of ultrathin ceria film which can be attributed to oxide-support interaction.

Control over stoichiometry of the prepared films was achieved using the interaction of the films with metallic cerium, as described in [106], [108]. Depending on the amount of added cerium, films with different stoichiometry were obtained. LEED measurements as well as detailed STM images revealed (1×1), (√7×√7)R19°, (3×3) and (4×4) surface reconstructions. Analysis of the stoichiometry of the films corresponding to each reconstruction revealed their higher degree of reduction compared to the continuous ceria films [108] and better correspondence with the stoichiometry expected for the corresponding phases of bulk reduced ceria, CeO_2, i-Ce_7O_{12}, Ce_3O_5, and c-Ce_2O_3 (Table 3.5.1). Such correspondence together with small film thickness allows us to make an assumption of homogeneous reduction of the films.

Quantitative analysis of the LEED diffraction patterns allowed estimation of ceria lattice parameter for different stoichiometry of the films. In bulk reduced ceria Ce^{3+} ions feature an increased atomic radius compared to the Ce^{4+} ions resulting in a linear dependence of the bulk lattice parameter on oxygen content in the sample and on the corresponding sample stoichiometry. Experimental lattice parameter obtained in the present inverse catalyst samples shows a linear dependence of the bulk lattice parameter on the sample stoichiometry, too, but with a distinctly different slope. In agreement with the previous observations 2-3 ML thick CeO_2(111) layers on Cu(111) exhibit 2% lattice contraction compared to bulk CeO_2. However, the dependence of the lattice parameter on the sample stoichiometry in inverse model catalysts is stronger than in the bulk resulting in 1% lattice expansion of 2-3 ML thick c-Ce_2O_3(111) layer on Cu(111) compared to c-Ce_2O_3 bulk (Figure 5 of the manuscript).

The prepared inverse reduced ceria films oxidized from background UHV atmosphere during several hours of measurement indicating a high reactivity of the prepared inverse model catalysts. Future studies of the prepared inverse CeO_{1-x}/Cu(111) catalytic system may include characterization of surface catalytic reactions influenced by the combination of ordering of surface oxygen vacancies and strong oxide-support interaction.

Surface reconstruction	Expected stoichiometry CeOx, x=	Estimated stoichiometry CeOx, x=
1×1 high temperature oxidation	2	1.99
1×1 low temperature oxidation	2	1.90
(√7×√7)R19°	1.7	1.69
3×3	1.67	1.60
4×4	1.5	1.54

Table 3.5.1. Estimated and expected stoichiometry of ceria thin films with different types of reconstructions of surface oxygen vacancies.

My contribution to this work was preparation and characterization of the prepared inverse model system, analysis of the acquired STM, LEED and XPS data and writing a manuscript.

Ordered phases of reduced ceria as inverse model catalysts

Andrii Tovt, Vitalii Stetsovych[a], Filip Dvořák[b], Viktor Johánek, and Josef Mysliveček*
Faculty of Mathematics and Physics, Department of Surface and Plasma Science, Charles University in Prague, V Holesovičkách 2, 18000 Praha 8, Czech Republic

Abstract

Inverse model catalysts represent valuable systems for studying metal-oxide interactions and finite size effects in heterogeneous catalysis. To maximize the potential of model catalytic studies, high level of control over model catalyst properties is desirable. Here we introduce experimental approaches for obtaining inverse ceria/copper model catalysts of well-defined crystallographic phases CeO_2, ι-Ce_7O_{12}, $CeO_{1.67}$, and c-Ce_2O_3 supported on Cu(111). The presented cerium oxide thin films are ultrathin (2 monolayers), discontinuous, and feature highly defined stoichiometry and crystallographic structure with characteristic (1×1), (√7×√7)R19°, (3×3), or (4×4) electron diffraction patterns. Compared to thicker films and bulk ceria, the prepared ultrathin cerium oxides exhibit a distinctly different dependence of the lattice constant on the stoichiometry, and show activation barrier preventing their complete oxidation. These phenomena illustrate that metal-oxide interactions and finite size effects strongly influence the behavior of the presented inverse model catalysts indicating their prospective use in disentangling complex functionalities of ceria/copper catalytic systems.

Introduction

Inverse oxide-metal catalysts have attracted attention in the last decade due to new catalytic functionalities obtained as a result of replacing the classical catalyst morphology – metal nanoparticles on an oxide support [1–3] with "inverse" morphology – oxide nanoislands on a metal support [4–6]. This changes qualitatively the nature of the active sites exposed at the oxide-metal interface, and the related spillover processes, potentially resulting in a significant enhancement of activity, e.g. in the water-gas shift reaction [4–7]. Oxide nanoparticles in the inverse oxide-metal catalysts often take the form of ultrathin oxide films with thickness of units of monolayers (ML). With decreasing thickness of the oxide film, the influence of the metal substrate becomes important, determining the structural, electronic and chemical properties of the oxide via charge transfer and epitaxial strain imposed on the oxide [6,8]. The "inverse" geometry thus provides new degrees of freedom for controlling the physicochemical properties of metal-oxide systems, both in the basic research and in potential applications.

Ceria is known for its excellent ability to store and release oxygen and, therefore, finds its application in various fields of modern technology. It proves to be effective in gas sensors [9], fuel cells [10], and three-way automotive catalysis [11]. Epitaxial films of ceria are often prepared as supports for model catalysts. Continuous CeO_2(111) thin films were prepared on different metal substrates {Cu(111) [12–14], Ru(0001) [15], Au(111) [4], Pt(111) [16]} and thoroughly investigated by experimental surface science methods. Discontinuous CeO_2(111) ultrathin films prepared as inverse model catalysts on Au(111) and Cu(111) substrates exhibited a considerable activity in the water-gas shift reaction [7,17]. Besides the active sites at the metal-oxide interface [7], ultrathin CeO_2(111) films reveal their different structural, chemical and electronic behavior compared to the thicker or bulk CeO_2(111). The oxide-support interaction results in partial reduction of the ultrathin ceria, and, in 1 ML thick films, to the emergence of (2×2) reconstruction of oxygen vacancies [18]. Lattice mismatch between the Cu(111) single crystal and the CeO_{2-x}(111) layer stimulates the formation of Moiré superstructures [19,20].

Broadly investigated active sites on the ceria surfaces are the oxygen vacancies [21,22]. In model thin film CeO_2(111) catalysts, the concentration of the oxygen vacancies can be changed by various reducing strategies [16,23–25]. Oxygen vacancies in ceria tend to organize in the bulk as well as on the surface resulting in several distinct crystallographic phases of reduced ceria observed experimentally on bulk and thin film samples [26–28]. We have developed a robust experimental procedure for preparing continuous thin films with nominal CeO_2, Ce_7O_{12}, Ce_3O_5 and Ce_2O_3 stoichiometry [13,28–30] exhibiting characteristic (1×1), (√7×√7)R19°, (3×3), and (4×4) surface reconstructions easily identified by low-energy electron diffraction (LEED). Well-defined concentration and spatial coordination of these ordered phases of reduced ceria allow

performing advanced model catalytic studies including studies of the spatial coordination of O vacancies on the chemical reactivity of ceria [31,32].

In the present work, we prepare ordered phases of reduced ceria as inverse model catalysts on a Cu(111) surface. We observe effects of the finite size and of the proximity of the copper substrate on the physicochemical properties of such inverse model catalysts and introduce the newly developed model catalysts as prospective systems for advanced model studies in heterogeneous catalysis.

Experimental

The experiments were performed on the ultra-high vacuum (UHV) apparatus operating at base pressure of 10^{-8} Pa and combining experimental methods of Scanning Tunneling Microscopy (STM), X-ray Photoelectron Spectroscopy (XPS), and Low-energy Electron Diffraction (LEED). Cu(111) single crystal substrate (MaTecK) was cleaned via repeated cycles of Ar sputtering and subsequent annealing in UHV. In order to achieve the two-dimensional growth of the inverse model catalyst, and to avoid the oxidation of the Cu substrate during the preparation procedure, cerium oxide thin films were prepared using method developed by Berner et al. [16]. Metallic cerium was deposited on Cu(111) surface at room temperature and then annealed at 900 K in UHV for 10 minutes. Cerium was deposited on the substrate from Ta crucible heated via electron bombardment. For obtaining the desired cerium oxide stoichiometry and structure, cerium deposit was then exposed to oxidizing and/or reducing treatments as proposed by Stetsovych et al. [29]. The oxidizing treatment consists of the exposure of the sample to O_2 atmosphere at room temperature [$p(O_2)=2.6\times10^{-5}$ Pa] and subsequent annealing at 700 K in UHV for 5 minutes. The reducing treatment consists of evaporation of metallic cerium onto the sample in UHV and subsequent annealing at 900K in UHV for 5 minutes. The average film thickness was determined using quartz crystal microbalance. Photoelectron spectroscopy of the Ce 3d, Cu $2p_{3/2}$ and O 1s core levels was performed with an X-ray radiation of 1486.6 eV (Al K_α) at normal emission. XPS data were processed using KolXPD software [33]. The deconvolution of Ce 3d spectra revealing the relative concentration of Ce^{3+} and Ce^{4+} ions in the cerium oxide samples was performed according to the procedure developed by Skála et al. [34,35]. STM measurements were performed using tips mechanically cut from Pt-Ir wire and thermally annealed in vacuum. STM images were obtained via tunneling into the unoccupied states of the sample. Samples were further characterized with LEED. Image processing and analysis of the STM and LEED data was performed using Gwyddion software [36]. All measurements were performed at room temperature. Due to the increased reactivity of reduced phases of ceria compared to stoichiometric CeO_2, and due to the small volume of ceria in the prepared inverse model catalysts, the samples tend to progressively oxidize from the residual H_2O atmosphere in the experimental apparatus. The stability of a particular ordering of O vacancies in the sample is in the order of tens of minutes.

Results

Preparation of the inverse model catalyst template

As a starting point for all presented experiments an inverse model catalyst template was prepared following the method of Berner et al. [16]. The STM, LEED and XPS of Ce 3d of the sample during preparation of the template are shown in Figures 1a, 1b, and 2a, 2b. Figures 1a and 2a describe the sample after deposition of metallic cerium and vacuum annealing. The amount of Ce on the sample is 1 ML [1ML represents 7.9×10^{14} cm^{-2} Ce atoms, equivalent of Ce atom density in one monolayer of $CeO_2(111)$]. Small islands were observed on the STM images and LEED revealed weak $CeO_2(111)(1\times1)$ spots which can be attributed to partial oxidation of cerium at the surface. XPS of Ce 3d spectra (Figure 2a) reveals a metallic Ce^0 contribution together with a small Ce^{3+} contribution accompanied by a small oxygen peak in XPS of O 1s (not shown).

To obtain the inverse model catalyst template, the predominantly metallic Ce deposit is subject to oxidizing treatment. Exposure to 12 L of oxygen at room temperature and subsequent annealing in UHV at 700 K leads to the formation of flat two-dimensional ceria islands as shown in Figure 1b. Coverage of ceria on the inverse model catalyst template is 50% and the local thickness of the ceria islands is 2-3 ML. LEED exhibits bright $CeO_2(111)(1\times1)$ spots. In some cases, rotational domains are observed (cf. Figure 3c). Areas with 1 ML thick $CeO_2(111)$, and the (2×2) LEED patterns associated with 1 ML thick areas [18] are not

observed on the inverse model catalyst templates. Analysis of the XPS spectra (Figure 2b) reveals the presence of both Ce^{4+} and Ce^{3+} doublets corresponding to the effective stoichiometry of $CeO_{1.85}$ indicating incomplete ceria oxidation. It is interesting to note that repeated oxidizing treatments of the inverse model catalyst templates do not result in further decreasing the Ce^{3+} concentration. The equivalent oxygen content in the inverse model catalyst templates in our experiment does not exceed $CeO_{1.9}$. This is in contrast with analogous oxidizing treatments applied on thicker continuous cerium oxide films in Ref. [13] that can be used to achieve oxygen content of up to CeO_2.

Fully oxidized inverse model catalyst CeO_2(111)/Cu(111)

In order to achieve stoichiometric ultrathin films of CeO_2 on Cu(111), inverse model catalyst template must be heated in oxygen background atmosphere [20]. Fully oxidized inverse model catalyst CeO_2(111)/Cu(111) obtained by annealing at 750 K in oxygen background atmosphere ($p = 2.6\times10^{-5}$ Pa) for 5 min is presented in Figures 1c, 1d and 2c. LEED diffraction pattern does not change. STM reveals coalescence of the ceria islands. CeO_2 coverage of the inverse model catalyst remains 50% and the local thickness of the ceria islands 2-3 ML. Detailed STM images reveal the presence of an oxidized copper substrate in between cerium oxide islands (Figure 1d and inset). XPS spectra show a decrease of the Ce^{3+} concentration resulting, effectively, in $CeO_{1.99}$ stoichiometry (Figure 2c).

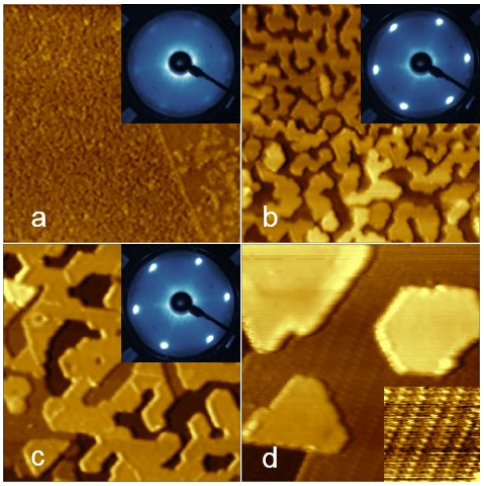

Figure 1. a) STM and LEED data of metallic Ce deposit on Cu(111); b) inverse model catalyst template; c) fully oxidized inverse model catalyst CeO_2(111)/Cu(111); d) detailed STM image of the fully oxidized inverse model catalyst revealing oxidized Cu(111) substrate (inset). The size of the STM images in a-c is 100×100 nm, in d – 30×30 nm, inset 12×12 nm. LEED images were taken at electron energy of 35 eV.

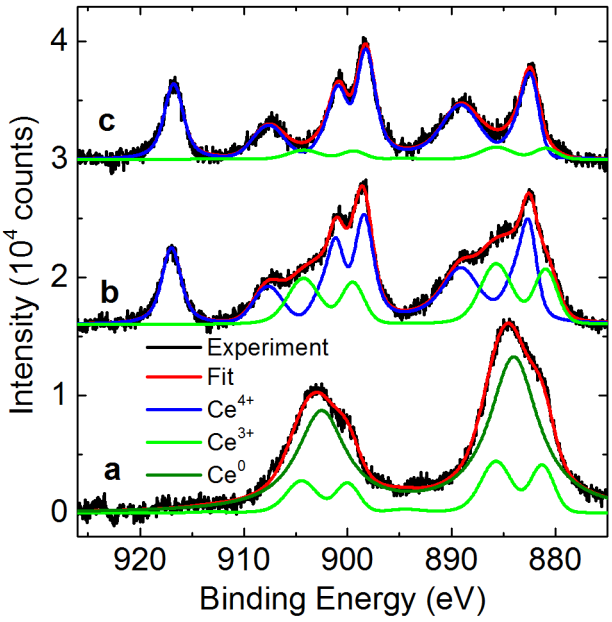

Figure 2. Ce 3d XPS spectra of a) metallic Ce deposit on Cu(111); b) inverse model catalyst template; c) fully oxidized inverse model catalyst CeO_2(111)/Cu(111)

Inverse model catalysts ι-Ce_7O_{12}, Ce_3O_5, and c-Ce_2O_3 on Cu(111)

In order to prepare inverse model catalysts of ordered reduced phases of ceria [13] the inverse model catalyst templates were modified using the experimental approach developed by Stetsovych et al. [29] repeatedly applying the reduction steps of deposition of small amounts of metallic cerium and annealing at 900 K in UHV. Depending on the total amount of the deposited cerium, different stoichiometries and crystallographic structures are obtained in the inverse model catalyst geometry, cf. Figure 3. Metallic cerium reacts with the existing CeO_x islands leaving clean Cu(111) substrate in between the islands. In analogy with the experiments on thicker continuous ceria layers presented in Ref. [13], inverse model catalysts of reduced ceria exhibit sharp LEED patterns of four main geometries, (1×1) (Figure 3a-c), (√7×√7)R19° (Figure 3d-f), (3×3) (Figure 3g-i), and (4×4) (Figure 3j-l). The notations of the surface reconstructions refer to CeO_2(111), designated as 1×1. Samples in Figure 3 are carefully prepared to show only the diffraction belonging to one particular surface reconstruction. Generally, prepared inverse model catalysts of reduced ceria may exhibit a mixture of two surface reconstructions [13]. From left to right, samples in Figures 3a, d, g, j correspond to increasing amount of deposited Ce, and thus increasing degree of reduction of the samples. STM images show increasing coverage of the ceria islands (Figures 3a, d, g, j). The thickness of the islands remains 2-3 ML.

In high-resolution STM images, structures with periodicity corresponding to the size of the surface unit cells in real space can be observed (Figures 3b, e, h, k); the unit cells of the surface reconstructions are outlined red, and the unit cells of the original 1×1 ordering of the inverse model catalyst template are outlined black. In analogy, black and red outlines indicate the 1×1 unit cells and the unit cells of the surface reconstructions in the LEED images of the reciprocal space (Figures 3 c, f, i, l). In Figures 3e and 3f, mutual rotation of the original and the reconstructed structures by 19° is apparent. For this purpose an STM image showing a coexistence of the (√7×√7)R19° and (1×1) reconstructed areas was chosen for Figure 3e.

In the inverse model catalyst samples, the reconstructions described above correspond to the reconstructions generally observed in supported ceria films on metals [13,28]. Reconstructions which can be found on bulk-like reduced ceria (√3×√3, √7×√3 [28]) are not observed here. This allows us to interpret the (1×1), (√7×√7)R19°, (3×3), and (4×4) reconstructions in analogy with the previous studies as thin films of bulk reduced ceria phases ι-Ce_7O_{12} (Figure 3d-f), Ce_3O_5 (Figure 3g-i), and c-Ce_2O_3 (Figure 3j-l) demonstrating that besides the possibility to prepare these structures on singular [13,37] and vicinal [38]

metal substrates, they can also be created as ultrathin 2-3 ML discontinuous layers, i.e. inverse model catalysts.

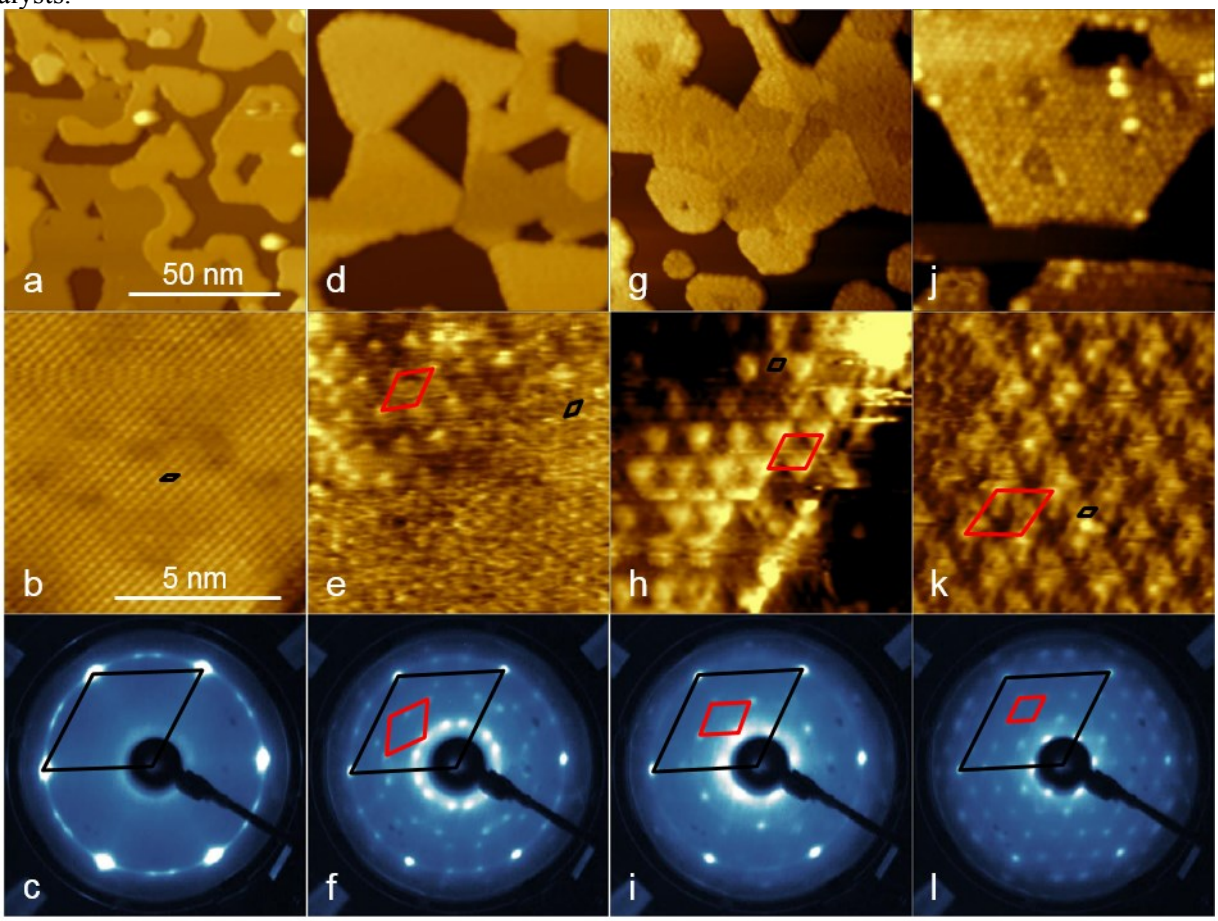

Figure 3. STM and LEED of inverse model catalyst samples with different stoichiometry: (a-c) – inverse model catalyst template with 1×1 reconstruction; (d-f) – ι-Ce_7O_{12} R19° surface with √7×√7 reconstruction; (g-i) - $CeO_{1.67}$ with 3×3 reconstruction; (j-l) – c-Ce_2O_3 surface with 4×4 reconstruction. Unit cells of the surface reconstructions are highlighted red, basic 1×1 unit cell black. The size of the STM images a), d), g), f) is 100×100 nm^2, b), e), h), k) – 9×9 nm^2. LEED images were taken at the electron energy of 35 eV.

Discussion

Finite size effects on the stoichiometry of the inverse model catalysts

Identification of the prepared inverse model catalysts with ordered crystallographic phases of reduced ceria, CeO_2, ι-Ce_7O_{12}, Ce_3O_5, and c-Ce_2O_3 implies a well-defined stoichiometry of the inverse model catalysts of CeO_2, $CeO_{1.71}$, $CeO_{1.67}$, and $CeO_{1.5}$. We determine the stoichiometry of the samples from XPS of Ce3d shown in Figure 4. The spectra are fitted for Ce^{3+} and Ce^{4+} contributions according to the procedure developed by Skála et al [34,35], and the areas of Ce^{3+} and Ce^{4+} XPS peaks are converted to the effective stoichiometry CeO_x . Displayed are the spectra of the samples exhibiting only the diffraction belonging to a single particular surface reconstruction as in Figure 3. Results of the experimental determination of the sample stoichiometry are summarized in Table 1.

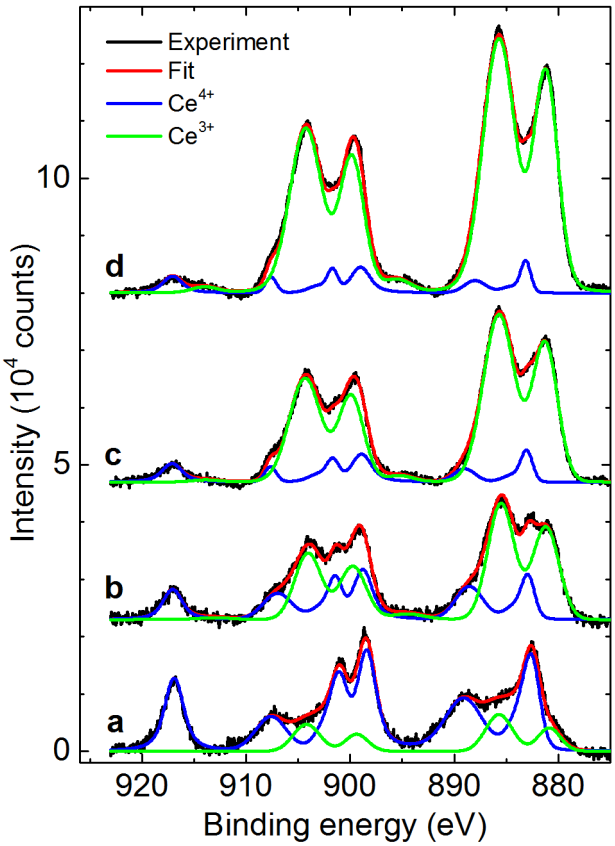

Figure 4. Ce 3d XPS spectra of a) 1×1 inverse model catalyst template; b) inverse model catalyst exhibiting LEED pattern (√7×√7)R19°; c) (3×3); d) (4×4). The results were fitted according to Skála et al. [34,35]. Ce^{3+} and Ce^{4+} contributions to the Ce 3d spectra are plotted in green and blue, respectively.

sample and its LEED	assigned crystallographic structure	expected stoichiometry CeO_x, x=	XPS stoichiometry this work CeO_x, x= (±0.03)	XPS stoichiometry thick films (10-15 ML)** CeO_x, x=
1×1 fully oxidized*	CeO_2(111)	2	1.99	1.98
1×1 template	CeO_2(111)	2	1.90	-
(√7×√7)R19°	ι-Ce_7O_{12}	1.71	1.69	1.86
3×3	Ce_3O_5	1.67	1.60	1.78
4×4	c-Ce_2O_3	1.5	1.54	1.50

*Table 1. Expected and experimentally determined stoichiometry of inverse model catalysts with different types of LEED patterns, cf. Figures 3 and 4. *from Figures 1c, 1d, 2c. **from the work of Duchoň et al. [13] and analysis of Ce 3d XPS measured at normal emission.*

The experimentally determined stoichiometry of the inverse model catalysts from Figures 3 and 4 corresponds very well to the expected stoichiometry. The difference between the expected and the determined

stoichiometry observed for 1x1 inverse catalyst templates (Figures 3a, 4a) can be diminished by full oxidation of the inverse catalyst template, cf. Figures 1 c, d, 2c. The observed agreement between the expected and the determined stoichiometry for the 2-3 ML thick discontinuous cerium oxide layers in the present inverse model catalysts is in contrast with the findings on thick continuous films of ordered reduced ceria [13]. For the (√7×√7)R19° and 3×3 LEED patterns the experimentally determined stoichiometry for 10-15 ML thick films departs significantly from the expected stoichiometry ([13], Table 1, last column). Duchoň et al. explain this discrepancy by surface segregation of the oxygen vacancies in the thicker films resulting in the formation of 2-4 ML reduced phase floating on top of a near-stoichiometric ceria film [13]. On such samples, XPS is detecting both the reduced ceria phase and the underlying near-stoichiometric substrate biasing the XPS data towards, apparently, higher Ce^{4+} content.

In the inverse model catalysts presented in this work the layers of stoichiometric as well as reduced ceria are 2-3 ML thick, i.e. < 1 nm. For such layers the information depth of XPS is higher than the layer thickness and all Ce atoms in the layer contribute to the experimentally detected Ce^{3+} signal. Given the correspondence of the experimentally determined stoichiometry with the expected stoichiometry we can propose that due to their limited thickness the inverse model catalysts introduced in this work represent homogeneous layers of the CeO_2(111), ι-Ce_7O_{12}, Ce_3O_5, and c-Ce_2O_3 crystallographic structures corresponding to the observed LEED patterns.

Finite size effect on the lattice parameter of the inverse model catalysts

LEED patterns of the inverse model catalyst samples exhibiting only diffraction belonging to one particular surface reconstruction can be analyzed quantitatively to obtain the lateral lattice parameter of the surface lattice. The lattice parameter is determined from the distance of 1×1 spots that can be identified in any of the (1×1), (√7×√7)R19°, (3×3), and (4×4) diffraction patterns (Figure 3c, f, i, l, black outlines). The lattice parameter expressed as a unit cell size of a corresponding cubic CeO_2 structure is plotted as a function of the expected sample stoichiometry in Figure 5.

In reduced bulk ceria Ce^{3+} ions exhibit an increased atomic radius compared to Ce^{4+} ions resulting in a linear dependence of the bulk lattice parameter on the oxygen content in the sample and on the sample stoichiometry. This bulk dependence is plotted as a reference in Figure 5 (grey line, [39]). Experimental lattice parameter obtained in the present inverse catalyst samples shows a linear dependence of the bulk lattice parameter on the sample stoichiometry, too, but with a distinctly different slope. In agreement with the previous observations 2-3 ML thick CeO_2(111) layers on Cu(111) (Figure 5, LEED pattern 1×1) exhibit 2% lattice contraction compared to bulk CeO_2 [19]. However, the dependence of the lattice parameter on the sample stoichiometry in inverse model catalysts is stronger than in the bulk samples resulting in 1% lattice expansion of 2-3 ML thick c-Ce_2O_3(111) layer on Cu(111) (Figure 5, LEED pattern 4×4) compared to c-Ce_2O_3 bulk.

Contraction of the lateral lattice parameter of the stoichiometric CeO_2(111) layers on Cu(111) has been previously identified as a finite size effect that can be ascribed predominantly to the finite thickness of the film [19]. We point out that the lateral lattice parameter of the ceria layer can almost freely adjust without being dictated by epitaxial relationships to the underlying Cu(111) [19]. This allowed to experimentally observe the dependence of the lattice parameter of CeO_2(111) films on Cu(111) as a function of film thickness [19,40]. In the present work, observations of inverse model catalysts allowed to determine the dependence of the lattice parameter of 2-3 ML thick ceria films as a function of the film stoichiometry.

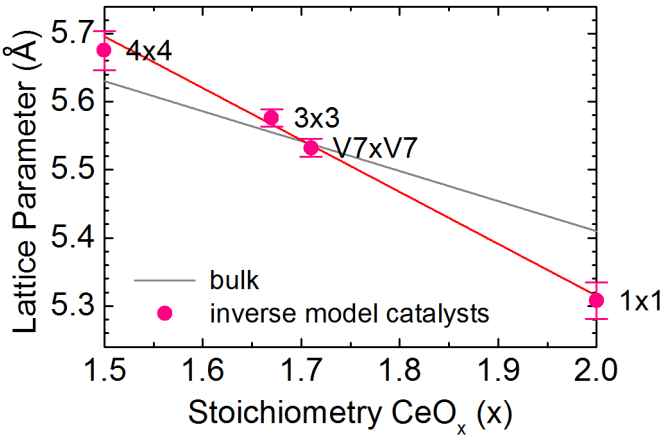

Figure 5: Lattice parameter of the 2-3 ML thick reduced ceria in the inverse model catalysts (points) and the corresponding linear fit (red line). Dependence of the bulk lattice parameter on the ceria stoichiometry is indicated by grey line [39].

Barrier to complete oxidation of the inverse model catalysts

Our experiments show that the prepared inverse model catalysts of 2-3 ML thickness cannot, effectively, be fully oxidized by exposures to O_2 background of $p(O_2) = 2.6\times10^{-5}$ Pa at room temperature, in contrast to the thicker CeO_x films of 10-15 ML thickness studied by Duchoň et al. [13]. The stoichiometry as derived from the Ce 3d XPS data did not exceed $CeO_{1.9}$ in the 1×1 inverse model catalyst templates prepared by O_2 exposure at RT. To fully oxidize the 2-3 ML thick films annealing of the 1×1 inverse catalyst templates in the oxygen background at 750 K is required indicating the activated nature of the oxidation (cf. Figures 1, 2).

The appearance of Ce^{3+} ions in the ceria samples is most often discussed in terms of the presence of oxygen vacancies when two electrons from the removed lattice O^{2-} ion localize on the nearby Ce atoms creating 2 Ce^{3+} ions per bulk or surface O vacancy [41,42]. However, the charge accumulated on the Ce^{3+} sites in ceria samples does necessarily originate from the removed lattice O. For ceria thin films supported on metal substrates, charge transfer from the substrate to the film is observed when the electrons from the substrate localize in the ceria and generate Ce^{3+} ions. For CeO_2(111) layers on Cu(111), conversion of all Ce^{4+} ions at the copper-ceria interface to Ce^{3+} is predicted based on ab-initio calculations [18]. For 2-3 ML thick CeO_2(111) layers in the present inverse model catalysts, the conversion of all interface Ce^{4+} atoms to Ce^{3+} would result in the Ce^{3+} concentration in the samples of 1/3-1/2 with Ce^{3+} ions localized at the metal-oxide interface. Considering the inelastic mean free paths of Ce 3d XPS photoelectrons in CeO_2 (11.83 Å for Al Kα [43]) this translates to effective stoichiometries determined from the XPS intensity of the Ce^{3+} and Ce^{4+} ions of $CeO_{1.86}$ and $CeO_{1.93}$ for 2 ML and 3 ML thick ceria layers, respectively. Thus, charge transfer from the surface can fully account for the observed limiting $CeO_{1.9}$ stoichiometry observed for the 1×1 inverse model catalyst templates.

To assess the eventual role of oxygen vacancies in the oxidation behavior of the prepared model catalysts, we have determined the relative areas of the lattice O 1s signal with respect to the Ce 3d signal in a number of inverse model catalyst samples. We plot the lattice O/Ce ratio as a function of their stoichiometry determined from XPS of Ce 3d. The results are shown in Figure 6. The inset shows the example of the identification and fitting of the lattice O 1s peak. In the range of ceria stoichiometries between $CeO_{1.5}$ and $CeO_{1.9}$ the lattice O/Ce ratio fluctuates at apparently constant value. We can fit an expected linear dependence on the experimental data (red line in Figure 6) between $CeO_{1.5}$ and $CeO_{1.9}$. It becomes apparent that the expected changes in the lattice O/Ce ratio are smaller than the precision of the measurement.

For the inverse model catalyst stoichiometries exceeding $CeO_{1.9}$ obtained by high temperature oxidation of the 1×1 inverse model catalyst templates, however, O/Ce ratio clearly exceeds the values expected for the stoichiometric CeO_2. This is another illustration of the fact that exceeding the $CeO_{1.9}$ stoichiometry in the 2-3 ML thick ceria films is accompanied with oxidation of the Cu substrate. The

oxidation is observed in the STM images in the exposed Cu areas between ceria islands (Figure 1 d). Since, apparently, recombination of the surface O vacancies on ceria with O_2 is a process active already at room temperature [13], we suggest that the activation barrier for achieving CeO_2 stoichiometry in the 2-3 ML thick ceria films is related to the activated nature of Cu oxidation [44]. The presence of the copper oxide on the surface of the model catalysts may diminish the charge transfer between the Cu substrate and the ceria islands and suppress the formation of Ce^{3+} ions in the inverse copper-ceria catalysts.

While the dependence of the lattice O/Ce ratio on the stoichiometry of the ceria in the inverse model catalysts is hidden in the error of the lattice O/Ce ratio determination, the dependence of the lattice O peak binding energy is well resolved. The dependence is plotted in Figure 7. We observe a continuous shift of the lattice O binding energy by approximately 0.5 eV between $CeO_{1.5}$ and CeO_2 stoichiometries in agreement with previous experimental observations [12,29,45].

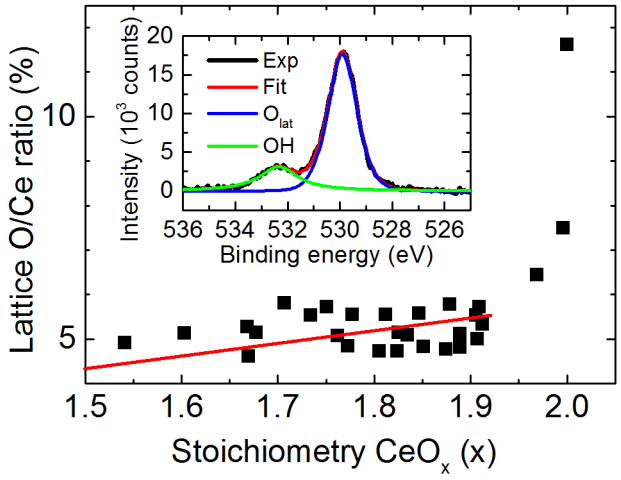

Figure 6. Dependence of the O 1s/Ce 3d peak area ratio on the stoichiometry of the inverse model catalysts. The inset shows the decomposition of the O 1s peak into the lattice O and surface hydroxyl contributions [22].

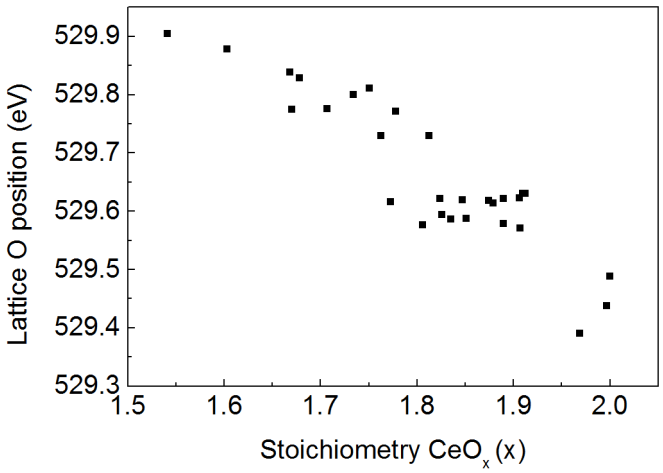

Figure 7. Dependence of the O 1s peak position on the stoichiometry of the inverse model catalysts.

Conclusions

In the present work, we have prepared inverse model catalysts of CeO_x/Cu in the form of highly ordered, discontinuous, and ultra-thin CeO_x films on Cu(111). Investigations using surface science methods reveal that the prepared inverse model catalysts represent 2-3 monolayer thick films of ordered cerium oxides CeO_2(111), ι-Ce_7O_{12}, Ce_3O_5, and c-Ce_2O_3(111). The prepared cerium oxide films exhibit diffraction patterns and stoichiometries precisely corresponding to the structure and stoichiometry of bulk cerium oxides potentially bringing a high level of control over the oxygen vacancy concentration and coordination in the inverse model CeO_x/Cu catalysts.

Experimental observations reveal pronounced size effects and metal-oxide interactions that codetermine the physicochemical behavior of the CeO_2(111), ι-Ce_7O_{12}, Ce_3O_5, and c-Ce_2O_3(111) inverse model catalysts. Particularly, limited thickness of the films determines their lateral strain, and the charge transfer from the Cu surface their oxidation properties. Introducing the present inverse model CeO_x/Cu catalysts opens the way towards designing new experiments in model catalysis aiming on disentangling and optimizing the roles of the oxygen vacancy concentration, coordination, oxide strain, and metal-oxide interactions in the catalysts of copper-ceria, and generally, metal-ceria catalytic systems.

Author information

Corresponding Author
*E-mail: josef.myslivecek@mff.cuni.cz. Phone: +420 221 912 333. Fax: +420 284 685 095.
Present Addresses
[a] Johannes Kepler University, Linz, Austria.
[b] University of Pardubice, Faculty of Chemical Technology, Nám. Čs. Legií 565, 53002 Pardubice, Czech Republic.
Notes
The authors declare no competing financial interest

Acknowledgements:

The authors would like to thank Dan Mazur for fruitful discussions. This work was supported by the Czech Science Foundation (GAČR 105-13/201462). A.T., V.S. and F.D. acknowledge the support of the Grant Agency of the Charles University (GAUK 105-10/250115, GAUK 105-10/259650).

References:

[1] C.T. Campbell, Ultrathin metal films and particles on oxide surfaces: structural, electronic and chemisorptive properties, Surf. Sci. Rep. 27 (1997) 1–111. doi:10.1016/S0167-5729(96)00011-8.

[2] C.R. Henry, Surface studies of supported model catalysts, Surf. Sci. Rep. 31 (1998) 231–325. doi:10.1016/S0167-5729(98)00002-8.

[3] H.-J. Freund, Clusters and islands on oxides: from catalysis via electronics and magnetism to optics, Surf. Sci. 500 (2002) 271–299. doi:10.1016/S0039-6028(01)01543-6.

[4] J.A. Rodríguez, J. Hrbek, Inverse oxide/metal catalysts: A versatile approach for activity tests and mechanistic studies, Surf. Sci. 604 (2010) 241–244. doi:10.1016/j.susc.2009.11.038.

[5] F.P. Netzer, F. Allegretti, S. Surnev, Low-dimensional oxide nanostructures on metals: Hybrid systems with novel properties, J. Vac. Sci. Technol. B Microelectron. Nanom. Struct. 28 (2010) 1. doi:10.1116/1.3268503.

[6] F.P. Netzer, "Small and beautiful" – The novel structures and phases of nano-oxides, Surf. Sci. 604 (2010) 485–489. doi:10.1016/j.susc.2010.01.002.

[7] J.A. Rodriguez, J. Graciani, J. Evans, J.B. Park, F. Yang, D. Stacchiola, et al., Water-Gas Shift Reaction on a Highly Active Inverse CeO_x/Cu(111) Catalyst: Unique Role of Ceria Nanoparticles, Angew. Chemie Int. Ed. 48 (2009) 8047–8050. doi:10.1002/anie.200903918.

[8] S.D. Senanayake, D. Stacchiola, J.A. Rodriguez, Unique Properties of Ceria Nanoparticles Supported on Metals: Novel Inverse Ceria/Copper Catalysts for CO Oxidation and the Water-Gas Shift Reaction, Acc. Chem. Res. 46 (2013) 1702–1711. doi:10.1021/ar300231p.

[9] G. Eranna, B.C. Joshi, D.P. Runthala, R.P. Gupta, Oxide Materials for Development of Integrated Gas Sensors – A Comprehensive Review, Crit. Rev. Solid State Mater. Sci. 29 (2004) 111–188. doi:10.1080/10408430490888977.

[10] R. Fiala, M. Vaclavu, M. Vorokhta, I. Khalakhan, J. Lavkova, V. Potin, et al., Proton exchange membrane fuel cell made of magnetron sputtered Pt–CeO_x and Pt–Co thin film catalysts, J. Power Sources. 273 (2015) 105–109. doi:10.1016/j.jpowsour.2014.08.093.

[11] J. Kašpar, P. Fornasiero, M. Graziani, Use of CeO_2-based oxides in the three-way catalysis, Catal. Today. 50 (1999) 285–298. doi:10.1016/S0920-5861(98)00510-0.

[12] F. Dvořák, O. Stetsovych, M. Steger, E. Cherradi, I. Matolínová, N. Tsud, et al., Adjusting Morphology and Surface Reduction of CeO_2(111) Thin Films on Cu(111), J. Phys. Chem. C. 115 (2011) 7496–7503. doi:10.1021/jp1121646.

[13] T. Duchoň, F. Dvořák, M. Aulická, V. Stetsovych, M. Vorokhta, D. Mazur, et al., Ordered Phases of Reduced Ceria As Epitaxial Films on Cu(111), J. Phys. Chem. C. 118 (2014) 357–365. doi:10.1021/jp409220p.

[14] J. Mysliveček, V. Matolín, I. Matolínová, Heteroepitaxy of Cerium Oxide Thin Films on Cu(111), Materials (Basel). 8 (2015) 6346–6359. doi:10.3390/ma8095307.

[15] Y. Zhou, J.M. Perket, J. Zhou, Growth of Pt Nanoparticles on Reducible CeO_2 (111) Thin Films: Effect of Nanostructures and Redox Properties of Ceria, J. Phys. Chem. C. 114 (2010) 11853–11860. doi:10.1021/jp1007279.

[16] U. Berner, K.-D. Schierbaum, Cerium oxides and cerium-platinum surface alloys on Pt(111) single-crystal surfaces studied by scanning tunneling microscopy, Phys. Rev. B. 65 (2002) 235404. doi:10.1103/PhysRevB.65.235404.

[17] X. Zhao, S. Ma, J. Hrbek, J. a. Rodriguez, Reaction of water with Ce–Au(111) and CeO_x/Au(111) surfaces: Photoemission and STM studies, Surf. Sci. 601 (2007) 2445–2452. doi:10.1016/j.susc.2007.04.106.

[18] L. Szabová, O. Stetsovych, F. Dvořák, M. Farnesi Camellone, S. Fabris, J. Mysliveček, et al., Distinct Physicochemical Properties of the First Ceria Monolayer on Cu(111), J. Phys. Chem. C. 116 (2012) 6677–6684. doi:10.1021/jp211955v.

[19] O. Stetsovych, F. Dvořák, L. Szabová, S. Fabris, J. Mysliveček, V. Matolín, Nanometer-Range Strain Distribution in Layered Incommensurate Systems, Phys. Rev. Lett. 109 (2012) 266102. doi:10.1103/PhysRevLett.109.266102.

[20] F. Yang, J. Graciani, J. Evans, P. Liu, J. Hrbek, J.F. Sanz, et al., CO oxidation on inverse $CeO_{(x)}$/Cu(111) catalysts: high catalytic activity and ceria-promoted dissociation of O_2., J. Am. Chem. Soc. 133 (2011) 3444–51. doi:10.1021/ja1087979.

[21] D.R. Mullins, The surface chemistry of cerium oxide, Surf. Sci. Rep. 70 (2015) 42–85. doi:10.1016/j.surfrep.2014.12.001.

[22] D.R. Mullins, P.M. Albrecht, T.-L. Chen, F.C. Calaza, M.D. Biegalski, H.M. Christen, et al., Water Dissociation on CeO_2(100) and CeO_2(111) Thin Films, J. Phys. Chem. C. 116 (2012) 19419–19428. doi:10.1021/jp306444h.

[23] D.R. Mullins, P.V. Radulovic, S.H. Overbury, Ordered cerium oxide thin films grown on Ru(0001) and Ni(111), Surf. Sci. 429 (1999) 186–198. doi:10.1016/S0039-6028(99)00369-6.

[24] Y. Lykhach, V. Johánek, H.A. Aleksandrov, S.M. Kozlov, M. Happel, T. Skála, et al., Water Chemistry on Model Ceria and Pt/Ceria Catalysts, J. Phys. Chem. C. 116 (2012) 12103–12113. doi:10.1021/jp302229x.

[25] G.D. Wang, D.D. Kong, Y.H. Pan, H.B. Pan, J.F. Zhu, Low energy Ar-ion bombardment effects on the CeO_2 surface, Appl. Surf. Sci. 258 (2012) 2057–2061. doi:10.1016/j.apsusc.2011.04.103.

[26] E.A. Kümmerle, G. Heger, The Structures of C–$Ce_2O_{3+\delta}$, Ce_7O_{12}, and $Ce_{11}O_{20}$, J. Solid State Chem. 147 (1999) 485–500. doi:10.1006/jssc.1999.8403.

[27] H. Wilkens, O. Schuckmann, R. Oelke, S. Gevers, A. Schaefer, M. Bäumer, et al., Stabilization of the ceria ι-phase (Ce_7O_{12}) surface on Si(111), Appl. Phys. Lett. 102 (2013) 111602. doi:10.1063/1.4795867.

[28] R. Olbrich, G.E. Murgida, V. Ferrari, C. Barth, A.M. Llois, M. Reichling, et al., Surface Stabilizes Ceria in Unexpected Stoichiometry, J. Phys. Chem. C. 121 (2017) 6844–6851. doi:10.1021/acs.jpcc.7b00956.

[29] V. Stetsovych, F. Pagliuca, F. Dvořák, T. Duchoň, M. Vorokhta, M. Aulická, et al., Epitaxial Cubic Ce_2O_3 Films via Ce–CeO_2 Interfacial Reaction, J. Phys. Chem. Lett. 4 (2013) 866–871. doi:10.1021/jz400187j.

[30] J.I. Flege, B. Kaemena, S. Gevers, F. Bertram, T. Wilkens, D. Bruns, et al., Silicate-free growth of high-quality ultrathin cerium oxide films on Si(111), Phys. Rev. B. 84 (2011) 235418. doi:10.1103/PhysRevB.84.235418.

[31] F. Dvořák, M. Farnesi Camellone, A. Tovt, N. Tran, F.R. Negreiros, M. Vorokhta, et al., Creating single-atom Pt-ceria catalysts by surface step decoration, Nat. Commun. 7 (2016) 10801. doi:10.1038/ncomms10801.

[32] F. Dvořák, L. Szabová, V. Johánek, M. Farnesi Camellone, V. Stetsovych, M. Vorokhta, et al., Bulk Hydroxylation and Effective Water Splitting by Highly Reduced Cerium Oxide: The Role of O

Vacancy Coordination, ACS Catal. 8 (2018). doi:10.1021/acscatal.7b04409.

[33] https://www.kolibrik.net/kolxpd/.

[34] T. Skála, F. Šutara, K.C. Prince, V. Matolín, Cerium oxide stoichiometry alteration via Sn deposition: Influence of temperature, J. Electron Spectros. Relat. Phenomena. 169 (2009) 20–25. doi:10.1016/j.elspec.2008.10.003.

[35] T. Skála, F. Šutara, M. Škoda, K.C. Prince, V. Matolín, Palladium interaction with CeO_2 , Sn–Ce–O and Ga–Ce–O layers, J. Phys. Condens. Matter. 21 (2009) 055005. doi:10.1088/0953-8984/21/5/055005.

[36] D. Nečas, P. Klapetek, Gwyddion: an open-source software for SPM data analysis, Open Phys. 10 (2012) 181–188. doi:10.2478/s11534-011-0096-2.

[37] T. Duchoň, F. Dvořák, M. Aulická, V. Stetsovych, M. Vorokhta, D. Mazur, et al., Comment on "Ordered Phases of Reduced Ceria as Epitaxial Films on Cu(111)," J. Phys. Chem. C. 118 (2014) 5058–5059. doi:10.1021/jp412439b.

[38] M. Aulická, T. Duchoň, F. Dvořák, V. Stetsovych, J. Beran, K. Veltruská, et al., Faceting Transition at the Oxide–Metal Interface: (13 13 1) Facets on Cu(110) Induced by Carpet-Like Ceria Overlayer, J. Phys. Chem. C. (2015). doi:10.1021/jp5099359.

[39] A. Trovarelli, P. Fornasiero, Catalysis by ceria and related materials, 2nd ed., World Scientific, Singapore, 2013.

[40] K. Mašek, J. Beran, V. Matolín, RHEED study of the growth of cerium oxide on Cu(111), Appl. Surf. Sci. 259 (2012) 34–38. doi:10.1016/j.apsusc.2012.06.014.

[41] N. Skorodumova, S. Simak, B. Lundqvist, I. Abrikosov, B. Johansson, Quantum Origin of the Oxygen Storage Capability of Ceria, Phys. Rev. Lett. 89 (2002) 166601. doi:10.1103/PhysRevLett.89.166601.

[42] J.-F. Jerratsch, X. Shao, N. Nilius, H.-J. Freund, C. Popa, M.V. Ganduglia-Pirovano, et al., Electron Localization in Defective Ceria Films: A Study with Scanning-Tunneling Microscopy and Density-Functional Theory, Phys. Rev. Lett. 106 (2011) 246801. doi:10.1103/PhysRevLett.106.246801.

[43] S. Tanuma, C.J. Powell, D.R. Penn, Calculations of electron inelastic mean free paths (IMFPS). IV. Evaluation of calculated IMFPs and of the predictive IMFP formula TPP-2 for electron energies between 50 and 2000 eV, Surf. Interface Anal. 20 (1993) 77–89. doi:10.1002/sia.740200112.

[44] T. Matsumoto, R.A. Bennett, P. Stone, T. Yamada, K. Domen, M. Bowker, Scanning tunneling microscopy studies of oxygen adsorption on Cu(111), Surf. Sci. 471 (2001) 225–245. doi:10.1016/S0039-6028(00)00918-3.

[45] D.. Mullins, S.. Overbury, D.. Huntley, Electron spectroscopy of single crystal and polycrystalline cerium oxide surfaces, Surf. Sci. 409 (1998) 307–319. doi:10.1016/S0039-6028(98)00257-X.

Conclusions

Chemical industry has become one of the most important branches in modern industry. Major part of reactions used in modern chemistry are based on catalysts. Commercial catalysts represent complicated systems making their characterization and understanding of their performance in catalytic reactions more challenging. Model catalysis is a perspective approach in understanding the key parameters of the real catalytic systems. Studying the model systems provides an opportunity to develop real catalysts with enhanced activity, selectivity and stability.

In this work, the role of surface defects on ceria in the stabilization of Pt single atoms on ceria as well as in water splitting over ceria was studied. Experimental results combined with DFT calculations revealed the step edges of ceria to be the active surface sites for stabilization of Pt^{2+} atoms. In the presence of excess oxygen, CeO_2 step can stabilize one or more monodispersed Pt^{2+} ions per step edge adsorption site. Partial reduction of the ceria film leads to complete reduction of step edges which lose their ability to stabilize Pt^{2+} ions. At partially reduced ceria surfaces as well as at surfaces with low density of steps, Pt deposit coalesces into Pt^0 clusters. Charge transfer between these clusters and cerium oxide was measured and its highest value was revealed to be for clusters containing from 30 to 70 Pt atoms: 0.1 electrons per Pt atom. For bigger Pt clusters, charge transfer is decreased.

Oxygen vacancies on ceria play key role in water splitting. Present work revealed, that the activity of reduced ceria film not only depends on the concentration of oxygen vacancies, but also on their position with respect to each other. Hence, Ce_2O_3 films with 4×4 reconstruction had the highest reactivity towards water giving highest H_2 production during TPD. Results also proved that the OH^- in the bulk of c-Ce_2O_3 is mediated by a particular spatial coordination of O vacancies: a network of next-nearest-neighbor (NNN) O vacancies in bixbyite c-Ce_2O_3, and by pairs of NNN O vacancies in less-reduced CeO_x phases.

Finally, inverse model CeO_x/Cu(111) systems with precisely controlled morphology and stoichiometry were prepared and analyzed. The results revealed the existence of an activation barrier for oxidation of the ultrathin ceria films on Cu(111) due to the oxide-support interaction. Complete oxidation of the film could only be achieved at elevated temperatures together with the oxidation of the substrate. Results revealed (1×1), (√7×√7)R19°, (3×3) and (4×4) surface reconstructions for the reduced films and with stoichiometry corresponding to the expected values of CeO_2, Ce_7O_{12}, Ce_3O_5, and Ce_2O_3 corresponding to the bulk reduced phases of ceria.

The results concerning the role of defects on ceria surfaces obtained in this work represent an important step towards understanding the surface related phenomena in catalysis over ceria. Controlling the concentration and the coordination of oxygen vacancies in ceria is a perspective approach that can improve the functionality of ceria-based heterogeneous catalysts, and that can be related to the more general concept of strain engineering of oxide catalytic materials. The developed methods of adjusting density of monoatomic step edges and concentration of oxygen vacancies on ceria provide a powerful tool for future studies of the redispersion of metal particles on cerium oxide surfaces. Applying these methods in inverse model catalysis provides a perspective of development of inverse catalysts with enhanced catalytic activity, selectivity and stability.

Appendix

Publications:

1. Lykhach, Y; Kozlov, SM; Skala, T; **Tovt, A**; Stetsovych, V; Tsud, N; Dvorak, F; Johanek, V; Neitzel, A; Myslivecek, J; Fabris, S; Matolin, V; Neyman, KM; Libuda, J., "Counting electrons on supported nanoparticles," *Nat. Mater.*, vol. 15, no. 3, pp. 284–288, 2016.
2. Dvorak, F; Camellone, MF; **Tovt, A**; Tran, ND; Negreiros, FR; Vorokhta, M; Skala, T; Matolinova, I; Myslivecek, J; Matolin, V; Fabris, S., "Creating single-atom Pt-ceria catalysts by surface step decoration," *Nat. Commun.*, vol. 7, 2016.
3. Dvořák, F; Szabová, L; Johánek, V; Camellone, MF; Stetsovych, V; Vorokhta, M; **Tovt, A**; Skála, T; Matolínová, I; Tateyama, Y; Mysliveček, J; Fabris, S; Matolín, V. "Bulk Hydroxylation and Effective Water Splitting by Highly Reduced Cerium Oxide: The Role of O Vacancy Coordination," *ACS Catal.*, vol.8, no.5, pp. 4354-4363, 2018.

Manuscripts:

1. **Andrii Tovt**, Luigi Bagolini, Filip Dvořák, Nguyen-Dung Tran, Mykhailo Vorokhta, Klára Ševčíková, Viktor Johánek, Matteo Farnesi Camellone, Tomáš Skála, Iva Matolínová, Josef Mysliveček, Stefano Fabris and Vladimír Matolín "Controlling Pt dispersion on ceria by surface oxygen content," ready for submission.
2. **Andrii Tovt**, Vitalii Stetsovych, Filip Dvořák, Viktor Johánek, and Josef Mysliveček. "Ordered phases of reduced ceria as inverse model catalysts," submitted 13th July 2018 to *Applied Surface Science*.

Conference presentations:

1. **Tovt A.I.**, Gerasimov O.V. "Algorithms of multiple ciphering with the help of simple ciphering systems" (November 2011) Conference Presentation, Uzhgorod, Ukraine.
2. **Tovt A.I.** "Development of pseudo-5-channel surround sound system" (December 2012) Conference Presentation, Uzhgorod, Ukraine.
3. **Tovt A.I.** "Realization of message encryption system using holographic images" (May 2013) Conference Presentation, Master thesis, Uzhgorod, Ukraine.
4. Dvořák F., Stetsovych V., Vorokhta M., **Tovt A.**, Balakin D., Skála T., Matolínová I., Johánek V., Mysliveček J., Matolín V. "Reaction pathways for reversible and irreversible decomposition of water on reduced ceria". (September 2014) Poster presentation. ECOSS 30 Antalya, Turkey.

5. **Andrii Tovt,** Vitalii Stetsovych, Filip Dvořák, Tomáš Duchoň, Tomáš Skála, Josef Mysliveček, Iva Matolínová, Vladimír Matolín. "Ordered phases of reduced ceria thin films on Cu(111) observed by STM". (July 2015) Poster presentation. MCE Workschop 15 Rauischholzhasen, Germany.
6. Filip Dvořák, Matteo Farnesi Camellone, **Andrii Tovt,** Nguyen-Dung Tran, Fabio R. Negreiros, Mykhailo Vorokhta, Tomáš Skála, Iva Matolínová, Josef Mysliveček, Vladimír Matolín, Stefano Fabris. "Step edges on ceria stabilize Pt^{2+} ions". (September 2015) Poster presentation, competition for Best Poster Prize. ECOSS 31 Barcelona, Spain.

Foreign working visits:

1. Experimental measurements of WO_x nanorods using advanced multi-probe AFM at Nanofunctionality Integration Group, supervised by Prof. Nakayama, T. National Institute of Material Science, Tsukuba, Ibaraki prefecture, Japan.
2. Characterization of reduction/oxidation properties of Pt/Ceria model systems using LEEM surface science method at synchrotron BESSY, Berlin, Germany.

References

[1] E. Gallei and E. Schwab, "Development of technical catalysts," *Catal. Today*, vol. 51, no. 3–4, pp. 535–546, 1999.

[2] R. Schlogl, "Heterogeneous catalysis — still magic or already science," *Top. Catal.*, vol. 104, no. 1, pp. N3–N4, 1993.

[3] D. W. Goodman, "Catalysis: from single crystals to the 'real world,'" *Surf. Sci.*, vol. 299–300, no. C, pp. 837–848, 1994.

[4] J. C. Bertolini, "Model catalysis by metals and alloys: From single-crystal surfaces to well-defined nano-particles," *Catal. Today*, vol. 138, no. 1–2, pp. 84–96, 2008.

[5] H. J. Freund, H. Kuhlenbeck, J. Libuda, G. Rupprechter, M. Baumer, and H. Hamann, "Bridging the pressure and materials gaps between catalysis and surface science: clean and modified oxide surfaces," *Top. Catal.*, vol. 15, no. 2–4, pp. 201–209, 2001.

[6] S. Zhang, L. Nguyen, Y. Zhu, S. Zhan, C. K. F. Tsung, and F. F. Tao, "In-situ studies of nanocatalysis," *Acc. Chem. Res.*, vol. 46, no. 8, pp. 1731–1739, 2013.

[7] M. Bäumer, J. Libuda, K. M. Neyman, N. Rösch, G. Rupprechter, and H.-J. Freund, "Adsorption and reaction of methanol on supported palladium catalysts: microscopic-level studies from ultrahigh vacuum to ambient pressure conditions," *Phys. Chem. Chem. Phys.*, vol. 9, no. 27, pp. 3541–3558, 2007.

[8] W. Huang, "Oxide Nanocrystal Model Catalysts," *Acc. Chem. Res.*, vol. 49, no. 3, pp. 520–527, 2016.

[9] H. Oosterbeek, "Bridging the pressure and material gap in heterogeneous catalysis: cobalt Fischer–Tropsch catalysts from surface science to industrial application," *Phys. Chem. Chem. Phys.*, vol. 9, no. 27, pp. 3570–3576, 2007.

[10] J. V. Lauritsen, R. T. Vang, and F. Besenbacher, "From atom-resolved scanning tunneling microscopy (STM) studies to the design of new catalysts," *Catal. Today*, vol. 111, no. 1–2, pp. 34–43, 2006.

[11] J. M. Thomas, "Heterogeneous catalysis: Enigmas, illusions, challenges, realities, and emergent strategies of design," *J. Chem. Phys.*, vol. 128, no. 18, 2008.

[12] F. Devred, P. Dulgheru, and N. Kruse, "Elementary Steps in Heterogeneous Catalysis," *Compr. Inorg. Chem. II (Second Ed. From Elem. to Appl.*, vol. 7, pp. 7–38, 2013.

[13] V. I. Bukhtiyarov, "The study of the nature of adsorbed species to build a bridge between surface science and catalysis: Problems of pressure and material gap," *Kinet. Catal.*, vol. 44, no. 3, pp. 420–431, 2003.

[14] G. A. Somorjai, R. L. York, D. Butcher, and J. Y. Park, "The evolution of model catalytic systems; studies of structure, bonding and dynamics from single crystal metal surfaces to nanoparticles, and from low pressure ($p=10^{-3}$ Torr) to high pressure ($p=10^{-3}$ Torr) to liquid interfaces," *Phys. Chem. Chem. Phys.*, vol. 9, no. 27, pp. 3500–3513, 2007.

[15] R. T. Vang, E. Lægsgaard, and F. Besenbacher, "Bridging the pressure gap in model systems

for heterogeneous catalysis with high-pressure scanning tunneling microscopy," *Phys. Chem. Chem. Phys.*, vol. 9, no. 27, pp. 3460–3469, 2007.

[16] S. B. Roobol *et al.*, "The Reactor AFM: Non-contact atomic force microscope operating under high-pressure and high-temperature catalytic conditions," *Rev. Sci. Instrum.*, vol. 86, no. 3, p. 033706 (7pp), 2015.

[17] P. Rzeszotarski and Z. Kaszkur, "Surface reconstruction of Pt nanocrystals interacting with gas atmosphere. Bridging the pressure gap with in situ diffraction.," *Phys. Chem. Chem. Phys.*, vol. 11, no. 26, pp. 5416–5421, 2009.

[18] D. W. Goodman, "Model catalysts: From imagining to imaging a working surface," *J. Catal.*, vol. 216, no. 1–2, pp. 213–222, 2003.

[19] F. M. Hoffmann, "Fourier transform infrared reflection absorption spectroscopy studies of adsorbates and surface reactions: Bridging the pressure gap between surface science and catalysis," *J. Vac. Sci. Technol. A Vacuum, Surfaces, Film.*, vol. 11, no. 1993, p. 1957, 1993.

[20] W. Weiss and R. Schlögl, "An integrated surface science approach towards metal oxide catalysis," *Top. Catal.*, vol. 13, pp. 75–90, 2000.

[21] S. M. McClure, M. Lundwall, F. Yang, Z. Zhou, and D. W. Goodman, "CO Oxidation on $Rh/SiO_2/Mo(112)$ Model Catalysts at Elevated Pressures," *J. Phys. Chem. C*, vol. 113, no. 22, pp. 9688–9697, 2009.

[22] F. Gao and D. W. Goodman, "Model Catalysts: Simulating the Complexities of Heterogeneous Catalysts," *Annu. Rev. Phys. Chem.*, vol. 63, no. 1, pp. 265–286, 2012.

[23] A. A. Latimer, F. Abild-Pedersen, and J. K. Nørskov, "A Theoretical Study of Methanol Oxidation on $RuO_2(110)$: Bridging the Pressure Gap," *ACS Catal.*, vol. 7, no. 7, pp. 4527–4534, 2017.

[24] J. Assmann *et al.*, "Heterogeneous oxidation catalysis on ruthenium: Bridging the pressure and materials gaps and beyond," *J. Phys. Condens. Matter*, vol. 20, no. 18, 2008.

[25] A. P. Seitsonen and H. Over, "Intimate interplay of theory and experiments in model catalysis," *Surf. Sci.*, vol. 603, no. 10–12, pp. 1717–1723, 2009.

[26] M. Jørgensen and H. Grönbeck, "Scaling Relations and Kinetic Monte Carlo Simulations to Bridge the Materials Gap in Heterogeneous Catalysis," *ACS Catal.*, vol. 7, no. 8, pp. 5054–5061, 2017.

[27] S. Liang, C. Hao, and Y. Shi, "The Power of Single-Atom Catalysis," *ChemCatChem*, vol. 7, no. 17, pp. 2559–2567, 2015.

[28] J. Liu, "Catalysis by Supported Single Metal Atoms," *ACS Catal.*, vol. 7, no. 1, pp. 34–59, 2017.

[29] B. Han, R. Lang, B. Qiao, A. Wang, and T. Zhang, "Highlights of the major progress in single-atom catalysis in 2015 and 2016," *Cuihua Xuebao/Chinese J. Catal.*, vol. 38, no. 9, pp. 1498–1507, 2017.

[30] S. Mitchell, J. M. Thomas, and J. Pérez-Ramírez, "Single atom catalysis," *Catal. Sci. Technol.*, vol. 7, no. 19, pp. 4248–4249, 2017.

[31] P. Hu *et al.*, "Electronic metal-support interactions in single-atom catalysts," *Angew. Chemie - Int. Ed.*, vol. 53, no. 13, pp. 3418–3421, 2014.

[32] X.-F. Yang, A. Wang, B. Qiao, J. Li, J. Liu, and T. Zhang, "Single-atom catalysts: a new frontier in heterogeneous catalysis.," *Acc. Chem. Res.*, vol. 46, no. 8, pp. 1740–8, 2013.

[33] H. Zhang, G. Liu, L. Shi, and J. Ye, "Single-Atom Catalysts: Emerging Multifunctional Materials in Heterogeneous Catalysis," *Adv. Energy Mater.*, vol. 8, no. 1, pp. 1–24, 2018.

[34] G. S. Parkinson, "Unravelling single atom catalysis: The surface science approach," *Cuihua Xuebao/Chinese J. Catal.*, vol. 38, no. 9, pp. 1454–1459, 2017.

[35] H. Wei *et al.*, "FeO_x -supported platinum single-atom and pseudo-single-atom catalysts for chemoselective hydrogenation of functionalized nitroarenes," *Nat. Commun.*, vol. 5, no. 457, pp. 1–8, 2014.

[36] S. Sun *et al.*, "Single-atom catalysis using Pt/graphene achieved through atomic layer deposition," *Sci. Rep.*, vol. 3, pp. 1–9, 2013.

[37] Y. Chen, Z. Huang, Z. Ma, J. Chen, and X. Tang, "Fabrication, characterization, and stability of supported single-atom catalysts," *Catal. Sci. Technol.*, vol. 7, pp. 4250–4258, 2017.

[38] T. Yang, R. Fukuda, S. Hosokawa, T. Tanaka, S. Sakaki, and M. Ehara, "A Theoretical Investigation on CO Oxidation by Single-Atom Catalysts M_1/γ-Al_2O_3 (M=Pd, Fe, Co, and Ni)," *ChemCatChem*, vol. 9, no. 7, pp. 1222–1229, 2017.

[39] J. L. Shi *et al.*, "An oxidized magnetic Au single atom on doped TiO_2(110) becomes a high performance CO oxidation catalyst due to the charge effect," *J. Mater. Chem. A*, vol. 5, no. 36, pp. 19316–19322, 2017.

[40] J. Liang, X. Yang, C. Xu, T. Zhang, and J. Li, "Catalytic ativities of single-atom catalysts for CO oxidation: Pt^1/FeO_xvs. Fe^1/FeO_x," *Cuihua Xuebao/Chinese J. Catal.*, vol. 38, no. 9, pp. 1566–1573, 2017.

[41] Z. Y. Li, Z. Yuan, X. N. Li, Y. X. Zhao, and S. G. He, "CO oxidation catalyzed by single gold atoms supported on aluminum oxide clusters," *J. Am. Chem. Soc.*, vol. 136, no. 40, pp. 14307–14313, 2014.

[42] H. Gao, "CO oxidation mechanism on the γ-Al_2O_3 supported single Pt atom: First principle study," *Appl. Surf. Sci.*, vol. 379, pp. 347–357, 2016.

[43] M. Moses-Debusk *et al.*, "CO oxidation on supported single Pt atoms: Experimental and ab initio density functional studies of CO interaction with Pt atom on θ-Al_2O_3(010) surface," *J. Am. Chem. Soc.*, vol. 135, no. 34, pp. 12634–12645, 2013.

[44] B. Qiao, J. Lin, A. Wang, Y. Chen, T. Zhang, and J. Liu, "Highly active Au^1/Co_3O_4single-atom catalyst for CO oxidation at room temperature," *Cuihua Xuebao/Chinese J. Catal.*, vol. 36, no. 9, pp. 1505–1511, 2015.

[45] B. Qiao *et al.*, "Highly Efficient Catalysis of Preferential Oxidation of CO in H_2-Rich Stream by Gold Single-Atom Catalysts," *ACS Catal.*, vol. 5, no. 11, pp. 6249–6254, 2015.

[46] S. Li *et al.*, "Interplay between the spin-selection rule and frontier orbital theory in O_2 activation and CO oxidation by single-atom-sized catalysts on TiO_2 (110)," *Phys. Chem.*

Chem. Phys., vol. 18, no. 36, pp. 24872–24879, 2016.

[47] S. Yamazoe, K. Koyasu, and T. Tsukuda, "Nonscalable oxidation catalysis of gold clusters," *Acc. Chem. Res.*, vol. 47, no. 3, pp. 816–824, 2014.

[48] Y. Tang, S. Zhao, B. Long, J. C. Liu, and J. Li, "On the Nature of Support Effects of Metal Dioxides MO_2(M = Ti, Zr, Hf, Ce, Th) in Single-Atom Gold Catalysts: Importance of Quantum Primogenic Effect," *J. Phys. Chem. C*, vol. 120, no. 31, pp. 17514–17526, 2016.

[49] J. Lin, X. Wang, and T. Zhang, "Recent progress in CO oxidation over Pt-group-metal catalysts at low temperatures," *Cuihua Xuebao/Chinese J. Catal.*, vol. 37, no. 11, pp. 1805–1813, 2016.

[50] B. Qiao *et al.*, "Single-atom catalysis of CO oxidation using Pt^1/FeO_x," *Nat. Chem.*, vol. 3, no. 8, pp. 634–641, 2011.

[51] J.-X. Liang *et al.*, "Theoretical and Experimental Investigations on Single-Atom Catalysis: Ir^1/FeO_x for CO Oxidation," *J. Phys. Chem. C*, vol. 118, no. 38, pp. 21945–21951, 2014.

[52] J.-X. Liang, X.-F. Yang, A. Wang, T. Zhang, and J. Li, "Theoretical investigations of non-noble metal single-atom catalysis: Ni_1/FeO_x for CO oxidation," *Catal. Sci. Technol.*, vol. 6, no. 18, pp. 6886–6892, 2016.

[53] B. Qiao *et al.*, "Ultrastable single-atom gold catalysts with strong covalent metal-support interaction (CMSI)," *Nano Res.*, vol. 8, no. 9, pp. 2913–2924, 2015.

[54] C. Wang *et al.*, "Water-Mediated Mars-Van Krevelen Mechanism for CO Oxidation on Ceria-Supported Single-Atom Pt^1 Catalyst," *ACS Catal.*, vol. 7, no. 1, pp. 887–891, 2017.

[55] X. Wang *et al.*, "The synergy between atomically dispersed Pd and cerium oxide for enhanced catalytic properties," *Nanoscale*, vol. 9, no. 20, pp. 6643–6648, 2017.

[56] J. Lin *et al.*, "Remarkable performance of Ir^1/FeO_x single-atom catalyst in water gas shift reaction," *J. Am. Chem. Soc.*, vol. 135, no. 41, pp. 15314–15317, 2013.

[57] S. C. Ammal and A. Heyden, "Titania-Supported Single-Atom Platinum Catalyst for Water-Gas Shift Reaction," *Chemie-Ingenieur-Technik*, vol. 89, no. 10, pp. 1343–1349, 2017.

[58] H. Fei *et al.*, "Atomic cobalt on nitrogen-doped graphene for hydrogen generation," *Nat. Commun.*, vol. 6, pp. 1–8, 2015.

[59] N. Cheng *et al.*, "Platinum single-atom and cluster catalysis of the hydrogen evolution reaction," *Nat. Commun.*, vol. 7, pp. 1–9, 2016.

[60] X. Li *et al.*, "Single-Atom Pt as Co-Catalyst for Enhanced Photocatalytic H_2 Evolution," *Adv. Mater.*, vol. 28, no. 12, pp. 2427–2431, 2016.

[61] J. Xing *et al.*, "Stable isolated metal atoms as active sites for photocatalytic hydrogen evolution," *Chem. - A Eur. J.*, vol. 20, no. 8, pp. 2138–2144, 2014.

[62] G. Gao, Y. Jiao, E. R. Waclawik, and A. Du, "Single Atom (Pd/Pt) Supported on Graphitic Carbon Nitride as an Efficient Photocatalyst for Visible-Light Reduction of Carbon Dioxide," *J. Am. Chem. Soc.*, vol. 138, no. 19, pp. 6292–6297, 2016.

[63] Y. Shi *et al.*, "Single-atom catalysis in mesoporous photovoltaics: The principle of utility

maximization," *Adv. Mater.*, vol. 26, no. 48, pp. 8147–8153, 2014.

[64] A. Corma, O. G. Salnikov, D. A. Barskiy, K. V. Kovtunov, and I. V. Koptyug, "Single-atom gold catalysis in the context of developments in parahydrogen-induced polarization," *Chem. - A Eur. J.*, vol. 21, no. 19, pp. 7012–7015, 2015.

[65] B. Zhang, H. Asakura, J. Zhang, J. Zhang, S. De, and N. Yan, "Stabilizing a Platinum[1] Single-Atom Catalyst on Supported Phosphomolybdic Acid without Compromising Hydrogenation Activity," *Angew. Chemie - Int. Ed.*, vol. 55, no. 29, pp. 8319–8323, 2016.

[66] X.-L. Ding, D. Wang, R.-J. Li, H.-L. Liao, Y. Zhang, and H.-Y. Zhang, "Adsorption of a single gold or silver atom on vanadium oxide clusters," *Phys. Chem. Chem. Phys.*, vol. 18, no. 14, pp. 9497–9503, 2016.

[67] E. Fako, Z. Łodziana, and N. López, "Comparative single atom heterogeneous catalysts (SAHCs) on different platforms: a theoretical approach," *Catal. Sci. Technol.*, pp. 4285–4293, 2017.

[68] T.-Y. Chang *et al.*, "Direct Imaging of Pt Single Atoms Adsorbed on TiO_2(110) Surfaces," *Nano Lett.*, vol. 14, no. 1, pp. 134–138, 2014.

[69] J. C. Liu, Y. G. Wang, and J. Li, "Toward Rational Design of Oxide-Supported Single-Atom Catalysts: Atomic Dispersion of Gold on Ceria," *J. Am. Chem. Soc.*, vol. 139, no. 17, pp. 6190–6199, 2017.

[70] Y. T. Kim *et al.*, "Fine size control of platinum on carbon nanotubes: From single atoms to clusters," *Angew. Chemie - Int. Ed.*, vol. 45, no. 3, pp. 407–411, 2006.

[71] C. Ratnasamy and J. P. Wagner, "Water Gas Shift Catalysis," *Catal. Rev.*, vol. 51, no. 3, pp. 325–440, 2009.

[72] Z. Chen, D. Higgins, A. Yu, L. Zhang, and J. Zhang, "A review on non-precious metal electrocatalysts for PEM fuel cells," *Energy Environ. Sci.*, vol. 4, no. 9, p. 3167, 2011.

[73] C. G. Granqvist, "Transparent conductors as solar energy materials: A panoramic review," *Sol. Energy Mater. Sol. Cells*, vol. 91, no. 17, pp. 1529–1598, 2007.

[74] M. S. Whittingham, "Lithium batteries and cathode materials," *Chem. Rev.*, vol. 104, no. 10, pp. 4271–4301, 2004.

[75] G. Eranna, B. C. Joshi, D. P. Runthala, and R. P. Gupta, "Oxide materials for development of integrated gas sensors - A comprehensive review," *Crit. Rev. Solid State Mater. Sci.*, vol. 29, no. 3–4, pp. 111–188, 2004.

[76] J. Meyer, S. Hamwi, M. Kröger, W. Kowalsky, T. Riedl, and A. Kahn, "Transition metal oxides for organic electronics: Energetics, device physics and applications," *Adv. Mater.*, vol. 24, no. 40, pp. 5408–5427, 2012.

[77] M. Calatayud, A. Markovits, M. Menetrey, B. Mguig, and C. Minot, "Adsorption on perfect and reduced surfaces of metal oxides," *Catal. Today*, vol. 85, no. 2–4, pp. 125–143, 2003.

[78] R. A. Van Santen, I. Tranca, and E. J. M. Hensen, "Theory of surface chemistry and reactivity of reducible oxides," *Catal. Today*, vol. 244, pp. 63–84, 2015.

[79] G. L. Haller and D. E. Resasco, "Metal Support Interaction - Group-VIII Metals and

Reducible Oxides," *Adv. Catal.*, vol. 36, pp. 173–235, 1989.

[80] U. Diebold, "The surface science of titanium dioxide," *Surf. Sci. Rep.*, vol. 48, no. 5–8, pp. 53–229, 2003.

[81] L. Kundakovic and M. Flytzani-Stephanopoulos, "Reduction characteristics of copper oxide in cerium and zirconium oxide systems," *Appl. Catal. A Gen.*, vol. 171, no. 1, pp. 13–29, 1998.

[82] S. A. C. Carabineiro, N. Bogdanchikova, P. B. Tavares, and J. L. Figueiredo, "Nanostructured iron oxide catalysts with gold for the oxidation of carbon monoxide," *RSC Adv.*, vol. 2, no. 7, p. 2957, 2012.

[83] J. Rosen, G. S. Hutchings, and F. Jiao, "Ordered mesoporous cobalt oxide as highly efficient oxygen evolution catalyst," *J. Am. Chem. Soc.*, vol. 135, no. 11, pp. 4516–4521, 2013.

[84] Y. Gorlin *et al.*, "In situ X-ray absorption spectroscopy investigation of a bifunctional manganese oxide catalyst with high activity for electrochemical water oxidation and oxygen reduction," *J. Am. Chem. Soc.*, vol. 135, no. 23, pp. 8525–8534, 2013.

[85] G. C. Bond and S. F. Tahir, "Vanadium oxide monolayer catalysts Preparation, characterization and catalytic activity," *Appl. Catal.*, vol. 71, no. 1, pp. 1–31, 1991.

[86] Y. Borchert, P. Sonström, M. Wilhelm, H. Borchert, and M. Bäumer, "Nanostructured praseodymium oxide: Preparation, structure, and catalytic properties," *J. Phys. Chem. C*, vol. 112, no. 8, pp. 3054–3063, 2008.

[87] D. R. Mullins, "The surface chemistry of cerium oxide," *Surf. Sci. Rep.*, vol. 70, no. 1, pp. 42–85, 2015.

[88] E. Aneggi, M. Boaro, C. De Leitenburg, G. Dolcetti, and A. Trovarelli, "Insights into the redox properties of ceria-based oxides and their implications in catalysis," *J. Alloys Compd.*, vol. 408–412, pp. 1096–1102, 2006.

[89] C. D. Duprez, T. Birchem, and E. Rohart, "Oxygen storage and mobility on model three-way catalysts," *Top. Catal.*, vol. 16/17, no. 1–4, pp. 49–56, 2001.

[90] N. V. Skorodumova, S. I. Simak, B. I. Lundqvist, I. A. Abrikosov, and B. Johansson, "Quantum origin of the oxygen storage capability of ceria," *Phys. Rev. Lett.*, vol. 89, no. 16, p. 166601/1-166601/4, 2002.

[91] J. F. Jerratsch *et al.*, "Electron localization in defective ceria films: A study with scanning-tunneling microscopy and density-functional theory," *Phys. Rev. Lett.*, vol. 106, no. 24, pp. 1–4, 2011.

[92] X. Shao, J.-F. Jerratsch, N. Nilius, and H.-J. Freund, "Probing the 4f states of ceria by tunneling spectroscopy," *Phys. Chem. Chem. Phys.*, vol. 13, no. 27, p. 12646, 2011.

[93] S. Fabris, G. Vicario, G. Balducci, S. De Gironcoli, and S. Baroni, "Electronic and atomistic structures of clean and reduced ceria surfaces," *J. Phys. Chem. B*, vol. 109, no. 48, pp. 22860–22867, 2005.

[94] G. Kresse, P. Blaha, J. L. F. Da Silva, and M. V. Ganduglia-Pirovano, "Comment on 'Taming multiple valency with density functionals: A case study of defective ceria,'" *Phys. Rev. B* -

Condens. Matter Mater. Phys., vol. 72, no. 23, pp. 6–9, 2005.

[95] T. Staudt, Y. Lykhach, L. Hammer, M. A. Schneider, V. Matolín, and J. Libuda, "A route to continuous ultra-thin cerium oxide films on Cu(111)," *Surf. Sci.*, vol. 603, no. 23, pp. 3382–3388, 2009.

[96] S. M. Kozlov, F. Viñes, N. Nilius, S. Shaikhutdinov, and K. M. Neyman, "Absolute surface step energies: Accurate theoretical methods applied to ceria nanoislands," *J. Phys. Chem. Lett.*, vol. 3, no. 15, pp. 1956–1961, 2012.

[97] F. Šutara *et al.*, "Epitaxial growth of continuous CeO_2(111) ultra-thin films on Cu(111)," *Thin Solid Films*, vol. 516, no. 18, pp. 6120–6124, 2008.

[98] T. Duchoň *et al.*, "Exploiting micro-scale structural and chemical observations in real time for understanding chemical conversion: LEEM/PEEM studies over CeO_x–Cu(111)," *Ultramicroscopy*, vol. 183, pp. 1339–1351, 2017.

[99] J.-L. Lu, H.-J. Gao, S. Shaikhutdinov, and H.-J. Freund, "Morphology and defect structure of the CeO_2(111) films grown on Ru(0001) as studied by scanning tunneling microscopy," *Surf. Sci.*, vol. 600, no. 22, pp. 5004–5010, 2006.

[100] D. R. Mullins, P. V. Radulovic, and S. H. Overbury, "Ordered cerium oxide thin films grown on Ru(0001) and Ni(111)," *Surf. Sci.*, vol. 429, no. 1, pp. 186–198, 1999.

[101] K. Mašek, J. Beran, and V. Matolín, "RHEED study of the growth of cerium oxide on Cu(111)," *Appl. Surf. Sci.*, vol. 259, pp. 34–38, 2012.

[102] G. Adachi and N. Imanaka, "The Binary Rare Earth Oxides," *Chem. Rev.*, vol. 98, no. 4, pp. 1479–1514, 1998.

[103] F. Dvořák *et al.*, "Adjusting morphology and surface reduction of CeO_2(111) thin films on Cu(111)," *J. Phys. Chem. C*, vol. 115, no. 15, pp. 7496–7503, 2011.

[104] W. Xiao, Q. Guo, and E. G. Wang, "Transformation of CeO_2(111) to Ce_2O_3(0001) films," vol. 368, pp. 527–531, 2003.

[105] D. R. Mullins, M. D. Robbins, and J. Zhou, "Adsorption and reaction of methanol on thin-film cerium oxide," *Surf. Sci.*, vol. 600, no. 7, pp. 1547–1558, 2006.

[106] V. Stetsovych *et al.*, "Epitaxial cubic Ce_2O_3 films via Ce-CeO_2 interfacial reaction," *J. Phys. Chem. Lett.*, vol. 4, no. 6, pp. 866–871, 2013.

[107] J. Mysliveček, V. Matolín, and I. Matolínová, "Heteroepitaxy of cerium oxide thin films on Cu(111)," *Materials (Basel).*, vol. 8, no. 9, pp. 6346–6359, 2015.

[108] T. Duchoň *et al.*, "Ordered phases of reduced ceria as epitaxial films on Cu(111)," *J. Phys. Chem. C*, vol. 118, no. 1, pp. 357–365, 2014.

[109] V. P. Zhdanov and B. Kasemo, "Kinetic models of oxygen supply from CeO_x to active nanometer particles of three-way catalysts," *Appl. Surf. Sci.*, vol. 135, no. 1–4, pp. 297–306, 1998.

[110] R. Di Monte and J. Kašpar, "On the role of oxygen storage in three-way catalysis," *Top. Catal.*, vol. 28, no. 1–4, pp. 47–57, 2004.

[111] S. E. Golunski, H. A. Hatcher, R. R. Rajaram, and T. J. Truex, "Origins of low-temperature three-way activity in Pt/CeO_2," *Appl. Catal. B, Environ.*, vol. 5, no. 4, pp. 367–376, 1995.

[112] J. Kašpar, P. Fornasiero, and M. Graziani, "Use of CeO_2-based oxides in the three-way catalysis," *Catal. Today*, vol. 50, no. 2, p. 285, 1999.

[113] M. A. Henderson, C. L. Perkins, M. H. Engelhard, S. Thevuthasan, and C. H. F. Peden, "Redox properties of water on the oxidized and reduced surfaces of CeO_2(1 1 1)," *Surf. Sci.*, vol. 526, no. 1–2, pp. 1–18, 2003.

[114] D. R. Mullins *et al.*, "Water Dissociation on CeO_2(100) and CeO_2(111) Thin Films," *J. Phys. Chem. C*, vol. 116, no. 36, pp. 19419–19428, 2012.

[115] Ko, G. H. Simon, H. P. Rust, G. Pacchioni, M. Heyde, and H. J. Freund, "Measuring the Charge State of Point Defects on MgO/ Ag(001)," *J. Am. Chem. Soc.*, vol. 131, no. 1, p. 17544, 2009.

[116] M. Setvín, M. Wagner, M. Schmid, G. S. Parkinson, and U. Diebold, "Surface point defects on bulk oxides: atomically-resolved scanning probe microscopy," *Chem. Soc. Rev.*, vol. 46, no. 7, pp. 1772–1784, 2017.

[117] F. Dvořák, "Interaction of simple molecules with reducible oxides: model studies of H_2O/CeO_x and CO/CuO_x," Doctoral Thesis, Charles University in Prague, 2014.

[118] G. Binnig and H. Rohrer, "Scanning tunneling microscopy," *Surf. Sci.*, vol. 126, no. 1–3, pp. 236–244, 1983.

[119] G. Binnig, H. Rohrer, C. Gerber, and E. Weibel, "Surface studies by scanning tunneling microscopy," *Phys. Rev. Lett.*, vol. 49, no. 1, pp. 57–61, 1982.

[120] C. J. Chen, "Introduction to Scanning Tunneling Microscopy Second Edition," *Oxford Univ. Press*, p. (2008), 2008.

[121] V. Mironov, "Fundamentals of Scanning Probe Microscopy," *The Russian Academy Of Sciences, Institute For Physics Of Microstructures*, 2004.

[122] F. Máca, "Electronic Structure and STM Images of Na on Al(111)," *Surf. Interface Anal*, vol. 27, September 1998, pp. 555–557, 1999.

[123] D. Drakova, G. Doyen, and F. Máca, "Theory of STM and STS on p(2x2)Na/A1(111)," *Surf. Sci.*, vol. 352–354, pp. 704–710, 1996.

[124] F. Máca, W. A. Hofer, and J. Redinger, "Ab initio simulations and STM-images for Co/Pt(110) surfaces," *Surf. Sci.*, vol. 482–485, pp. 844–849, 2001.

[125] F. Besenbacher, J. V. Lauritsen, T. R. Linderoth, E. Lægsgaard, R. T. Vang, and S. Wendt, "Atomic-scale surface science phenomena studied by scanning tunneling microscopy," *Surf. Sci.*, vol. 603, no. 10–12, pp. 1315–1327, 2009.

[126] O. Stetsovych, F. Dvořák, L. Szabová, S. Fabris, J. Mysliveček, and V. Matolín, "Nanometer-range strain distribution in layered incommensurate systems," *Phys. Rev. Lett.*, vol. 109, no. 26, pp. 1–5, 2012.

[127] R. T. Vang, J. V. Lauritsen, E. Lægsgaard, and F. Besenbacher, "Scanning tunneling microscopy as a tool to study catalytically relevant model systems," *Chem. Soc. Rev.*, vol. 37,

no. 10, p. 2191, 2008.

[128] S. Morita, “Roadmap of scanning probe microscopy,” 2006.

[129] O. Guise, H. Marbach, J. T. Yates, M. C. Jung, J. Levy, and J. Ahner, “Development and performance of the nanoworkbench: A four tip STM for conductivity measurements down to submicrometer scales,” *Rev. Sci. Instrum.*, vol. 76, no. 4, 2005.

[130] E. Papis-Polakowska *et al.*, “X-Ray photoelectron spectroscopy-methodology and application,” *Acta Phys. Pol. A*, vol. 125, no. 4, pp. 1061–1064, 2014.

[131] F. Dvořák *et al.*, “Creating single-atom Pt-ceria catalysts by surface step decoration,” *Nat. Commun.*, vol. 7, 2016.

[132] V. Matolín, I. Matolínova, L. Sedlek, K. C. Prince, and T. Skla, “A resonant photoemission applied to cerium oxide based nanocrystals,” *Nanotechnology*, vol. 20, no. 21, 2009.

[133] V. Smidt, “Photoionization of Atoms and Molecules Using Synchrotron Radiation,” *IEEE Trans. Nucl. Sci.*, vol. 28, no. 2, pp. 1215–1219, 1981.

[134] M. Salmeron, “Ambient pressure photoelectron spectroscopy: A new tool for surface science and nanotechnology,” *Surf. Sci. Rep.*, vol. 63, no. December 2007, pp. 169–199, 2008.

[135] K. Heinz, “Leed and Dleed As Modern Tools for Quantitative Surface-Structure Determination,” *Rep Prog Phys*, vol. 58, no. 6, pp. 637–704, 1995.

[136] D. A. King, “Thermal desorption from metal surfaces: A review,” *Surf. Sci.*, vol. 47, no. 1, pp. 384–402, 1975.

[137] A. M. de Jong and J. W. Niemantsverdriet, “Thermal desorption analysis: Comparative test of ten commonly applied procedures,” *Surf. Sci.*, vol. 233, no. 3, pp. 355–365, 1990.

[138] D. Nečas and P. Klapetek, “Gwyddion: An open-source software for SPM data analysis,” *Cent. Eur. J. Phys.*, vol. 10, no. 1, pp. 181–188, 2012.

[139] J. Libra, “KolXPD: Software for spectroscopy data measurement and processing.” [Online]. Available: https://www.kolibrik.net/science/kolxpd/.

[140] G. Sauerbrey, “Verwendung von Schwingquarzen zur Wägung dünner Schichten und zur Mikrowägung,” *Zeitschrift für Phys.*, vol. 155, no. 2, pp. 206–222, 1959.

[141] T. Skála, F. Šutara, K. C. Prince, and V. Matolín, “Cerium oxide stoichiometry alteration via Sn deposition: Influence of temperature,” *J. Electron Spectros. Relat. Phenomena*, vol. 169, no. 1, pp. 20–25, 2009.

[142] T. Skála, F. Šutara, M. Škoda, K. C. Prince, and V. Matolín, “Palladium interaction with CeO_2, Sn-Ce-O and Ga-Ce-O layers,” *J. Phys. Condens. Matter*, vol. 21, no. 5, 2009.

[143] “Igor Pro - Overview.” [Online]. Available: http://www.wavemetrics.com/products/igorpro/igorpro.htm.

[144] J. Graciani *et al.*, “Highly active copper-ceria and copper-ceria-titania catalysts for methanol synthesis from CO_2,” *Science*, vol. 345, no. 6196, pp. 546–550, 2014.

[145] C. T. Campbell, “The Effect of Size-Dependent Nanoparticle Energetics on Catalyst

Sintering," *Science*, vol. 298, no. 5594, pp. 811–814, 2002.

[146] A. Bruix *et al.*, "A new type of strong metal-support interaction and the production of H_2 through the transformation of water on $Pt/CeO_2(111)$ and $Pt/CeO_{(x)}/TiO_2(110)$ catalysts.," *J. Am. Chem. Soc.*, vol. 134, no. 21, pp. 8968–74, 2012.

[147] G. N. Vayssilov *et al.*, "Support nanostructure boosts oxygen transfer to catalytically active platinum nanoparticles," *Nat. Mater.*, vol. 10, no. 4, pp. 310–315, 2011.

[148] M . S . Chen and D . W . Goodman, "The Structure of Catalytically Active Gold on Titania *American Association for the Advancement of Science*, URL : http://www.jstor.org/stable/3839205," *Adv. Sci.*, vol. 306, no. 5694, pp. 252–255, 2010.

[149] U. Landman, B. Yoon, C. Zhang, U. Heiz, and M. Arenz, "Factors in gold nanocatalysis: Oxidation of CO in the non-scalable size regime," *Top. Catal.*, vol. 44, no. 1–2, pp. 145–158, 2007.

[150] P. L. Hansen, "Atomic resolved imaging of dynamic shape changes in supported copper nanocrystals," *Science*, vol. 205, no. March, pp. 2053–2055, 2002.

[151] A. Bruix *et al.*, "Maximum Noble-Metal Efficiency in Catalytic Materials: Atomically Dispersed Surface Platinum," *Angew. Chemie Int. Ed.*, vol. 53, no. 39, pp. 10525–10530, 2014.

[152] Q. Fu, H. Saltsburg, and M. Flytzani-Stephanopoulos, "Active nonmetallic Au and Pt species on ceria-based water-gas shift catalysts," *Science*, vol. 301, no. 5635, pp. 935–938, 2003.

[153] S. J. Tauster, S. C. Fung, R. T. K. Baker, and J. A. Horsley, "Strong Interactions in Supported-Metal Catalysts," *Science*, vol. 211, no. 4487, pp. 1121–1125, 1981.

[154] O. Dulub, W. Hebenstreit, and U. Diebold, "Imaging cluster surfaces with atomic resolution: The strong metal-support interaction state of pt supported on $TiO_2(110)$," *Phys. Rev. Lett.*, vol. 84, no. 16, pp. 3646–3649, 2000.

[155] C. T. Campbell, "Catalyst-support interactions: Electronic perturbations," *Nat. Chem.*, vol. 4, no. 8, pp. 597–598, 2012.

[156] G. K. Wertheim, S. B. Dicenzo, and S. E. Youngquist, "Unit charge on supported gold clusters in photoemission final state," *Phys. Rev. Lett.*, vol. 51, no. 25, pp. 2310–2313, 1983.

[157] W. E. Kaden *et al.*, "Understanding surface core-level shifts using the Auger parameter: A study of Pd atoms adsorbed on ultrathin SiO_2 films," *Phys. Rev. B - Condens. Matter Mater. Phys.*, vol. 89, no. 11, pp. 1–8, 2014.

[158] A. W. Grant and C. T. Campbell, "Cesium adsorption on $TiO_2(110)$," *Phys. Rev. B*, vol. 55, no. 3, pp. 1844–1851, 1997.

[159] M. Hatanaka *et al.*, "Ideal Pt loading for a Pt/CeO_2-based catalyst stabilized by a Pt-O-Ce bond," *Appl. Catal. B Environ.*, vol. 99, no. 1–2, pp. 336–342, 2010.

[160] R. Fiala *et al.*, "Proton exchange membrane fuel cell made of magnetron sputtered $Pt–CeO_x$ and Pt–Co thin film catalysts," *J. Power Sources*, vol. 273, pp. 105–109, 2015.

[161] N. J. Castellani, M. Branda, K. M. Neyman, and F. Illas, "Density Functional Theory Study of the Adsorption of Au Atom on Cerium Oxide : Effect of," pp. 4948–4954, 2009.

[162] T. Zambelli, J. Wintterlin, J. Trost, and G. Ertl, "Identification of the 'Active Sites' of a Surface-Catalyzed Reaction," *Science*, vol. 273, no. 5282, pp. 1688–1690, 1996.

[163] J. V. Barth, G. Costantini, and K. Kern, "Engineering atomic and molecular nanostructures at surfaces," *Nature*, vol. 437, no. 7059, pp. 671–679, 2005.

[164] S. M. Kozlov and K. M. Neyman, "O vacancies on steps on the CeO_2(111) surface," *Phys. Chem. Chem. Phys.*, vol. 16, no. 17, p. 7823, 2014.

[165] M. V. Twigg, "Progress and future challenges in controlling automotive exhaust gas emissions," *Appl. Catal. B Environ.*, vol. 70, no. 1–4, pp. 2–15, 2007.

[166] M. Boaro, C. De Leitenburg, G. Dolcetti, and A. Trovarelli, "The dynamics of oxygen storage in ceria-zirconia model catalysts measured by CO oxidation under stationary and cycling feedstream compositions," *J. Catal.*, vol. 193, no. 2, pp. 338–347, 2000.

[167] G. Zhou *et al.*, "High activity of $Ce_{1-x}Ni_xO_{2-y}$ for H_2 production through ethanol steam reforming: Tuning catalytic performance through metal-oxide interactions," *Angew. Chemie - Int. Ed.*, vol. 49, no. 50, pp. 9680–9684, 2010.

[168] A. Hornés *et al.*, "Inverse CeO_2/CuO catalyst as an alternative to classical direct configurations for preferential oxidation of CO in hydrogen-rich stream," *J. Am. Chem. Soc.*, vol. 132, no. 1, pp. 34–35, 2010.

[169] A. Kubacka *et al.*, "Tungsten as an interface agent leading to highly active and stable copper-ceria water gas shift catalyst," *Appl. Catal. B Environ.*, vol. 132–133, pp. 423–432, 2013.

[170] S. Abanades and G. Flamant, "Thermochemical hydrogen production from a two-step solar-driven water-splitting cycle based on cerium oxides," *Sol. Energy*, vol. 80, no. 12, pp. 1611–1623, 2006.

[171] W. C. Chueh, M. Abbott, D. Scipio, and S. M. Haile, "High-flux solar-driven thermochemical dissociation of CO_2 and H_2O using ceria redox reactions," *Science*, vol. 63, no. December, p. 2010, 2010.

[172] J. M. Thomas, "Heterogeneous catalysis and the challenges of powering the planet, securing chemicals for civilised life, and clean efficient utilization of renewable feedstocks," *ChemSusChem*, vol. 7, no. 7, pp. 1801–1832, 2014.

[173] B. Yildiz, "Stretching the energy landscape of oxides - Effects on electrocatalysis and diffusion," *MRS Bull.*, vol. 39, no. 2, pp. 147–156, 2014.

[174] J. A. Rodríguez and J. Hrbek, "Inverse oxide/metal catalysts: A versatile approach for activity tests and mechanistic studies," *Surf. Sci.*, vol. 604, no. 3–4, pp. 241–244, 2010.

[175] J. A. Rodriguez *et al.*, "Water-gas shift reaction on a highly active inverse CeO_x/Cu(111) catalyst: Unique role of ceria nanoparticles," *Angew. Chemie - Int. Ed.*, vol. 48, no. 43, pp. 8047–8050, 2009.

[176] F. P. Netzer, "'Small and beautiful' - The novel structures and phases of nano-oxides," *Surf. Sci.*, vol. 604, no. 5–6, pp. 485–489, 2010.

[177] F. P. Netzer, F. Allegretti, and S. Surnev, "Low-dimensional oxide nanostructures on metals: Hybrid systems with novel properties," *J. Vac. Sci. Technol. B, Nanotechnol. Microelectron.*

Mater. Process. Meas. Phenom., vol. 28, no. 1, pp. 1–16, 2010.

[178] S. D. Senanayake, D. Stacchiola, and J. Rodriguez, "Unique Properties of Ceria Nanoparticles Supported on Metals: Novel Inverse Ceria/Copper Catalysts for CO Oxidation and the Water-Gas Shift Reaction," *Acc. Chem. Res.*, vol. 46, no. 8, pp. 1702–1711, Aug. 2013.

[179] J. A. Rodriguez, S. Ma, P. Liu, J. Hrbek, J. Evans, and M. Perez, "Activity of CeO_x and TiO_x Nanoparticles Grown on Au(111) in the Water-Gas Shift Reaction," *Science*, vol. 318, no. 5857, pp. 1757–1760, 2007.